Titre: Title:	Solid Particle Erosion Mechanisms of Protective Coatings for Aerospace Applications
Auteur: Author:	Étienne Bousser
Date:	2013
Type:	Mémoire ou thèse / Dissertation or Thesis
Référence: Citation:	Bousser, É. (2013). Solid Particle Erosion Mechanisms of Protective Coatings for Aerospace Applications [Thèse de doctorat, École Polytechnique de Montréal]. PolyPublie. https://publications.polymtl.ca/1126/

URL de PolyPublie: PolyPublie URL:	https://publications.polymtl.ca/1126/
Directeurs de recherche: Advisors:	Ludvik Martinu, & Jolanta-Ewa Sapieha
Programme: Program:	Génie physique

UNIVERSITÉ DE MONTRÉAL

SOLID PARTICLE EROSION MECHANISMS OF PROTECTIVE COATINGS FOR AEROSPACE APPLICATIONS

ETIENNE BOUSSER

DÉPARTEMENT DE GÉNIE PHYSIQUE

ÉCOLE POLYTECHNIQUE DE MONTRÉAL

THÈSE PRÉSENTÉE EN VUE DE L'OBTENTION

DU DIPLÔME DE PHILOSOPHIÆ DOCTOR

(GÉNIE PHYSIQUE)

AVRIL 2013

UNIVERSITÉ DE MONTRÉAL

ÉCOLE POLYTECHNIQUE DE MONTRÉAL

Cette thèse intitulée:

SOLID PARTICLE EROSION MECHANISMS OF PROTECTIVE COATINGS FOR AEROSPACE APPLICATIONS

présentée par : BOUSSER Etienne
en vue de l'obtention du diplôme de : Philosophiæ Doctor
a été dûment acceptée par le jury d'examen constitué de :

M. DESJARDINS Patrick, Ph. D., président
Mme SAPIEHA Jolanta Ewa, Ph. D., membre et directrice de recherche
M. MARTINU Ludvik, Ph. D., membre et codirecteur de recherche
M. LÉVESQUE Martin, Ph. D., membre
M. MATTHEWS Allan, Ph. D., membre

To Caroline, with whom I share the most wonderful life.

ACKNOWLEDGMENTS

First of all, I wish to thank my thesis directors, Professors Jolanta Sapieha and Ludvik Martinu for taking a chance on a mechanical engineer who had much to learn on physical science. I thank you both for your guidance and support, but most of all for the trust you place in me.

Furthermore, I would like to thank Professor Patrick Desjardins, Professor Allan Matthews, and Professor Martin Lévesque for accepting to evaluate my PhD thesis and be members of the jury.

I would like to thank all the partners I've had the pleasure of working with on this project: Pratt and Whitney Canada, MDS Coatings Technologies, Bell Helicopter Textron Ltd, McGill University, Université de Sherbrooke and the Nation Research Council's Aerospace Research Institute. I would also like to acknowledge the financial support from the Natural Sciences and Engineering Research Council (NSERC) of Canada, the Consortium for Research and Innovation in Aerospace in Québec (CRIAQ) and the Fonds de recherche du Québec - Nature et Technologies (FQRNT).

During the more than nine years I've spent at the Functional Coatings and Surface Engineering Laboratory (FCSEL), I've had the pleasure of working with many gifted and kind people. Most are colleagues and some have become friends, but all have contributed in their way to the person and researcher I am today. Thanks to: Aram Amassian, Marwan Azzi, Bill Baloukas, Moushab Benkahoul, Samih Beskri, Jiri Capek, Marie-Maude de Denus Baillargeon, Mariusz Dudek, Jean-Philippe Fortier, Simon Gaudet, Srinivasan Guruvenket, Soroush Hafezian, Matej Hala, Salim Hassani, Christophe Hecquet, Pawel Jedrzejowski, Ganesh Kamath, Jean-Michel Lamarre, Stéphane Larouche, Duanji Li, Simon Loquai, Viktor Marushka, Jean-Philippe Masse, Matjaz Panjan , Thomas Poirié, Fabrice Pougoum, Édouard Proust, Alexis Ragusich, Philippe Robin, Thomas Schmitt, Luc Vernhes, Richard Vernhes, Nicolas Viau and Oleg Zabeida. I apologize in advance if I have forgotten anyone; nothing is meant by it except that I am forgetful.

I would like to thank all the co-authors of my papers and all who've helped one way or another in the advancement of my project. In particular, I could not have done any of the work without the technical assistance of Sébastien Chenard, Yves Drolet and particularly Francis Turcot with whom I've spent many hours making things work.

I would like to specifically thank Professor Rony Snyders from the Université de Mons for his friendship and the many collaborative projects we've worked on together. I also owe him a large debt of gratitude for making me rediscover my love for the beautiful game.

Finally, I can't express enough my gratitude to my parents who have been my greatest role models and given so much that has made me the person I am today. Last but not least, is the love and thanks I have for my wife Caroline. Without her, no part of this project would have been possible. Thank you for our wonderful life together.

RÉSUMÉ

Le progrès économique et technologique ainsi que les considérations environnementales nécessitent la conception d'équipements de plus en plus performants, sollicitant les composantes aux limites de leur capacité. Une conséquence importante de cette demande accrue au niveau de la performance est que les lacunes de type tribologique, telles que la dégradation du lubrifiant, l'usure excessive et la tribocorrosion, peuvent être amplifiées de façon significative, menant à des coûts d'exploitation additionnels, une efficacité moindre et une défaillance prématurée. Puisque les processus tribologiques découlent de l'interaction entre au moins deux corps en mouvement relatif dans un environnement donné, l'ingénierie de surface peut permettre de conférer aux surfaces la performance de pointe requise lorsque les conditions de fonctionnement sont très exigeantes. Dans ce contexte, la conception de systèmes de matériaux appropriés doit être guidée par une connaissance poussée des mécanismes de dégradation et de la réponse de la surface au chargement et à la déformation, qui agissent souvent de façon synergique.

L'érosion par impact de particules solides (EIPS) survient lorsque des particules solides dures, présentes dans l'environnement, sont entraînées par un fluide et impactent les surfaces de composantes. Ce type de dommage est spécifiquement marqué dans la première section d'un moteur d'avion, où les pales du compresseur peuvent s'éroder à un point tel que la performance aérodynamique et même l'intégrité structurale sont compromises. Ainsi, de nombreux travaux de recherche ont été réalisés dans les secteurs académique et industriel afin de comprendre les mécanismes de perte de matière impliqués dans l'EIPS et afin de développer des technologies protectrices dans le but d'améliorer la durée de vie utile des composantes. Un exemple est l'utilisation de revêtements protecteurs durs afin de limiter l'érosion des composantes de moteur d'avion, qui sont pour la plupart métalliques.

Dans cette optique, l'objectif principal de ce projet de doctorat est d'étudier les mécanismes de perte de matière pendant l'EIPS de couches dures protectrices, incluant les systèmes nanocomposites et nanostructurés. De plus, étant donné la nature complexe des mécanismes d'EIPS, des méthodologies expérimentales rigoureuses doivent être mises en œuvre, et les effets de tous les paramètres de test impliqués doivent être entièrement compris. Dans cette thèse de doctorat, l'importance de la méthodologie expérimentale est mise de l'avant tout au long du

projet, afin d’étudier de façon éclairée les mécanismes d’EIPS des matériaux fragiles et des revêtements dures.

Dans l’étape initiale de cette thèse, nous avons étudié l’effet de l’ajout de silicium (Si) sur la microstructure, les propriétés mécaniques et, plus spécifiquement, sur la résistance à l’EIPS de couches épaisses de type CrN. Nous avons observé que l’ajout de Si améliorait de façon significative la résistance à l’érosion et que l’EIPS était corrélée avec les valeurs de microdureté, *i.e.* les couches ayant la microdureté la plus élevée présentaient aussi les taux d’érosion (*TE*) les plus bas. En fait, les *TE* se sont révélés être beaucoup plus dépendants de la dureté de surface que ce qui avait été proposé auparavant pour les mécanismes d’érosion fragiles.

À partir de ces résultats initiaux, quatre objectifs spécifiques ont été formulés pour ce projet de doctorat: a) développer une méthodologie solide pour la caractérisation de l’EIPS des systèmes de revêtements, b) étudier les effets des propriétés des particules sur les mécanismes d’EIPS des matériaux fragiles, c) déterminer la relation entre les propriétés mécaniques de revêtements et leur comportement sous EIPS, et d) développer une méthodologie expérimentale *in situ* résolue dans le temps afin d’étudier les mécanismes d’EIPS des systèmes de revêtements protecteurs. Les résultats principaux sont présentés sous forme d’articles évalués par des pairs.

Dans le premier article, nous examinons les effets des propriétés des particules sur le comportement sous EIPS de six matériaux massiques fragiles, à l’aide de poudre de verre et d’alumine. Tout d’abord, nous appliquons une méthodologie solide afin de caractériser précisément les propriétés élasto-plastiques et de rupture des matériaux étudiés. Nous corrélons ensuite le *TE* mesuré avec les paramètres des matériaux à l’aide d’une étude morphologique et d’une analyse des modèles d’érosion quasi-statiques élasto-plastiques. Finalement, afin de comprendre les effets des impacts sur les particules elles-mêmes et dans le but de supporter le modèle basé sur la dissipation d’énergie, nous examinons la distribution de taille des particules des poudres avant et après érosion. Nous démontrons que pour les deux poudres utilisées le mécanisme de perte de matière est celui par fissuration latérale, que les exposants de vitesse sont plus élevés qu’anticipé originalement ce qui suggère que le mécanisme d’accumulation de dommages dépende de la vitesse et qu’il est corrélé à la pression d’écoulement plastique de la cible, et que les effets d’accumulation de dommages sont plus prononcés dans le cas de la poudre de verre, moins dure que l’alumine, à cause de la dissipation d’énergie par divers moyens.

Dans le second article, nous étudions les mécanismes d'érosion pour plusieurs revêtements durs déposés par pulvérisation magnétron pulsée en courant continu. Nous validons d'abord une nouvelle méthodologie permettant de mesurer de façon précise le volume perdu, et nous démontrons l'importance d'optimiser les paramètres de test afin d'obtenir des résultats exempts d'artéfacts expérimentaux. Nous corrélons ensuite les *TE* mesurés avec les propriétés des matériaux déterminées par indentation résolue en profondeur. Afin de comprendre les mécanismes de perte de matière, nous étudions en détail trois systèmes de revêtements à l'aide de la caractérisation de la rupture et d'une étude morphologique des surfaces érodées. Finalement, nous examinons les distributions de taille de particules des poudres avant et après érosion, afin de comprendre le rôle de la rupture des particules. Nous démontrons que les *TE* mesurés sont très dépendants de la dureté de la cible et ne corrèlent pas avec la ténacité du revêtement. En fait, le mécanisme d'enlèvement de matière apparaît suite à l'indentation ductile et la coupure répétée de la surface par les particules. La fragmentation des particules n'est pas suffisamment importante pour influencer les résultats de façon significative.

L'étude détaillée des mécanismes d'EIPS des revêtements protecteurs s'avère très ardue puisque les tests d'EIPS classiques sont reconnus comme étant inexacts à cause de leur nature agressive et des nombreuses incertitudes méthodologiques. Dans le troisième article, nous présentons une nouvelle méthodologie expérimentale *in situ* pour évaluer l'érosion en temps réel utilisant une microbalance de cristal de quartz, développée afin d'étudier le processus d'EIPS des systèmes de couches dures protectrices. À l'aide de la méthode de perte de masse classique d'EIPS, nous validons et discutons des avantages et défis liés à la nouvelle méthode. De plus, cette technique résolue dans le temps nous permet de discuter de phénomènes transitoires présents durant l'EIPS de systèmes de couches dures protectrices, offrant un éclairage nouveau sur le processus d'érosion.

ABSTRACT

Economic and technological progress, as well as environmental concerns, require that modern equipment be designed with ever more stringent performance criteria, frequently pushing components to the very limits of their capabilities. One major consequence of this increased demand on performance is that tribological deficiencies, such as lubrication breakdown, excessive wear and tribo-corrosion, can be significantly amplified, leading to unnecessary operational costs, decreased efficiency and premature failure. Because tribological processes result from the interaction of two or more bodies in relative motion in a particular environment, surface engineering can be used to confer to surfaces the high performance needed for demanding operational conditions. In this context, the design of the appropriate material system must be guided by an accurate understanding of the degradation mechanisms and the surface response to loading and deformation, frequently acting in synergy.

Solid Particle Erosion (SPE) occurs in situations where hard solid particles present in the environment are entrained in a fluid stream, and impact component surfaces. This type of damage is most prominent in the first stage of the aircraft engine, where the compressor blades can be eroded to such an extent that aerodynamic performance and even structural integrity are compromised. Consequently, much work has been done in academia and industry in order to understand the material loss mechanisms present in SPE and to develop protective technologies that will increase component lifetimes. One such technology is the use of hard protective coatings to impede the erosion of the predominantly metallic engine components.

Accordingly, the main objective of this PhD project is to investigate the material loss mechanisms during SPE of hard protective coatings, including nanocomposite and nanostructured systems. In addition, because of the complex nature of SPE mechanisms, rigorous testing methodologies need to be employed and the effects of all testing parameters need to be fully understood. In this PhD project, the importance of testing methodology is addressed throughout in order to effectively study the SPE mechanisms of brittle materials and coatings.

In the initial stage of this thesis, we studied the effect of the addition of silicon (Si) on the microstructure, mechanical properties and, more specifically, on the SPE resistance of thick CrN-based coatings. It was found that the addition of Si significantly improved the erosion resistance and that SPE correlated with the microhardness values, *i.e.* the coating with the highest

microhardness also had the lowest erosion rate (*ER*). In fact, the *ER*s showed a much higher dependence on the surface hardness than what has been proposed for brittle erosion mechanisms.

Based on these initial results, the specific objectives of this PhD project are fourfold: a) to develop a robust methodology for the SPE characterization of coated systems, b) to investigate the effects of particle properties on the SPE mechanisms of brittle materials, c) to establish a systematic relationship between the mechanical properties of coated surfaces and their SPE behavior, and d) to develop an *in situ* real-time testing methodology to investigate SPE mechanisms of hard protective coating systems. The main results are presented in the form of articles in refereed journals.

In the first article, we study the effects of the particle properties on the SPE behavior of six brittle bulk materials using glass and alumina powders. First, we apply a robust methodology to accurately characterize the elasto-plastic and fracture properties of the studied materials. We then correlate the measured *ER* to materials' parameters with the help of a morphological study and an analysis of the quasi-static elasto-plastic erosion models. Finally, in order to understand the effects of impact on the particles themselves and to support the energy dissipation-based model proposed here, we study the particle size distributions of the powders before and after erosion testing. It is shown that tests using both powders lead to a material loss mechanism related to lateral fracture, that the higher than predicted velocity exponents point towards a velocity-dependent damage accumulation mechanism correlated to target yield pressure, and that damage accumulation effects are more pronounced for the softer glass powder because of kinetic energy dissipation through different means.

In the second article, we study the erosion mechanisms for several hard coatings deposited by pulsed DC magnetron sputtering. We first validate a new methodology for the accurate measurement of volume loss, and we show the importance of optimizing the testing parameters in order to obtain results free from experimental artefacts. We then correlate the measured *ER*s to the material parameters measured by depth-sensing indentation. In order to understand the material loss mechanisms, we study three of the coating systems in greater detail with the help of fracture characterization and a morphological study of the eroded surfaces. Finally, we study the particle size distributions of the powders before and after erosion testing in an effort to understand the role of particle fracture. We demonstrate that the measured *ER*s of the coatings are strongly dependent on the target hardness and do not correlate with coating toughness. In fact, the material removal mechanism is found to occur through repeated ductile indentation and cutting of the surface by the impacting particles and that particle breakup is not sufficiently large to influence the results significantly.

Studying SPE mechanisms of hard protective coating systems in detail has proven to be quite challenging in the past, given that conventional SPE testing is notoriously inaccurate due to its aggressive nature and its many methodological uncertainties. In the third article, we present a novel *in situ* real-time erosion testing methodology using a quartz crystal microbalance, developed in order to study the SPE process of hard protective coating systems. Using conventional mass loss SPE testing, we validate and discuss the advantages and challenges related to such a method. In addition, this time-resolved technique enables us to discuss some transient events present during SPE testing of hard coating systems leading to new insights into the erosion process.

TABLE OF CONTENTS

LIST OF TABLES

LIST OF FIGURES

LIST OF ACRONYMS AND SYMBOLS

Abbreviations

AISI	American Iron and Steel Institute
ASTM	American Society for Testing and Materials
BK7	BK7 optical glass
BSG	Borosilicate glass
CAD	Cathodic arc deposition
c-Ge	Single crystal germanium
CRIAQ	Consortium for Research and Innovation in Aerospace in Quebec
c-Si	Single crystal silicon
CVD	Chemical vapor deposition
DA	Damage accumulation
DC	Direct current
DLC	Diamond-like carbon
DSI	Depth-sensing indentation
EBPVD	Electron-beam physical vapor deposition
EIPS	Érosion par impact de particules solides
ERD-TOF	Elastic recoil detection in the time of flight regime
FCSEL	Functional Coating and Surface Engineering Laboratory
FEG	Field emission gun
FEM	Finite element modeling
FIB	Focused ion beam
FOD	Foreign object damage

FQ	Fused quartz glass
FQRNT	Fonds de recherche du Québec - Nature et Technologies
FS	Frequency shift
HEPA	High-efficiency particulate air
HVN	Vickers hardness number
ISE	Indentation size effect
ISO	International Organization for Standardization
LDS	Laser diffraction spectroscopy
MeN	Transition metal nitride
MS	Magnetron sputtering
NSERC	Natural Sciences and Engineering Research Council
PC	Protective coating
PDCMS	Pulsed DC magnetron sputtering
PECVD	Plasma enhanced chemical vapor deposition
PVD	Physical vapor deposition
QCM	Quartz crystal microbalance
RF	Radio-frequency
RQMP	Regroupement Québecois sur les Matériaux de Pointe
SEM	Scanning electron microscope
SLG	Soda-lime glass
SPE	Solid particle erosion
SS410	AISI 410 stainless steel
SZM	Structure zone model
TBC	Thermal barrier coating

Ti64	Titanium alloy with 6% aluminum and 4% vanadium
XRD	X-ray diffraction

Symbols

$3D$	Three-dimensional
$(h/t)_c$	Indentation depth over coating thickness ratio at which circular cracking occurs
a	Model based coefficient for hardness deconvolution
A	Projected contact area
AE	Area exposed to the flow of particles
$at.\%$	Atomic percentage
B	Fitting constant in Oliver and Pharr model
c	Crack length
$C_0, C_1, C_2, etc.$	Fitting coefficients in area function
c_l	Lateral crack length
c_r	Half-penny crack length
C_{Si}	Silicon content
D	Particle size
d	Diagonal of the residual trace
d_c	Depth of the crack beneath the surface
d_d	Spacing between diffracting planes
d_g	Grain size
E	Young’s modulus
$E*$	Normalized delivered energy flux

E_f	Coating Young’s modulus
E_i	Diamond Young’s modulus
E_p	Particle Young’s modulus
E_r	Reduced Young’s modulus
ER	Erosion rate
$ER*$	Normalized erosion rate
ER_{90}	90^o erosion rate
ER_{conv}	Erosion rate evaluated by conventional mass loss technique
ER_{QCM}	Erosion rate evaluated by QCM technique
f	Natural frequency
F	Fraction of particles which cut the target in an ideal manner
f_0	Crystal fundamental resonant frequency
f_L	Loaded natural frequency
f_r	Particle feed rate
f_u	Unloaded natural frequency
g	Tabor material specific constant
G	Toughness
H	Hardness
h	Indentation depth
H/E	Elastic strain to failure
H/K_{IC}	Index of brittleness
H^3/E^2	Yield pressure

H_c	Composite hardness
h_c	Indentation contact depth
h_c/t	Normalized contact depth
h_f	Fitting constant in Oliver and Pharr model
H_f	Actual coating hardness
H_i	Intrinsic hardness
h_{max}	Penetration depth at maximum load
H_p	Particle hardness
h_{res}	Residual indentation depth
H_s	Substrate hardness
H_t	Target material hardness
H_v	Vickers hardness
k	Hall-Petch material constant
K	Ratio of the vertical and horizontal forces applied to the particle tip
K_c	Fracture toughness
KE	Kinetic energy
K_{IC}	Mode I fracture toughness
K_{ICp}	Particle fracture toughness
K_{ICt}	Target material fracture toughness
L	Lateral distance
$L*$	Normalized inter-particle spacing
L_d	Distance between the disks in double disk apparatus

L_L	Lateral fracture threshold
L_R	Radial fracture threshold
m	Fitting constant in Oliver and Pharr model
M	Meyer index
m_0	Total coating mass per unit surface area before SPE testing
$\dot{m}_L$	Mass loss rate per unit of surface area
$\dot{m}_p$	Particle mass feed rate in QCM testing
m_L	Incremental mass loss per unit of surface area
M_p	Projected mass of particles
m_p	Particle mass
m_p^*	Total particle mass impacting the exposed QCM surface
m_{pi}	Incremental projected mass of particles
n	Velocity exponent
n_d	Integer in Bragg's law
N_q	Frequency constant for the AT-cut quartz crystal
P	Applied load
p_0	Mean contact pressure
P_m	Maximum load during indentation
PR	Particle penetration ratio into the mask
q	ISE Constant
r	Radius
R	Distance of each point in the scan to the centerline

R^2	Coefficient of determination
r_d	Radial distance between the wear scars and the rotation axis in double disk apparatus
R_e	Elastic recovery
r_n	Nozzle inner radius
r_p	Particle radius
R_p	Index of plasticity
R_{pBerk}	Index of plasticity measured with Berkovich indenter
R_{pCC}	Index of plasticity measured with cube-corner indenter
s	Offset in double disk apparatus
S	Material stiffness
S_m	Material stiffness at maximum load
t	Coating thickness
T^*	Generalized substrate temperature
TE	Taux d'érosion
V	Velocity
V_b	Substrate bias during deposition
V_{crit}	Critical velocity
V_e	Volume lost per impact
V_p	Particle velocity
V_{total}	Total volume loss after SPE testing
WD	Working distance
W_e	Elastic work of indentation

W_{irr}	Irreversible work of indentation
W_p	Plastic work of indentation
$wt\%$	Mass fraction
W_{total}	Total work of indentation
z	Depth of penetration during particle impact
Z	Measured depth of a given point in a scan
Z_f	Z-Factor of a film
z_m	Maximum depth of penetration

Greek symbols

α	Indentation fracture toughness constant
β	Factor depending on the indenter geometry
Δf	Observed change in oscillation frequency of the crystal
Δm	Mass loss
Δm_p	Mass of particles the sample is exposed to
ΔV	Elementary volume ring
Δx	Scan lateral resolution
ε	Strain
η	Constant that depends on indenter geometry
θ	Incidence angle
θ_d	Diffraction angle
λ	Wave length
μ	Shear modulus

μ_f	Film shear modulus
μ_q	Quartz shear modulus
v	Poisson coefficient
v_i	Diamond Poisson coefficient
ρ	Density
ρ_p	Particle density
ρ_q	Quartz density
σ	Stress
σ_{stat}	Standard deviation
σ_y	Yield strength (elastic limit)
χ	Ratio between the length and width of the cut
ψ	Cone half angle
ω	Angular velocity

LIST OF APPENDIX

CHAPTER 1 INTRODUCTION

Economic and technological progress as well as environmental concerns require that modern equipment be designed with ever more stringent performance criteria, frequently pushing components to the very limits of their capabilities. One major consequence of this increased demand on performance is that tribological deficiencies, such as lubrication breakdown, excessive wear and tribo-corrosion, can be significantly amplified, leading to unnecessary operational costs, decreased efficiency and premature failure. Because tribological processes result from the interaction of two or more bodies in relative motion in a particular environment, surface engineering can be used to confer to surfaces the high performance needed for demanding operational conditions. In this context, the design of the appropriate material system must be guided by an accurate understanding of the degradation mechanisms and the surface response to loading and deformation, frequently acting in synergy.

With sales of 12 Billion Canadian Dollars annually, the aerospace industry is the fourth in importance in the province of Quebec and the first in terms of exports with 80% of its production sold outside of the country. Its 235 companies employ 40,000 skilled workers and its average annual growth rate over the 25 years preceding 2010 was of 8.5% [1]. In order to maintain and increase this level of economic performance, new materials need to be developed to enhance overall aircraft efficiency through improved component lifetimes. One field of interest where research and development are needed is that of problems related to Solid Particle Erosion (SPE) of various aircraft components during the military or civilian missions. Sand or dust in the environment can cause significant damage to components such as helicopter rotor blades, compressor and turbine blades of jet engines, windshields or any exposed surfaces.

Research into SPE has been ongoing for more than 50 years but the protection of parts from the negative effects of SPE, by using surface treatment technologies, really started in the late 1980s in the USSR in order to protect military aircraft operating in the harsh environments of Afghanistan. Shortly thereafter, during the first Gulf War in the early 1990s, Great Britain's Royal Air Force reported helicopter engine lifetimes of only 20 hours because of SPE-related performance degradation [2]. Since then, SPE has remained a pressing issue for the aerospace industry. In fact, Pratt & Whitney announced in 2004 that because of the premature wear by SPE of certain components, modifications would be made to the F135 engine of the new F35 Joint

Strike Fighter [3]. Finally, in 2010, the eruption of the Icelandic volcano Eyjafjallajökull led to one of the largest air travel shutdown since World War II because of the risks of visibility degradation by windscreen SPE and engine stalling through particulate ingestion and melting in the high temperature sections of the engine.

The damage to jet engines by SPE occurs primarily in the compressor section where the ingested particles follow trajectories which are strongly influenced by their size and speed, and the engine geometry (Figure 1.1).

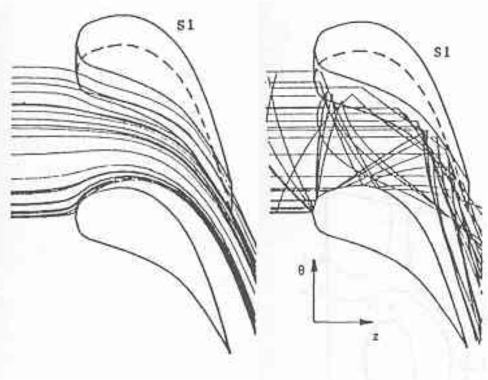

Figure 1.1: Trajectories in a compressor flow path for (a) 2.5 μm particles and (b) 135 μm particles [4].

Combined to the complex geometrical shapes of the engine components, these lead to particles impacting surfaces at many angles of incidence: from grazing angle to perpendicular impacts. In fact, compressor blades typically show preferential erosion of the trailing edge where the particles impact with trajectories nearly parallel to the surfaces (Figure 1.2).

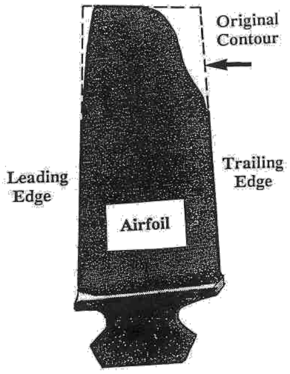

Figure 1.2: Typical damage to a compressor blade [5].

In order to minimize the ingestion of particles, filters and inertial particle separators are used but are not entirely efficient in stopping small sized particles from entering the engine. In addition, these components add weight to the aircraft while diminishing the overall performance of the engine. For these reasons, hard protective coatings (PCs) have been increasingly used in such applications in order to improve component lifetime while not adding significant weight.

The PC can drastically improve resistance to SPE by conferring to surfaces mechanical properties that are not possible to be attained with bulk materials. A full engine test conducted by the US Navy [6], in conjunction with the University of Cincinnati, showed the highly protective nature of the soviet developed SPE protective coatings based on a Ti/TiN multilayer structure. In that study, half of the compressor blades were coated and after more than 7 kg of ingested sand, these were relatively unworn when compared to the uncoated blades (Figure 1.3).

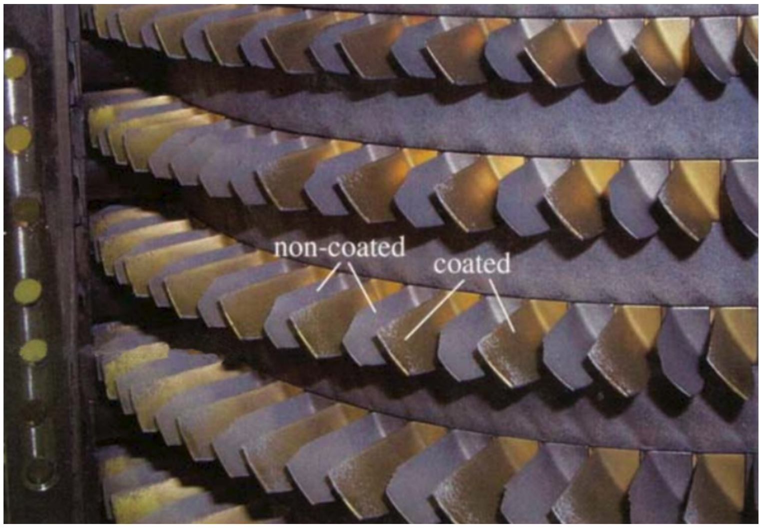

Figure 1.3: GE T64 jet engine compressor with half the blades coated with a TiN-based multilayer coating [7].

In the years since these first developments, many different coating systems in terms of architecture and composition have been proposed and studied. However, in order to select the optimal coating for particular operational conditions, it is necessary to understand the material loss mechanisms under SPE.

The surfaces of the components to be protected are generally metallic (stainless steel or titanium alloys) and the impacting particle will remove material predominantly through micro-cutting or ploughing. Conversely, the protective coatings are composed of much harder ceramic materials, such as titanium nitride-based compounds, and will present much more complex erosion behaviors. In fact, it has been shown that brittle materials exhibit surface removal mechanisms closely related to fracture modes encountered during indentation (Figure 1.4) where different types of deformation (elastic and plastic) and cracking (Hertzian, radial and lateral) can occur depending on indenter geometry, applied load and surface properties. Consequently, transitions can occur between the different SPE material removal process depending on operational conditions and, in particular, on particle properties such as shape, size and brittleness.

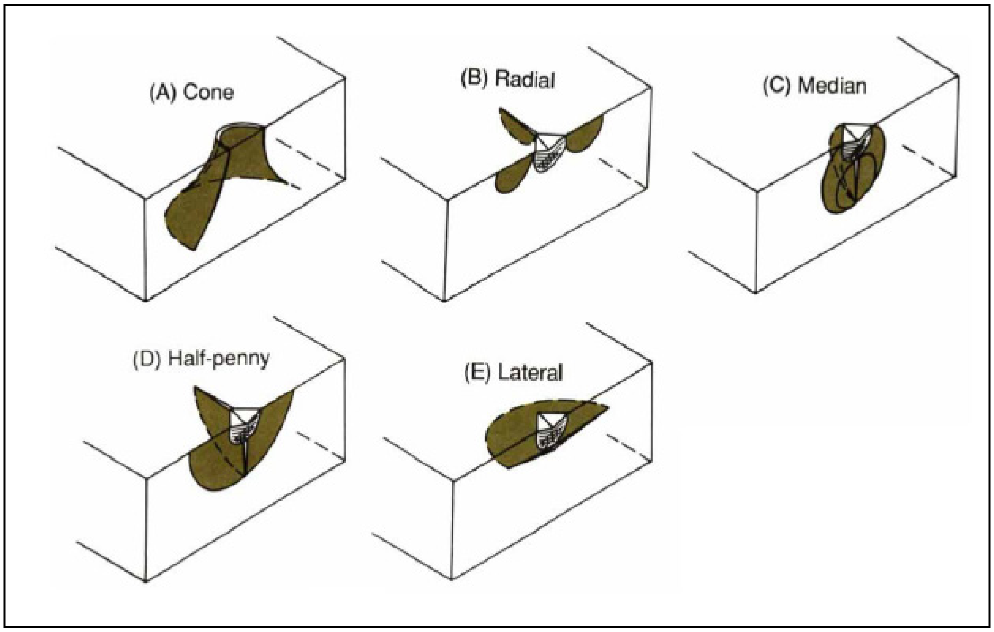

Figure 1.4: Modes of fractures during indentation of brittle surfaces [8].

Because of the complex nature of SPE mechanisms, rigorous testing methodologies need to be employed and the effects of all testing parameters need to be fully understood. Unfortunately, most published studies on SPE protective coatings cannot be compared quantitatively because of a lack of methodological consistency.

In this PhD project, the importance of testing methodology will be addressed throughout in order to effectively study the SPE mechanisms of brittle materials and coatings. In this chapter, the context and the objectives of the project will be presented.

1.1 Context

From a very young age, I was greatly interested in all that involves aircraft and their use. Indeed, this passion led me to start my studies at the Collège Militaire Royal of St-Jean where I pursued a career in aviation. That adventure only lasted one year, but it nevertheless led me to complete a degree in Mechanical engineering at the École Polytechnique de Montréal with a concentration in aerospace engineering. Unfortunately, the importance given to materials science in the program was very small at the time and for that reason, I chose to work in the field of industrial mechanical engineering upon finishing my degree. For three years, I worked for SKF Canada Ltd, as an application and reliability engineer. One of my responsibilities was to design bearing and sealing systems for a variety of applications such as paper machine hot press rolls, wood chippers, train wheel assemblies, watercraft turbine impellers, etc. In the later part of my employment with SKF, I was also tasked in increasing machinery lifetimes and reliability for many different industrial clients through implementing predictive maintenance programs on site.

In my capacity as a reliability engineer, I discovered a general lack of knowledge on tribological issues such as wear, friction and lubrication. This was not surprising to me because I had only spent about three or four hours of course time on tribology-related topics during all of my engineering studies. This lack of training seemed to be generalized in industry, as illustrated by the millions of dollars I have witnessed to be lost through the lack of proper tribological knowhow.

In an effort to reorient my career towards the field of protective coatings research, I was welcomed in the Functional Coating and Surface Engineering Laboratory (FCSEL) in January 2004 where my Master's project was focused on the study of hard nanocomposite coatings, especially their mechanical properties. At first, I collaborated with Pawel Jedrzejowski, a recent PhD recipient, on an *in situ* growth study of TiN-based nanocomposite coatings which was later published in Applied Physics Letters [9]. Afterwards, I worked on the re-design and implementation of an increased capacity plasma enhanced chemical vapor deposition (PECVD) chamber and undertook the task of re-optimizing the deposition conditions of the TiN-based nanocomposite coatings.

In the subsequent years, I worked extensively on the development of the tribo-mechanical characterization capabilities of the FCSEL, by contributing to the grant application process, investigating future equipment functionalities and purchasing and commissioning new equipment. Subsequently, I developed and implemented new indentation, scratch and erosion testing methodologies while training many users of the new equipment.

Being one of the most experienced users within the FCSEL, I also participated in numerous projects in collaboration with industrial (DAC aviation, DALSA Semiconductors, MDS Coatings Technologies, Novelis Inc., Pratt & Whitney, Bell Helicopter Textron, etc.), institutional (NRC, VAMAS, NPL, etc.) and academic (Aachen University, Institut national de la recherche scientifique, McGill University, Université de Mons, etc.) partners. These collaborations have led to five publications as co-author which are presented in Table 1.2.

Following my transfer to the PhD program in 2006, I was fully integrated into a new project in collaboration with several industrial partners and the Consortium for Research and Innovation in Aerospace in Quebec (CRIAQ) on the development and testing of protective coatings for aerospace applications. It was based on the needs of this collaborative project that I undertook my PhD research project.

1.2 Preliminary study on the effect of microstructure on the SPE of CrSiN

In a preliminary study that was accomplished in the context of this thesis, we studied the effect of the addition of silicon (Si) on the microstructure, mechanical properties and, more specifically, on the SPE resistance of thick CrN-based coatings. The article was published in *Surface and Coatings Technology* [10] and is presented in Appendix A.

This study was a continuation of the work done by the FCSEL's post-doctoral fellow M. Benkahoul *et al.* [11] in which they demonstrated the increased hardness of CrSiN coatings when compared to the basic CrN coating. They showed that the maximum hardness (24 GPa) was attributed to solid solution hardening at a Si content of 2.3 at.%. As the silicon content increased, Si segregation to the grain boundaries occurred and the hardness dropped due to the formation of a weaker Si_3N_4 matrix.

In our study, we tested all the samples under the same SPE conditions (normal impact angle and a particle velocity of V_p = 70 m/s) and found that the addition of Si significantly improved the erosion resistance. In addition to using nanoindentation for hardness evaluation, we also used Vickers microindentation to evaluate the hardness at a similar scale as that found during a typical

SPE impact event. Interestingly, we concluded that the SPE results correlated much better with the microhardness values and that the coating with the highest microhardness also had the lowest erosion rate (*ER*). This suggested that the microstructure at the scale of the single particle impact volume of interaction played a large role in the erosion processes.

However, there were two additional findings that had the greatest impact on the orientation of the research in this thesis. First of all, it was found that circular cracking during Vickers indentation of hard coatings on ductile substrates was not representative of coating toughness. In fact, we found that ring cracking resulted from the inability of the coating to accommodate the important plastic deformation of the substrate. This meant that toughness could not be evaluated by indentation for hard coatings deposited on highly compliant ductile substrates. The second and most important finding was that the *ER*s showed a very strong dependence on the surface hardness. We believed that this finding could be a result of a mechanism based on a transition to micro-chipping as proposed by Shipway and Hutchings [12], but that was yet to be confirmed in the case of the studied PC.

These findings led to three interrogations which form the backbone of this thesis: i) what is the material loss mechanism of hard protective coatings during erosion; ii) what is the role of toughness on the erosion mechanism; and iii) what is the role of particle properties on the strong dependence of *ER* on the hardness of the target material?

1.3 Objectives

Based on the results from the preliminary study on the CrN-based coatings and on the needs of the collaborative projects with our industrial partners, the main objective of this PhD project is to investigate the material loss mechanisms during SPE of hard protective coatings, including nanocomposite and nanostructured systems. In particular, this research is focused on SPE using angular particles at relatively low velocities (below 100 m/s).

In order to accomplish the main goal of the project, the specific objectives are to:

- Develop a robust methodology for the SPE characterization of coated systems;
- Investigate the effects of particle properties on the solid particle erosion mechanisms of brittle materials;

- Establish a systematic relationship between the mechanical properties of coated surfaces and their SPE behavior;
- Develop an *in situ* real time testing methodology to investigate SPE mechanisms of hard protective coating systems.

1.4 Thesis outline

Including this first introductory chapter, the thesis is divided into seven chapters and one appendix. In chapter 2, the important elements necessary to comprehend the content of this research project are reviewed, namely surface mechanical response, surface engineering techniques, nanocomposite coatings, solid particle erosion of materials and coatings. The following chapter (chapter 3) is an overview of the experimental techniques and methodologies that were used during the project for coating deposition, solid particle erosion testing, and microstructural and mechanical characterization.

In chapter four (Article 1), we study the effects of the particle properties on the SPE behavior of six brittle bulk materials using glass and alumina powders. First, we apply a robust methodology to accurately characterize the elasto-plastic and fracture properties of the studied materials. We then correlate the measured *ER* to materials' parameters with the help of a morphological study and an analysis of the quasi-static elasto-plastic erosion models. Finally, in order to understand the effects of impact on the particles themselves and to support the energy dissipation-based model proposed here, we study the particle size distributions of the powders before and after erosion testing. It will be shown that tests using both powders lead to a material loss mechanism related to lateral fracture, that the higher than predicted velocity exponents point towards a velocity-dependent damage accumulation mechanism correlated to target yield pressure, and that damage accumulation effects are more pronounced for the softer glass powder because of kinetic energy dissipation through different means.

In the fifth chapter (Article 2), we study the erosion mechanisms for several hard coatings deposited by pulsed DC magnetron sputtering. We first validate a new methodology for the accurate measurement of volume loss, and we show the importance of optimizing the testing parameters in order to obtain results free from experimental artefacts. We then correlate the measured erosion rates to the material parameters measured by depth-sensing indentation. In order to understand the material loss mechanisms, we study three of the coating systems in greater detail with the help of fracture characterization and a morphological study of the eroded surfaces. Finally, we study the particle size distributions of the powders before and after erosion testing in an effort to understand the role of particle fracture. It will be shown that the measured *ER*s of the coatings are strongly dependent on the target hardness and do not correlate with coating toughness. In fact, the material removal mechanism will be found to occur through repeated ductile indentation and cutting of the surface by the impacting particles and that particle breakup is not sufficiently large to influence the results significantly.

Studying SPE mechanisms of hard protective coating systems in detail has proven to be quite challenging in the past, given that conventional SPE testing is notoriously inaccurate due to its aggressive nature and its many methodological uncertainties. In the sixth chapter (Article 3), we present a novel *in situ* real-time erosion testing methodology using a quartz crystal microbalance, developed in order to study the SPE of hard protective coating systems. Using conventional mass loss SPE testing, we validate and discuss the advantages and challenges related to such a method. In addition, this time-resolved technique will enable us to discuss some transient events present during SPE testing of hard coating systems leading to new insights into the erosion process.

Finally, in chapter 7, the work accomplished in this thesis will be summarized and the open questions and possible avenues of future research will be discussed. In the appendix, the article on the “Effect of microstructure on the erosion resistance of Cr-Si-N coatings” is presented. In the following Table 1.1, we present a list of the four publications directly related to this thesis, while Table 1.2 presents the five publications resulting from collaborations but not directly related to the project, and Table 1.3 presents a list of my invited talks, conference proceedings and other contributions.

Table 1.1: Peer reviewed publications resulting from this PhD project.

E. Bousser, M. Benkahoul, L. Martinu, J.-E. Klemberg-Sapieha «Effect of microstructure on the erosion resistance of Cr-Si-N coatings». *Surface & Coatings Technology*, 203 (2008) 776.

E. Bousser, L. Martinu, J.-E. Klemberg-Sapieha «Effect of erodent properties on the solid particle erosion mechanisms of brittle materials». *Journal of Materials Science*, Accepted, February 12th 2013.

E. Bousser, L. Martinu, J.-E. Klemberg-Sapieha «*In Situ* Real-Time Solid Particle Erosion Testing Methodology for Hard Protective Coatings». *Surface & Coatings Technology*, Submitted, February 21st 2013.

E. Bousser, L. Martinu, J.-E. Klemberg-Sapieha «Solid Particle Erosion Mechanisms of Hard Protective Coatings». *Surface & Coatings Technology*, Submitted, March 14th 2013.

Table 1.2: Peer reviewed publications resulting from collaborations.

S. Ligot, T. Godfroid, D. Music, **E. Bousser**, J.M. Schneider, R. Snyders «Tantalum-doped Hydroxyapatite Thin Films: Synthesis and Characterization». *Acta Materiala*, 60 (2012) 3435.

D. Li, S. Guruvenket, S. Hassani, **E. Bousser**, M. Azzi, J.A. Szpunar, J.E. Klemberg-Sapieha «Effect of Cr interlayer on the adhesion and corrosion enhancement of nanocomposite TiN-based coatings deposited on stainless steel 410». *Thin Solid Films*, 519 (2011) 3128.

R. Snyders, **E. Bousser**, D. Music, J. Jensen, S. Hocquet, J.M. Schneider «Influence of the chemical composition on the mechanical properties of RF sputtered hydroxyapatite coatings». *Plasma Processes and Polymers*, 5 (2008) 168.

R. Snyders, **E. Bousser**, P. Amireault, J.-E. Klemberg-Sapieha, E. Park, K. Taylor, L. Martinu «Tribo-mechanical properties of DLC coatings deposited on nitrided biomedical stainless steel». *Plasma Processes and Polymers*, 4 (2007) S640.

P. Jedrzejowski, A. Amassian, **E. Bousser**, J. Klemberg-Sapieha, L. Martinu «Real Time *In-Situ* Growth Study of TiN- and TiCxNy- Based Superhard Nanocomposite Coatings Using Spectroscopic Ellipsometry». *Applied Physics Letters*, 88 (2006) 71915-1.

Table 1.3: Invited talks, conference proceedings and other contributions.

Invited talks

E. Bousser, L. Martinu, J.-E. Klemberg-Sapieha, « Erosion Mechanisms of Hard Nanocomposite Coatings ». Invited presentation, ICMCTF, 2012. San Diego, CA USA.

Conference proceedings, oral and poster presentations

E. Bousser, L. Martinu, J.-E. Klemberg-Sapieha, « In-situ Real Time Solid Particle Erosion Testing Methodology for Hard Protective Coatings ». Presentation, ICMCTF, 2013. San Diego, CA USA.

E. Bousser, L. Martinu, J.-E. Klemberg-Sapieha, « Characterization and understanding of the solid particle erosion mechanisms of hard coating systems ». Presentation, SVC conference, 2013. Providence, RI USA.

E. Bousser, L. Martinu, J.-E. Klemberg-Sapieha, «Multi-functional Analysis of Erosion Resistant Coatings Using the OPX-MCT Apparatus». Presentation, CSM User Meeting, 2011. Boston, MA USA.

E. Bousser, S. Hassani, J.-E. Klemberg-Sapieha, L. Martinu, «Mechanisms of Erosion Resistance in Brittle Materials and Coatings». Presentation, FCSE, 2011. Montreal, QC Canada.

E. Bousser, S. Guruvenket, S. Hassani, D. Li, M. Azzi, J.-E. Klemberg-Sapieha, L. Martinu, «Protective TiN-based Nanocomposite Coatings for Tribological and Aerospace». Presentation, ICMCTF, 2011. San Diego, CA USA.

E. Bousser « Methodology for the Evaluation of Solid Particle Erosion Mechanisms in Brittle Substrates and Coatings » Presentation, Final meeting CRIAQ – Project 1.20, 2010. Montreal, QC Canada.

E. Bousser « Erosion Performance of TiN/VN coatings » Presentation, Annual meeting CRIAQ – Project 1.20, 2008. Montreal, QC Canada.

E. Bousser, M. Benkahoul, M. Azzi, L. Martinu, J.-E. Klemberg-Sapieha « Performance of Cr-Si-N erosion resistant coatings for aerospace applications » Poster, ICAP, 2008. Churchill College, Cambridge, UK.

M. Benkahoul, **E. Bousser**, L. Martinu, J.-E. Klemberg-Sapieha « Microstructure, mechanical and tribological properties of Cr–Si–N coatings prepared by pulsed dual magnetron sputtering ». Poster, FCSE, 2008. Montreal, QC Canada.

E. Bousser, M. Benkahoul, P.Robin, L. Martinu, J.-E. Klemberg-Sapieha «Effect of microstructure on the erosion resistance of Cr-Si-N coatings ». Presentation, ICMCTF, 2008. San Diego, CA USA. Silver Medal student award winner.

E. Bousser, J.-E. Klemberg-Sapieha « Erosion resistance coatings for aerospace ». Presentation, INNO 08, 2008. Montreal, QC Canada.

E. Bousser « Erosion evaluation of coatings » Presentation, Annual meeting CRIAQ – Project 1.20, 2007. Montreal, QC Canada.

E. Bousser, S. Hassani, J.-E. Klemberg-Sapieha « State of the art in erosion resistant coatings » Presentation, kick-off meeting CRIAQ – Project 1.20, 2006. Montreal, QC Canada.

E. Bousser, P. Jedrzejowski, A. Amassian, L. Martinu and J.-E. Klemberg-Sapieha « Growth study of TiN- and TiCxNy-based superhard nanocomposite ». Presentation, AVS Symposium, 2006. San Francisco, CA USA.

E. Bousser, P. Jedrzejowski, A. Amassian, R. Snyders, L. Martinu and J.-E. Klemberg-Sapieha « Towards the application of nanocomposite coatings ». Poster, ICMCTF, 2006. San Diego, CA USA.

P. Jedrzejowski, A. Amassian, **E. Bousser**, L. Martinu and J.-E. Klemberg-Sapieha « In situ growth monitoring of nanocomposite TiN/SiN1.3 and TiCxNy/SiCN films using spectroscopic ellipsometry ». Proceedings, 48th Annual Technical Conference - Society of Vacuum Coaters, 2005, p 68-73.

CHAPTER 2 LITERATURE REVIEW

2.1 Surface mechanical response

The appropriate material's selection for a given application must be guided by an accurate understanding of the intervening tribological process which results from the interaction of two or more bodies in a particular environment. The behavior of the system will be intimately related to the surface response to loading and deformation [13], which can generally be classified in three types:

1) Elastic deformation,
2) Plastic or permanent deformation, and
3) Fracture behavior.

2.1.1 Elastic response

It is common to characterize the mechanical behavior of a material by its strain (ε) response under an applied stress (σ) as illustrated in Figure 2.1 where the tensile behaviors of brittle and ductile samples are presented.

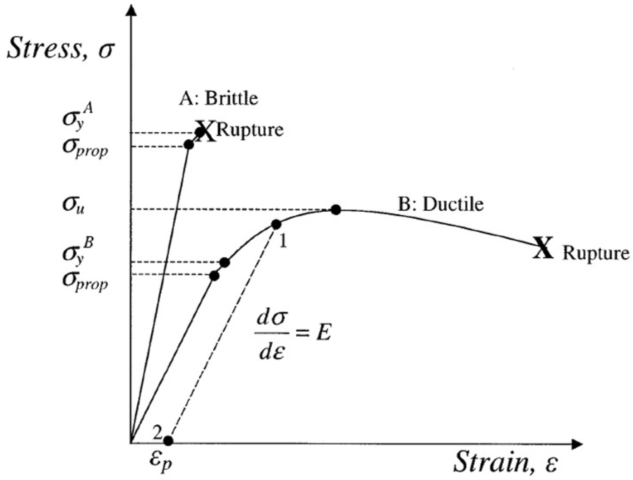

Figure 2.1: Schematic representation of brittle and ductile material behavior under tensile testing [14].

In the first portion of the curves, we observe the elastic response of the material which is characterized by being fully reversible and linear as defined by Hooke's law with the material's Elastic or Young's modulus (*E*) as the proportionality constant so that,

$$\sigma = E\varepsilon \,. \tag{2.1}$$

In this regime, the material will fully recover its original shape once the load is removed.

2.1.2 Plastic response

Above a certain stress, plastic deformation occurs: the material no longer recovers and a residual strain is observed upon unloading. The stress above which plastic deformation is observed, which also corresponds to the stress where Hooke's law is no longer respected, is the proportionality limit. However, since it is impossible to determine this exact stress, in practice the transition from elastic to ductile behavior is defined by convention as the stress at which 0.2% of residual strain is observed. This stress is the material's yield strength or elastic limit (σ_y).

In practice, it is not simple to obtain σ_y of a surface, in particular in the case of coatings or surface treatments. For that reason, the material strength is generally represented by the Hardness (*H*) which can be obtained by surface indentation. Hardness can be defined as a material's ability to resist deformation under indentation, but unlike σ_y, it is a measure of the elastic and plastic deformations. Nonetheless, it has been shown by Tabor [15] to be directly related to σ_y by:

$$H = g\sigma_y \tag{2.2}$$

where *g* is a material specific constant (for metals, *g* ≈ 3). This equation has been found to be inaccurate for hard elastic materials, and a more accurate relationship between *H* and σ_y for elastic perfectly plastic materials was proposed by Hill [16] where:

$$\frac{H}{\sigma_y} = \frac{2}{3} + \frac{2}{3}\ln\left[\frac{E/\sigma_y + 2(1-2\nu)}{3(1-\nu)}\right] \tag{2.3}$$

and *ν* is the material's Poisson coefficient.

The strength of a material is a function of many parameters. At the atomic scale, bonding and interatomic distance are indicative of a material's strength as can be seen in Figure 2.2, where hardness is plotted against lattice energy. In fact, covalent materials will generally present a higher strength than ionically bonded materials because of their higher lattice energies and smaller interatomic distances.

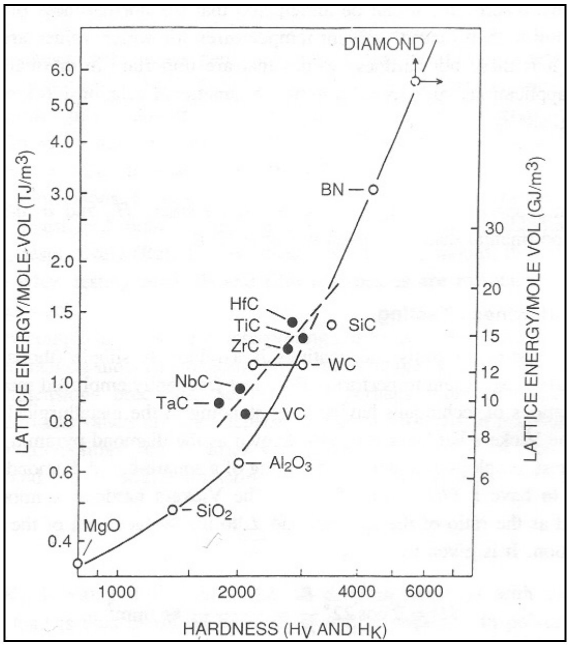

Figure 2.2: Relationship between bonding energy and material hardness [17].

However, real materials are not ideal and their strength will also be strongly affected by imperfections in their structure such as lattice dislocations, inclusions, voids or cracks. These can act to locally concentrate the stress field and cause localized failure. In the case of ductile materials, dislocation motion is relatively uninhibited, hence failure is caused by dislocation slip which leads to plastic deformation. For brittle materials, where dislocation motion is limited, failure is caused by crack propagation, enhanced by stress concentration factors.

2.1.3 Fracture response

When the stress applied to a material exceeds a certain limit, fracture occurs. In the case of brittle materials the fracture will be sudden with very little plastic deformation prior to rupture (example A in Figure 2.1), while for ductile materials, significant plastic deformation occurs before the onset of rupture (example B in Figure 2.1). In fact, fracture in ductile materials usually arises through fatigue processes where a crack is initiated at a zone of locally concentrated stress and propagates to a critical length after which sudden rupture occurs.

The fracture behavior of materials is represented by the toughness (G) described as the ability of a material to absorb energy without fracture, and by the fracture toughness (K_c) which is the ability of a material to resist crack growth.

Crack propagation may occur through three crack tip separation modes as illustrated in Figure 2.3: Mode I is the opening mode where the tensile stress is normal to the crack faces; Mode II is the sliding mode where the shear stress is normal to the crack propagation direction; and Mode III is the tearing mode where the shear stress is parallel to the propagation direction.

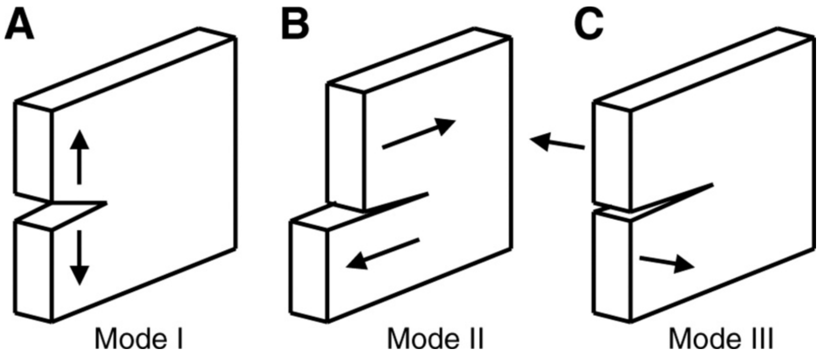

Figure 2.3: Crack tip separation modes [18].

The characterization of fracture behavior using the mode I fracture toughness (K_{IC}) is by far more common in materials engineering because it represents the plane strain critical stress-intensity factor for an existing crack to propagate catastrophically. It can therefore be used to quantitatively compare the fracture behavior of engineering materials.

2.1.4 Material parameter relationships

In tribological contacts of coated surfaces, the surface response can be estimated using relationships between the different material parameters. One such relationship is the *H/E* ratio which has been shown by Leyland and Matthews [19] to be descriptive of several mechanical contact situations related to tribological processes. In fact, it can be found in several of the models proposed to calculate fracture toughness by sharp probe indentation, most notably in the work by Lawn and coworkers [20-22]. It has also been shown to be an indicator of surface resistance to sliding wear [23, 24] of coated surfaces, and to be an important predictor of the amount of energy dissipated through plastic deformation during indentation [25, 26].

Another important relationship is the material yield pressure, which is related to H^3/E^2 and is a measure of the material's resistance to the onset of plastic deformation. This parameter was first proposed by Johnson [27] for a contact between an axy-symmetrical solid and an elasto-plastic plane surface. It has been shown to correlate with various tribological situations [28, 29]. Specifically, Hassani *et al.* [30] showed, using finite element modeling, a strong correlation between the SPE of various coatings and their H^3/E^2 ratios.

Finally, the strength and fracture resistance of materials are generally considered to be independent. In fact, very hard materials are more brittle and susceptible to fracture. The susceptibility of a surface to cracking can be represented by the index of brittleness (H/K_{IC}) which has been shown to accurately represent the onset of fracture under pyramidal indentation of brittle materials [31].

2.2 Surface engineering for enhanced tribological performance

It is not always possible to select a bulk material to protect surfaces from tribological degradation because of structural integrity requirements of the affected component or simply because the required properties cannot be obtained in any structural material. Therefore, surface treatments have been used for centuries (if not millennia) to improve the tribomechanical performance of surfaces. Modern surface engineering techniques can be classified into two groups.

The first one involves local modification of the component's surface to increase hardness. This can be achieved through the formation of hard phases by heat treatment, strain hardening through mechanical means (*e.g.* shot peening) or diffusion-controlled processes where atoms (typically nitrogen or carbon) are diffused into the surface and react to create a hard protective layer.

The second group of surface engineering techniques involves the deposition of a hard coating system on the surface to be protected. In general, the design and fabrication of protective coating systems is complex due to the multi-layer nature of the final structure most often consisting of a surface layer, followed by the hard coating and other functional interfacial layers in order to ensure proper adhesion, corrosion resistance and/or thermal conductivity.

A large number of deposition techniques are available for hard coating deposition, and they can be classified into three categories:

1) Wet chemical plating techniques involve the deposition of a coating in an electrolytic bath. These techniques are widely used most notably in the aerospace industry for the deposition of thick hard chrome and cadmium protective coatings. Much work is underway to replace these wet techniques because the electrolytes that are used are often harmful to humans and the environment (*e.g.* hexavalent chromium).
2) Thermal and cold spray coatings are deposited by the projection of a powder feedstock onto the substrate to be coated. In thermal spraying, the particles are heated during projection by electrical or chemical means and the coating is formed by the accumulation of the deformed impacted particles (splats). Thick thermal sprayed coatings are being increasingly studied for their use as protective coatings in many different tribological applications such as thermal barrier coatings for jet engine turbines and anti-galling coatings in industrial valves. They are industrially interesting because of their high deposition rate and relatively low implementation costs.
3) Vapor phase techniques are used for the deposition of a very large variety of coatings used in many applications such as optical interference filters on ophthalmic lenses, thin film photovoltaic solar cells, erosion resistant coatings in aircraft jet engines and even wear resistant drill bits for household use. Vapor deposited coatings are relatively thin (typically from below 1 μm to 10 or 20 μm) but can be deposited on many types of substrates in a highly controlled manner. These techniques are generally regarded as being environmentally friendly and have been recently used to replace polluting techniques such as electrolytic deposition of hard chrome coatings.

2.2.1 Vapor deposition techniques

Vapor deposition methods can be separated into two classes depending on the source of the vapor phase. Chemical Vapor Deposition (CVD) techniques use a gas-phase primary source, which can be activated in many ways including a glow discharge in the case of Plasma Enhanced Chemical Vapor Deposition (PECVD). CVD techniques can be difficult to implement industrially because of the often hazardous gaseous precursors that are used such as titanium tetrachloride ($TiCl_4$), which is corrosive, and silane (SiH_4), which is pyrophoric. Nonetheless, they have been used industrially for many years. With the increased understanding of the plasma physics and chemistry involved and because the resulting coatings present a highly controlled microstructure through the control of process parameters and may be deposited on components with complex geometries, PECVD is being used in a widening number of industrial applications.

The second type of vapor deposition techniques is by Physical Vapor Deposition (PVD) where the vaporized material originates from a solid target. There is a great variety of techniques to achieve this, and they can be classified into two sub-categories: evaporation and momentum-transfer sputtering. In the case of evaporation, the source material can be vaporized using several methods including resistance heating, induction heating, electron beam evaporation, laser ablation and electric arc evaporation. In particular, the Cathodic Arc Deposition (CAD) method, where the target material (cathode) is vaporized using an electric arc, is widely used in the deposition of hard, dense and thick protective coatings. Because of historic reasons and high deposition rates, the use of CAD for the deposition of erosion resistant coatings for aerospace applications is widespread.

The second category of PVD techniques is the sputter deposition method where material is vaporized from the target through the momentum transfer from impinging ions which are generated in a glow discharge or from an ion beam. Nearly all target materials can be sputtered and compound films can be deposited by using a reactive atmosphere during the process. Like PECVD, this deposition technique is widely used because it is possible to control the microstructure and the resulting properties through the control of the process parameters. In this project, a variant of the sputtering deposition technique was used for all depositions. In the next section, the Pulsed DC Magnetron Sputtering (PDCMS) process will be presented in greater detail and the effect of process parameters on microstructure will be discussed.

2.2.2 Sputter-deposition of coatings and their microstructure

In a planar diode DC sputtering configuration, a glow discharge is created between the target material to be vaporized which is held at a negative potential (cathode) and the substrate holder which is at a positive potential (anode). As the potential is applied, the electrons that are naturally present in the chamber are accelerated towards the anode and ionize atoms in the working gas (usually argon). The ionized atoms in the plasma are then accelerated to the cathode with high energies and impact the target material generating secondary electrons and, if their kinetic energy is sufficient, ejecting target atoms or molecules by momentum transfer. These ejected particles then condense on the substrate surface following a line-of-sight trajectory.

In planar diode DC sputtering the ionization efficiency is low and the discharge cannot be maintained at low pressures because the probability of primary electron collisions is significantly reduced. The secondary electrons extracted from the target serve to maintain the discharge but they cannot offset this effect. In order to curtail this problem, Magnetron Sputtering (MS) is used to increase ionization efficiency by applying magnetic fields to confine the electrons near the target surface. The sputtering yield is increased and the discharge can be maintained at lower pressures thus increasing deposition rates.

In traditional DC sputtering, only metallic targets are used as it would be impossible to maintain a discharge over highly resistive insulating materials due to charge accumulation on the target surface. The same can be said when depositing compound films in a reactive environment with metallic targets: an insulating oxide or nitride layer is formed, leading to increased charge accumulation, thus lowering sputtering rate and increasing the probability of arcing. The PDCMS technique is used to bypass this problem. Instead of applying a constant negative potential to the cathode, a cyclic potential is applied where the sputtering occurs during the negative part of the cycle and the accumulated charge is removed during the positive part of the cycle. In this way, the effects of target poisoning are significantly reduced.

The film growth and microstructure are directly related to the mobility of the condensing atoms (adatoms) once on the substrate surface. Adatom mobility will depend on process parameters such as pressure, substrate temperature, substrate bias and the proportion of condensing atoms that are ionized. In conventional MS techniques, the ionization proportion is very small and energy must be injected into the growth process by other means such as surface heating or through ion bombardment using an external ion source such as ion beam or additional glow discharge.

The effects of process parameters on the resulting microstructure have been studied extensively and are described by various Structure Zone Models (SZMs) proposed by Movchan and Demchishin for evaporated films [32], Thornton [33], Messier *et al.* [34], and Kelly and Arnell [35] for sputtered films, and more recently by Anders [36] for sputtered films taking into account the ionization of the condensing atoms. In Figure 2.4, the SZM proposed by Anders is presented where the effects of generalized substrate temperature (T^*) and normalized delivered energy flux (E^*) on the coating microstructure can be seen.

Four characteristic coating microstructures can be found (illustrated in Figure 2.5 for more clarity). When adatom mobility is low, coatings will be under-dense and present columnar structures with important defect and porosity densities due to open grain boundaries and shadowing effects (Zone 1 to Zone T). As temperature and ion energy fluxes increase, mobility is enhanced leading to grain and surface diffusion processes that enable increased densification and competitive growth (Zone T to Zone 2). Finally, further increases in mobility led to bulk diffusion which promotes a transition from a columnar structure to a coarse grain structure (Zone 2 to Zone 3). In protective coatings for tribological applications, microstructural parameters such as density, crystallinity and grain size will greatly influence performance by affecting material parameters such as hardness, toughness, corrosion resistance and residual coating stresses.

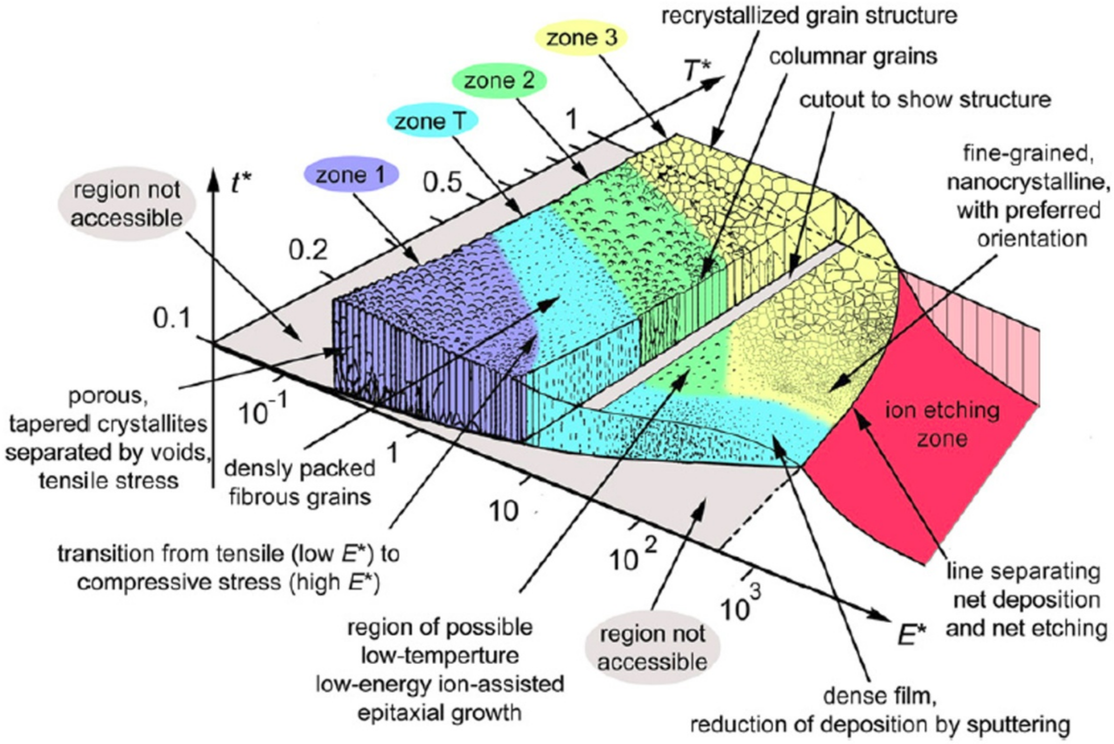

Figure 2.4: Representation of the structure zone model proposed by Anders [36] showing the effects of deposition parameters on the coating microstructure.

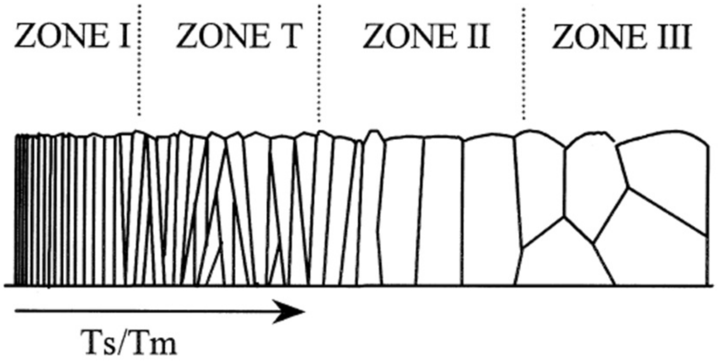

Figure 2.5: Illustration of the four characteristic coating microstructures [34].

While an important component of the overall residual stress is the difference in thermal expansion coefficient between the coating and the substrate, it has been shown that the residual stress in coating systems is also related to microstructure. Open microstructures presenting voids such as in Zone 1, and to a lesser extent in Zone T, will generally have tensile intrinsic residual stresses due to attractive atomic forces acting across the voids [37]. On the other hand, denser films obtained through ion bombardment generally present compressive stresses which strongly depend on the energy of the impinging ions controlled through the species ionization and the substrate bias. These bombarding particles are implanted in the forming coating, causing lattice distortion which can lead to very important compressive residual stresses (up to -10 GPa) [37]. The high compressive stresses that are generally found in hard protective coatings can be beneficial to stall fracture processes by acting to close forming cracks. On the other hand, high stresses, be they tensile or compressive, can lead to coating delamination. Therefore, in such situations, interface engineering to maximize adhesion is crucial.

As will be discussed in greater detail in the next section, the hardness of the coating can also be controlled through the microstructure. First of all, the elastic component of hardness will be affected by the residual stress in a coating by changing the average interatomic distance in the stressed lattice. For example, high hardness is generally observed in highly compressively stressed coatings. On the other hand, defects such as voids, dislocation and incorporated atoms will negatively affect material strength and thus reduce hardness. Finally, since plastic flow can be limited by impeding dislocation movement, grain boundaries can be used to enhance yield strength. Thus by refining the microstructure, a higher hardness can be obtained. This is the basis on which nanocomposite coatings have been developed as will be presented in the next section.

2.3 Nanocomposite coatings

As has been discussed previously, hardness depends in part on the nature of the interatomic bond where covalently bonded materials present the highest hardness values. Thus, only a few materials can be classified as being super hard ($H > 40$ GPa), such as diamond ($H = 70$ to 100 GPa) and several variants of the B-C-N system ($H \geq 50$ GPa) such as c-BN, BC and β-C_3N_4. As these materials are relatively rare and present certain shortcomings like being difficult to synthesize, several methods exist to improve material strength through other means.

The first approach is through alloying by adding different elements to a crystalline structure. Hardening is achieved by changing the nature of the interatomic bonds and by deforming the crystal lattice. Examples of this type of hardening are TiAlN, TiCN and to a certain extent CrSiN.

Another approach is to limit dislocation motion by introducing grain boundaries, flaws, precipitates and/or other dislocations. In fact, it has been shown independently by Hall [38] and Petch [39], that the yield strength is inversely proportional to the square root of the grain size. Applied to hardness, the Hall-Petch equation can be expressed as [37]:

$$H = H_i + kd_g^{-1/2} \tag{2.4}$$

where H_i is the intrinsic hardness, k is a material constant and d_g is the grain size. Thus, this hardening mechanism can be achieved by controlling the microstructure as described by the various SZMs and in certain cases by controlling the nanostructure.

2.3.1 Multilayer nanostructured coatings - nanolaminates

The first studies on the creation of superhard heterostructures were conducted on multilayer coatings of two repeating materials with a periodicity of a few nanometers. In studies on the TiN/VN [40] and TiN/NbN [41] systems, maximum hardness enhancement can be observed for a periodicity between 4 and 8 nm, as illustrated in Figure 2.6 taken from [42].

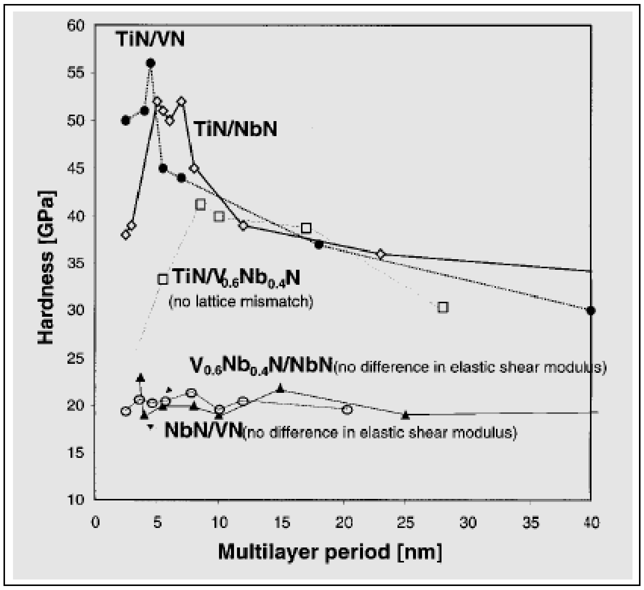

Figure 2.6: Hardness as a function of nanolaminate periodicity [42].

The hardness enhancement mechanism was found to be the hindering of dislocation movement across sharp interfaces by a mismatch between the elastic moduli of the layers [42]. If the mismatch is not present, no enhancement can be achieved, as is also illustrated in Figure 2.6 for the NbN/VN and VNbN/NbN systems. In addition, in order to maximize the hardness enhancement, the thickness of each layer must be such that dislocation motion is inhibited in the layer itself. Several studies have shown that these nanostructured multilayer coatings present enhanced mechanical and tribological properties [43-45]. However, manufacturing these types of coatings is a complex process because the periodicity must be precisely controlled and the interfaces must remain sharp, a condition that is difficult to apply to complex 3D objects.

2.3.2 Nanocomposite coatings

Nanocomposite coatings are heterogeneous structures composed of nanometric crystalline particles in an amorphous or polycrystalline matrix. In these materials, hardness is enhanced by blocking dislocation motion through grain size reduction. Greater cohesive forces at the grain boundaries prevent grain slip and maintain the validity of the Hall-Petch relation [14]. However, as illustrated in Figure 2.7, under a critical grain size an inverse Hall-Petch effect can be observed because of grain boundary slipping [46].

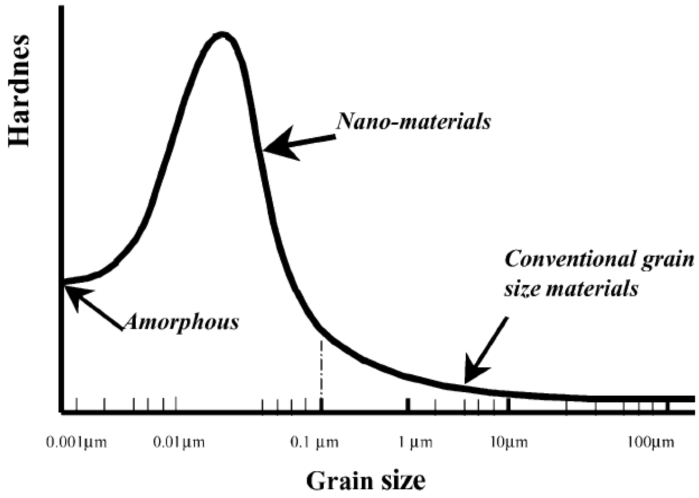

Figure 2.7: Typical evolution of hardness as a function of material grain size [46].

The research on nanocomposite materials has matured over the last 15 years and a great variety of nanocomposite materials have been developed. Their design largely depends on the application, and the composition of the crystalline phase and the matrix are selected accordingly. One of the most studied nanocomposite systems is composed of nano-crystalline TiN in an amorphous SiN matrix [42, 47-50]. For such as system, Veprek et al [49] demonstrated that maximum hardness is achieved at the percolation limit of the amorphous phase in the three-dimensional network of nanocrystalline grains (typically between 5 and 10 nm in size). In addition, transmission electron microscopy studies have shown that maximum hardness is achieved when particle sizes and shapes are relatively regular, and randomly oriented. This nanostructure is presented in Figure 2.8. It should be noted that more recently Jedrzejowski *et al.* [9] proposed a new realistic microstrutural model where grains would be partially inter-connected, and large enough to contain a limited number of defects.

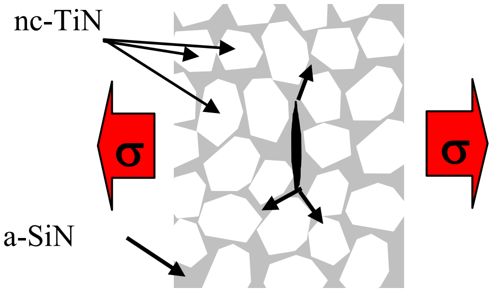

Figure 2.8: Schematic representation of a nanocomposite system where a defect in the amorphous matrix is shown. The material is composed of nanocrystalline grains typically 5 to 10 nm in size separated by an amorphous matrix one or two monolayers thick.

In such nanocomposite systems, particles smaller than 10 nm cannot accommodate plastic deformation because dislocations cannot form and thus, the mechanical strength of the grains will tend toward the theoretical strength of the material. Therefore, the strength of the system can only be limited by defects in the amorphous phase that is only one or two monolayers thick [49].

2.4 Solid particle erosion of materials

Erosion can be defined as the wear of a surface through interaction with particles and/or a fluid. Four types can be indentified:

1) Solid particle erosion,
2) Liquid impingement erosion,
3) Hot gas erosion, and
4) Cavitation erosion.

In this project, we focus exclusively on the Solid Particle Erosion (SPE) of surfaces through purely mechanical means. In fact, all types of erosion, and most tribological processes for that matter, can exhibit enhanced material loss when a corrosive environment is present. In order to study the mechanisms of SPE of coated systems we have strived to completely isolate the mechanical material loss mechanisms.

SPE occurs when hard solid particles are entrained by a fluid and impact a target surface. During this dynamic process, the particle kinetic energy (*KE*) is partially dissipated through a variety of mechanisms such as ductility, fracture, heating, phase transformations, etc. These mechanisms will be defined by the particle, target and operational properties as presented in Figure 2.9. These parameters are usually dependent on the application, but can also vary significantly during a cycle of operation, for example in the case of a jet engine that needs to operate at ground level or at 10,000 meters of altitude, in Dubai in a desert environment or in Quebec during a snow storm.

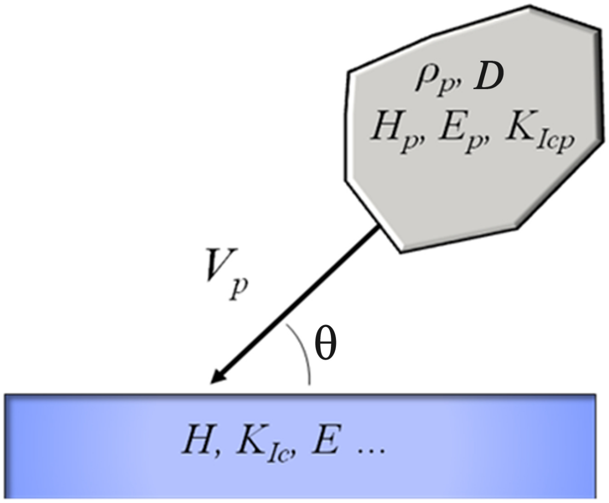

Figure 2.9: Illustration of the particle, target and operational parameters affecting SPE.

Typically, the SPE behavior of a material can be classified according to two types: ductile or brittle (see Figure 2.10). The first is characterized by material removal through plastic flow (ploughing or cutting) and typically presents maximum erosion at a low angle of incidence (20 to 40 degrees). On the other hand, brittle erosion is characterized by a maximum of material loss at a normal angle of incidence where the maximum of particle *KE* is transferred to the target and dissipated by crack initiation, propagation and intersection.

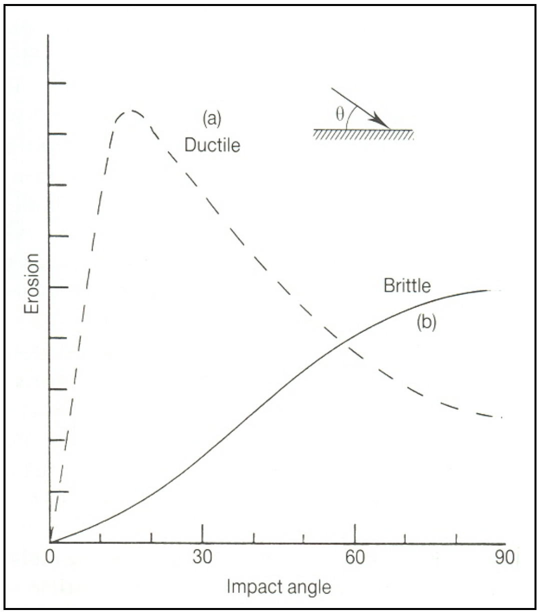

Figure 2.10: Typical SPE behavior for ductile (a) and brittle(b) materials [51].

In order to design hard coating systems for enhanced SPE protection, a full understanding of the material loss mechanisms is necessary. In this section, we will present ductile and brittle mechanisms of SPE, the transitions between mechanisms that can occur and the influence of the particle properties of the SPE behavior.

2.4.1 Ductile SPE mechanisms

Already in the late 1950s, the ductile SPE behavior of materials was being studied by several groups. Finnie [52] was the first to propose a mechanism based purely on surface cutting by the impacting particles. In his model, the volume removed by the impacting particle is a function of the particle trajectory which can be calculated from the forces acting on the particle tip during penetration into the target. The volume removed per impact (V_e) is expressed by:

$$V_e = \frac{m_p V_p^2}{\sigma_y \chi K}\left(\sin 2\theta - \frac{6}{K}\sin^2\theta\right) \text{ if } \tan\theta \le \frac{K}{6} \tag{2.5}$$

$$V_e = \frac{m_p V_p^2}{\sigma_y \chi K}\left(\frac{K}{6}\cos^2\theta\right) \text{ if } \tan\theta \ge \frac{K}{6} \tag{2.6}$$

where θ is the angle of incidence, m_p is the particle mass, V_p is the particle velocity, K is the ratio of the vertical and horizontal forces applied to the particle tip, and χ is the ratio between the length and width of the cut.

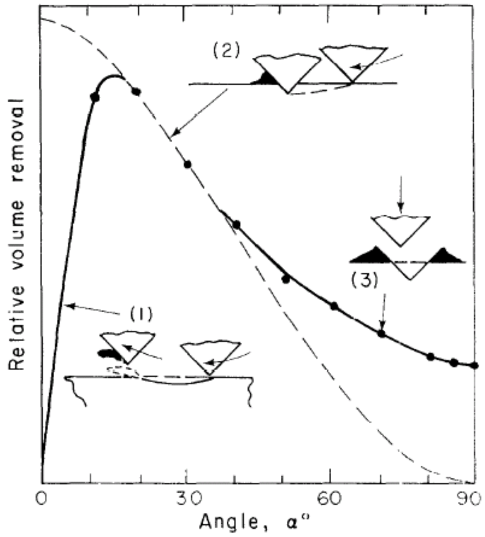

Figure 2.11: Proposed mechanisms explaining the ductile behavior of materials [53].

Finnie's model is presented in Figure 2.11 where curves 1 and 2 represent the modeled behavior, and curve 3 shows typical experimental observations. This cutting model predicts quite well the angle of maximum erosion rate (*ER*) which is at the transition between cutting without particle immobilization and ploughing with immobilization at higher angles of incidence. In fact, it has been verified that experimental results are accurately predicted at low to moderate angles, but not at higher angles ($\theta > 40^{\circ}$) where the model significantly under-evaluates the material loss [53]. In more recent work, Finnie *et al.* [54] found that the observed behavior at large angles of incidence could be explained by the dispersion of angles of incidence due to the increased surface roughness resulting from multiple particle impacts.

Although the plastic cutting mechanism is widely accepted for low angles of incidence, many different mechanisms have been proposed for ductile SPE behavior at high angles of incidence: embrittlement by work hardening [51], secondary erosion by particle fragmentation [55], localized temperature increase during impact [56], and fatigue by repeated plastic deformation [57, 58].

Another important observation about the cutting model is that it predicts that the volume removed scales with the square of V_p. However, experimentally the velocity exponent (n) is generally found to be between 2.3 to 3.0. Finnie and McFadden [59] found that higher values of n are the result of particle rotation during impact. The resulting volume removed by a single particle can be expressed as [53]:

$$V_e = \frac{F m_p^2 V_p^n}{\sigma_y} f(\theta) \tag{2.7}$$

where F is the fraction of particles which cut the target in an ideal manner, and n is typically between 2.2 and 2.4. Sheldon and Kanhere [60] and later Hutchings [51] showed that if particles were spherical, the modeled exponent would be further increased to a value of 3.

Another important aspect of SPE of ductile materials, especially at high angles of incidence, is the influence of strain rate effects on erosion behavior. Finnie *et al.* [61] showed that annealed metals largely exhibited erosion rates inversely proportional to hardness measured prior to testing (see Figure 2.12 where the inverse of *ER* is plotted against *H*). However, it can be seen in the same figure that metals with a low rate of strain hardening, such as steels, show much higher *ER*s than predicted and that work hardening and heat treatment had largely no effect. Hutchings [51] proposed that these observations can be explained by the high strain rates present during particle impact (10^6 s^{-1}) and the strain hardening ability of the materials. In fact, he showed that at such strain rates, conventional strengthening mechanisms have a greatly diminished influence and that a much better predictor of SPE is the hardness of the surface after strain hardening by erosion.

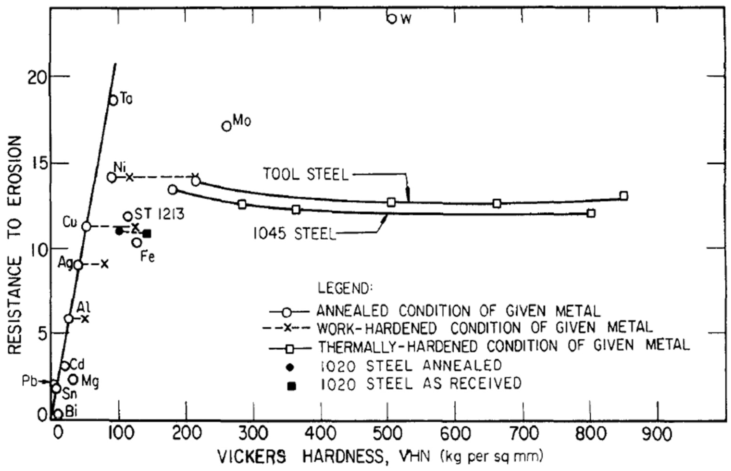

Figure 2.12: Illustration of the effect of strain hardening ability on the erosion of ductile materials [61].

2.4.2 Brittle SPE mechanisms

A maximum *ER* observed at normal incidence (see curve b in Figure 2.10) is generally indicative of a brittle mode of SPE during which the *KE* of the particle during impact is dissipated in part through crack initiation and propagation. Several types of cracking have been observed and they are analogous to those seen during indentation of surfaces. First, in the case of large rounded particles traveling at low velocity, it is likely that only elastic deformation of the surface occurs. Nevertheless, at a critical tensile stress, circular cracks may propagate from surface flaws and form cone like cracking that propagate into the material (see Figure 2.13 (A)). Significant volume loss will then occur when multiple cracks intersect.

Hertzian cracking (Figure 2.13 (A)) SPE is not frequently found since large particles such as those responsible for that type of impact damage are relative rare. In fact, it is much more common to encounter small angular particles travelling at high velocities. Small particle impact damage will resemble the type of cracking observed during indentation of brittle materials with a sharp pyramidal tip as illustrated in Figure 2.13 (B) to (E).

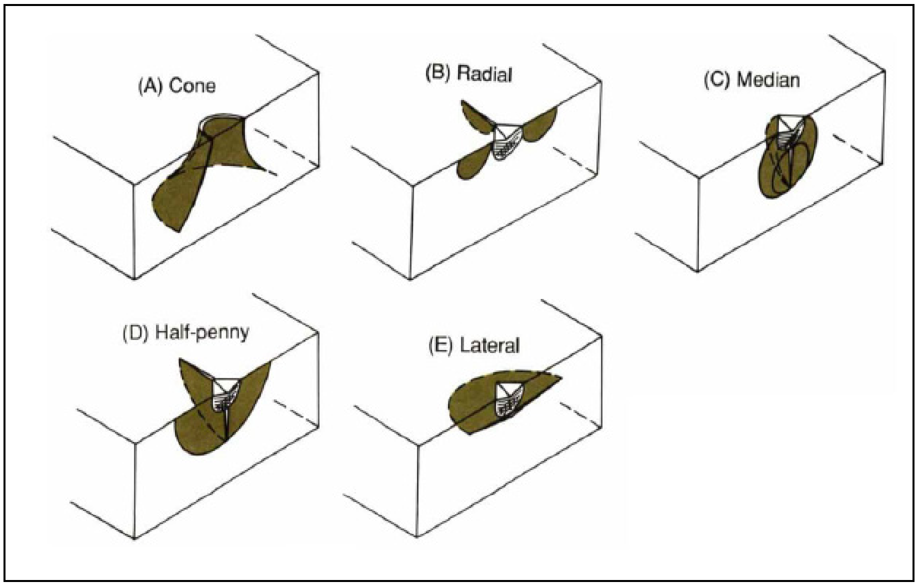

Figure 2.13: Idealized indentation crack morphologies observed for brittle surfaces [8].

At the moment of impact, the large contact pressure creates a zone of plastic deformation that increases in size until the particle reaches a maximum depth of penetration. When the pressure reaches a critical level, median and radial cracking develop (Figure 2.13 B and C) and can coalesce into half-penny cracking (Figure 2.13 D). Upon unloading, lateral cracking may propagate below the plastically deformed zone in order to relax strain mismatch between the plastically and elastically deformed zones. Severe target erosion will occur when lateral cracks intersect and propagate towards the surface (Figure 2.14).

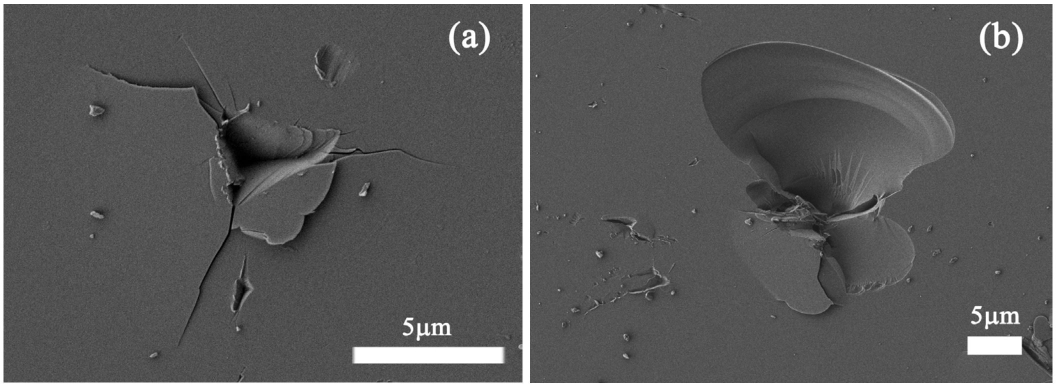

Figure 2.14: Residual impressions left on fused quartz glass by the impact of 70 μm alumina particles at a velocity of 45 m/s.

Early models of brittle SPE such as those developed by Sheldon and Finnie [62] and later by Oh *et al.* [63] were based on the intersection and delamination of conical Hertzian cracking. However, with the development of electron microscopy techniques, a plastically deformed zone could be seen beneath indentations, even in the case of highly brittle materials such as glass. From these observations, several models of brittle SPE by elasto-plastic indentation have been developed.

The evolution of the median/radial crack system was first described by Lawn and Fuller [64] who showed that, upon unloading, the half-penny crack length c_r could be expressed by:

$$\frac{P_m}{c_r^{3/2}} = \beta K_{IC} \tag{2.8}$$

where P_m is the maximum load during indentation, K_{IC} is the material's fracture toughness (in tensile crack opening mode), and β is a factor depending on the indenter geometry.

Although the use of equation 2.8 for the lateral crack system has no theoretical justification [65], Evans *et al.* [66] found that the radial and lateral crack lengths where proportional to each other. Therefore, Evans [66], and then Wiederhorn *et al.* [67], used equation 2.8 to calculate the lateral crack length c_l, and evaluate the cylindrical volume loss during a single sharp particle impact using,

$$V_e = \pi c_l^2 d_c \tag{2.9}$$

where d_c is the depth of the crack beneath the surface which was estimated to be directly proportional to the depth of maximum penetration (z_m).

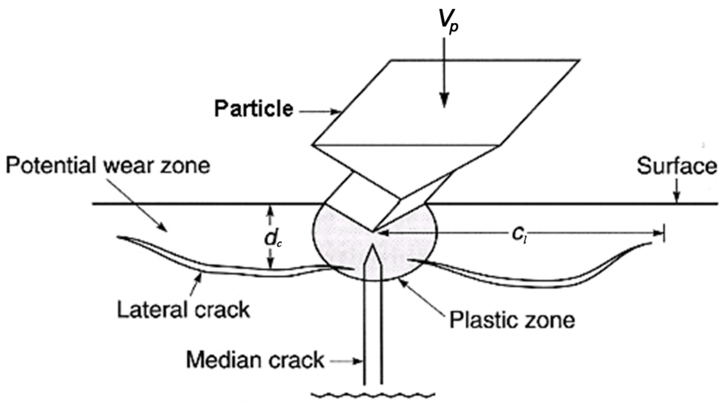

Figure 2.15: Schematic representation of lateral cracking following solid particle impact, adapted from [51].

What differentiates the two models is the manner by which P_m and z_m are evaluated. Evans analyzed the problem dynamically and calculated P_m from the maximum dynamic pressure during impact and z_m from the contact time. The total volume loss per impact was found to be represented by:

$$V_e \propto V_p^{19/6} D^{11/3} \rho_p^{19/12} H^{-1/4} K_{IC}^{-4/3}, \tag{2.10}$$

where D and ρ_p are, respectively, the particle radius and density, and H is the target hardness.

On the other hand, Wiederhorn *et al.* modeled the impact as a quasi-static indentation where the particle kinetic energy is completely dissipated through the plastic deformation of the target which in turn induces lateral fracture.

The work done to arrest the penetration of the particle can be expressed as:

$$W_{total} = \int_0^{z_m} P(z)dz \tag{2.11}$$

where P is the load applied to the impacting particle and z is the depth of penetration.

During quasi-static indentation, the load will be dependent on the mean contact pressure, which will be equal to the hardness, namely:

$$p_o = H = \frac{P}{A(z)} \tag{2.12}$$

where *A(z)* is the projected contact area between the particle and the impacted surface. Approximating the angular particle's *A(z)* as that of an idealized cone,

$$A(z) = \pi z^2 \tan^2 \psi \, , \tag{2.13}$$

where ψ is the cone half angle. We find, by combining equations 2.11, 2.12 and 2.13 and integrating, that

$$z_m = \left(\frac{3 * KE}{H\pi \tan^2 \psi} \right)^{1/3} \tag{2.14}$$

and

$$P_m = H\pi \tan^2 \psi \cdot z_m^2 \, . \tag{2.15}$$

Using

$$KE = \frac{1}{2} m_p V_p^2 \propto D^3 \rho_p V_p^2 \, , \tag{2.16}$$

the volume removed by a single impact modeled by quasi-static elasto-plastic indentation can therefore be expressed by:

$$V_e \propto V_p^{22/9} D^{11/3} \rho_p^{11/9} H^{1/9} K_{IC}^{-4/3} \, . \tag{2.17}$$

Both these models have been found to closely predict erosion behavior of materials under a lateral fracture material removal mechanism and remain to this day widely accepted. However, as mentioned previously, the equation used to predict *c* was developed for a half-penny crack system and not for lateral cracking. In addition, the depth from which the lateral cracks are believed to propagate is below the plastic zone and not at the maximum depth of penetration. In order to correct these two deficiencies, Buijs [68] refined the quasi-static model by using the lateral fracture system analysis proposed by Marshal *et al.* [21]. The approach was later expanded by Slikkerveer *et al.* [69] using a more complex representation of the lateral crack system. Although this more complex approach did not find a better correlation with the experimental data when compared to the models proposed by Evans and Wiederhorn *et al.*, Slikkerveer at al. showed, using a wide range of particle sizes and velocities, that SPE depends on particle parameters (V_p, D and ρ_p) only through the particle *KE*.

2.4.3 Mechanism transitions in the SPE of brittle materials

It has long been observed that apparently brittle materials such as glass can exhibit ductile behavior under certain conditions. In fact, more than 40 years ago Sheldon and Finnie showed that by reducing the size of the particles (9 μm in Figure 2.16), a clear transition between brittle and ductile behavior could be seen in typically brittle soda-lime glass.

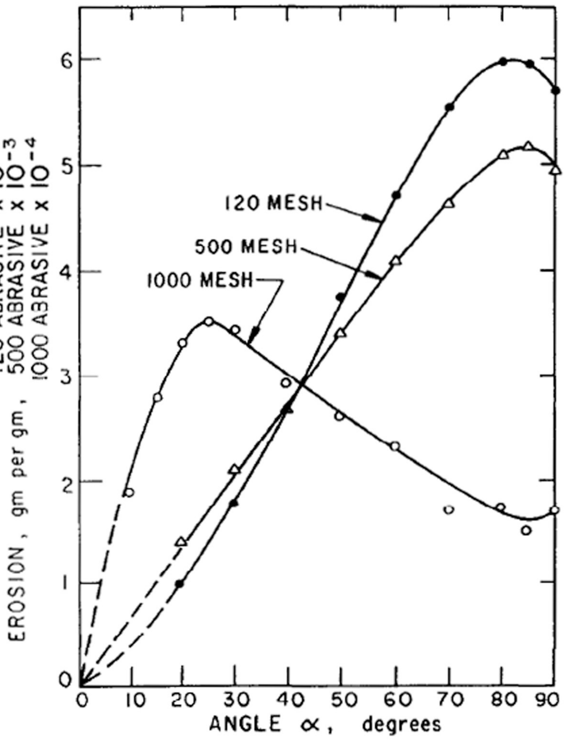

Figure 2.16: Illustration of the brittle to ductile transition for glass when the abrasive particle size is reduced from 127 μm (120 Mesh) to 9 μm (1000 Mesh) [70].

Mechanism transition does not only occur between ductile and brittle modes of erosion but also between the different types of cracking that we have presented above. In one of his important articles, Hutchings [31] illustrated these transitions in the form of erosion maps with the transition threshold values being a function of the corresponding elastic (Young's Modulus [*E*]), plastic (hardness [*H*]) and fracture (fracture toughness [K_{IC}]) properties. Verspui *et al.* [71] elaborated on this approach and developed analytical expressions that predict these transitions in material behavior. They based their work on the analytical indentation models proposed by Wiederhorn and Lawn [72] for cone cracks, Lawn *et al.* [20] for the median/radial crack system and Marshall *et al.* [21] for the lateral crack system. They expressed the transition thresholds as critical velocities (V_{crit}) for a given particle size at which transition will occur.

In Figure 2.17 two typical erosion maps are presented. In these maps, presented by Bull in [73] for glass and for a TiN coating, we can distinguish five distinct SPE behaviors. First, when particles have a very low *KE*, only elastic deformation of the surface occurs (Zone I) and the particles rebound without causing any damage. When particle size increases, Hertzian cone cracks may form and coalesce (Zone II). This transition will only be seen for large particles because the contact pressure must remain below the yield strength of the material above which plastic flow will occur. In fact, we can see that purely elasto-plastic behavior (Zone III) occurs for relatively small particles impacting the surface at high velocity. Larger particle sizes, at high velocity, will lead to a direct transition from elastic behavior to radial/median cracking (Zone IV) or lateral fracture (Zone V). It should be noted that hard and tough materials (such as the TiN coating in Figure 2.17 (b)) can be used to translate the thresholds towards higher impact velocities, making the surface more resistant to SPE.

These transition maps are quite useful to understand the behavior of brittle materials under different erosive conditions. However, while the nature of the erodent particles can significantly influence SPE behavior in practice, in their analysis, Verspui *et al.* supposed spherical and ideally elastic particles. In the next section, we present the effects of the particle properties.

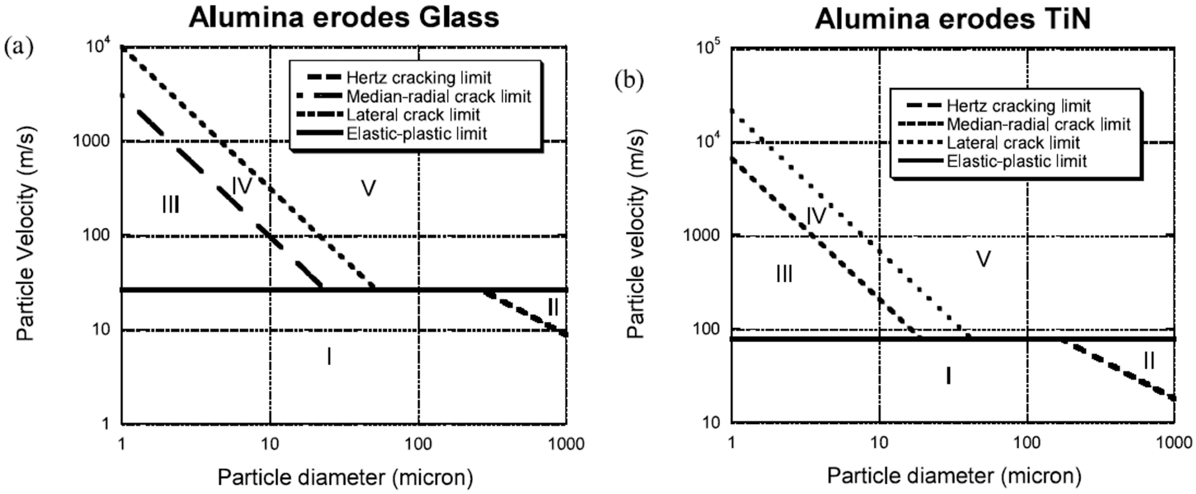

Figure 2.17: SPE mechanism transition maps for (a) Glass and (b) a TiN coating [73].

2.4.4 Effect of particle properties on SPE

The first property that can affect SPE is the particle geometry. In fact, the angularity of the impacting particles significantly affects material removal of all types from ductile cutting to brittle fracture. In terms of mechanism transitions in brittle materials, angular particles will nearly always cause elasto-plastic damage upon impact because of high contact stresses. Using the approach proposed by Verspui *et al.* [71], based on Hertz contact theory, it can be demonstrated that the SPE elasto-plastic transition for crystalline silicon occurs at V_{crit} = 65 m/s when impacted by a spherical alumina particle 50 µm in diameter, but only at 0.2 m/s if the same particle is angular. In addition, Verspui *et al.* showed that V_{crit} is constant regardless of particle size and that only target properties affect the onset of plastic flow. On the other hand, for angular particles, the plasticity threshold will be a function of the ratio of tip radius to particle radius where the tip radius is typically in the hundreds of nanometers while particles are in the tens of microns. In practice, this means that plasticity is instantaneous and therefore, Hertzian cracking is nearly impossible. It should be noted that, as stated by Verspui *et al.*, the angularity of the particle does not affect the critical velocities for radial and lateral cracking. However, because these types of fracture occur after the onset of plasticity, the radial and lateral fracture critical velocities will be lowered by the reduction of the plastic critical velocity.

All the models presented above consider that the particle *KE* is completely transferred to the surface. In reality, a great proportion of the energy is either returned to the particle through elastic recovery of the target surface or is dissipated through other means such as phase transformations, thermal effects, fracture mechanisms and particle deformation and fracture. While phase transformations and thermal effects are generally negligible for brittle materials, the most important additional source of *KE* dissipation during the erosion of hard materials is the fracture (or crushing) of particles.

Several authors have presented evidence of the fragmentation by collecting the particles after testing and observing the residual powder or measuring the particle size distribution before and after testing [74, 75]. A few have also imaged the particles during impact as illustrated in Figure 2.18 where we can see the breakup of a rounded 300 µm silica sand particle on impact with a tungsten carbide surface.

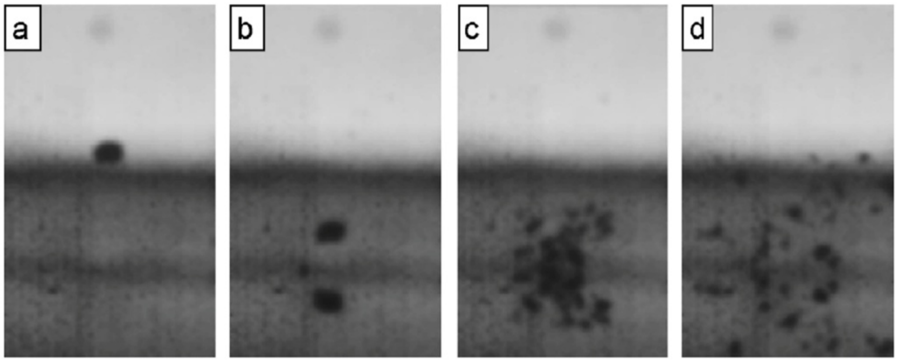

Figure 2.18: Fragmentation of a 300 μm sand particle upon impact with a tungsten carbide surface [76].

It has been shown that particles are generally crushed or fragmented when the ratio of particle hardness (H_p) over target hardness (H_t) falls below unity [12, 77, 78]. Although it has been proposed that the toughness of the particle plays a role in the fragmentation process [77], this has not been as conclusively demonstrated as for the role of surface hardness. Finally, it has also been suggested that particle breakup increases with the velocity at which the impact occurs [12].

Although limited work has been done to study the influence of particle fragmentation on SPE mechanisms, several authors have observed increases in erosion rates as the ratio H_p/H_t increases [12, 78]. In particular, Shipway and Hutchings [12] studied a wide range of materials eroded by three types of particles and found significant changes in erosion behavior as a function of H_p/H_t. They found that material loss mechanisms changed from micro-chipping for lower ratios to full lateral fracture at higher ratios. They also observed that the erosion rates increased further as velocity increased when $H_p/H_t < 1$ and hypothesized that this occurred because more damage needed to accumulate at low velocity before material removal occurred. In fact, Murugesh and Scattergood [77] have also observed the role of damage accumulation in the erosion of hard ceramics by softer particles.

These findings support the work by Wada [78] who proposed that the transitions would be affected by H_p/H_t as well as by the toughness of the particles. The modified transition map is presented in Figure 2.19 where the effect of the H_p/H_t ratio and the particle toughness on the SPE mechanisms can be seen. Wada theorized that as the H_p/H_t ratio decreases (the inverse is used in Figure 2.19) more *KE* is needed to generate plastic deformation (defined as scratching in Figure 2.19) and that the transition to lateral fracture is preceded by Hertzian fracture. It can also be seen that the transition thresholds can be translated by particle shape and toughness, and target toughness. It should be noted that this map is the result of experimental work and that no theoretical model has been proposed to explain these observations.

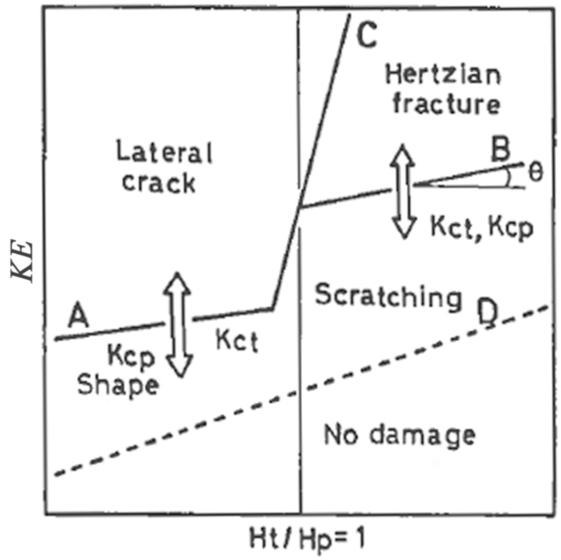

Figure 2.19: Effect of particle properties on SPE mechanism transitions (adapted from [78]).

2.4.5 SPE of ceramic materials

Hard bulk ceramic materials generally behave in a brittle manner under SPE, but the material loss mechanisms cannot be generalized because of their complex microstructures. The grain size of sintered ceramics has been shown to significantly affect the erosion process [79]. In fact, when the grains are small compared to the size of the damage caused by the particle impact, lateral fracture is the dominant mode of material removal. However, when the grain size is larger than impact damage, chipping grain ejection is observed. It has also been reported that when the size of the damage becomes comparable to the size of the grains, erosion rates increase dramatically because of grain boundary cracking and grain ejection [80].

As discussed previously, an important factor in the erosion of hard materials is the effect of particle properties. In fact, much of the work done on the influence of particle properties on erosion behavior was conducted on bulk ceramic materials such as Si_3N_4, Al_2O_3 or ZrO_2. As discussed previously, the particle breakup may lead to very low erosion rates and it may cause a change in material loss mechanism. For low H_p/H_t ratios, a micro-chipping mechanism has been observed [12, 31, 81] but little information on this fracture process can be found. It has generally been characterized by a smooth surface after erosion when compared to the very rough surfaces resulting from lateral fracture.

2.4.6 SPE of multi-phased materials

A more recent trend in hard materials is the development of multi-phase systems, which benefit from the strengths of the different phases such as high hardness, low friction or high toughness. These materials can be synthesized by a variety of methods such as sintering, laser cladding, weld overlay or thermal spray deposition.

In these multi-phase materials, the microstructural averaging of SPE is of great interest but can be quite complex and is strongly dependant on the phases in question and the SPE conditions such as particle size, velocity, impact angle, etc. For example, when the scale of damage is smaller than the phase size, it has been reported that the SPE behavior obeys an inverse law of mixtures of the erosion rates of both material phases [79]. This means that a relatively small volume fraction of the resistant phase may improve the erosion behavior significantly. However, if the impact damage size increases and becomes comparable or larger than the characteristic microstructural size scale, the behavior can become quite complex, accompanied by crack propagation through multiple phases and hard phase ejection.

Thick thermal sprayed coatings with complex microstructures are being increasingly studied as erosion resistant materials. These coatings are usually relatively thick (> 50 µm) and behave under SPE like bulk materials (no thickness or substrate effect). They are composed of two or more phases with one hard phase (*e.g.* Al_2O_3, WC, SiC, CrC and TiC), one binding matrix (*e.g.* Co, Cr and NiCr) and additional phases for added functionalities (*e.g.* ZrO_2 and Y_2O_3). Consequently, as is the case with bulk multi-phase materials, the many different SPE mechanisms that have been reported are strongly influenced by the heterogeneous microstructure and the scale of the impact damage. Most notably, cracking along grain boundaries (Figure 2.20 a) or between splats (Figure 2.20 b) have been reported to significantly contribute to the erosion of this category of materials.

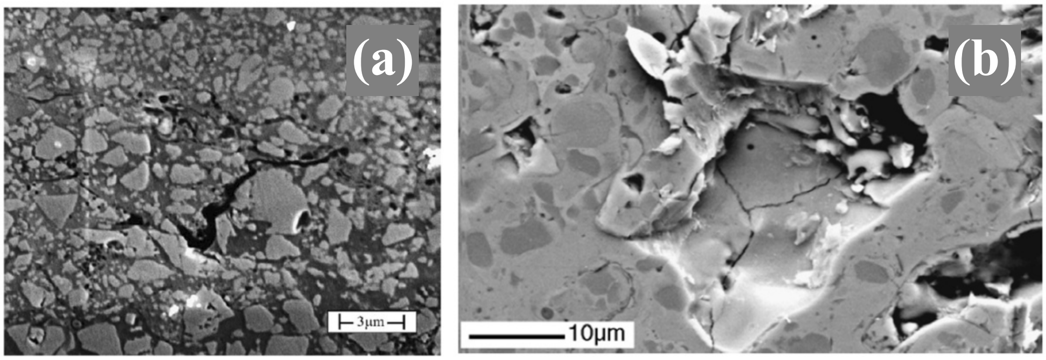

Figure 2.20: Illustration of complex fracture processes in multiphase materials: (a) grain boundary cracking [82] and (b) intersplat cracking [83].

2.5 Solid particle erosion of vapor deposited coatings

Most of the studies on the SPE of coatings found in the literature are very difficult or even impossible to compare because of a lack of methodological consistency. As will be discussed in the next chapter, establishing and following a rigorous experimental methodology is essential if meaningful SPE results are desired. In fact, the choice of particles (composition, size and shape), the type of nozzle (length and diameter), the erosion parameters (particle velocity, angle of incidence, working distance and feed rate) and the mass (or volume) loss evaluation technique are critical in defining a methodology for comparison purposes. For example, if erosion rates are evaluated when the coating has been pierced and the substrate influences the results, meaningful interpretation of erosion data becomes very difficult.

Nonetheless, over the last 25 years many studies have been conducted on the SPE of coating systems with most of them being comparative investigations designed to evaluate the performance of specific coatings. The great majority of studies have concentrated on two coating families: TiN-based systems (TiN [84-96], TiAlN [85, 92, 95, 97, 98], TiCN [84, 85, 95, 99], TiSiN [100, 101], TiSiCN [102-104], and many multilayer variations [45, 94, 105-107]) and, carbon-based systems (diamond [81, 108-122], diamond-like carbon (DLC) [123] and tetragonal carbon (ta-C) [124]). To a lesser extent, other nitride (CrN-based [10, 85, 91, 92, 96, 98, 125], WN [126] and ZrN [85]) and some carbide (TiC-based [127, 128], and BC [129-131]) systems have also been studied. Very little work has been done on boride-based systems.

2.5.1 SPE of TiN-based coatings

Up until today, TiN-based coatings are the most frequently used industrial SPE resistant coatings in aircraft engines. Consequently, many studies have been performed on monolithic and multilayer coatings. In particular, Immarigeon *et al.* [87] illustrated great differences that can be observed for TiN monolithic coatings prepared by different deposition techniques. In their study, thick PVD deposited coatings were shown to have the lowest *ER*s, but they suggested that poor adhesion may have skewed some of the results. The large spread in coating thicknesses may also have strongly influenced the results as shown by Hassani *et al.* [30]. Using finite element modeling (FEM), they showed that an increase in *ER* could be predicted for the TiN coatings with thicknesses below 8 µm.

As discussed previously, SPE resistance can be enhanced by using materials with high toughness to prevent crack growth and high hardness to dissipate the particle kinetic energy through fragmentation. Consequently, alloyed and nanocomposite TiN-based coatings have also been investigated. A system that is now being implemented industrially is TiAlN which has been shown to not only possess high SPE resistance [92, 97] but also good stability at higher temperature [132-134]. In this category, TiCN has also shown much promise [86, 95, 99]. Nanocomposite TiSiN and TiSiCN coatings have also been studied, but to a lesser extent. In fact, only Zeng *et al.* [100] have studied TiSiN while Wei and coworkers [102-104] have published results for the TiSiCN system. Zeng *et al.* showed that TiSiN nanocomposite coatings were more resistant than TiN and other nitride coatings, and Wei and coworkers showed that TiSiCN coatings deposited by a hybrid deposition method with a hexamethyldisilazane precursor were highly resistant as well when compared to TiN, CrN and ZrN.

2.5.2 SPE of multilayer coatings

In practice, many erosion resistant coatings use multilayer architectures because these offer a possibility of depositing thicker coatings by relaxing residual stresses and also because erosion resistance may be enhanced by an appropriate multilayer design. In fact, Hassani *et al.* [135, 136] showed by modeling different multilayer configurations by FEM that it was possible to reduce maximum tensile stresses during impact through load spreading and thus increase the velocity threshold at which cracking begins. However, their study was limited to small spherical particles and their proposed guidelines for improved performance cannot be generalized since it has been shown that multilayer architecture must be optimized for the erosion conditions such as particle velocity, shape, size and composition.

In a recent PhD thesis and in two subsequent articles, Borawski *et al.* [106, 107, 137] studied the design of TiN-based multilayer coatings for SPE enhancement under different erosive conditions. Using various coating designs composed of hard TiN and ductile Ti layers, they have shown that two layer coatings (adhesive layer and top layer) are more resistant under SPE by small, hard and angular particles (alumina) while multilayer architectures are more resistant to SPE by large rounded particles (quartz and glass). They explain these findings by the fact that the damage caused by alumina is generally confined to a small volume in the top layer: the coating is therefore eroded layer by layer. In that case, the ductile interlayers of the multilayer coating would not be beneficial to erosion resistance. On the other hand, the stress field generated during impact by large rounded particles encompasses a larger volume of the coating. Therefore, the crack tip blunting effect of the ductile layers and the deflection of cracks at interfaces would be beneficial to enhance SPE resistance.

2.5.3 SPE of carbon-based coatings

Carbon based coatings are the second major coating group to be studied for their SPE resistance. In addition to possessing very high hardness, some of these materials are interesting candidates for optical applications in aerospace and in particular as infra-red transparent windows. Notably, Grögler *et al.* [108] found that CVD diamond coatings have exceptional resistance to SPE when compared to TiN and TiAlN. However, these results may be severely skewed due to the fact that the TiN and TiAlN coatings in the reported study had thicknesses below 6 µm leading to a substrate effect, while the diamond coatings all had a thickness greater than 10 µm which probably greatly diminished substrate influence. However, other studies have also demonstrated the highly resistant nature of thick diamond coatings.

The largest contribution in the field comes from Wheeler and Wood who have studied in detail the material removal mechanisms during high energy SPE of thick CVD diamond [81, 109-120]. They have shown that during high velocity (V_p > 200 m/s) sand erosion of such thick coatings, only minor chipping occurs at first. As the amount of sand impacted on the surface increases, they show that damage accumulation occurs at the interface between the coating and the substrate, causing localized delamination, even when the coating is 200 µm thick. They verified the delamination by scanning acoustic microscopy where the white regions indicate debonding and by scanning electron microscopy where cracks can be seen at the interface of the coating and the substrate (Figure 2.21).

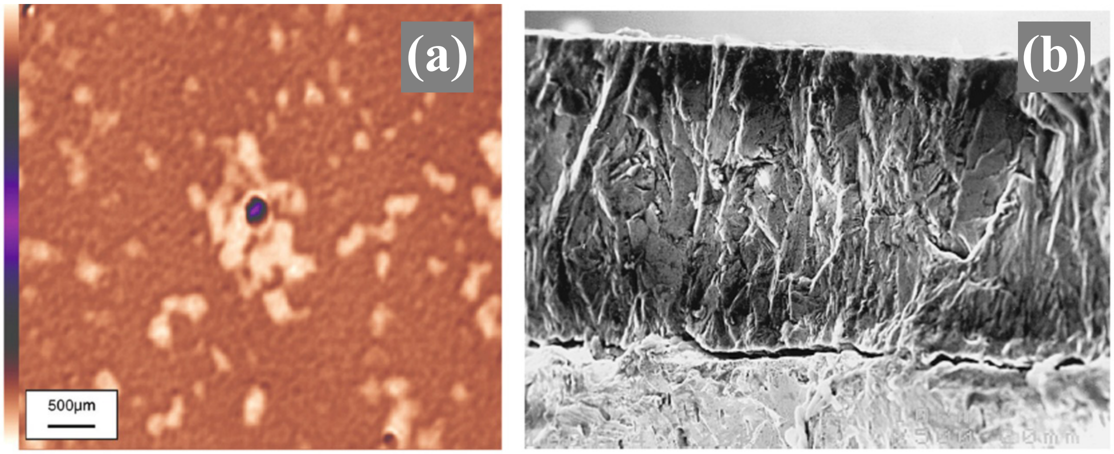

Figure 2.21: Erosion of thick diamond films by large and high speed sand particles with interfacial (a) debonding [118] and (b) cracking [119].

The authors explain that after delamination, the stress waves caused by subsequent particle impacts will be reflected at the rear surface where debonding has occurred and cause increased tensile stresses at the surface of the coating leading to cracking and eventually to pin-hole like erosion craters (Figure 2.22). In a separate study [112], they have shown that when using diamond particles, a lateral fracture mechanism of material loss is observed.

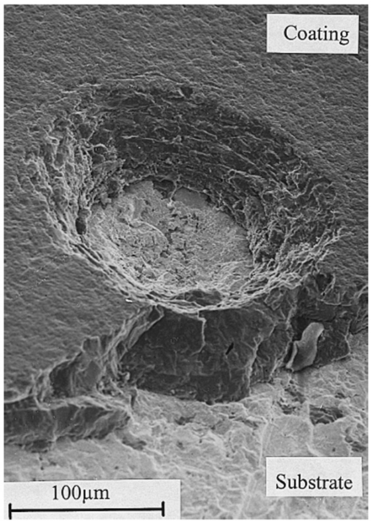

Figure 2.22: Pin-hole erosion crater in a thick diamond coating [120].

2.5.4 SPE of other coating systems

Many other different coating compositions and configurations have been studied. In particular, the group of Tabakoff have evaluated many different coatings found in aerospace applications (Pt-Al, Rd-Pt-Al, CrC, NiCrC, Cr, WC-Co, TiC, TiN, Al_2O_3 and CVD diamond) in a specially constructed high temperature erosion test rig that simulates, as closely as possible, the particle impact conditions found in the engine [5, 121, 128, 138-151]. Although most of their studies were comparative, they have shown that in many cases the increased ductility at high temperature is beneficial for erosion resistance of hard coatings.

Another notable contribution is the work by Wellman, Nicholls and coworkers in the field of electron-beam deposited (EBPVD) thermal barrier coatings (TBCs) [152-163]. They studied and modeled the role of the highly strongly columnar nature of these coatings on the solid particle erosion and foreign object damage behavior. They showed that the microstructure plays a very important role in the material loss mechanisms of these coatings. In fact, three types of damage mechanisms were observed. Under small particle impact, steady state erosion is caused by near surface cracking of the coating while leaving the rest of the columnar structure sound (Mode I, Figure 2.23 (a)). Under larger particles, the impacts will lead to damage on the scale of multiple columns, first by plastic columnar compaction (Mode II, Figure 2.23 (b)), and then by large scale columnar cracking which they designate as FOD or foreign object damage (Mode III, Figure 2.23 (c)).

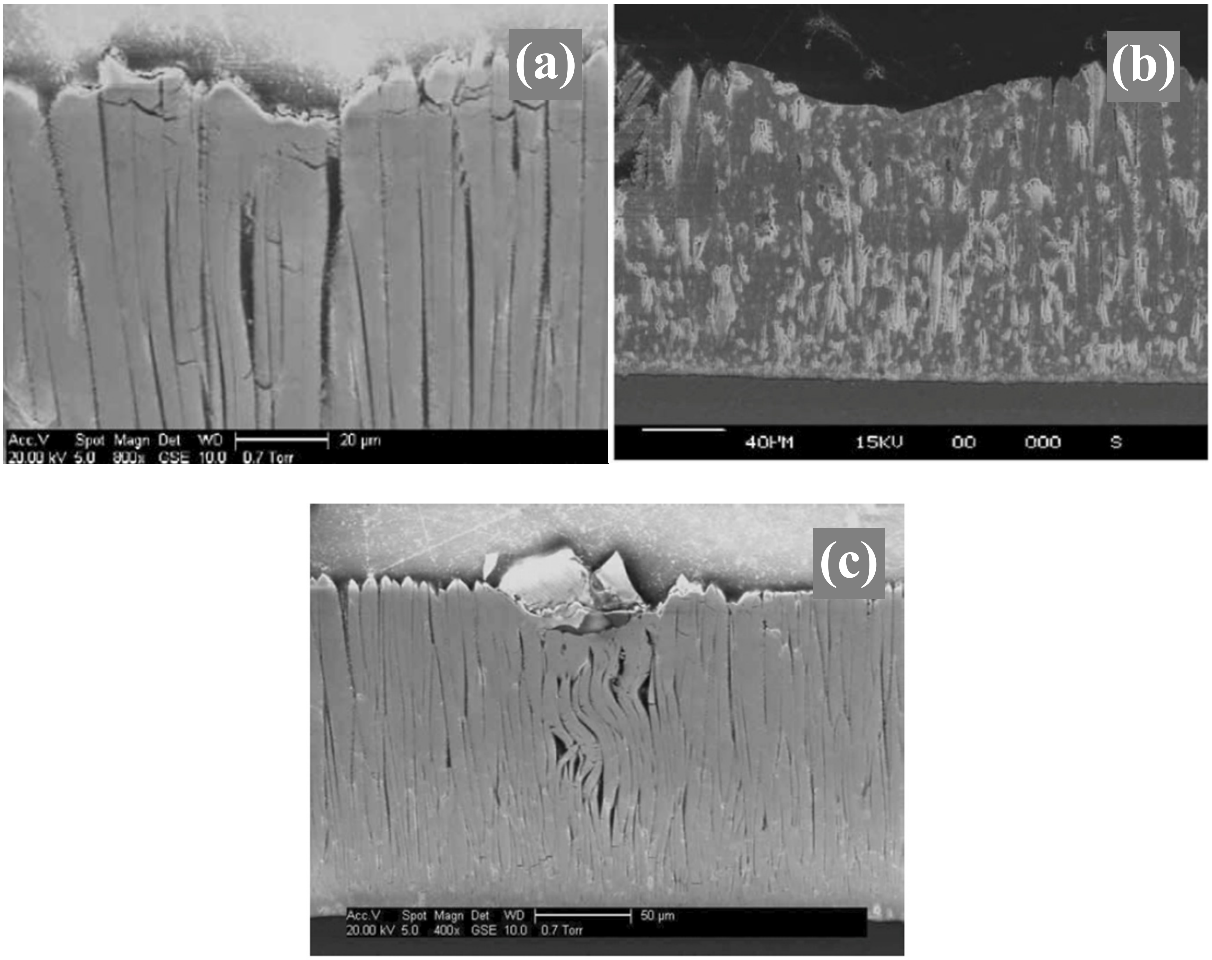

Figure 2.23: Damage mechanism observed in EBPVD TBC: (a) Near surface cracking, (b) columnar compaction and (c) foreign object damage [156].

In this chapter, we have presented the important elements necessary to comprehend the content of this research project, namely surface mechanical response, surface engineering techniques, nanocomposite coatings, solid particle erosion of materials and coatings. As we have illustrated in the final section, coated systems can present complex SPE mechanisms and therefore, rigorous testing methodologies need to be employed for accurate characterization and the effects of all testing parameters need to be fully understood. In the following chapter, we will present an overview of the experimental techniques and methodologies that were used during the project for coating deposition, solid particle erosion testing, and microstructural and mechanical characterization.

CHAPTER 3 EXPERIMENTAL METHODOLOGY

3.1 Coating deposition by pulsed DC magnetron sputtering

All the coatings were deposited by reactive PDCMS in a reactor designed and constructed in-house (Figure 3.1). The system is equipped with two magnetron sputtering sources powered by a pulsed DC Pinnacle Plus+ power supply. The pulse shape and duty cycle (percentage of time during a pulse when sputtering occurs) can be controlled by adjusting the pulse frequency, the pulse reversal time and by choosing the proper regulation mode (current, voltage or power). These settings, combined to the response of the power supply and sputter target properties, define the sputter yield and deposition rate. In this project, we used duty cycles above 80% in order to obtain deposition rates as high as possible (above 1 μm/hour) so as to minimize the deposition time of thick coatings (below 12 hours).

The chamber was designed to accommodate the samples vertically on a rotating, biased and heated substrate holder. The vertical position of the substrates during deposition was critical in the design, in that it avoided contamination of the surface by flaking from the chamber walls which occurred when depositing coatings thicker than 5 μm. The substrate holder was biased by using a capacitively coupled radio-frequency (RF) plasma and heated using a ceramic resistance positioned behind the substrates. Heating was regulated with the help of a controller using the heater temperature as a calibrated reference for the substrate temperature. The base pressure of the reactor was typically below 1 x 10^{-6} Torr, which was achieved after 6 to 10 hours of pumping using a turbomolecular pump.

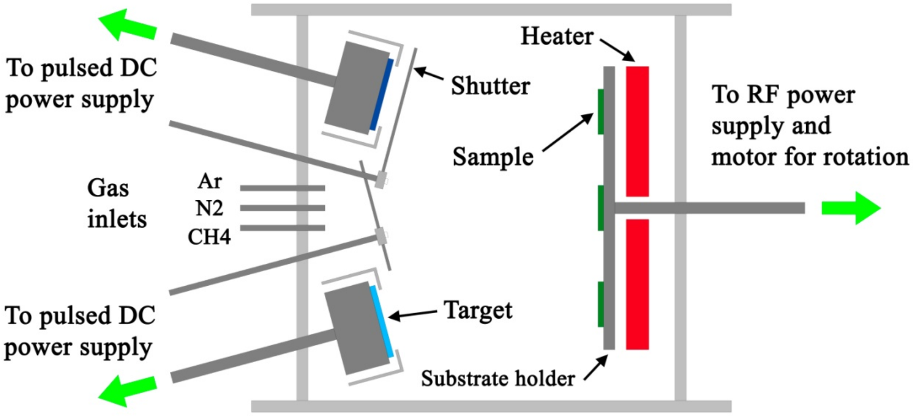

Figure 3.1: PDCMS deposition system with dual magnetron configuration.

Although many different substrates were used, the depositions were made on four main substrates: single crystal silicon (c-Si), Ti-6Al-4V (Ti64), AISI 410 stainless steel (SS410) and Quartz Crystal Microbalance (QCM) resonators. Prior to deposition, the substrates were cleaned with detergent by hand and then with acetone and isopropanol in an ultrasonic bath for 15 minutes. In order to remove the formation of a surface oxide layer, the substrate surfaces were sputter cleaned at a negative bias and the sputter targets were cleaned by initializing the discharge at their surface while maintaining the shutters closed, so as to not deposit on the substrates. In general, these two cleaning steps occurred at the same time for a duration of 15 minutes. However, when depositing on the QCM substrates, the sputter time was minimized (1 or 2 minutes) so as to sputter away the gold electrode of the QCM (for adhesion purposes), but not too much of the quartz crystal itself.

During deposition, the biased substrates where heated between 100 and 500 ^{o}C and rotated at approximately four revolutions per minute in order to maximize deposition uniformity over the whole sample surface. In order to promote adhesion, a thin chromium or titanium layer (< 1 µm) was first deposited, followed by the coating. The silicon content in the ternary coatings was adjusted by changing the current on the Si target and the carbon content in the quaternary coating was controlled by the flow of CH_4 during deposition. The specifics of the deposition of the coatings are detailed in the published articles.

3.2 Gas blast solid particle erosion testing

Two main types of solid particle erosion testing apparatus exist: the centrifugal-accelerator tester and the gas-blast tester (Figure 3.2). The first is based on the projection of particles through centrifugal forces. The particles are fed through the center of a rotating disk, accelerated through radial ceramic tubes and ejected onto samples placed around the disk. In this PhD project, the second type of SPE testing system was used, where the particles are accelerated by pressurized air. It was designed and built based on the specifications found in the ASTM standard G76 [164] for erosion testing by solid particle impingement using a gas jets. The basic design of our system consists of an abrasive blasting unit (S.S. White Airbrasive unit) that regulates the velocity and feed rate of the particles, a work chamber where the testing occurs and a combined sample and nozzle holder for accurate sample positioning with respect to the particle stream.

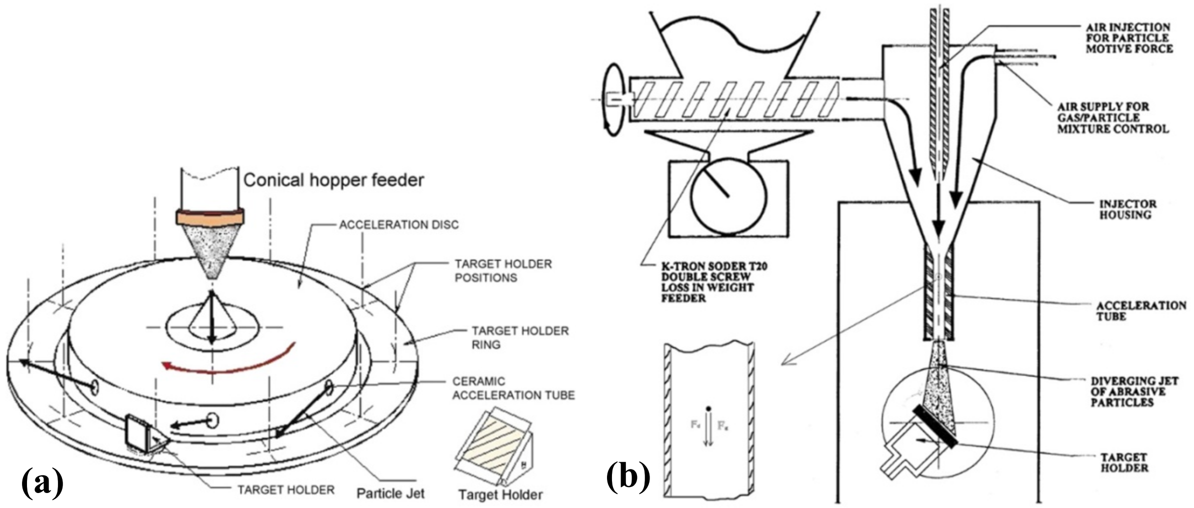

Figure 3.2: Types of SPE testers: (a) centrifugal-accelerator and (b) gas-blast [165].

At first, the work chamber consisted of a glove box with an industrial dust collector. However, in order to collect the used powder more efficiently, a new sealed work chamber was designed to completely contain the used particles with the help of a HEPA filter (Figure 3.3). The chamber also includes two quartz windows in order to observe the sample during erosion testing and also to eventually install a camera for more detailed observations of the impact phenomena and material loss mechanisms. The chamber was also designed to be installed on a high capacity balance to closely monitor the mass of particles that impact the sample surface during testing. However, due to instabilities in the recorded mass when the shutter, protecting the sample surface, was actuated, the blasting unit itself was mounted on a balance with a 30 kg capacity and precise to 0.1 g (Sartorius LE29000).

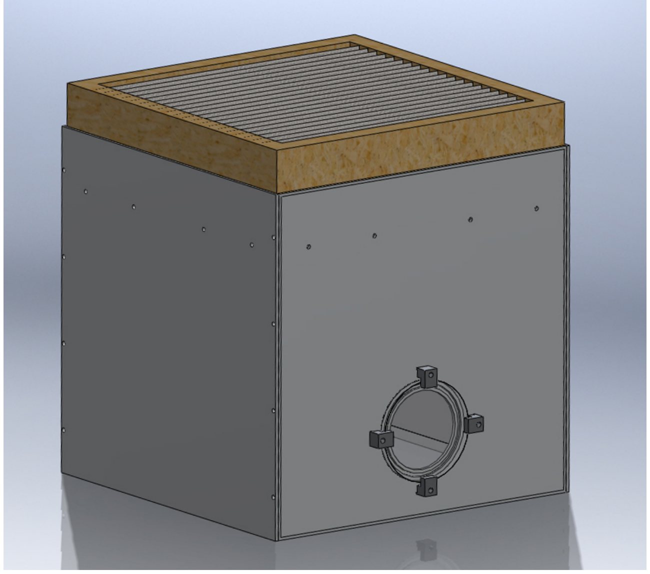

Figure 3.3: SPE testing chamber with windows and HEPA filter.

The particle velocity is controlled by adjusting the back pressure of the abrasive blasting unit and the particle feed rate by adjusting the unit's shaker amplitude as well as the back pressure. The particles are accelerated towards the sample surface by a tungsten carbide cylindrical nozzle. In this work, two types of nozzles were used: a long nozzle respecting the ASTM G76 standard (inner diameter of 1.14 mm and length of 36 mm) and a short nozzle for an increased divergent particle flow (inner diameter of 1.14 mm and length of 9 mm). The sample and nozzle holder is designed to accurately control the angle of incidence by pivoting the arm on which the nozzle is positioned (see Figure 3.4) and to adjust the distance between the nozzle outlet and the sample surface (working distance).

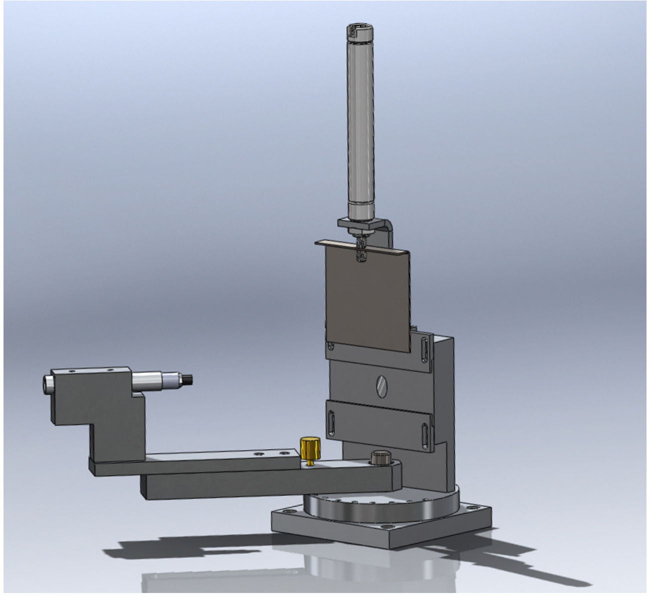

Figure 3.4: Sample and nozzle holder for SPE testing with retractable shutter.

A pneumatically actuated shutter is also installed on the sample holder. Before testing, the shutter is closed to shield the sample surface from the particle stream while the sand blasting system is turned on and the flow of particles is stabilized. This usually takes approximately two minutes. The shutter is then opened and, for the duration of the test, the mass of particles impacting the surface (leaving the sand blast unit) is monitored. The standard test consists in exposing the sample surface for a fixed total mass of powder and evaluating the amount of volume loss. The erosion rate of the tested sample is calculated by dividing the worn volume by the total mass of particles that have impacted the surface.

3.2.1 Particle velocity calibration

The dependence of particle velocity on the blasting unit's back pressure was measured using a double disk time-of-flight technique based on the methodology proposed by Ruff and Yves [166]. The method consists of two disks rotating at a fixed angular velocity (ω). The first disk has an opening that lets the particles penetrate and impact the second disk. Knowing the geometry of the apparatus and ω, the average particle velocity can be evaluated by measuring the offset (s) between the wear scar left on the second disk when compared to a reference mark made by line of sight through the slit while the disks are at rest (see Figure 3.5). The particle velocity can therefore be expressed by,

$$V_p = \frac{2\pi r_d \omega L_d}{s}, \tag{3.1}$$

where r_d is the radial distance between the wear scars and the rotation axis of the disks and L_d is the distance between the disks that the particles must travel before impacting the surface of the second disk.

Figure 3.5: Optical image of typical velocity calibration wear scars with the offset s indicated.

Because the offset is often evaluated visually, this calibration technique can be inaccurate due to broad wear scars caused by large particle velocity distributions in the divergent flow exiting the nozzle. In order to minimize the experimental error, we developed a double disk apparatus with removable glass slide samples on the second disk (Figure 3.6). This enabled us to evaluate the offset by profilometry (Figure 3.7) leading to much lower experimental errors on the velocity measurements. In fact, the standard deviations are generally lower than 10% as illustrated by the error bars in Figure 3.8. It should be noted that the velocity will not only depend on back pressure but also on the size and shape of the particles, the nozzle geometry and the length and size of tubing of the blasting unit. Every time one of these parameters changes, the particle velocity will need to be recalibrated. In the example in Figure 3.8, the measurements were made for alumina powder using the short nozzle and a working distance (*WD*) of 100 mm.

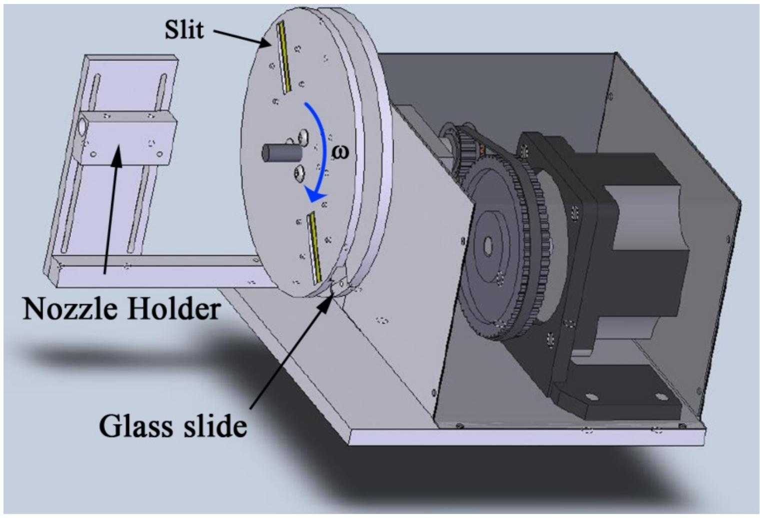

Figure 3.6: Double disk apparatus for time-of-flight evaluation of particle velocity.

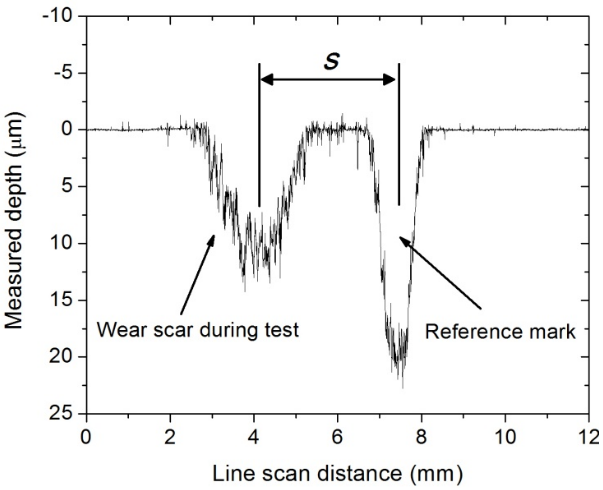

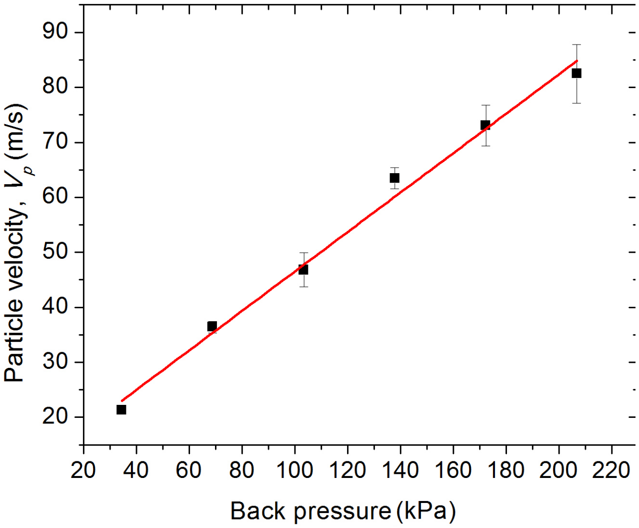

Figure 3.7: Depth profile of the wear scars produced during a velocity calibration test. The measurement of *s* is indicated.

Figure 3.8: Alumina powder velocity calibration using a short nozzle and *WD* = 100 mm.

3.2.2 Erosion wear scar geometry

The particle plume exiting a cylindrical nozzle will be divergent and will depend on several parameters such as nozzle geometry and internal roughness, and particle velocity, shape and size. In practice, the divergence can vary widely and has been found to be directly influenced by the length of the nozzle when the air flow in the nozzle is not fully developed [167]: this generally occurs for an aspect ratio (nozzle length over inner diameter) below 20 (ASTM recommends a minimum of 25). Above this ratio, the length of the nozzle has been shown to have little effect on plume geometry [168]. In this project, the short nozzle, that was used, did not have a sufficiently large aspect ratio (≈8) for fully developed flow and, consequently, presented a divergence angle as high as 15 degrees. On the other hand, the long nozzle had an aspect ratio of approximately 32 leading to a highly focused particle plume with a divergence angle below 6 degrees.

The shape of the particle plume will directly determine the radial distribution of particles that impact the surface of the sample during testing. Shipway and Hutchings [169] proposed that the probability function of the mass of particles impacting the surface should be described by a Gamma function, but found discrepancies with experimental erosion wear scars. More recently, Ghobeity *et al*. [170] found that a Weibull radial probability distribution function was much more representative and agreed well with experimental values. In fact, they found that this probability function, combined with the measured linear radial decrease in velocity from the centerline of the jet outwards, predicted accurately the observed erosion wear scars produced by a cylindrical nozzle. In general, the typical wear scars generated from tests with a cylindrical nozzle are axisymmetrical and present a Gaussian type of profile. We present a full topographical map of one such scar in a single crystal silicon sample (Figure 3.9).

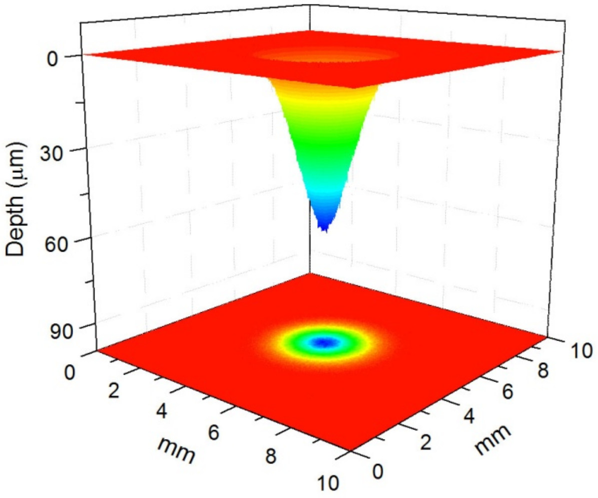

Figure 3.9: 3D topographical map of an SPE wear scar in c-Si.

In the past 15 years, much work on the influence of process parameters on the shape of erosion scars has been done in the context of abrasion jet micromachining of glass for flat panel displays

[69, 71, 167, 170-181]. In particular, the work of Papini, Spelt and coworkers [167, 170, 174-181] has led to many interesting findings on the importance of working parameters such as feed rate and *WD* on the erosion process. As we will discuss in the next sections, the Gaussian profile of the wear scar has enabled us to measure the volume loss of eroded samples using a simple profilometry methodology and other results regarding particle interference effects have helped us to optimize our erosion testing methodology.

3.2.3 Volume loss measurement

In a great majority of SPE studies, the material loss is evaluated by measuring the mass loss of the sample after testing and then converting it to volume loss by dividing it by the density of the material. In fact, this is the methodology that is proposed in the ASTM standard G76. In the case of tests on hard coatings, this approach can be very difficult to implement for several reasons, as detailed below.

The mass losses are often very small and close to the readability limit of most analytical balances (typically 0.01 mg). In order to avoid this problem, large erosion scars can be made on the samples, but at the cost of using a significant portion of the studied sample. In the case of coating development, this can pose a problem because of the limited availability of sample surface area for testing. Regardless of the size of the eroded surface area, when testing fairly thin coatings (<10 µm), the mass loss will always have to remain very small (typically well below 1 mg) in order to avoid piercing the coating. This results in a large probability of handling errors during the weighing process leading to invalid mass loss measurements. Finally, another major issue with the mass loss SPE evaluation for coatings is the difficulty in acquiring the coating density. Consequently in many studies, the density is estimated or simple ignored, leading to inaccurate evaluation of erosion rates.

In this PhD project, when it was necessary to measure them, all mass losses were evaluated using the Sartorius LE225D analytical balance that has a readability precision of 0.01 mg and a repeatability better than 0.02 mg. As for the volume loss measurements, they were determined with the Conscan module of a CSM instruments Micro-Combi Tester. This profilometer is a confocal white light profilometer that acquires topographical data using a white light source that is dispersed trough a lens with high chromatic aberration, dispersing each wavelength to a different depth along the optical axis. Consequently, the strongest spectral response of the reflected light will give the distance of the surface at that point. This technique acquires the topographical data point by point along a scanned line and then a full three dimensional map is constructed by stitching all the scanned lines.

The methodology developed for the evaluation of the volume loss resulting from erosion tests using a cylindrical nozzle is described in detail in Chapter 5 where it is used for the evaluation of SPE mechanisms of hard protective coatings. In that study, we validate the methodology using brittle bulk materials of known density and compare the erosion results obtained by mass loss measurements and by volume loss measurements.

Summarizing, our approach consists in obtaining a line profile scan of the erosion scar and calculating the volume loss by numerical integration (Figure 3.10). We use a Gaussian function to identify the centerline of the profile and then calculate the total volume loss using:

$$V_{total} = \sum \Delta V = \sum \pi R Z \Delta x \tag{3.2}$$

where ΔV is an elementary volume ring, R is the distance of each point in the scan to the centerline, Z is the measured depth of the given point and Δx is the lateral resolution of the scan. It should be noted that for shallow and/or noisy wear scars, the fitted Gaussian function is used to evaluate the volume of revolution. Finally, the surface curvature of each scan is removed by modelling a polynomial function through the non-eroded part of the scan.

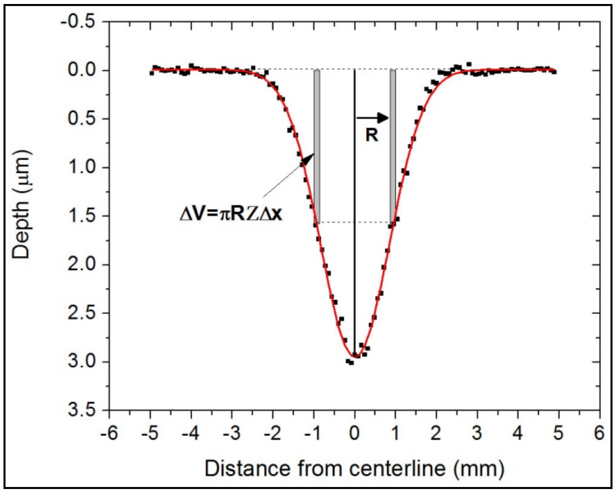

Figure 3.10: Parameters and Gaussian fit used in numerical volume integration of SPE experimental data.

3.2.4 SPE methodology optimization

In order to optimize the SPE tests of coated samples, several parameters needed to be considered. In practical terms, our first priority was to minimize the diameter of the wear scar because of the limited surface area size of each sample. A small wear scar would also be practical for the implementation of the volume loss measurement methodology described above. In order to achieve this, the *WD* between the nozzle outlet and the sample surface needed to be as small as possible, as illustrated in Figure 3.11 where line profiles of erosion scars are presented for tests with distances from 20 to 40 mm. However, we could not test below 20 mm because of the space needed for the shutter to operate properly.

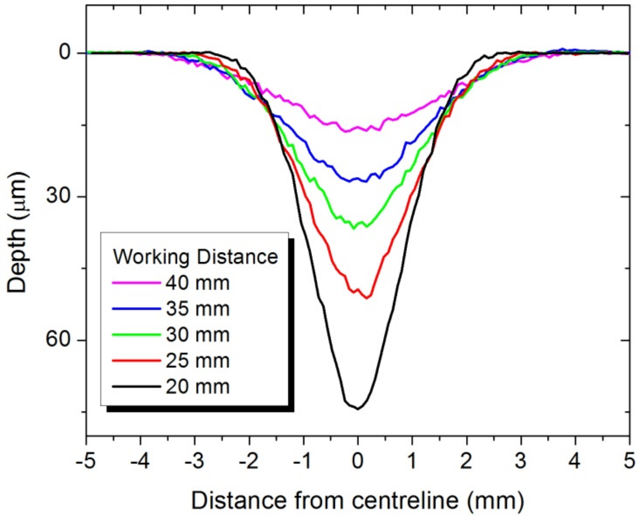

Figure 3.11: SPE scar profiles on c-Si after exposure to 2 g of alumina powder at varying *WD*s.

The most important issue in optimizing the methodology was to ensure that the measured erosion rates were only material dependent and not influenced by testing parameters. In fact, several studies have shown that particle interactions during erosion testing can significantly affect the measured rates through interference effects. Notably, Shipway and Hutchings [169] showed that particle interactions do not generally occur within the nozzle itself but in the volume between the nozzle outlet and the sample surface as particles rebound on the surface, screening the incoming particles. They found that the particle flux (feed rate per surface area) is a determining factor in predicting particle interference effects. In a more recent series of articles, combining experimental and modeling results, Papini, Spelt and coworkers [167, 170, 174, 176, 178, 180] showed for normal incidence SPE that the erosion rates decrease for increasing *WD* because of an increased inter-particle collision probability when the volume between the nozzle outlet and the surface increases. Therefore, in order to optimize the testing methodology of our erosion test rig using the long aspect ratio nozzle, we present in Chapter 5 a study on the effects of feed rate and *WD* on the SPE of brittle bulk materials and show that particle interference effects can reduce erosion rates by as much as 40 %.

3.2.5 Particle size distribution

To study the effect of SPE testing on the particles themselves, the particle size distributions of the used powders were measured by laser diffraction spectroscopy (LDS) using a Coulter LS200 with a Micro Volume Module. During testing, a 750 nm laser beam is scattered when passing through a suspension of the powder to characterize and then, using the signal from the scattered light, the particle sizes are calculated using an appropriate diffraction model. The Fraunhofer diffraction model is generally used, but because the powders studied in this project possessed wide size distributions with non-negligible amounts of particles of small dimensions (*i.e.* < 10 μm), we used a model based on the Lorenz-Mie theory of scattering by a sphere. The effects of assuming a spherical particle on the size distributions of angular particles is addressed in Chapter 4.

3.2.6 *In situ* quartz-crystal microbalance SPE testing

The final aspect of SPE testing that we have addressed in this research project is the development of an in situ characterization technique of coating erosion mechanisms. The description and validation of the technique is presented in detail in Chapter 6 but in summary, the method consists in using the very high sensitivity to mass changes of coated quartz crystal microbalances (QCMs) in the study of SPE mechanisms of hard monolithic and multilayer coatings.

In this study, we used 5.98 MHz QCM samples (PBG Milano), a Sycon STM-100 thin film deposition rate monitor and LabView software to record *in situ* the frequency response under erosion of the coated QCM resonators. The mass change on the surface of the resonator causes a change in the natural frequency (*f*) of the crystal: a decrease for a mass gain and an increase for a mass loss.

For uncoated crystals and thin elastic films, the mass loss (m_L in [g/cm^2]) can be calculated from the frequency change (Δf in [Hz]) using the Sauerbrey equation [182],

$$m_L = -\frac{\Delta f \cdot N_q \cdot \rho_q}{f_o^{\,2}} \tag{3.3}$$

where,

N_q is the frequency constant for the AT-cut quartz crystal (1.668X10^5 Hz*cm),

ρ_q is the density of quartz (2.648 g/cm^3), and

f_o is the fundamental resonant frequency of the crystal in Hz (we used the frequency of the crystal prior to testing).

Because the Sauerbrey equation does not take into account the change in elastic properties caused by the deposited film, the Z-Match method [183] is used for thick coatings where,

$$m_L = \left[\frac{N_q \rho_q}{\pi Z f_L}\right] \tan^{-1}\left[Z_f \tan\left(\frac{\pi(f_u - f_L)}{f_u}\right)\right]; \tag{3.4}$$

and where

f_u is the unloaded natural frequency in Hz, f_L is the loaded natural frequency in Hz, and

$Z_f = \left[\frac{\rho_q \mu_q}{\rho_f \mu_f}\right]^{1/2}$ is the Z-Factor of the film; μ and ρ are the shear modulus and density of the quartz (index q) and of the film (index f).

3.3 Mechanical characterization

As discussed in the previous chapter, the evaluation of mechanical properties of surfaces, including coatings, is not often possible through conventional means such as tensile testing. Consequently, indentation techniques have evolved considerably over the last few decades and can be used to evaluate elastic, plastic and fracture properties.

Hardness is essentially the contact pressure when an indenter of known geometry is pressed into a materials surface. Therefore, it can be expressed by the ratio of the applied load (P) over the projected contact area (A),

$$H = \frac{P}{A} \tag{3.5}$$

and is expressed in Pa or more commonly in GPa.

In practice, it can be evaluated in many different ways mostly depending on the class of studied materials (metals, ceramics, biological, etc.) and the corresponding scale of hardness. However, regardless of the technique used, hardness measurements will only yield comparative results since the obtained values strongly depend on the geometry of the bodies on contact. It is therefore very important to thoroughly understand the indentation process in order to obtain representative results.

The evaluation of hardness has evolved from the comparative evaluation of mineral hardness through scratching (Mohs scale), to the hardness evaluation of metallic materials with spherical indenters (Brinell and Rockwell tests) and finally to measurements using sharp pyramidal diamond indenters (Vickers, Knoop, Berkovich and cube-corner indenters) for probing properties at much smaller depths and in harder materials. These different indentation techniques have been extended to evaluate other mechanical properties such as Young’s modulus, fracture toughness and other elastic and plastic behaviors. They can be categorized into three different indentation methodologies: static, quasi-static and dynamic indentation. In this work, we used static indentation techniques using a Vickers and cube-corner tips and the quasi-static method by depth-sensing indentation using a Berkovich tip geometry.

3.3.1 Vickers hardness testing

Static-type tests involve the indentation of the surface at a given load and the evaluation of the hardness by measuring the dimensions of the residual mark left by a tip of known geometry. The available tip geometries are quite varied but for hard ceramic materials, the Vickers tip geometry has been extensively used. The ASTM standard C1327 [184] gives detailed instructions for the evaluation of hardness of ceramic materials using this type of indenter.

As illustrated in Figure 3.12, a Vickers indenter is a square base pyramidal diamond tip with an angle of 136° between faces. From this geometry, hardness is calculated using:

$$H_v = \frac{P}{A} = 2\cos 22^0 \frac{P}{d^2}, \tag{3.6}$$

where d is the diagonal of the residual trace and H_v is in GPa. The Vickers hardness is often expressed in terms of Vickers hardness number (HVN) which can be calculated using the same formula, but with P in kgf and d in mm.

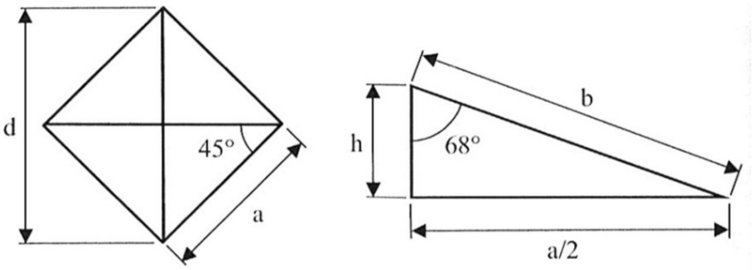

Figure 3.12: Geometrical description of a Vickers type indenter [185].

When using Vickers indentation for the hardness evaluation of coated samples, special considerations must be taken into account. While indenting a coated surface, the volume of plastic deformation below the indenter may extend into the substrate and not be wholly contained within the coating. Therefore, the measurement will be greatly affected by the hardness value of the substrate which is usually much smaller than that of the coatings in the case of hard coatings deposited on metallic substrates. In such a case, a method must be used to deconvolute the coating hardness (H_f) and the substrate hardness (H_s) from the composite hardness (H_c) that is measured. Using a geometrical approach, the relationship between the hardnesses can be expressed by:

$$H_c = H_s + a\left(H_f - H_s\right), \tag{3.7}$$

where a is a model based coefficient. Many models have been elaborated to evaluate a, most notably models proposed by Jonsson and Hogmark [186], Burnett and Rickerby [187, 188], Chicot and Lesage [189], Korsunsky *et al.* [190] and Ichimura *et al.* [191].

In addition to extracting the coating hardness from the measured one, special care must be taken when analyzing very small indentations because of the so called indentation size effect (ISE). As the indentation depth decreases, the measured hardness has been shown to increase in an exponential manner due to grain size effects and measurement errors, among other causes. Although the ISE can vary widely from one material to another and there is still much debate about its origins [192], it can be expressed in general by [187, 188]:

$$H = qd^{M-2}, \tag{3.8}$$

where q is a constant and M is the material dependent Meyer index.

3.3.2 Depth-sensing indentation

Due to the difficulties in evaluating hardness at very shallow depths using static indentation techniques such as Vickers indentation, the quasi-static technique of depth-sensing indentation has been developed and is extensively used for the measurement of mechanical properties of coatings and thin films. In addition to reducing errors in the evaluation of hardness, it also permits the measurement of elastic and fracture properties.

It is customary to use a diamond tip with the three sided pyramidal Berkovich geometry in depth-sensing indentation because it has the same area-to-depth relationship as a Vickers indenter, but not the chisel edge tip defect typically found in Vickers indenters. The increased sharpness of the Berkovich tip is well suited for very shallow indentation of coatings.

As in static indentation testing, during depth-sensing indentation a load is progressively applied up to a maximum value and the tip is then retracted. The technique is considered quasi-static because during indentation, the load and the displacement of the tip is continuously monitored and recorded. It is from this load-displacement curve (Figure 3.13 (b)) that the mechanical properties can be extracted. The development of the mechanics behind the technique dates back several decades and is still ongoing, but the most significant contribution in the field comes from Oliver and Pharr [193] who in a 1992 paper detailed a procedure for the evaluation of hardness and Young’s modulus that is still extensively used today for elasto-plastic materials.

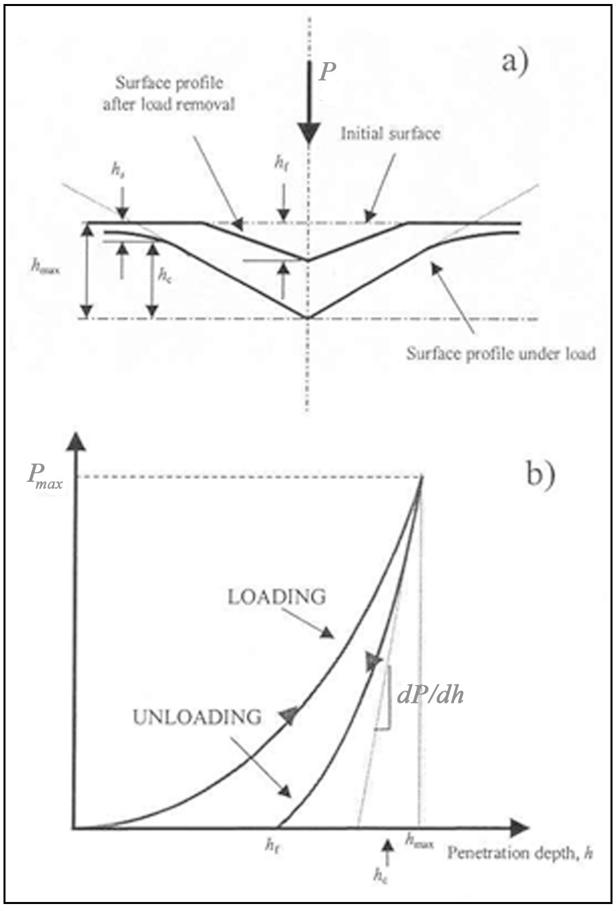

Figure 3.13: Depth-sensing indentation: (a) surface profile under indentation and (b) typical load-displacement curve (adapted from [185]).

The loading part of the load-displacement curve is the elasto-plastic response of the material to loading while the unloading portion of the curve is purely elastic. The reduced indentation modulus can be calculated using:

$$E_r = \frac{S\sqrt{\pi}}{2A}, \tag{3.9}$$

where A is the projected contact area and $S = \frac{dP}{dh}$ is the stiffness of the material at maximum load. The reduced modulus is the composite modulus of the contact between the diamond tip and the surface and can be expressed using Hertz elastic contact theory by:

$$\frac{1}{E_r} = \frac{1-\nu^2}{E} + \frac{1-\nu_i^2}{E_i}, \tag{3.10}$$

where E is the indentation modulus, v is the Poisson coefficient of the indented material, E_i is the Young's modulus of diamond (1140 GPa), and ν_i is the Poisson coefficient of diamond (0.07). It should be noted that often only the reduced modulus is reported. This is generally accepted because of the very high stiffness of the diamond tip and the small influence of the Poisson coefficient.

In order to calculate the stiffness of the material from the load-displacement data, Oliver and Pharr proposed to model the purely elastic unloading curve using:

$$P = B\left(h - h_f\right)^m, \tag{3.11}$$

where B, h_f and m are fitting constants and h is the depth of penetration at a given load. This expression can then be differentiated and using h_{max}, the stiffness at maximum load can be calculated.

The contact area between the indenter and the material is a function of the depth of penetration into the surface. However, as illustrated in Figure 3.13 (a), the surface will be deflected as the indenter penetrates into the material. This means that the actual depth at which the material is in contact with the indenter is smaller than the total displacement of the tip (h_{max}). The contact depth (h_c) can be evaluated from the elastic behavior of the material using:

$$h_c = h_{\max} - \eta \frac{P_m}{S_m}, \tag{3.12}$$

where η is a constant that depends on indenter geometry (0.75 is typically used) and S_m is the stiffness of the material at P_m.

Additionally, because the indenter is not an ideal pyramid and generally has a significantly rounded (or cleaved) tip, the contact area as a function of depth has to be carefully calibrated. In this work, we calibrated the contact area by indenting in a fused quartz standard of known modulus at various contact depths. Thus, using the fused quartz experimental data and equation 3.9, the indenter's projected area at a given contact depth can be calculated. The tip's area function is then modeled by fitting the obtained data by the polynomial function:

$$A = C_o h_c^2 + C_1 h_c + C_2 h_c^{1/2} + C_3 h_c^{1/4} + C_4 h_c^{1/8} + \ldots, \tag{3.13}$$

where C_o, C_1, C_2 *etc* are fitting coefficients.

It should be noted that because of the high precision needed for accurate depth sensing indentation at very shallow depths, the system compliance (sources of deformation other than from the tip and tested material) must be calibrated regularly and the drift rate must be recorded and compensated for before each test.

Finally, using the calculated stiffness and contact area, the reduced modulus of the tested material can be found using equation 3.9. In addition, the hardness is calculated using

$$H = \frac{P_m}{A = f(h_c)}. \tag{3.14}$$

Therefore, in depth-sensing indentation, the hardness is the contact pressure at P_m where the deformation is elastic and plastic. On the contrary, in static indentation tests, the deformation of the measured residual trace is only plastic, with the elastic component being neglected. For large indentations in metallic materials, this is not an unreasonable approach, but for small indentations in highly elastic materials, this will lead to a significant overestimation of hardness values.

Care must be taken when indenting relatively thin films in order to extract meaningful data without an undue contribution from the substrate to the measured properties. For hardness, the rule that is often applied is to only use data from depths smaller than 10% of the total coating thickness. This approach may yield acceptable data in certain cases, but too many exceptions to the rule have been identified in order to generalize its use. In fact, the contribution of the substrate will greatly depend on the size of the plastic zone below the indenter which has been shown to exhibit a complex relationship between the elastic and plastic properties of the material [194] and of the substrate if the plastic zone exceeds the coating thickness. In the case of the elastic modulus, in nearly every case, the substrate will influence the measured values since a coating-substrate system will act like two springs in series, which means that the composite spring constant (or modulus) will always be dependent of both contributions.

The relatively new ISO standard ISO14577-4 [195] proposes a systematic approach to analyzing depth-sensing data in the case of coated systems. It shows that to evaluate the hardness of a hard coating on a softer substrate, measurements must be made from low to high penetration depths. The hardnesses at depths where no substrate effect is affecting the results will be constant and can be seen as representative of the coatings' hardness. In the case of modulus, the influence of the substrate will linearly increase as a function of depth and by extrapolating the data to zero depth, the coatings' reduced modulus can be evaluated without the influence of the substrate.

Additional information about energy dissipation processes can be extracted from the load-displacement curves. In fact, the proportion of energy recovered after complete unloading is commonly referred to as the materials elastic recovery (R_e) while its complement, the energy dissipated by plastic means, is the materials index of plasticity (R_p). As illustrated in Figure 3.14, the total (W_{total}) and elastic (W_e) energies are evaluated by integration of the areas below the loading and unloading curves, respectively. The plastic energy (W_p) is then calculated by subtracting the elastic from the total energy. As a close approximation, the elastic recovery can be evaluated using the measured displacements of the tip during indentation using:

$$R_e = \frac{W_e}{W_{total}} \approx \frac{h_{\max} - h_{res}}{h_{\max}}, \tag{3.15}$$

where h_{res} is the residual indentation depth after the complete withdrawal of the tip.

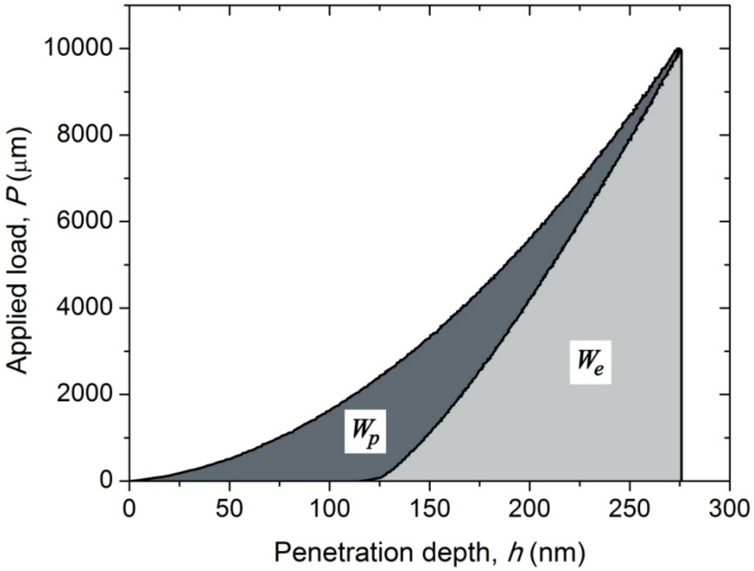

Figure 3.14: Load-displacement curve with the indicated areas representing the work of indentation dissipated trough plastic means (W_p) and stored through elastic means (W_e).

3.3.3 Toughness evaluation by indentation

An extension of the static indentation technique is its use in characterizing the fracture toughness of materials. As described previously, in the case of brittle erosion mechanisms, material fracture may occur during indentation when the strain exceeds a certain threshold and through the extension of existing subsurface flaws. In the case of sharp pyramidal indenters pressed into the surface of a brittle material, controlled radial cracks are generated at the corners of the indentations and can be used for the quantification of fracture toughness (Figure 3.15).

In this work, we used Vickers and cube-corner indenters to generate half-penny cracking in coated and uncoated materials. We then evaluated fracture toughness using the equation developed by Lawn *et al*. [20] and Anstis *et al*. [22]:

$$K_{IC} = \alpha\left(\frac{E}{H}\right)^{1/2}\frac{P}{c^{3/2}}, \qquad (3.16)$$

where α is a constant related to the indenter geometry, *E* is the Young's modulus evaluated by depth-sensing indentation, *H* is the hardness evaluated from the residual impression by SEM, *P* is the applied load and *c* is the crack length measured from the centre of the indentation to the tip of the crack. Our methodologies for the evaluation of fracture properties of bulk materials and coatings are respectively presented in Chapters 4 and 5.

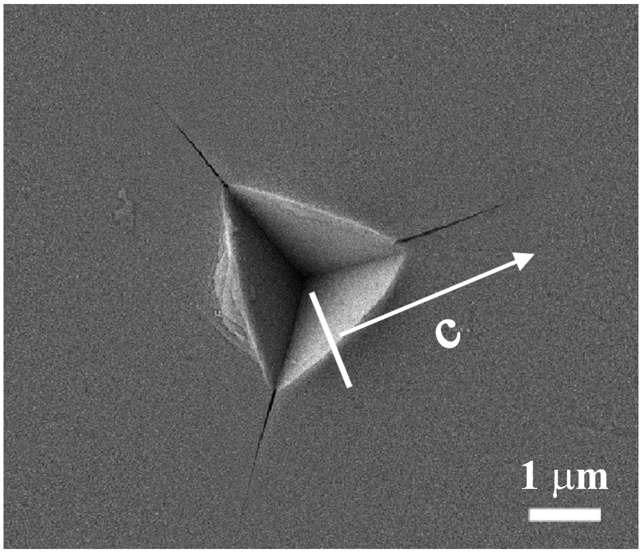

Figure 3.15: Half-penny crack extending from a cube-corner indentation with the crack length *c* indicated.

3.4 Microstructural characterization

3.4.1 Scanning electron microscopy

Scanning electron microscopy (SEM) is a widely used surface imaging technique that can yield many different types of information such as topographical, chemical and crystallographic data. In this project, SEM was used primarily for its topographical capabilities to analyze solid particle impact damage, characterize the powder used for erosion testing, as well as to measure the thickness and observe the microstructure of deposited coatings.

In SEM, the image is acquired by collecting the signal generated by a focused electron beam that is scanned over the surface of the studied sample. The electrons are accelerated with sufficient energy to interact with the atoms at the surface and generate several signals including primary backscattered electrons from elastic atomic collisions, secondary electrons from inelastic collisions and X-rays. The X-ray and backscattered signals are sensitive to the atomic number of the surface atoms while the secondary electrons, due to their very small volume of interaction, are much more sensitive to surface topography.

In this work, we primarily used the JEOL JSM-7600F SEM equipped with a field emission gun (FEG) electron source. The SEM-FEG permits high resolution imaging at very low acceleration voltages, which means the coatings could be imaged without the use of a conductive layer. On the other hand, all the observations on insulating samples such as the glasses studied in Chapter 4 necessitated the deposition by sputtering of a thin conductive gold layer. Most coating cross-sections were prepared by cleaving the samples, but some were milled using the focused ion beam technique described in the next section.

3.4.2 Focused ion beam milling

The equipment configuration and operation of the focused ion beam (FIB) apparatus is very similar to that of an SEM but uses a beam of ions for the imaging and milling of the sample surface. In order to obtain very clean cross-sections of coatings, we used a Hitachi FB2000A with a Gallium ion source to machine a trench, exposing the cross-section of the sample. At first, a layer of tungsten is deposited over a section of the surface to protect it from being sputtered away and then a step-like trench is machined (Figure 3.16). The samples are then transferred to the SEM for imaging.

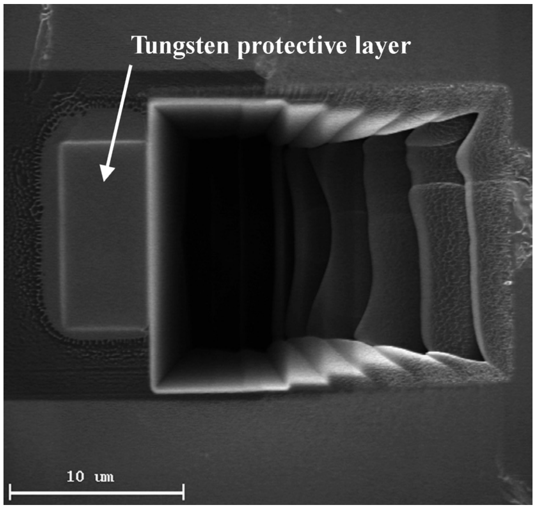

Figure 3.16: Step-like trench milled by focused ion beam to expose sample cross-section.

3.4.3 X-ray diffraction spectroscopy

The crystalline structure, grain size (d_g) and preferential crystallographic orientation (texture) of the films in Appendix A were determined by X-ray diffraction (XRD) using a Philips X'Pert diffractometer with monochromatized Cu K_α radiation. In XRD, the radiation of wave length λ is diffracted by crystallographic planes at a characteristic diffraction angle θ_d according to Bragg's law,

$$2d_d \sin\theta_d = n_d \lambda \tag{3.17}$$

where d_d is the spacing between diffracting planes and n_d is an integer.

From this equation, it can be seen that as the spacing between the atomic planes changes, the characteristic angle of diffraction will also change. Consequently, it is possible to identify the crystalline phases present in the material through comparison with material databases. For measurement of coatings, the incidence angle of the incoming beam of radiation is kept as small as possible in order to maximize the signal from the coating and minimize that of the substrate. Finally, from the width of the peaks of the diffraction spectra, it is possible to obtain the crystalline grain sizes of the constituting phases by using the Scherrer formula.

In this chapter, we have described the important elements of the experimental methodology used in this PhD project, namely the coating deposition technique of pulsed DC magnetron sputtering, the gas blast erosion testing methods used to evaluate the SPE of the bulk and coated samples, the different techniques used for the evaluation of mechanical properties and finally the microstructural characterization techniques used to describe surface morphology and coating microstructure. As we have illustrated throughout this chapter, the proper understanding and application of the characterization techniques is essential for the assessment of multi-parameter correlations. This includes calibration, validation and proper application of the techniques, as well as applying rigorous analysis methods and the validation of the obtained data. This philosophy will be illustrated in the following three chapters, where we present three original articles which describe the research that enabled us to meet the objectives we have set for this PhD project. In chapter four, we study the effects of the particle properties on the SPE behavior of six brittle bulk materials using glass and alumina powders. Subsequently, in chapter five, we study the erosion mechanisms of hard protective coatings deposited by pulsed DC magnetron sputtering. Finally, in chapter six, we present a novel *in situ* real-time erosion testing methodology using a quartz crystal microbalance, developed in order to study the SPE of hard protective coating systems.

CHAPTER 4 EFFECT OF ERODENT PROPERTIES ON THE SOLID PARTICLE EROSION MECHANISMS OF BRITTLE MATERIALS

Article 1: Effect of Erodent Properties on the Solid Particle Erosion Mechanisms of Brittle Materials

E. Bousser, L Martinu, J.E. Klemberg-Sapieha*

Engineering Physics Department, École Polytechnique de Montréal, P.O. Box 6079, Station Centre-ville, Montréal, Québec, Canada H3C 3A7

Abstract

In order to study the effects of particle properties on the solid particle erosion mechanisms of brittle bulk materials, six target materials were tested using two different powders (alumina and glass) at velocities ranging from 25 to 75 m/s. Following in depth characterizations of the targets and of the particles before and after testing, it was found that lateral fracture was the dominant material removal mechanism as predicted by the elasto-plastic theory of erosion. In the case of glass powder, for which the hardness of the particle is lower than the hardness of the target, particle deformation and fragmentation where found to be important factors explaining lower erosion rates. The higher than predicted velocity exponents point towards a velocity-dependent damage accumulation mechanism which was found to be correlated to target yield pressure (H^3/E^2). Although damage accumulation seems to be necessary for material removal when using both powders, the effect is more pronounced for the softer glass powder because of kinetic energy dissipation through different means.

Keywords: Solid Particle Erosion, Brittle Materials, Wear Mechanisms, Toughness, Particle Fragmentation, Damage Accumulation, Yield Pressure (H^3/E^2).

* Corresponding author: tel.: +514-340-5747, fax: +514-340-3218

Email: jsapieha@polymtl.ca

4.1 Introduction

Solid particle erosion (SPE) occurs when hard particulate matter is entrained by a fluid and impacts a surface with sufficient energy to cause damage, ultimately leading to material removal. In the case of aircraft engines, hard particles such as sand or volcanic ash are ingested during takeoff or landing in harsh environments. In order to counter the negative aerodynamic effects caused by this surface damage, much effort has been put into developing hard protective coating systems to increase component lifetimes. The surfaces to be protected are generally metallic (stainless steel or titanium alloys), and they erode in a predominantly plastic mode of material removal through micro-cutting or ploughing mechanisms [51, 52, 196]. However, the protective coatings, applied to impede erosion, are generally composed of much harder ceramic materials such as titanium nitride-based compounds, and they erode in a brittle manner through crack initiation and propagation [51, 66, 67, 69, 197-199].

It has been established that brittle materials exhibit surface removal mechanisms very similar to those encountered during indentation. For large round particles, Hertzian cracks will form and can coalesce into deep wormhole-like craters [116, 200]. For small angular particles, the damage will strongly depend on the particle's kinetic energy (*KE*) and will progress from plastic cutting or ploughing of the surface for low energies to radial/median cracking at higher energies. This can result in lateral fracture removing significant amounts of matter [66, 67, 198]. In one of his important articles, Hutchings [31] illustrated these transitions in the form of erosion maps derived for a given material with the transition threshold values being a function of the corresponding elastic (Young's Modulus [E]), plastic (hardness [H]) and fracture (fracture toughness [K_{IC}]) properties.

In the case of sharp particles eroding brittle surfaces, the mechanism of material removal most often observed is that of lateral fracture. Based on the work by Marshall, Lawn and Evans [20, 21, 197, 201], several indentation-based analytical models have been developed for the SPE by lateral fracture, among which both Evans [66] and Wiederhorn *et al.* [202] proposed interpretations based on elasto-plastic indentation. The former adopted a dynamic approach for the calculation of the particle penetration depth and the maximum applied load while the latter used a quasi-static approach where the particle's *KE* is transferred to the target by the work of indentation. In a series of more recent papers, Buijs [68] and Slikkerveer *et al.* [69] further developed the quasi-static model by using the analytical model for lateral fracture originally developed by Marshall *et al.* [21].

In order to compare different materials, rigorous testing methodologies need to be employed and the effects of all testing parameters need to be fully understood. One important aspect to consider is the selection of the erodent. As recommended by the ASTM G76 standard for gas-blast erosion testing [164], many studies use alumina as the erodent of choice for SPE testing while others use SiC, silica, and single crystal silicon, and some even use diamond powders. In service, however, the sand that will be ingested in an engine will be composed of many different types of particles. In the cases where hard and multilayer coatings protect engine components [10, 87, 147], these particles would be significantly softer than the eroded target material. Given the technological importance, there is a need to understand the erosion mechanisms present when softer particles impact harder surfaces.

Only a limited number of studies have investigated the effect of particle properties on erosion mechanisms [12, 74, 77, 78, 203, 204]. Significant decreases in erosion rates (*ER*) have been observed as the ratio of particle hardness over target hardness (H_p/H_t) increases [12, 78]. It has also been proposed [12, 74, 77, 203] that damage needs to accumulate before material removal occurs when particle *KE* is small or when the particles are softer than the substrate. However, the process by which *KE* is dissipated during the erosion process as a function of the particle properties and the effect of particle fragmentation on the lateral fracture erosion mechanism are not yet fully understood. Furthermore, the role of the target and particle material properties on the observed damage accumulation (DA) mechanism has not been investigated.

In order to study the effects of the particle properties on the SPE behavior of brittle bulk materials, we first apply a robust methodology to accurately characterize the elasto-plastic and fracture properties of the studied materials. We then correlate the measured *ER* to materials' parameters with the help of a morphological study and an analysis of the quasi-static elasto-plastic erosion models. Finally, in order to understand the effects of impact on the particles themselves and to support the energy-dissipation-based model proposed here, we study the particle size distributions of the powders before and after erosion testing.

4.2 Experimental methodology

Six target materials with varying elasto-plastic and fracture properties were tested using two different types of angular particles (see Tables 4.1 and 4.3). The target materials were chosen so as to possess a hardness comparable to that of the glass particles and a much lower hardness than that of the alumina particles. Also, all target materials were amorphous or monocrystalline in order to avoid alternative SPE mechanisms such as grain ejection or grain boundary crack propagation. Each of the six target materials were tested using alumina particles at four different velocities, and using glass particles at three velocities.

4.2.1 Solid particle erosion testing

The SPE tests were carried out in an in-house gas-blast erosion system based on the specifications of ASTM standard G76 [164]. The particle velocity (V_p) was controlled by adjusting the back pressure of the abrasive blasting unit (S.S. White Airbrasive unit). The dependence of velocity on the back pressure was measured using a double disk time-of-flight technique [166]. The particle feed rate was controlled by adjusting the unit's shaker amplitude and the back pressure. In order to verify and stabilize the feed rate prior to each test, the sand-blast unit was turned on for several minutes, while the sample was shielded by a retractable shutter. Only when the feed rate had stabilized at a rate of 1±0.3 g/min was the test started.

The whole unit was mounted on a 30 kg capacity balance precise to 0.1 g (Sartorius LE29000) in order to closely monitor the particle feed during each test. All tests were performed with the particle flow impacting the surface at normal incidence, and the working distance between the outlet of the nozzle and the surface of the sample was kept constant at 20 mm. For all tests, a tungsten carbide nozzle with an inner diameter of 1.14 mm and a length of 36 mm was used.

During each test, the sample was exposed to the particle flow for a precise mass of erodent: between 1 and 50 g, depending on the target and particle materials and V_p. The *ER* was calculated by dividing the measured volume of material loss by the mass of erodent used for that test. It was assumed that all the mass of erodent impacted the target since the diameter of the resulting wear scars was at least three times smaller than the size of the eroded specimen.

The volume loss measurements were accomplished by confocal white light profilometery (CSM instruments MCT Conscan module) that enabled us to obtain a topographical map of the eroded surfaces. In this way, we were able to map a complete 3D profile of the wear scar left on the surface. However, such a scan is very time consuming, which is why we developed a technique using the volume of revolution obtained by numerical integration of a single-line scan at the maximum depth of the erosion wear scar. For each testing condition, three to six repetitions were made so as to evaluate the experimental error of the measurement.

4.2.2 Single impact morphology

In addition to the above "traditional" SPE tests, we exposed the specimens to the particle stream for a very short amount of time (around one second) in order to observe single impacts of particles on the target surfaces. We then imaged the resulting morphology of the impact craters by scanning electron microscopy (SEM, Jeol JSM7600F).

4.2.3 Elasto-plastic properties

The elasto-plastic properties of the target materials were evaluated by depth-sensing nanoindentation (Hysitron Triboindenter). The hardness (H) and reduced modulus (E_r) were measured using a diamond tip of Berkovich geometry and the data was analyzed using the widely accepted Oliver and Pharr methodology [193]. Prior to testing, the tip geometry and system compliance were calibrated using a fused silica standard. Before each indentation, the drift of the system was measured by maintaining the tip in contact with the surface at a load of 2 μN for 80 seconds while monitoring displacement and then fitting the drift during the last 40 seconds of this hold segment. This measured drift, which was typically less than 0.1 nm/s, was then subtracted from the measured load-displacement curve prior to analysis. Each target material was indented by four or five repetitions of a 5X5 indentation array with a spacing of 20 μm between indentations. In order to evaluate the elasto-plastic properties as a function of depth, the indentation load within each array was decreased incrementally from a maximum of 10 mN (7.6 mN for Ge) for the first indentation down to 0.4 mN for the last. The load function used for these indentations was trapezoidal with a 5 s loading segment followed by a 2 s holding segment, and finished with a 5 s unloading segment.

The proportion of energy dissipated by plastic means during an indentation is known to be highly dependent on the geometry of the indenter [205]. For that reason, we chose to evaluate the materials index of plasticity (R_p), defined as the ratio of plastic work over the total work during an indentation test, using Berkovich and cube corner indenters. The latter more closely resembles the geometry of both types of particles used in this study.

Each material was indented using a 10x10 indentation array with a spacing of 20 μm between indentations for the cube corner geometry, and 100 μm for the Berkovich indenter. In the case of the cube corner tests, the load between indentations was increased from 0.02 mN to a maximum load ranging from 3.2 mN to 10 mN, depending on when the onset of chipping occurred. For the Berkovich tests, higher loads were used (up to 100 mN) in order to achieve penetration depths similar to those obtained with the cube corner indenter. The total and elastic energies were evaluated for each indent by numerical integration of the areas below the loading and unloading curves, respectively. The plastic energy was calculated by subtracting the elastic from the total energy.

The elasto-plastic properties of the particles were also evaluated by depth sensing indentation. The particles were mounted in Bakelite and polished to a smooth finish. The surface was then imaged using the surface probe imaging capabilities of the indentation system, and several particles were indented using a constant load of 5 mN. The hardness and Young's modulus were then evaluated by averaging the results of at least 10 indentations.

4.2.4 Fracture properties

As toughness is one of the most important material parameters influencing the SPE of brittle materials according to the elasto-plastic models, we adopted a robust methodology for its evaluation. Therefore, we based our approach on the recent work by Jang and Pharr [206], who investigated, for highly brittle materials, the effect of indenter geometry on fracture toughness for the half-penny crack system. Their work considered the fracture toughness relation developed by Lawn *et al.* [20] and Anstis *et al.* [22]:

$$K_{IC} = \alpha \left(\frac{E}{H} \right)^{1/2} \frac{P}{c^{3/2}}, \tag{4.1}$$

where α is a constant related to the indenter geometry, E is the Young's modulus, H is the hardness, P is the applied load and c is the crack length measured from the centre of the indentation to the tip of the crack (see Figure 4.1). In our work, we used a cube corner tip geometry and $\alpha = 0.0535$, which corresponds to the average experimental value Jang and Pharr found for c-Ge and c-Si using a cube corner indenter. All the indentations were imaged by SEM in order to measure the crack lengths and residual impression sizes. The value of *c* was obtained by averaging the three crack lengths measured for each indentation from the SEM image, *H* was evaluated from the residual impression area, and *E* was calculated using:

$$\frac{1}{E_r} = \frac{1-\nu^2}{E} + \frac{1-\nu_i^2}{E_i} \tag{4.2}$$

where E_r is the reduced modulus evaluated by depth-sensing indentation, ν is the Poisson coefficient of the target material, E_i is the Young's modulus of diamond (1140 GPa), and ν_i is the Poisson coefficient of diamond (0.07).

The loads used to evaluate fracture toughness ranged from 1 mN to 50 mN for c-Ge and c-Si, to 100 mN for BK7, BSG and FQ and to 500 mN for SLG. Lower loads had to be used for c-Ge and c-Si because of chipping caused by lateral cracking, and higher loads were necessary for SLG because of its high indentation plasticity leading to lower relative crack lengths when compared to the indentation size.

In order to validate the assumption that the observed cracks were in fact of half-penny configuration, we evaluated the dependence of crack length on load. As discussed by Jang and Pharr, the stress intensity factor associated with a center-loaded half-penny crack is proportional to the applied load and inversely proportional to $c^{3/2}$. Therefore, assuming that K_{IC} is intrinsic to the material, and therefore constant, a log-log plot of *c* vs. *P* should have a slope of 2/3. We used only the indentations that met this condition for toughness evaluation using equation 4.1.

In addition to K_{IC} measurements, we evaluated the onset of fracture by radial and lateral cracking. Using low load (<10 mN) and high load (10 to 100 mN) cube corner indentations, we generated both types of cracks in all six target materials. The threshold values were evaluated by SEM imaging where radial cracking was considered as the first sign of cracking from one of the corners of the residual impression, and lateral fracture was noted at the first sign of chipping or material lift off (see Figure 4.1).

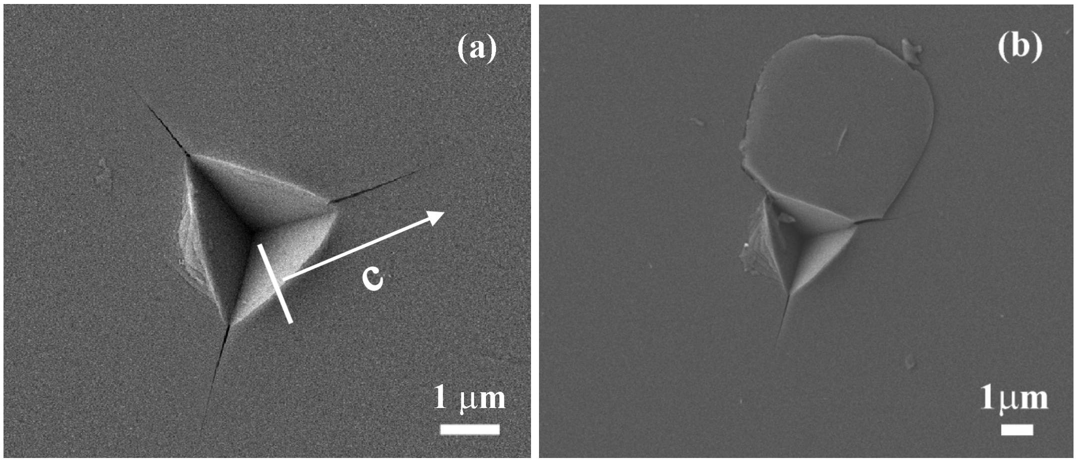

Figure 4.1: Erosion Examples of cracking under cube corner indentation: (a) half-penny cracking with crack length *c* indicated and (b) lateral cracking.

4.2.5 Particle size distribution characterization

To study the effect of erosion testing on the particles themselves, we collected the powder before and after testing. Close attention was taken to collecting as much of the used powder as possible. For this reason, these tests were conducted in a specially fabricated enclosed erosion chamber and the walls were carefully brushed clean after testing. Each of the six target materials were eroded by 5 g of each powder. We used an average V_p of 75 m/s, a 2 g/min particle feed rate, a normal angle of incidence and a working distance of 50 mm.

The particle size distributions of both types of powders were measured by laser diffraction spectroscopy (LDS) (Coulter LS200 with Micro Volume Module) using a laser with a wavelength of 750 nm to determine particle sizes from 0.4 to 2000 μm. Prior to the LDS measurement, the powder was carefully mixed. Each LDS measurement was computed by averaging 60 distribution profiles and we sampled each collected powder three times. As the light passes through a suspension of the powder to characterize, the light is scattered and particle sizes are computed using a model for light scattering by spherical particles. Because our powders possessed wide size distributions with non-negligible amounts of particles of small dimensions (*i.e.* < 10 μm), we used a model based on the Lorenz-Mie theory of scattering by a sphere [207]. The optical properties [208] used in the computation of particle sizes are presented in Table 4.3.

4.3 Results and discussion

4.3.1 Target material properties

In this first part of the work, we studied the target material mechanical properties by different indentation methods. H and E_r values using a Berkovich tip are presented in Figure 4.2 for the six target materials as a function of contact depth (h_c) for which the plastic zone under the indenter is fully developed (in all cases, $h_c > 40$ nm). We can see that all materials show constant properties over the whole measurement range, although higher variability can be observed in the case of c-Ge because of cracking even at these low loads. The H and E_r values in Table 4.1 were calculated by averaging the measurements over the whole range. Standard deviations for hardness varied from 0.6 to 1.9 %, and for reduced modulus from 0.7 to 3.5 % of the average value.

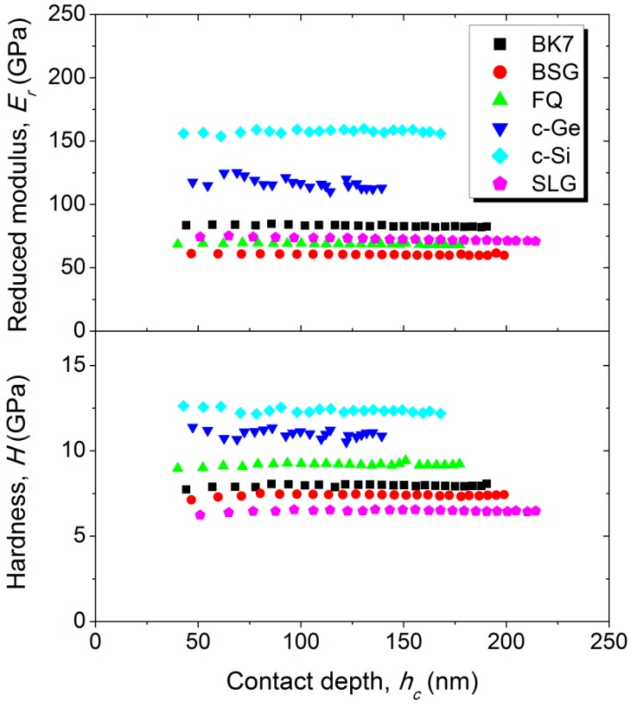

Figure 4.2: Depth profiles of H and E_r for all six target materials.

In Figure 4.3, we present the targets' R_p as a function of h_c measured using cube corner (a) and Berkovich (b) tips. For each material, the R_p value is in fact the complement of the material's elastic recovery, and thus it will equal zero when the indentation remains entirely in the elastic regime. As plasticity develops under the indenter, R_p increases as a power law function. This occurs during indentation because of an increasing strain with depth due to the presence of tip rounding. As the depth increases, the indentation strain levels off to a constant value related to the pyramidal indenter geometry, and the plasticity tends towards a steady state. The values presented in Table 4.1 were calculated by averaging the measurements in the steady state regime for each of the indenters. Standard deviations varied from 0.3 % to 2 % of the average value.

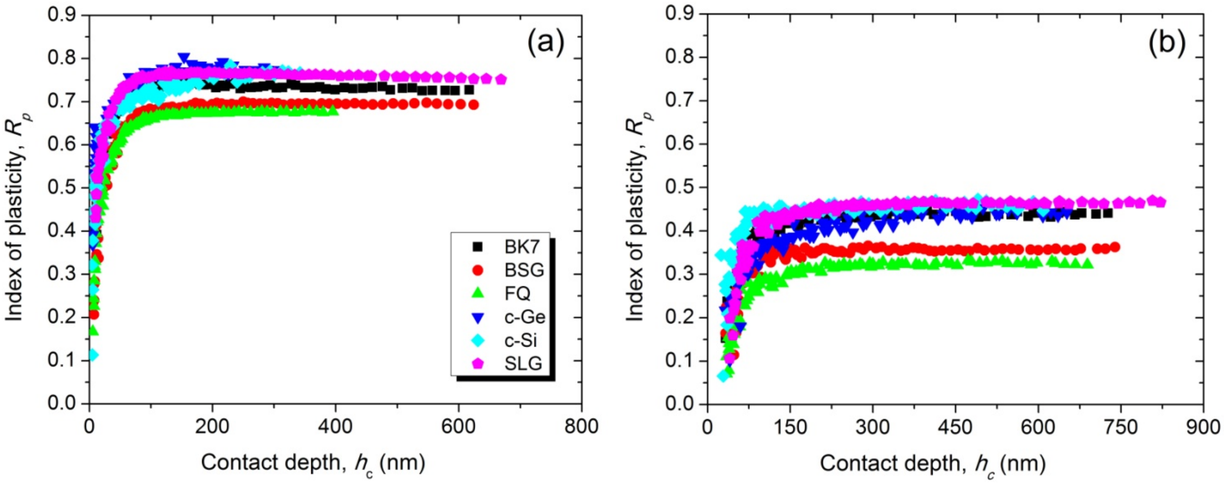

Figure 4.3: Depth profiles of plasticity for all target materials using (a) a cube corner indenter, and (b) a Berkovich indenter.

Table 4.1: Elasto-plastic properties of the target materials.

	Hardness H (GPa)	Reduced Modulus E_r (GPa)	Poisson Coefficient ν	Indentation Modulus E (GPa)	Elastic Strain to Failure H/E	Yield Pressure H^3/E^2 (GPa)	Cube-Corner Index of Plasticity R_{pCC}	Berkovich Index of Plasticity R_{pBerk}
BK7 optical glass (BK7)	8.0	83	0.21	86	0.09	0.07	0.73	0.44
Borosilicate glass (BSG)	7.4	60	0.20	61	0.12	0.11	0.69	0.36
Fused quartz glass (FQ)	9.2	69	0.17	71	0.13	0.15	0.67	0.33
Single crystal germanium (c-Ge)	11.0	118	0.25	123	0.09	0.09	0.78	0.44
Single crystal silicon (c-Si)	12.4	158	0.28	168	0.07	0.07	0.76	0.46
Soda-lime glass (SLG)	6.5	73	0.20	75	0.09	0.05	0.76	0.46

The fracture properties of the target materials evaluated by cube corner indentation are presented in Table 4.2. The toughness of each material was calculated using equation 4.1 and averaged over the whole range of measurement. The standard deviation of the evaluated K_{IC} varied from 4 to 9% of the average values. As illustrated in the c vs. P log-log plot (Figure 4.4), all the materials showed half-penny crack behavior, presenting a slope close to the theoretical value of 2/3.

In the case of FQ, one can observe a transition in behavior. Using the methodology proposed by Chicot *et al.* [209] for crack morphology transitions, we have found that this transition occurs because of a change in crack morphology from Palmqvist cracking to a full half-penny morphology. The calculated toughness for the FQ sample passes from 0.74 $\text{MPa}\sqrt{\text{m}}$ for low load indentations (indicated in parentheses in Table 4.2) to 0.55 $\text{MPa}\sqrt{\text{m}}$ for high load indentations. Since all contact loads during SPE impacts will be much greater than the transition load (P = 50 mN), the lower value of toughness will be used for subsequent SPE calculations.

The results from the radial and lateral crack initiation observations are also reported in Table 4.2. As illustrated in Figure 4.5, the radial and lateral cracking thresholds decrease with increasing material index of brittleness defined as the ratio of *H* over K_{IC}. c-Ge presents the lowest thresholds of all materials studied here. This index of brittleness was shown by Hutchings [31] to be important in predicting the transitions between different fracture mechanisms in SPE. In particular, it was shown that as H/K_{IC} increases, the lateral and radial fracture thresholds are reduced as also confirmed by our observations.

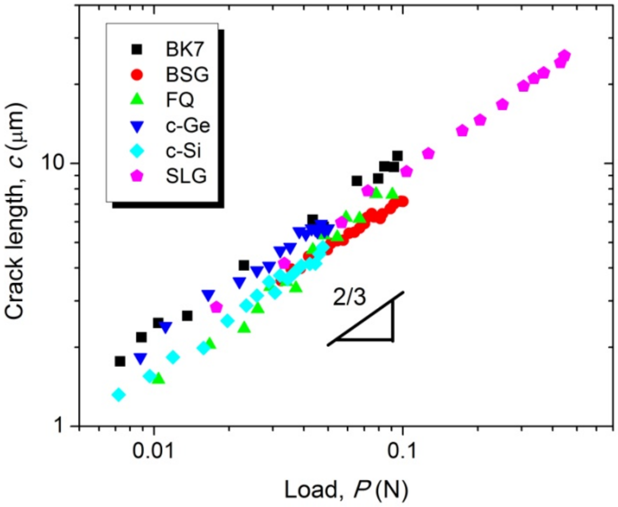

Figure 4.4: Measured crack lengths versus applied load for half-penny crack evaluation.

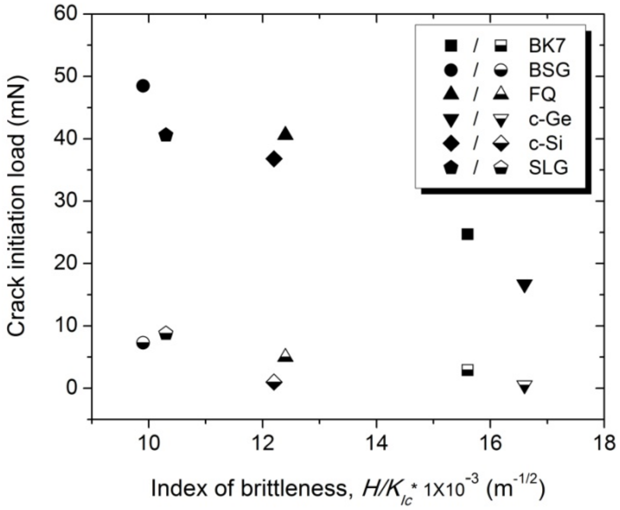

Figure 4.5: Threshold loads for lateral (solid symbols) and radial (empty symbols) cracking as a function of material index of brittleness.

Table 4.2: Fracture properties of the target materials.

	Fracture Toughness K_{IC} (MPa·√m)	Radial Fracture Threshold L_R (mN)	Lateral Fracture Threshold L_L (mN)
BK7	0.51	2.9	25
BSG	0.75	7.3	49
FQ	0.55(0.74)	5.0	41
c-Ge	0.66	0.5	17
c-Si	1.01	1.0	37
SLG	0.63	8.8	41

4.3.2 Erodent particle properties

The values of H and E_r for both types of particles are presented in Table 4.3. The indentation of the mounted particles was straightforward in the case of the glass powder, but not for the alumina powder. In fact, because of the high hardness of alumina, polishing frequently resulted in the particles being removed from the mounting resin, limiting thus the number of particles that could be probed. For that reason, the acquired data in the case of alumina particles is relatively limited. However, we were able to determine that the alumina powder was composed of particles with varying properties. Most particles were found to possess $H \approx 15$ GPa, but some of them had a hardness closer to 30 GPa. The hardest of the particles were most probably single crystal corundum while the lower hardness particles were composed of other less resistant crystalline phases. For computation purposes, an average hardness of 22 GPa is used in this study.

Even if direct measurement of K_{IC} for the particles was not possible, the reported values for glass vary between 0.5 and 0.8 MPa√m [65], and between 2 and 4 MPa√m [65, 77] for the alumina. Average values of 0.7 and 3 MPa√m were, respectively, used for glass and alumina particles in our calculations.

Table 4.3: Material properties of the erodent particles.

	Hardness H (GPa)	Poisson Coefficient v	Indentation Modulus E (GPa)	Density ρ (mm^3/g)	Fracture Toughness K_{IC} ($MPa\cdot\sqrt{m}$)	Median Particle Size D (um)	Refractive Index @ 550nm
Crushed Glass	6.8	0.20	81	2.5	0.5 to 0.8 (0.7)	141	1.52
Alumina	22	0.22	387	4.0	2 to 4 (3)	72	1.77

The particle size distributions of the powders are presented in Figure 4.6. The contribution to powder volume (or mass) is an important parameter in SPE since volume loss during an impact event is a function of the particle kinetic energy, which in turn is directly proportional to the mass. We can see from Figure 4.6 (a) that the glass powder is volumetrically composed of larger particles (mode of 174 µm) when compared to the alumina powder (mode of 78 µm). Because of the broad size distributions for both powders, we used the median particle size for our subsequent SPE calculations (141 µm for glass and 72 µm for alumina). The relative contribution to powder surface area as a function of particle size is presented in Figure 4.6 (b).

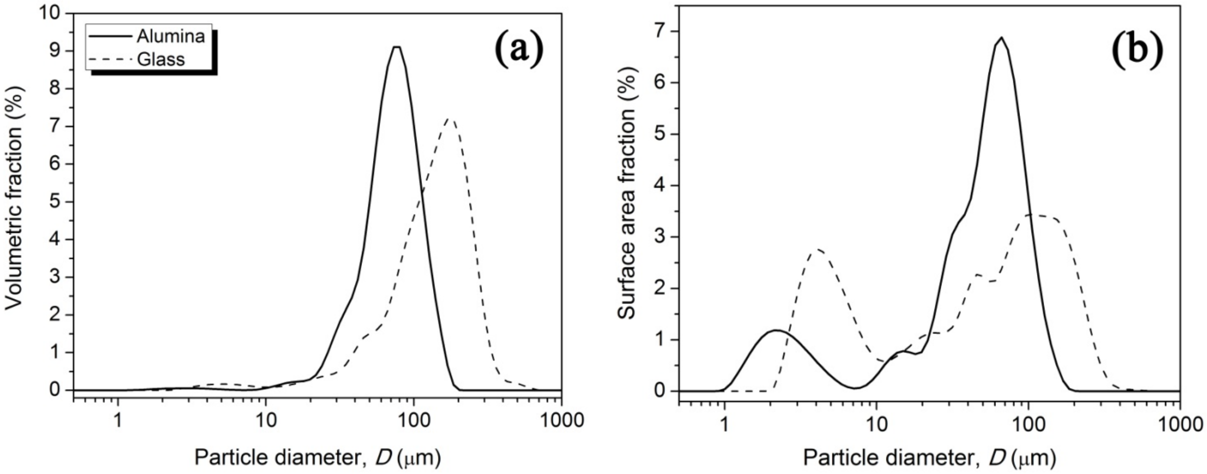

Figure 4.6: Differential contribution of particle size to powder (a) volume (or mass) and (b) area.

Micrographs of the glass and alumina powders before SPE are presented in Figures 4.7 (a) and (c). As can be observed, in both cases the particles are angular in morphology and of varying size and shape. It should be noted that the optical model used in analyzing the LDS data assumes light diffraction by particles of spherical shape. In order to understand the consequences of this discrepancy, a random sample of 50 particles of each powder from SEM micrographs were measured. Mean particle sizes of 136 μm and 75 μm were measured, respectively, for the glass and alumina particles, and the same average aspect ratio of 1.7:1 for both types. These particle sizes correlate well with the LDS data, but the high aspect ratio leads to a particle volume that is more than 30% smaller than the volume of a sphere of the same diameter.

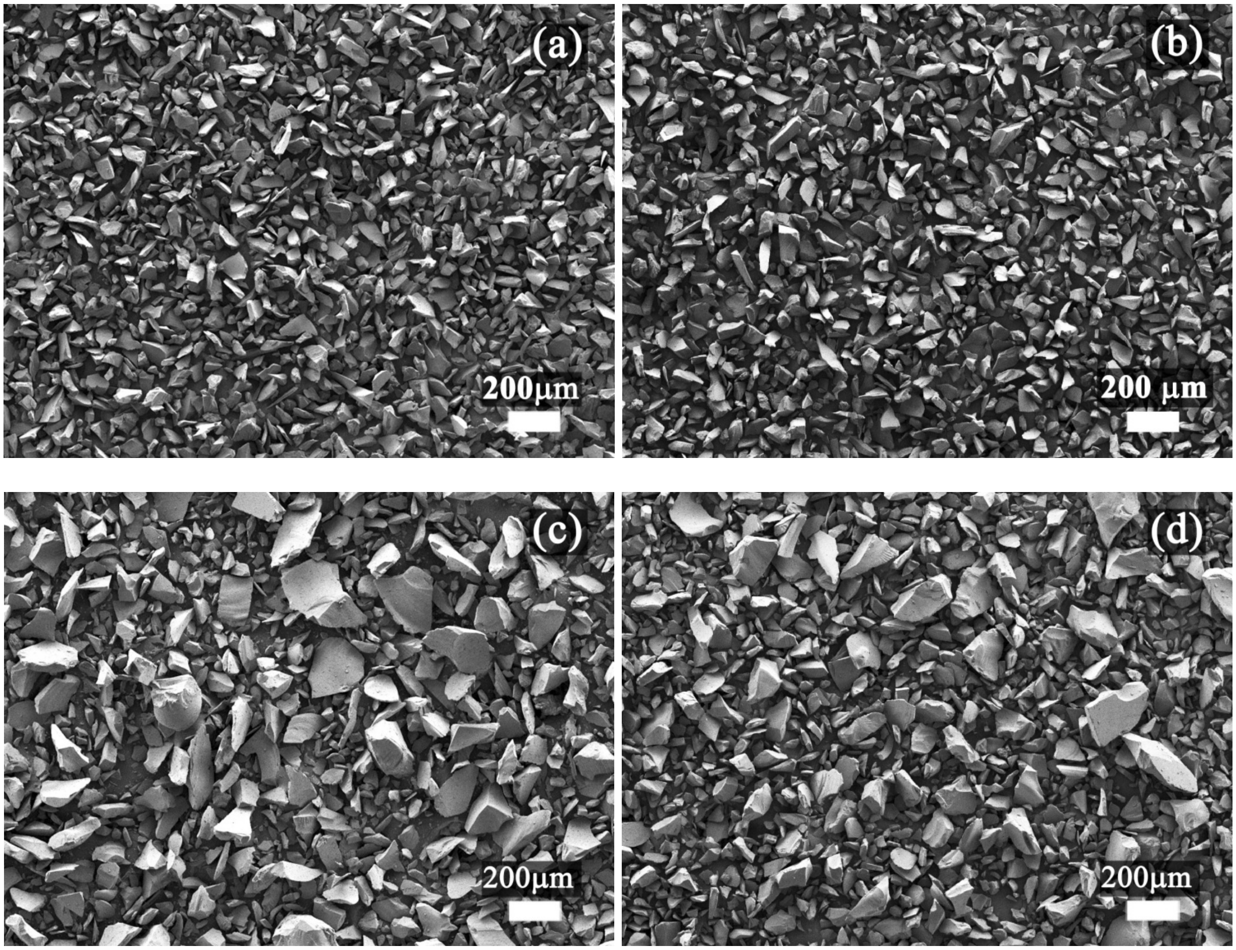

Figure 4.7: Differential micrographs of the alumina and glass powders before (a and c) and after (b and d) SPE testing.

4.3.3 Particle fragmentation

Particle size distribution measurements performed before and after SPE testing at 75 m/s are presented in Figure 4.8. It can be observed that the volumetric and surface area distributions remain nearly intact after SPE testing with alumina particles (Figures 4.8 (a) and (b)) but shift significantly to smaller sizes when using glass particles (Figures 4.8 (c) and (d)). After testing with alumina particles, the median particle size of the volumetric distribution shifts from 72 µm to an average of 69 µm (by ~ 4 %), while for glass particles the median decreases from 141 µm to 113 µm (by ~ 20 %).

The greater shift to smaller sizes in the case of SPE testing with glass powder indicates significant particle breakup when compared to the tests using alumina powder. In fact, the micrograph in Figure 4.7 (d) shows a change in particle size for the glass powder after impact which is not observed in the case of alumina powder (Figure 4.7 (b)). However, the broadening of the volumetric particle size distribution suggests that particle fracturing is probably not occurring through the entire volume of the glass particle, but rather that only a fracture of the particles' sharp corners is occurring during impact.

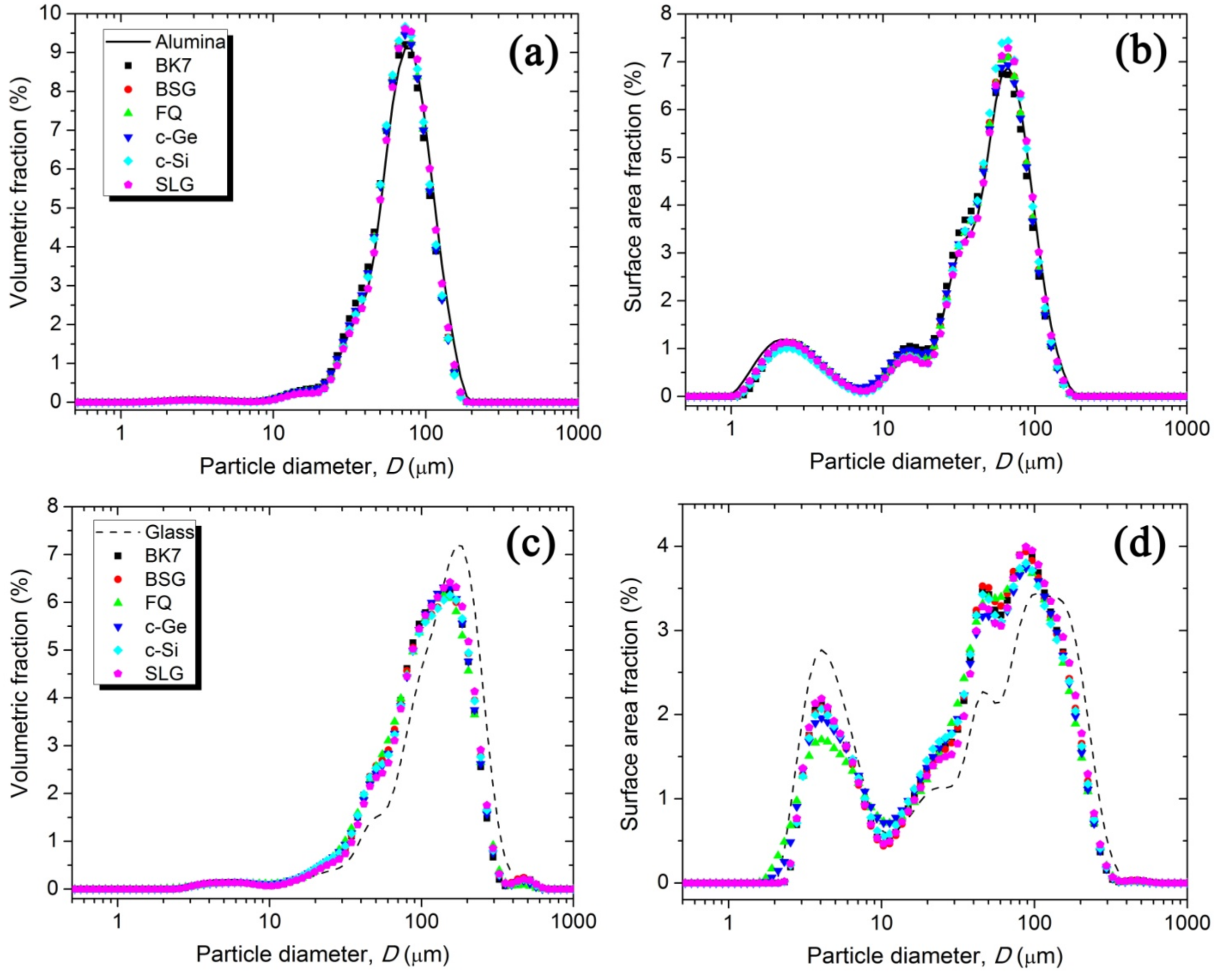

Figure 4.8: Effect of SPE at V_p = 75 m/s on the alumina powder volumetric (a) and surface area (b) distributions, and on the glass powder volumetric (c) and surface area (d) distributions.

For brittle materials, it is expected that during particle impact the *KE* will be dissipated by creating new fracture surfaces. Therefore, the change in powder surface area should be a good indicator of powder breakup during SPE. In order to quantify the degree of particle breakup, we calculated the powder specific surface area increase (change of surface area per volume of powder) in percentage when compared to the unused powder. It should be noted that only particles with sizes greater than 10 μm were used in the calculations since they were the only ones to present signs of breakup.

From Figures 4.8 (b) and (d), it can be clearly seen that the contribution of small dimension particles to total surface area is much greater in the case of the glass powder. However, these particles are not expected to be affected by erosion testing very much; because of their small sizes, they will be entrained in the flow of air at smaller velocities and then impact the tested surface with much lower kinetic energies. The resulting impact will most probably be elastic producing minimal damage to the particles or the surface. Evidence of this can be observed in Figures 4.8 (b) and (d) since there is no shift towards smaller dimensions in the distributions for small particles below 10 µm. In the case of the tests using glass powder, the amplitude in contribution to surface area is reduced for these smaller particles because of an increased contribution from the larger particles.

In Figure 4.9 we present these surface area changes as a function of the ratio of particle hardness to target surface hardness. It can be clearly seen that as the surface becomes harder than the impacting particle, up to five times more breakup occurs. We can observe a transition from a steady state value of around 5 %, when the particle is harder than the surface, to around 23 % for particles softer than the surface.

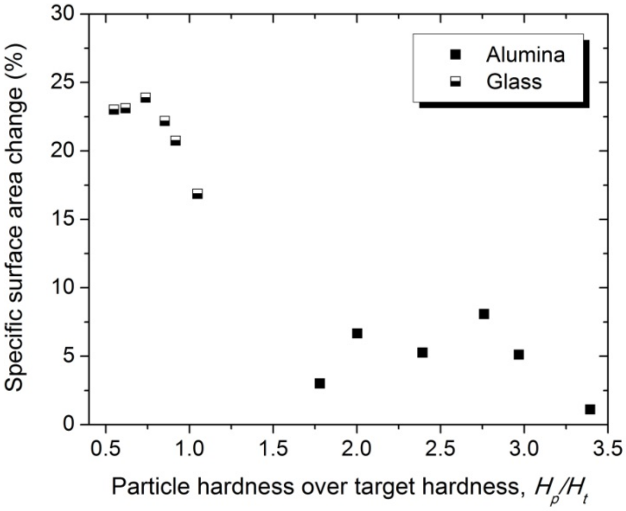

Figure 4.9: Changes in specific surface area as a function of the ratio H_p/H_t.

4.3.4 Erosion process analysis

The results of the SPE tests using alumina and glass powders are summarized in Figure 4.10, where the *ER* in terms of volume lost per impact (calculated using the median particle size) are presented. It should be noted that for the same velocity, the *KE* of the glass particles was nearly five times greater than that of the alumina particles. Nonetheless, the *ER* of the target materials eroded by alumina were nearly one order of magnitude greater than those for the targets eroded by glass. Two exceptions to this trend can be seen in Figure 4.10 (b), namely SLG and c-Ge eroded by glass, for which the *ER* are much greater than for the other materials.

As indicated in the literature, the standard deviation encountered in SPE testing is typically high, often more than 10 % of the mean value. In our study, however, we found an average standard deviation of 6 %. We believe that this variability is not caused by the measurement technique of volume loss, but rather by unstable back pressure and particle feed rates of the sand-blast unit.

The exponents of the power law function fitting the *ER* as a function of V_p are presented in parentheses within the legend of each graph. We have found that the exponents varied from 2.4 to 3.4 in the case of the alumina powder tests, and from 2.3 to 5.1 for the glass powder tests. The elasto-plastic models of erosion predict velocity exponents of 2.4 for the quasi-static model, and 3.2 for the dynamic model.

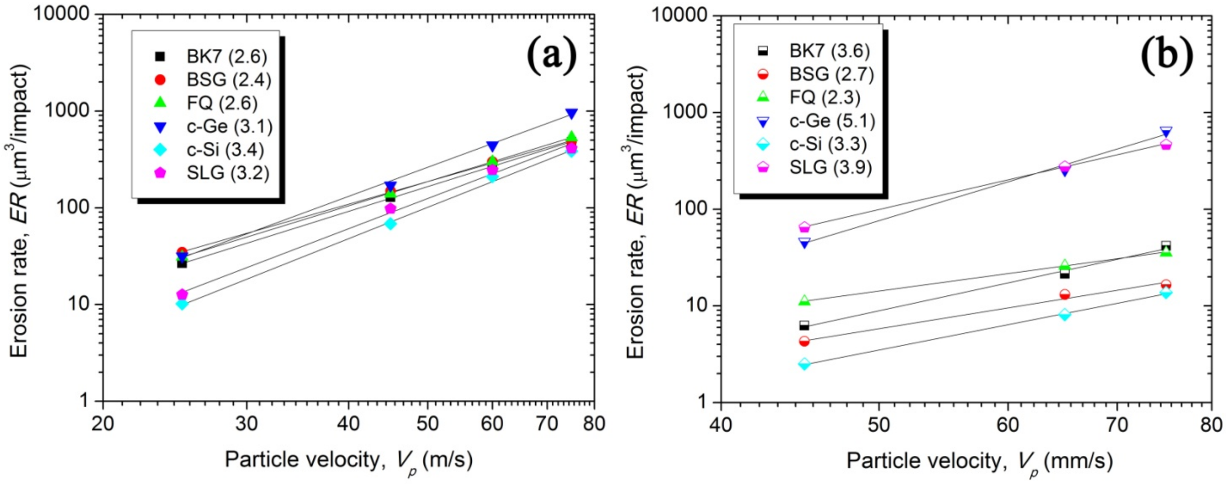

Figure 4.10: SPE rates for all six target materials using (a) alumina powder and (b) glass powder as a function of V_p.

For the single impact tests using alumina powder, all six target materials presented clear signs of material loss through lateral cracking, exactly as predicted by the elasto-plastic SPE models. In Figure 4.11, two typical examples of single impact craters of alumina particles on FQ glass at V_p = 45m/s are illustrated. In fact, there is a close resemblance between the SPE fracture mechanism and the one observed during indentation (compare with Figure 4.1), including plastic deformation, radial cracking and chipping due to lateral cracking. As noted previously, cracking will only occur when the impact load is higher than a certain threshold, and in the case of smaller particles, this may not occur. That is why, in both images, small impact craters are observed where only plastic deformation is present with no signs of cracking.

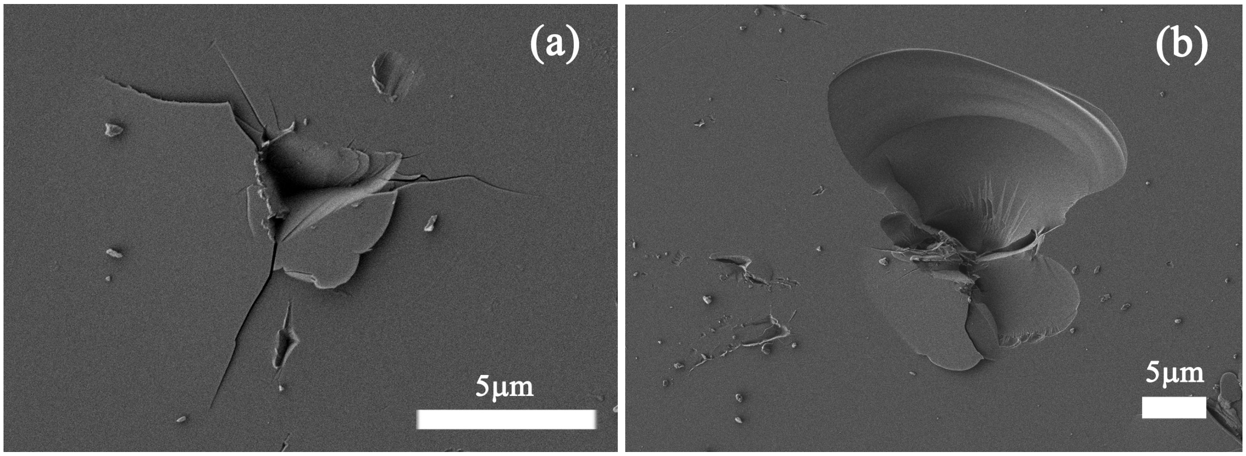

Figure 4.11: Residual impressions left on FQ glass by alumina particle impact at a velocity of 45 m/s.

In the case of single impact tests using glass powder with the same V_p of 45 m/s, the signs of damage were much less apparent than for the tests using alumina powder. In addition, debris left by crushed glass particles was extensively seen on all sample surfaces. From the micrographs presented in Figure 4.12 for impacts on BSG (a) and SLG (b), it can be seen that at least some of the particles were crushed onto the surface during impact and remained imbedded. It appears that even though *KE* is dissipated through particle deformation and fracture, sufficient energy remains to cause lateral fracture.

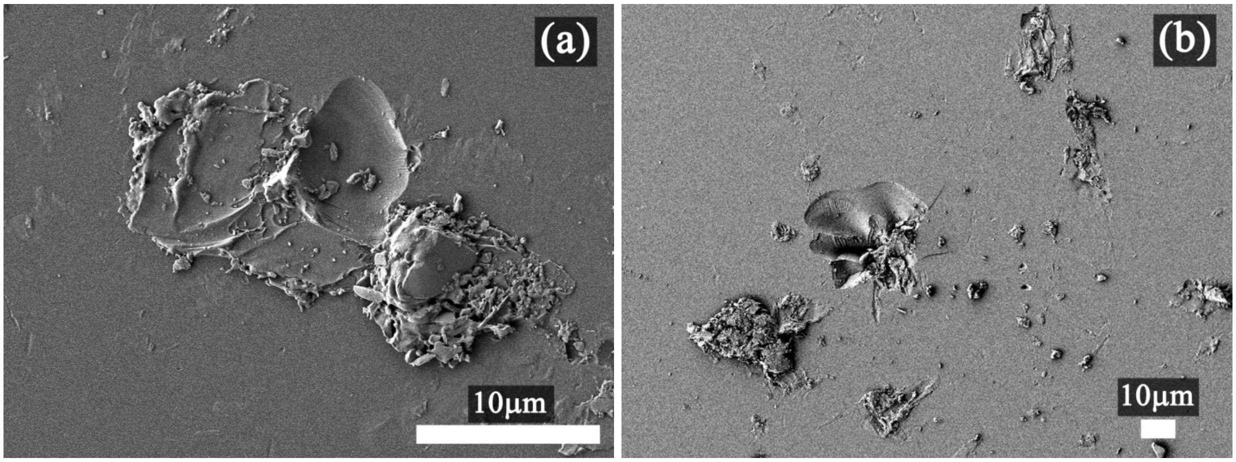

Figure 4.12: Glass particle debris after impact at 45m/s on (a) BSG and (b) SLG.

In order to differentiate the behavior of the target materials, we present in Figure 4.13 the glass particle single impact tests for all six target materials using a velocity of 75 m/s. From these micrographs, it can be clearly seen that two materials present drastically different behaviors than the other four. The c-Ge and SLG samples (respectively, Figures 4.13 (d) and (f)) show much more extensive surface damage, which explains why their SPE rates are higher by an order of magnitude (Figure 4.10 (b)). However, as will be discussed we believe that the mechanisms behind these increased *ER* are different for SLG and c-Ge.

Looking more closely at one of the impact sites of glass on c-Ge (Figure 4.14), the presence of many small erosion craters can be seen around the main impact site. It shows that upon impact, the particle breaks up and that the debris of this fragmentation causes the secondary craters formed by lateral fracture. In the case of the other target materials only plastic deformation with minimal cracking can be observed. Based on the fracture initiation results presented in Figure 4.5, we believe that secondary brittle fracture occurs only in the case of c-Ge because of its very low fracture threshold. Furthermore, if the amount of particle fragmentation scales with velocity, as is to be expected, then the amount of secondary erosion should increase with velocity as well. As a result, the SPE velocity exponent will be higher than predicted, which is precisely what is observed in the case of c-Ge(Figure 4.10 (b)). Because of this secondary erosion, the SPE of c-Ge by glass powder will not be considered in the detailed analysis of the erosion models that will follow. On the other hand, no secondary erosion was observed for SLG, which means that another erosion mechanism is responsible for the high SPE rates of SLG using glass powder. In the next section, we will explain the behavior of SLG when eroded by glass while investigating the effects of the particle hardness relative to that of the target material and considering elasto-plastic erosion mechanisms.

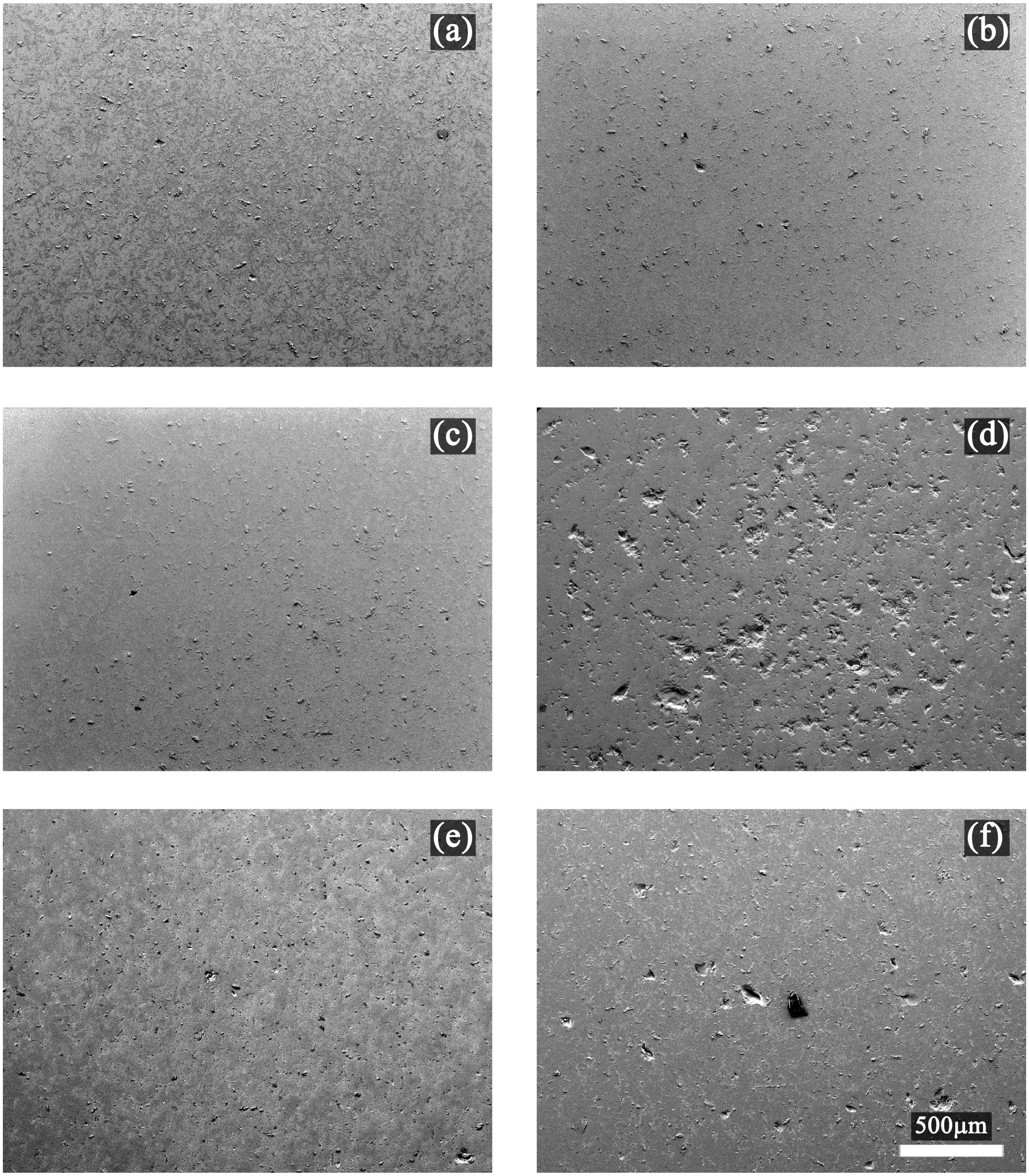

Figure 4.13: Single impact tests using glass powder at an average velocity of 75 m/s for target materials (a) BK7, (b) BSG, (c) FQ, (d) c-Ge, (e) c-Si and (f) SLG.

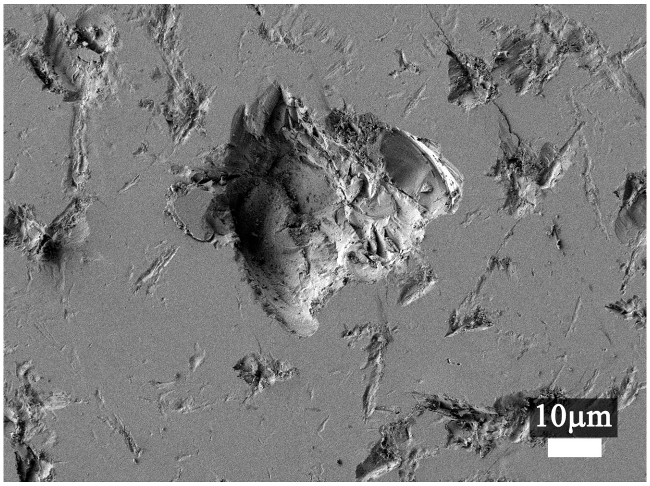

Figure 4.14: Single impact of glass particle with a velocity of 75 m/s on c-Ge.

4.4 General discussion

4.4.1 Analytical model based analysis

Shipway and Hutchings [12] studied a wide range of materials eroded by three types of particles and found significant changes in erosion behavior as a function of H_p/H_t. They concluded that material loss mechanisms changed from micro-chipping for lower ratios to full lateral fracture at higher ratios.

On the contrary, in our study the main material loss mechanism in all cases was observed to be by lateral fracture, as confirmed by the SEM micrographs. In the following analysis, we will correlate the measured erosion behavior to the quasi-static lateral fracture erosion model, and will investigate the effect of H_p/H_t on the erosion process. Specifically, for its simplicity and numerous experimental validations, our discussion is inspired by the quasi-static approach proposed by Wiederhorn *et al.* [67]. It should be noted that we have considered as negligible the *KE* dissipation mechanisms by phase transformation and by thermal effects when compared to the energy dissipated through fracture mechanisms. We believe this to be a reasonable assumption because of the low velocities (<100 m/s) and highly brittle nature of the target materials used in this study.

The quasi-static model is based on the assumption that a perfectly hard particle with a given *KE* indents the surface and induces lateral fracture that leads to material loss. The work of penetration done by the particle can be expressed as:

$$W_{total} = \int_0^{z_m} P(z)dz \tag{4.3}$$

where P is the load applied by the impacting particle and z is the depth of penetration.

As proposed by Bull [73], only part of the KE will contribute to the erosion process since the elastic work of indentation will be returned to the particle during rebound. As a result, the part of the particle KE that will lead to erosion will be equal to the irreversible work of indentation,

$$W_{irr} = KE \cdot R_p = \int_0^{z_m} P(z)dz\,. \tag{4.4}$$

During quasi-static indentation, the load will be dependent on the mean contact pressure, which will be equal to the hardness,

$$H = p_o = \frac{P}{A(z)}, \tag{4.5}$$

where $A(z)$ is the projected contact area between the particle and the impacted surface. Approximating the angular particle's $A(z)$ as that of an idealized cone,

$$A(z) = \pi z^2 \tan^2 \psi, \tag{4.6}$$

where ψ is the cone half angle, we find, by combining equations 4.4, 4.5 and 4.6 and integrating, that

$$z_m = \left(\frac{3 * W_{irr}}{H\pi \tan^2 \psi} \right)^{1/3} \tag{4.7}$$

and

$$P_m = H\pi \tan^2 \psi \cdot z_m^2\,. \tag{4.8}$$

The volume lost per impact (V_e) can be expressed by:

$$V_e = \pi c_l^2 d_c \tag{4.9}$$

where c_l is the length of the lateral crack and d_c is the depth of the crack beneath the surface. Although lateral cracks are thought to develop below the plastically deformed zone, we used the maximum penetration depth (z_m) in order to represent d_c in our analysis. Based on the model developed by Chen and Bull [194], that relates the size of the plastic deformation zone to the maximum penetration depth, the plastic zone radius will be 2.6 to 2.8 times larger than the maximum penetration depth for the materials studied in this work. Because of this relatively constant ratio, z_m can be used to represent d_c.

Based on the work by Lawn *et al.* [20] for the median/radial crack system, Evans *et al.* [66] showed empirically that c for lateral cracks could be expressed by:

$$\frac{P_m}{c^{3/2}} = \beta K_{IC} \tag{4.10}$$

where β is a constant that was found to be proportional to tan(ψ) for the radial crack system [20]. Although the use of equation 4.10 for the lateral crack system has no theoretical justification [65], Evans *et al.* [66] showed that the lateral crack length was proportional to the radial crack length. Based on these findings we have used the definition of β as proposed by Lawn *et al.* [20].

Based on this quasi-static analysis, we plot in Figure 4.15 the experimental SPE results versus the predicted volume loss for all six target materials eroded using both types of powders. The results of c-Ge eroded by glass are not presented because of the material's different erosion mechanism, as discussed earlier. In Figure 4.15 (a), we first consider that all particles retained a cube corner geometry with $\psi = 45.3^{\circ}$ during penetration into the target. In this first analysis, the data indicates that for both types of powders, the quasi-static model of erosion adequately predicts the experimental SPE behavior. However, it should be noted that the slopes of both sets of data (presented in parentheses within the legend of Figure 4.15) are slightly higher than unity because of the higher than predicted velocity exponents which will be analyzed in further detail in the next section. Also, we can see that SLG eroded by glass particles does not behave in the same manner as the other target materials.

In Figure 4.15 (b), we present the SPE data versus the predicted volume loss, but for deformable particles. When $H_p/H_t < 1$, the contact pressure will be limited by the particle hardness and not by the target hardness. In addition, it can be assumed that the particle will deform significantly during impact. We model this by a change in ψ but, not knowing the exact change in particle geometry during impact, we can only hypothesize as to the resulting cone angle. Because it is commonly used in indentation testing, we have employed a Berkovich indenter geometry to simulate the deformed particle. Therefore, for tests where $H_p/H_t < 1$, we used the cone angle of the Berkovich indenter geometry ($\psi = 70.3^{o}$) and the index of plasticity related to the indentation strain of this geometry. From Figure 4.15 (b), we can now see that the erosion results for all the glass powder tests follow the same trend. This confirms the hypothesis that the particle is deformed significantly during impact when $H_p/H_t < 1$.

Taking into account the particle deformation and the change in contact pressure, there still remains a large discrepancy between the tests using alumina and glass powders. One explanation could reside in the morphological difference between the erodents that were used. Since the glass particles are much less uniform than the alumina particles, it is conceivable that there is a lower probability of the particle impacting the surface on a sharp corner than for the more uniform alumina particles. However, the more probable explanation is that the particle *KE* dissipated by fragmentation is much greater in the case of the glass powder than for alumina powder. In fact, the trend observed in Figure 4.9 where the specific surface area change is nearly five times larger for tests using glass powder strongly supports this conclusion. In order to clarify these findings, the evaluation of energy dissipated by particle breakup will require further investigation. In particular, the use of a much narrower particle size distribution would be essential.

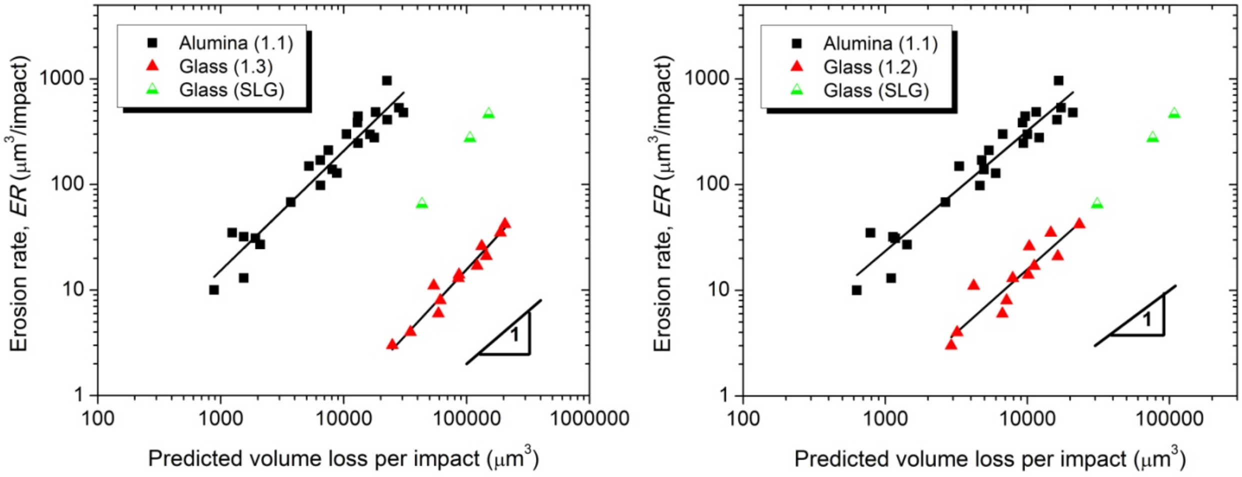

Figure 4.15: Experimental *ER* versus predicted volume loss by the quasi-static SPE model using (a) rigid particles and (b) deformable particles for $H_p/H_t<1$. Note that the tests on SLG with glass are represented by green half-empty triangles.

4.4.2 Influence of particle velocity

As indicated earlier, we found SPE velocity exponents with values ranging from 2.3 to 3.9 - excluding c-Ge which presented significant secondary erosion and a very high exponent of 5.1. Most of these exponents are much higher than the theoretical value of 2.4 predicted by the quasi-static model of erosion. While it is possible that the dynamic model may also apply with its higher exponent of 3.2, the large spread of measured velocity exponents points towards a material dependence, previously unreported. Since particles are susceptible to breakup or crushing during erosion, it has been suggested by several authors [12, 74, 77, 203] that DA may be necessary to achieve complete material removal from the target's surface. As argued by Shipway and Hutchings [12], it also stands to reason that the amount of DA needed will decrease as velocity increases. This would lead to more efficient material removal at higher velocities and thus to velocity exponents higher than theoretically predicted. Interestingly, the glass powder tests present higher velocity exponents suggesting a greater need for DA which is also suggested by the corresponding much lower measured *ER*.

In order to understand how DA depends on the target, we studied the correlation of the measured velocity exponents to target material properties. Interestingly, we did not find any significant correlation to the target fracture properties such as K_c, H/K_c and crack threshold loads. However, the plastic behavior of the target material appears to strongly influence DA. In Figure 4.16 we present the exponents as a function of material yield pressure (H^3/E^2) which is a measure of the material's resistance to the onset of plastic deformation. This parameter was first proposed by Johnson [27] for a contact between an axysymmetrical solid and an elasto-plastic plane surface. It has been shown to correlate with various tribological solicitations [19, 28]. Specifically, Hassani *et al.* [30] showed, using finite element modeling, a strong correlation between the SPE of various coatings and their H^3/E^2 ratios. They found from single impact simulations that SPE increased with decreasing H^3/E^2, but the effect of DA on velocity exponents was not studied. Nonetheless, the results in Figure 4.16 suggest that this dependence of SPE on H^3/E^2 is also important in terms of DA. As the resistance to plastic deformation increases, DA remains necessary even at higher velocities, which is translated into lower velocity exponents. This dependence of DA on yield pressure is supported by the good fit of the glass powder data in Figure 4.16. In fact, since a much greater part of the particle *KE* is dissipated in the case of glass, it stands to reason that more DA will be necessary for material removal.

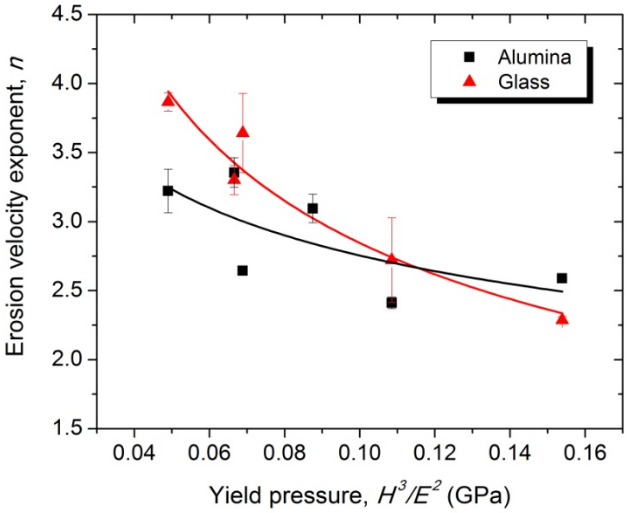

Figure 4.16: SPE velocity exponent as a function of yield pressure.

4.5 Conclusion

We tested six target materials with glass and alumina powders in order to study the effects of particle properties on the SPE mechanisms of brittle bulk materials. Following an in depth characterization of the targets and of the particles before and after SPE testing, we can conclude the following:

1) Tests using both powders revealed a material loss mechanism related to lateral fracture. A greater accumulation of damage appears to be necessary for material removal when using the softer glass powder. The Germanium sample presented signs of severe secondary erosion when using glass powder because of the breakup on impact of the glass particles and the very low fracture threshold of Germanium.
2) The increase of the powders' specific surface area shows that there is a close correlation of particle breakup with H_p/H_t. The glass powder size distributions showed a 23 % increase in specific surface area while the alumina powder presented only an increase of 5 %.
3) SPE tests with both types of particles are fairly well represented by the quasi-static elasto-plastic indentation approach. The divergence of the experimental results from the model can be explained by the higher than predicted velocity exponents.

4) Based on the analysis and modification of the quasi-static elasto-plastic indentation model for conditions where $H_p/H_t < 1$, we find that the deformation of the particle explains discrepancies between SLG and the other materials eroded by glass powder.

The higher than predicted velocity exponents are explained by a decrease in necessary damage accumulation for material removal when velocity increases. However, we have found that as the resistance to plastic deformation of the target materials (H^3/E^2) increases, the necessity of damage accumulation remains constant leading to lower velocity exponents.

4.6 Acknowledgments

The authors gratefully acknowledge the support of the Fonds de recherche du Québec - Nature et Technologies (FQRNT), the Consortium for Research and Innovation in Aerospace in Québec (CRIAQ) and the Natural Sciences and Engineering Research Council (NSERC) of Canada. The authors also wish to thank Francis Turcot for his invaluable technical expertise.

CHAPTER 5 SOLID PARTICLE EROSION MECHANISMS OF HARD PROTECTIVE COATINGS

Article 2: Solid Particle Erosion Mechanisms of Hard Protective Coatings

E. Bousser, L Martinu, J.E. Klemberg-Sapieha*

Engineering Physics Department, École Polytechnique de Montréal, P.O. Box 6079, Station Centre-ville, Montréal, Québec, Canada H3C 3A7

Abstract

In order to assess the material loss mechanisms of monolithic coatings subjected to solid particle erosion (SPE) using angular alumina particles with relatively low velocities (< 100m/s), we studied the erosion behavior of several hard coatings deposited by pulsed DC magnetron sputtering. We first validated a new methodology for the measurement of volume loss and optimized the testing conditions to obtain a measured erosion rate (*ER*) free from experimental artefacts. We then correlated the measured *ER*s to the mechanical properties, measured by depth sensing indentation, and found that the *ER* was strongly dependent on the target hardness (H_t) of the materials ($ER \propto H_t^{-6.8\pm0.5}$). In order to understand the material loss mechanisms, we studied three coating systems in greater detail with the help of fracture characterization and a morphological study of the eroded surfaces. It was found that fracture toughness was not a good predictor of *ER* and that the material removal was the result of ductile indentation and cutting. Finally, in an effort to understand the role of particle fracture, we measured the particle size distributions of the powders before and after erosion testing and found that particle breakup was proportional to the target hardness but not sufficiently large to explain the large drop in *ER*s with increasing H_t.

Keywords: Solid Particle Erosion (SPE), Coatings, Erosion Mechanisms, Hardness, Mechanical Properties.

* Corresponding author: tel.: +514-340-5747, fax: +514-340-3218 Email: jsapieha@polymtl.ca

5.1 Introduction

When aircraft operate in harsh environments where hard particulate matter is entrained by the air flow into the operating engine, severe wear of exposed components may occur through material removal by solid particle erosion (SPE). This type of damage is most prominent in the first stage of the aircraft engine, where the compressor blades can be eroded to such an extent that aerodynamic performance and even structural integrity are compromised. Consequently, much work has been done in academia and industry in order to understand the material loss mechanisms present in SPE and to develop protective approaches that will increase component lifetimes. One such technology is the use of hard protective coatings to impede the erosion of the predominantly metallic engine components.

Of the many different coating systems proposed for protection against SPE, two main categories emerge: TiN-based and carbon-based. Carbon-based films are predominantly thick diamond coatings deposited by chemical vapor deposition [81, 108, 117]. Due to their very high hardness, these have been found to be extremely resistant to SPE impact damage [108, 118]. However, they are difficult to implement in practice since they need to be deposited at temperatures that exceed the permissible limits of the metallic components. For that reason, the most frequently used coatings for SPE protection are TiN-based in monolithic [85, 87, 89, 91, 92] or multilayer [90, 105, 106] forms, which can be deposited on technologically relevant substrates.

Since the early 1990s, Ti/TiN multilayer systems have been used because their multilayer design offers the possibility of depositing thicker coatings by relaxing residual stresses and of enhancing erosion resistance. In fact, it has been shown by Borawski *et al.* [106] that multilayer architectures are more resistant to SPE when the stress field generated during impact encompasses a larger volume of the coating (large rounded particles) because of the crack tip blunting effect of the ductile layers and the deflection of cracks at interfaces. On the other hand, monolithic coatings are more durable under SPE by small, hard and angular particles because the damage is generally confined to a small volume in the top layer and therefore, the ductile interlayers of the multilayer coating would not be beneficial to erosion resistance.

The SPE resistance of monolithic coatings can be enhanced by using materials with high toughness to prevent crack growth, and high hardness to inhibit crack initiation by dissipating the particle kinetic energy through fragmentation and minimizing the penetration of the particle on impact. Consequently, alloyed and nanocomposite TiN-based systems are being investigated in greater numbers. One structurally hardened system that is now being implemented industrially is TiAlN, which has been shown to not only possess high SPE resistance [92, 97], but also good stability at higher temperature [132-134]. However, more recently, nanocomposite coatings have been shown to be promising candidates for SPE resistance because of their very high hardness and ability to slow crack propagation [29, 47, 49]. In fact, CrSiN [10], TiSiN [100] and TiSiCN [102, 103] systems have been shown to be highly resistant to SPE by small angular alumina particles.

In order to select the appropriate coating system, the material loss mechanisms must be properly understood. In the first place, the metallic surfaces to be protected (stainless steel or titanium alloys) erode in a predominantly plastic mode of material removal through micro-cutting or ploughing mechanisms [51, 52, 196]. On the contrary, the hard ceramic protective coatings are brittle in nature and will present much more complex erosion behaviors. In fact, it has been shown that brittle materials exhibit surface removal mechanisms very similar to those encountered during indentation [31]. In the case of large round particles, Hertzian cracks will form and can coalesce into deep wormhole-like craters [116, 200], while for sharp particles, the damage can progress from plastic cutting or ploughing of the surface for low energies to radial/median cracking at higher energies and finally to lateral fracture removing significant amounts of matter [66, 67, 198]. The transitions between mechanisms are a function of the coatings' corresponding elastic (Young's Modulus [E]), plastic (hardness [H]) and fracture (fracture toughness [K_{IC}]) properties [31].

In addition, it has been shown that the erodent particles can be crushed or fragmented upon impact when the hardness of the target (H_t) is greater than that of the particle (H_p) [12, 31, 76, 77]. As a result, the particle breakup may lead to very low erosion rates and may also cause a change in the material loss mechanism. For low H_p/H_t ratios, and low particle velocities, a micro-chipping mechanism has been observed by several authors [12, 31, 106] and has generally been characterized by a smooth surface after erosion when compared to the very rough surfaces resulting from lateral fracture of brittle materials [21].

While it has been observed that coatings exhibit the different brittle fracture modes (Hertzian, radial and lateral cracking) when impacted by large and/or highly energetic particles, there is no description of the mode of material loss when eroded by small angular particles with relatively low velocities (< 100m/s).

In the present paper, we study the above-mentioned mechanisms for several hard coatings deposited by pulsed DC magnetron sputtering. We first validate a new methodology for the accurate measurement of volume loss and we then correlate the measured erosion rates to the material parameters measured by depth-sensing indentation. Furthermore, in order to understand the material loss process, we study three of the coating systems in greater detail with the help of fracture characterization and a morphological evaluation of the eroded surfaces. Finally, in an effort to assess the role of particle fracture, we determine the particle size distributions of the powders before and after erosion testing.

5.2 Experimental methodology

5.2.1 Coating deposition

All coatings were deposited by reactive pulsed DC magnetron sputtering (PDCMS) in a vacuum system equipped with two magnetrons. The base pressure of the reactor, described in detail in [11], was below 1 x 10^{-6} Torr. Three different substrates were used: single crystal silicon (c-Si), Ti-6Al-4V (Ti64) and AISI 410 stainless steel (SS410). The metallic substrates were polished to a mirror-like finish and all substrates were cleaned in acetone and isopropanol using an ultrasonic bath. Then, the substrate surfaces were sputter cleaned in a capacitively coupled radio-frequency (RF) Ar plasma at a negative bias (V_b) of -600 V, in order to remove the surface oxide layer prior to deposition. Depending on the type of coating, the substrate deposition temperatures vary between 250 and 400 ^{o}C while V_b was between -50 and -200 V (summarized in Table 5.1).

In all cases, a thin chromium or titanium adhesion layer (< 0.5 μm) was first deposited. This was followed by the principal monolithic coating. Here we study binary (CrN and TiN), ternary (CrSiN and TiSiN) and quaternary (TiSiCN) material systems. The silicon content in the ternary coatings was adjusted by changing the current on the Si target and the carbon content in the quaternary coating was controlled by the flow of CH_4 during deposition. The thicknesses of the deposited films (t) were between 6 and 13 μm, as determined by scanning electron microscopy (SEM, Jeol JSM7600F). The coating deposition parameters and thicknesses are presented in Table 5.1.

Table 5.1: PDCMS deposition parameters and thicknesses of the coatings.

Coating	Substrate	Deposition Temperature (^oC)	Bias, V_b (-V)	Thickness, t (µm)
CrN-1	c-Si	250	100	8
CrN-1	Ti64	250	100	8
CrN-2	SS410	300	200	13
CrSiN-1	SS410	300	200	10
CrSiN-2	SS410	300	200	8
CrSiN-3	SS410	300	200	9
TiN-1	SS410	400	200	10
TiN-2	c-Si	400	100	8
TiN-2	Ti64	400	100	8
TiSiN-1	c-Si	400	50	6
TiSiN-1	Ti64	400	50	6
TiSiN-1	SS410	400	50	6
TiSiN-2	SS410	400	200	10
TiSiCN-1	SS410	400	200	10

5.2.2 Elasto-plastic properties

The elasto-plastic properties of the target materials were evaluated by depth-sensing indentation (Hysitron Triboindenter). The coating hardness (H_t) and reduced Young's modulus (E_r) were measured using a Berkovich geometry indenter and the data was analyzed using the widely accepted Oliver and Pharr methodology [193]. The tip geometry and system compliance were calibrated using a fused silica standard, and the system drift, typically less than 0.1 nm/s, was measured before each indentation by maintaining the tip in contact with the surface and monitoring the drift for 40 s. Each coating was probed by a 3x3 indentation array with a spacing of 100 µm between indentations. Each indentation was composed of a 25 cycle partial-unload load-function with the maximum load of each cycle (P_m) increasing from 10 mN to 1000 mN. For each load cycle, the load increased to P_m over 5 s followed by a 2 s holding segment, and finished with a 5 s unloading segment down to 80% of P_m (Figure 5.1). It should be noted that this type of indentation load-function was found to be valid for the hard ceramic coatings studied because they do not present strain hardening under the loading conditions considered here.

After removing failed indentations (generally caused by tip slippage), we used between 6 and 9 of the partial-unload indentations made in each coating to calculate the average elasto-plastic properties as a function of indentation contact depth (h_c) as well as the standard deviation. For each curve, the Young's modulus was calculated by extrapolating the linear part of the E_r curve (approximately $h_c/t < 0.1$) to $h_c/t = 0$ and the hardness by averaging the plateau portion of each H_t curve. In this manner, we obtained a depth profile of the elasto-plastic properties for each indentation.

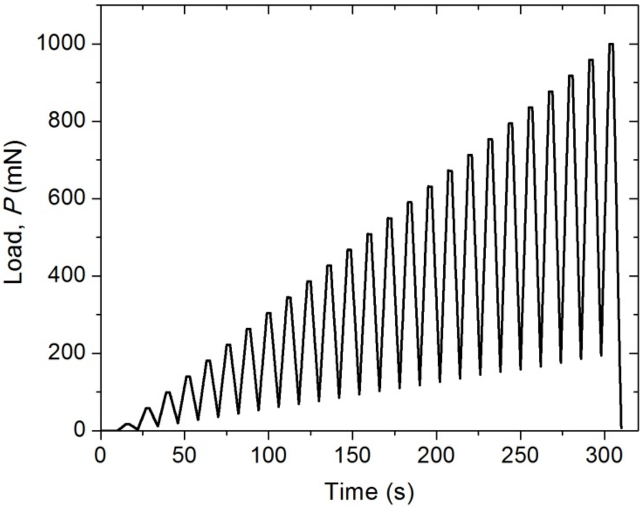

Figure 5.1: Partial-unload load-function used to obtain the coating mechanical properties.

The proportion of energy dissipated by plastic means during an indentation, the index of plasticity (R_p), is generally evaluated by dividing the irreversible work of indentation (W_p) over the total work (W_{total}). As a close approximation, in this study we calculated R_p using the indenter displacements using,

$$R_p = \frac{W_p}{W_{total}} \approx 1 - \frac{h_{\max} - h_{res}}{h_{\max}} \tag{5.1}$$

where h_{max} is the penetration depth at the maximum load applied during the cycle and h_{res} is the residual indentation depth calculated from the fitted function of the unload segment used in the Oliver and Pharr analysis. It should be noted that R_p is in fact the complement of the material's elastic recovery ($R_e = 1\text{-}R_p$), and thus it will equal zero when the indentation remains entirely in the elastic regime.

5.2.3 Fracture properties

In order to study the influence of fracture toughness on the SPE behavior of hard coatings, we deposited three coatings (CrN, TiN and TiSiN) on c-Si samples. These coatings were prepared in two thicknesses: one for SPE testing (6 to 8 μm) and one for toughness testing (3 to 6 μm). We evaluated their indentation fracture toughness by using a cube-corner indenter geometry, and we based our approach on the fracture toughness relation developed by Lawn *et al.* [20] and Anstis *et al.* [22]:

$$K_{IC} = \alpha \left(\frac{E_r}{H} \right)^{\frac{1}{2}} \frac{P}{c^{\frac{3}{2}}}, \tag{5.2}$$

where α is a constant related to the indenter geometry, E_r is the reduced Young's modulus previously evaluated by depth-sensing indentation, H is the hardness evaluated from the area of the residual impression, P is the applied load and c is the crack length measured from the centre of the indentation to the tip of the crack (see Figure 5.2). The value of c was obtained by averaging the three crack lengths measured for each indentation. In our work, we used $\alpha = 0.0535$, as found by Jang and Pharr [206] for c-Ge and c-Si using a cube corner indenter. All crack lengths and residual impression sizes of the indentations were measured using SEM.

In order to obtain toughness values as a function of depth, an array of 8x8 indentations was made on each coating with a spacing of 75 μm between the cub-corner indentations. The load between indentations within each array was decreased incrementally from 1000 mN to 25 mN for the CrN coating, 750 mN to 25 mN for the TiN coating and 500 mN to 25 mN for the TiSiN coating.

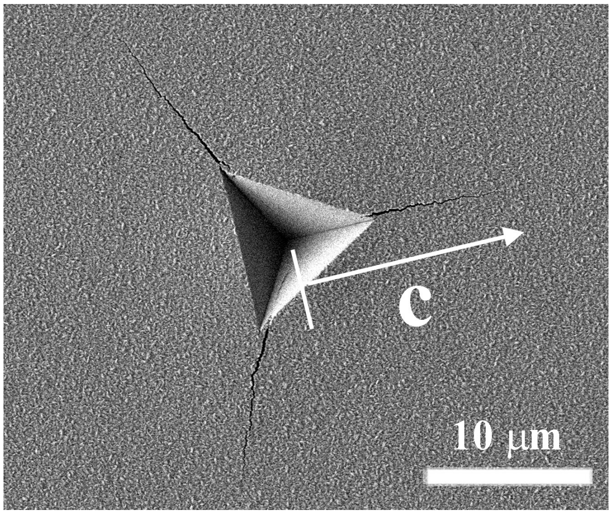

Figure 5.2: Example, on a CrN coating, of cracking under cube corner indentation with crack length *c* indicated.

5.2.4 SPE testing methodology

The SPE tests were carried out in an in-house gas-blast erosion system based on the specifications of ASTM standard G76 [164], using alumina powder with a median size of 72 µm. The particle velocity (V_p) was controlled by adjusting the back pressure of the abrasive blasting unit (S.S. White Airbrasive unit) and was measured using a double disk time-of-flight technique [166]. All tests were performed with the particle flow impacting the surface at normal incidence using a tungsten carbide nozzle with an inner diameter of 1.14 mm and a length of 36 mm. The whole unit was mounted on a 30 kg capacity balance precise to 0.1 g (Sartorius LE29000) in order to closely monitor the particle feed during each test. The particle feed rate (f_r) was controlled by adjusting the unit's shaker amplitude and the back pressure. In order to stabilize f_r before testing, the unit was turned on for several minutes while the sample was shielded by a retractable shutter.

During each test, the sample was exposed to the particle flow for a precise total mass of erodent so as to obtain an erosion scar between 1 and 4 µm in depth without piercing or delaminating the coating. The erodent mass used in each test depended on the target properties and V_p. The *ER* was calculated by dividing the measured volume of material loss by the mass of erodent used for that test. It was assumed that all the mass of erodent impacted the target since the diameter of the resulting wear scars was at least three times smaller than the size of the eroded specimen.

Furthermore, the relatively large depth of the erosion wear scar ensured that the running-in period of the erosion test could be considered as negligible and that the measured *ER* corresponds to the steady-state rate.

The volume loss measurements were accomplished with a confocal white light profilometer (Conscan module of a CSM instruments Micro-Combi Tester). Through topographical mapping of the eroded surfaces, we were able to obtain a complete 3D profile of the wear scar. As can be seen in Figure 5.3, wear scars generated from tests with cylindrical nozzles are axi-symmetrical and present a Gaussian type of profile. Ghobeity *et al.* [177] found this type of profile to be the result of a radial linear decrease of velocity from a maximum value found at the center of the nozzle combined to a Weibull radial mass flux probability distribution function of the particles exiting the nozzle.

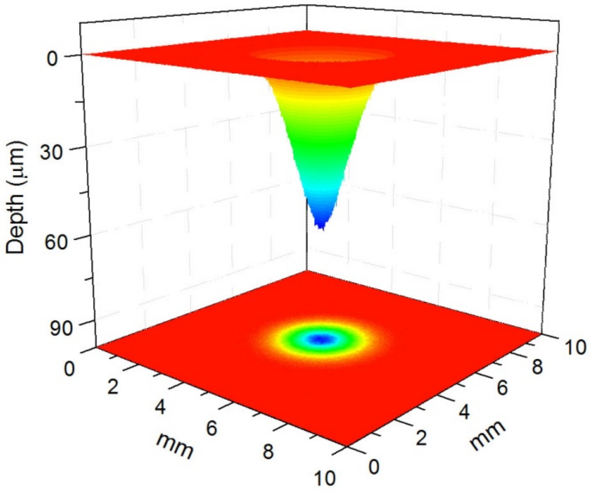

Figure 5.3: 3D topographical map of an SPE wear scar in c-Si.

Completing a full scan is very time consuming. Consequently, we adopted a new single profile-based technique. Our approach consisted in scanning a 2 mm wide region in the center of the wear scar (see Figure 5.4 (a)) and identifying the deepest point of the scar. We then extracted the line profile and used it to calculate the volume loss by numerical integration. First, a Gaussian function is fitted through the experimental data in order to identify the centerline of the profile and then, the distance of each point in the scan from this line (*R*) is calculated (see Figure 5.4 (b)). The total volume loss is then the summation of the elementary rings defined by $\Delta V = \pi R Z \Delta x$, where Z is the measured depth of the given point and Δx is the lateral resolution of the scan (4 µm in this study). For shallow, and sometimes noisy, wear scars, such as those found when eroding coatings, the fitted Gaussian function is used to evaluate the volume of revolution.

It should be noted that for coated samples, the surface curvature can also be an important factor to consider. One approach that can be used is to subtract a scan of the surface made before erosion from the post-erosion scan. However, difficulties in exact scan positioning and change in curvature due to stress relaxation after partial surface erosion make this technique less than ideal. In this study, we removed the surface curvature from the scan of eroded sample by modeling a polynomial function through the non-eroded part of the scan. For each wear scar, three repetitions of the volume measurement were made so as to evaluate the statistical error. Each of the line scans were made in different directions as illustrated in Figure 5.4 (a).

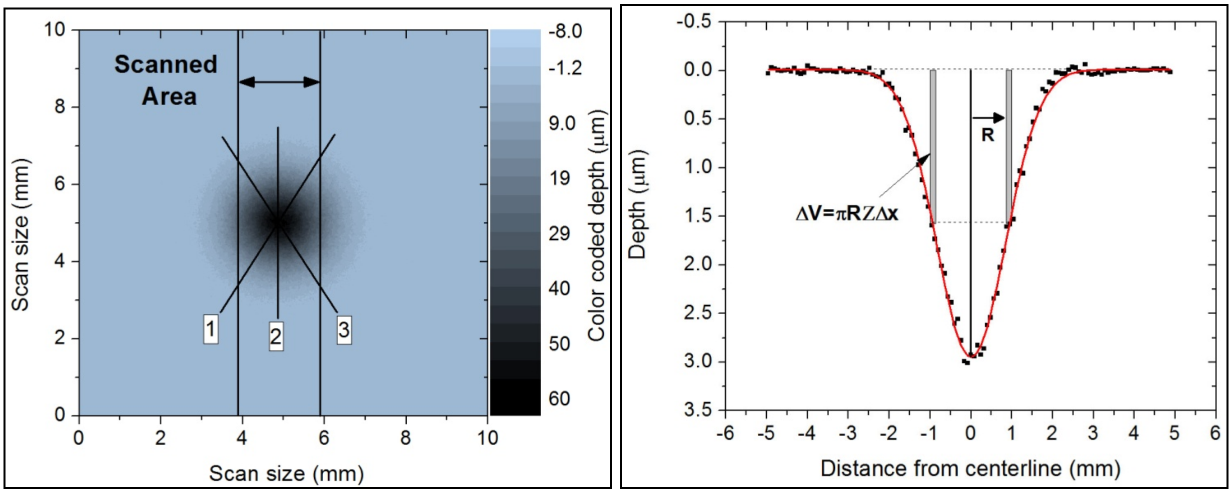

Figure 5.4: Volume loss measurement methodology: (a) Surface map of an SPE scar in c-Si indicating the scanned area and the three line scans; (b) Parameters and Gaussian fit used in numerical volume integration illustrated on CrN coating SPE experimental data.

5.2.5 Eroded surface morphology

The surface morphology of selected eroded samples has been imaged by SEM. In addition to imaging the surface following SPE testing, we imaged as well two of the samples after exposing them to the particle stream for a very short amount of time (around one second) in order to observe single impacts of particles on the target surfaces.

5.2.6 Particle size distribution characterization

To study the effect of erosion testing on the particles themselves, we collected the powder before and after SPE testing. Unlike the powder used for the SPE testing, the alumina powder used to study particle breakup was sifted prior to testing to narrow the particle size distribution. Each of the tested samples was impacted by 5 g of powder with V_p = 60 m/s, f_r = 1 g/min, a normal angle of incidence and a working distance (*WD*) of 50 mm. The particle size distributions were measured by laser diffraction spectroscopy (LDS) (Coulter LS200 with Micro Volume Module) using the scattered light of a 750 nm laser to determine particle sizes from 0.4 to 2000 μm. Each LDS measurement was computed by averaging 60 distribution profiles and each collected powder was sampled twice. Because the alumina powder possessed a significant amount of particles of small dimensions (*i.e.* < 10 μm), we used a model based on the Lorenz-Mie theory of scattering by a sphere [207].

5.3 Experimental results

5.3.1 Volume loss methodology validation

In order to evaluate the SPE of the coatings using the line scan volume loss methodology, we first validated the technique using several brittle bulk materials and compared the erosion rate (*ER*) results to those obtained using the mass loss method described in ASTM standard G76 [164]. All samples were tested with V_p = 45 m/s, *WD* = 20 mm and were exposed to 2 g of alumina powder.

The mass losses by SPE were evaluated using an analytical balance (Sartorius LE225D) with a readability precision of 0.01 mg and repeatability better than 0.02 mg. The samples were carefully weighed before and after each test with a minimum of manipulation in order to avoid mass losses from other sources than the erosion test. For each sample, three to six repetitions were made so as to evaluate the experimental error of the measurement. After all the weighing operations had been completed, the samples were scanned in order to evaluate the volume loss. This volume was then converted to a mass loss using the densities presented in Table 5.2. In addition, we performed a complete scan of the eroded surface of one of the tests conducted on the c-Si sample.

Table 5.2: Density of brittle bulk samples used to validate the volume loss measurement technique.

Brittle Bulk Samples	Density, ρ (g/cm^3)
BK7 glass (BK7)	2.5
Fused quartz glass (FQ)	2.2
Single crystal Germanium (c-Ge)	5.3
Single crystal Silicon (c-Si)	2.3
Soda-lime glass (SLG)	2.5

We present the results of this validation study in Figure 5.5 where we can see a very good agreement between the *ER*s measured by the two techniques as well as with the full surface scan in the case of the c-Si. It should also be noted that the experimental error (standard deviation here) is comparable for both techniques: 4 to 17 % for the mass loss technique and 4 to 13 % for the volume loss technique. In addition, it can be observed that the volume loss technique yields systematically slightly lower values than the conventional mass loss technique. The cause of this effect is not yet known and invites further investigation. Nevertheless, both techniques seem to yield equivalent results but the real advantage of the volume loss technique is seen when testing coatings where very shallow wear scars are necessary so as to not pierce the tested layer. In fact, SPE testing using a focused particle flow and a fairly short *WD* leads to very small mass losses which are very often at the readability limit of most analytical balances. Finally, if mass loss measurements are to be used, the densities of the coatings must be known since only the volume of matter lost will indicate the relative performance of the different surfaces. However, the densities of deposited coatings are generally not known.

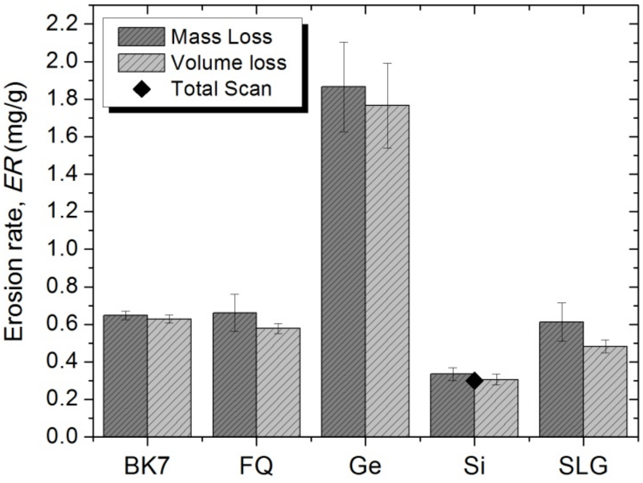

Figure 5.5: *ER* results of brittle bulk materials measured by the mass loss and volume loss techniques.

5.3.2 SPE methodology optimization

As has been reported by several authors [167, 169, 174, 180], particle interaction during erosion testing can significantly affect the measured rates. In order to optimize the SPE methodology and ensure the acquisition of good quality data, we evaluated the effect of *WD* and f_r on the SPE measurements.

As can be seen in Figure 5.6 (a), the working distance has a strong effect on the eroded surface area. When varying *WD* from 20 to 40 mm, the diameter of the eroded surface varies from 5.4mm to 8.0 mm. We therefore evaluated the effect of *WD* on *ER* by testing c-Si at *WD*s between 20 and 40 mm, at V_p = 45m/s and at three different f_r.

In Figure 5.6 (b), a general trend can be observed by which the *ER* decreases with increasing *WD* and this regardless of f_r. This is attributed to interference caused by particles rebounding off the sample surface and screening subsequent incoming particles. This effect has been shown to be caused by an increase in the probability of inter-particle collision as the volume between the nozzle outlet and the surface of the eroded sample increases [167]. However, for the two lower f_r values we observe a stabilization of the *ER* for short *WD*s, indicating a drop off of the particle interference effects.

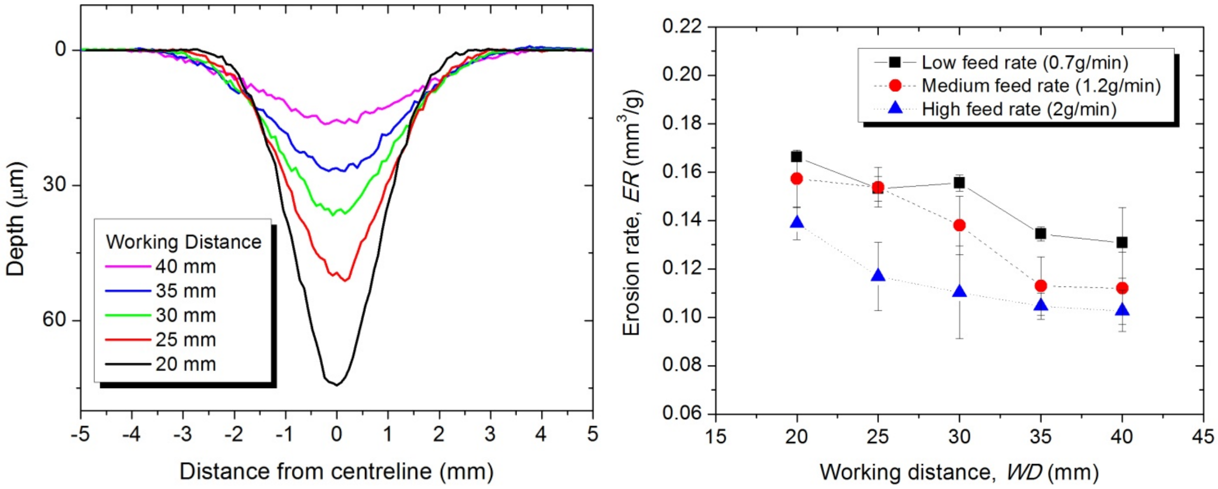

Figure 5.6: Effect of *WD* on SPE: (a) Erosion scar profiles and (b) Measured *ER* on c-Si at V_p = 45 m/s.

Using *WD* = 20 mm in order to minimize particle interference effects, we investigate the influence of f_r (0.4 to 3.2 g/min) on the measured erosion rate of c-Si tested at three different velocities (45, 50 and 60 m/s), and SLG tested at V_p = 45 m/s. In Figure 5.7, we can clearly distinguish a decreasing general trend for all four testing conditions, even though the *ER* amplitude varies according to material and V_p. In fact, the *ER* drop is of nearly 50% for all testing conditions, illustrating the importance of the particle interference effect. In Figure 5.8, we plot the normalized erosion rate (ER^*, ratio of *ER* over the *ER* obtained at f_r = 1 g/min) as a function of the normalized inter-particle spacing (L^*). This ratio, proposed by Papini [180] and based on an analysis by Shipway [169], represents the inter-particle distance in the flow before exiting the nozzle, divided by the particle radius and can be calculated from,

$$L^* = \frac{1}{r_p}\left(\frac{m_p \rho_p \pi r_n^2 V_p}{f_r}\right)^{1/3} \tag{5.3}$$

where r_p, m_p and ρ_p are, respectively, the particle radius, mass and density, and r_n is the nozzle inner radius.

From this figure, it can be clearly seen that the drop in *ER* is independent of the eroded material and is solely affected by the relative distance between particles in the flow which is represented here by L^*. The interference effect stabilizes above L^* = 22 which corresponds to f_r < 0.9 g/min for velocities greater than 30 m/s. This signifies that if $L^* < 22$, interference through inter-particle collisions will reduce the *ER* by screening incoming particles.

Therefore, all tests were conducted with a *WD* = 20 mm and a $f_r = 0.7 \pm 0.2$ g/min. All the coatings were tested at $V_p = 60$ m/s, and the CrN-1, TiN-2 and TiSiN-1 coatings on c-Si were evaluated using four additional velocities between 34 and 82 m/s. TiSiN-1 on Ti64 and SS410 were also tested at various velocities in order to investigate the effect of the substrate on the SPE.

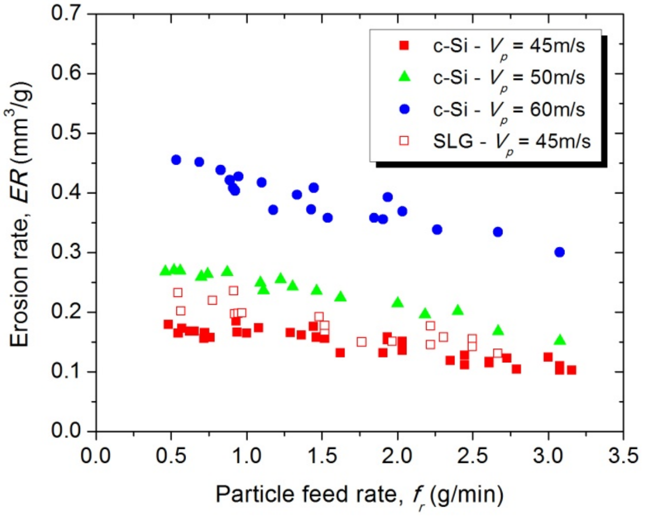

Figure 5.7: *ER* of c-Si and SLG as a function of f_r.

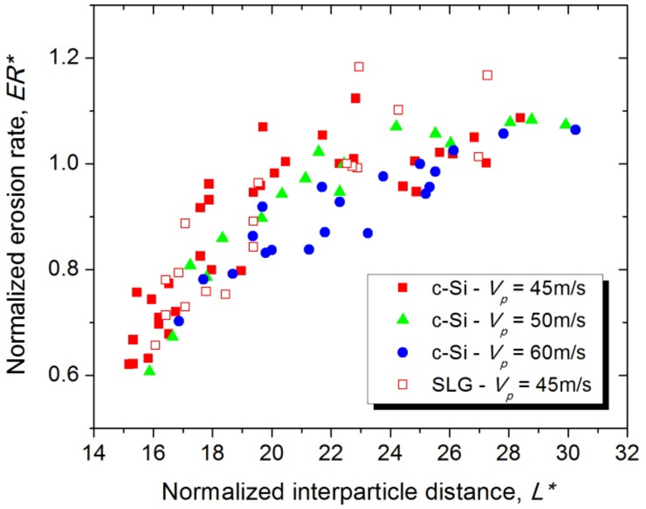

Figure 5.8: Normalized *ER* of c-Si and SLG as a function of normalized inter-particle spacing.

5.3.3 Overall SPE results

First of all, we present the surface elasto-plastic properties of the coatings in Table 5.3. The tested coatings present a wide range of H_t (21 to 36 GPa) and E_r (230 to 330 GPa) values. In addition, the elastic strain to failure (H_t/E_r) varies from 0.09 to 0.12 and the yield pressure (H_t^3/E_r^2) from 0.2 to 0.5. Standard deviations for H_t varied from 1 to 7 %, and for E_r from 2 to 7 % of the average value.

Table 5.3: Coating elasto-plastic properties and *ER* tested at V_p = 60 m/s, *WD* = 20 mm and f_r = 0.7 g/min.

Coating	Substrate	Hardness, H_t (GPa)	Reduced Modulus, E_r (GPa)	Index of Plasticity, R_p	Elastic Strain to Failure, H_t/E_r	Yield Pressure H_t^3/E_r^2 (GPa)	Erosion rate, *ER* (μm^3/impact)	Standard Deviation, σ_{stat} (μm^3/impact)
CrN-1	c-Si	23.5	242	0.55	0.097	0.22	5.3	0.2
CrN-1	Ti64	23.3	243	0.55	0.096	0.21	6.9	1.4
CrN-2	SS410	21.0	229	0.51	0.092	0.18	9.9	0.5
CrSiN-1	SS410	26.4	244	0.48	0.108	0.31	2.4	0.1
CrSiN-2	SS410	25.7	226	0.42	0.114	0.33	2.8	0.3
CrSiN-3	SS410	27.8	240	0.46	0.116	0.37	1.2	0.1
TiN-1	SS410	30.9	284	0.50	0.109	0.37	0.6	0.2
TiN-2	c-Si	27.0	329	0.61	0.082	0.18	1.4	0.1
TiN-2	Ti64	28.1	318	0.54	0.088	0.22	1.7	0.2
TiSiN-1	c-Si	29.3	251	0.46	0.117	0.40	1.4	0.1
TiSiN-1	Ti64	28.7	238	0.45	0.121	0.42	1.2	0.1
TiSiN-1	SS410	29.1	252	0.44	0.115	0.39	2.5	0.3
TiSiN-2	SS410	35.7	311	0.44	0.115	0.47	0.6	0.1
TiSiCN-1	SS410	33.1	312	0.53	0.106	0.37	0.5	0.1
No coating	Ti64	7	220	N/A	0.050	0.018	26.4	N/A
No coating	SS410	4.8	140	N/A	0.022	0.002	19.4	N/A

In Table 5.3, we present the *ER*s in terms of volume loss per particle impact calculated using the median particle size of 72 μm. As can be seen, the TiN-based coatings (TiN-1, TiSiN-2 and TiSiCN-1) deposited at high V_b offer the best protection against SPE. The *ER*s of the 14 coatings vary from 0.5 to 9.9 μm^3/impact and the standard deviations varied from 3 to 28% of the average

ER value but with a median value of 9%. The high spread in the experimental error is explained primarily by the difficulty in subtracting surface curvature from the wear scar scans when curvature was complex or when the wear scars were very shallow (< 1.5 μm in depth).

5.3.4 Erosion of coatings on c-Si

The SEM cross-sections of the three coatings deposited on c-Si are presented in Figure 5.9, where quite different microstructures can be observed. The CrN-1 and TiN-2 coatings, both 8 μm thick, have a columnar microstructure while the 6 μm thick TiSiN-1 coating presents a closely packed microstructure with very little directional growth except in the thin Ti adhesion layer.

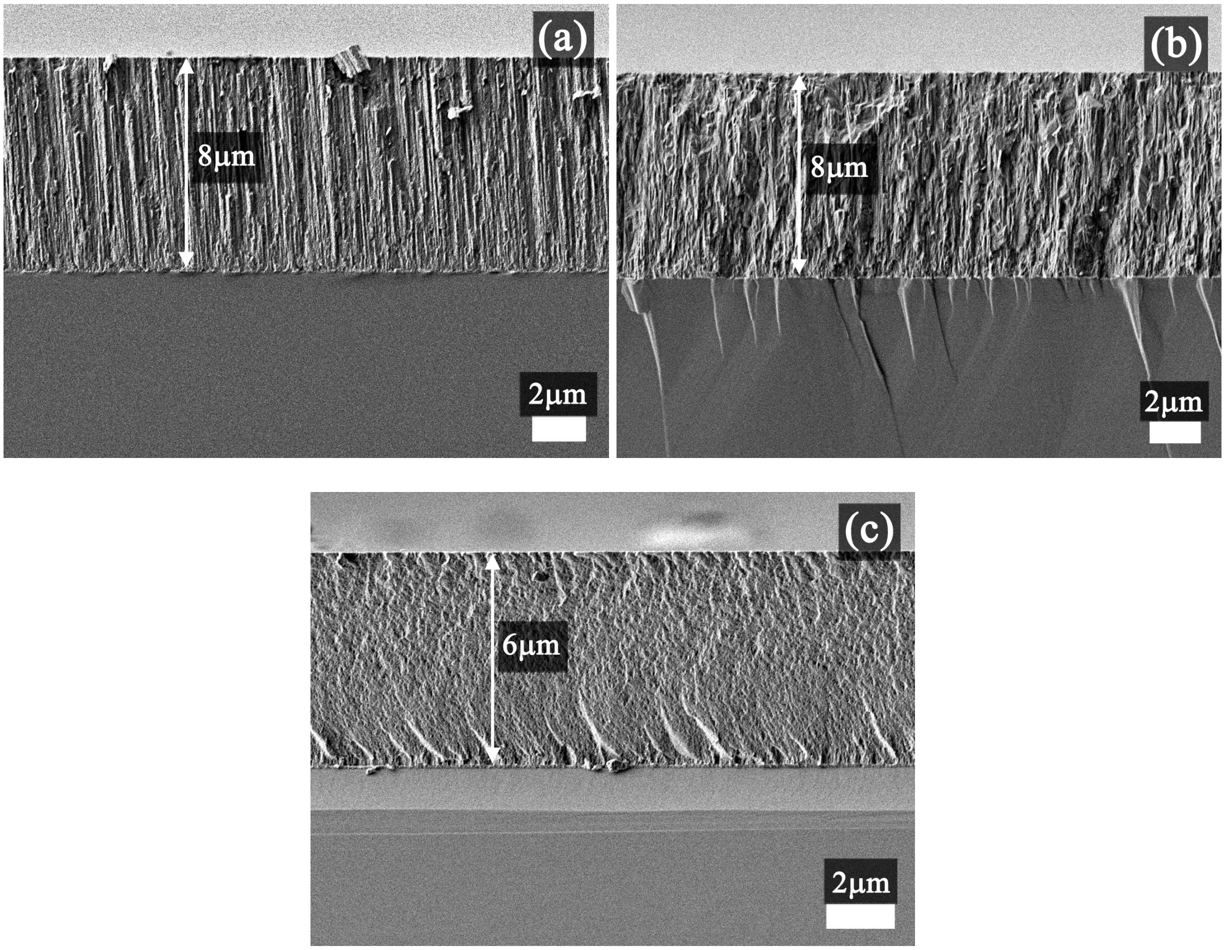

Figure 5.9: SEM cross-sections of the coatings deposited on c-Si: (a) CrN-1, (b) TiN-2 and (c) TiSiN-1.

5.3.4.1 Mechanical properties

The average values of H_t and E_r of the three coatings, measured by depth-sensing indentation, are presented in Figure 5.10 as a function of h_c divided by t. The average values of E_r for the three coatings are presented in parentheses in the upper legend and in the lower legend for H_t. Standard deviations for hardness varied from 1 to 3 %, and for reduced modulus from 2 to 4 % of the average value.

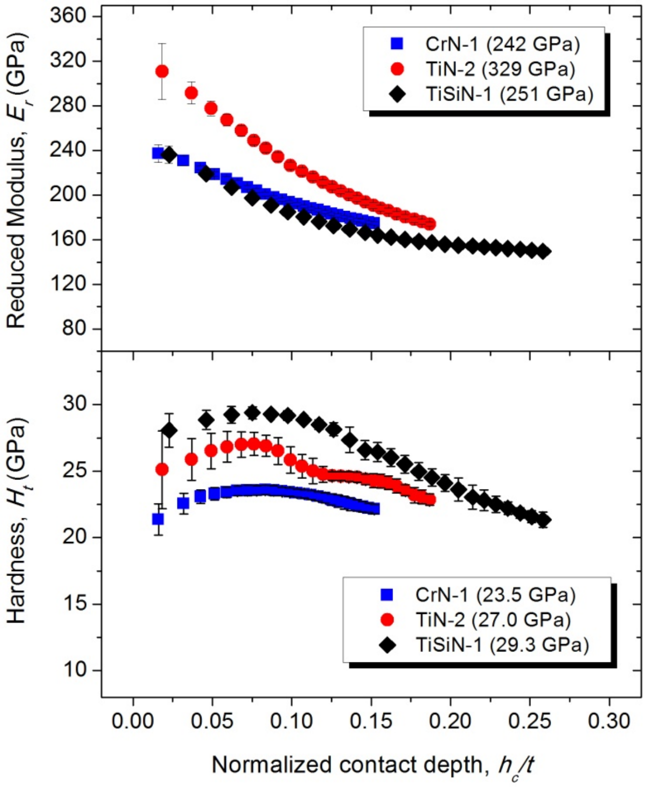

Figure 5.10: H_t and E_r for the three coatings deposited on c-Si as a function of h_c/t.

The K_{IC} of the three coatings, evaluated by cube corner indentation, are plotted in Figure 5.11 as a function of residual indentation depth (h_{res}) divided by t. In all three cases, we can see a significant increase in K_{IC} at smaller indentation depths indicating a marked substrate effect at higher loads. It is also possible that a transition from full half-penny cracking to Palmqvist cracking occurs [209] as the load decreases but a more in depth study would be necessary to differentiate these two effects. We used the plateau portion at lower h_{res}/t to calculate the average K_{IC} values (in parentheses in the legend). However, the TiN-2 coating was not sufficiently thick to generate cracking without substrate effect. On the other hand, from the observed trend we can safely say that K_{IC} is above 4.5 MPa√m. The standard deviation of the evaluated K_{IC} for CrN-1 and TiSiN-1 were respectively 4 and 10% of the average values.

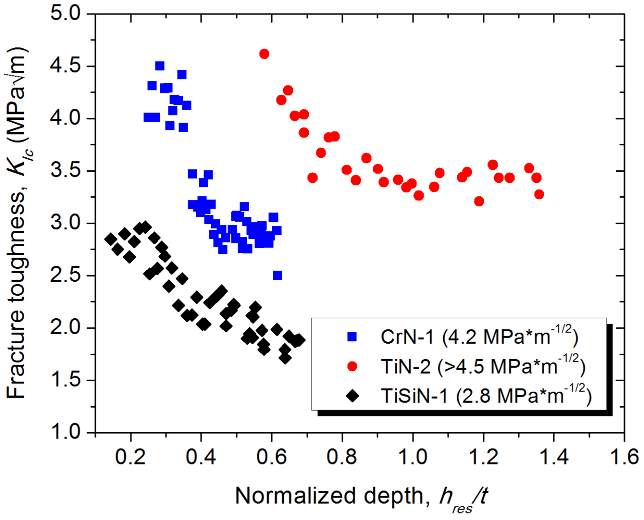

Figure 5.11: K_{IC} for the three coatings deposited on c-Si as a function of h_{res}/t.

5.3.4.2 SPE behavior

In Figure 5.12 (a), we present the SPE test results as a function of V_p for each of the three coatings deposited on c-Si which were tested at five different V_p. The *ER*s are presented in terms of volume loss per particle impact. It can be clearly seen that, regardless of velocity, the *ER*s of CrN-1 are much higher than those of TiN-2 and TiSiN-1 which are quite close. From these results, it seems that the K_{IC} has very little effect on the SPE behavior of these coatings and that H_t is the determining parameter. This is contrary to brittle SPE mechanisms reported in the literature where it is generally accepted that *ER* is inversely proportional to $(K_{IC})^{4/3}$and that H_t has very little effect [65, 66].

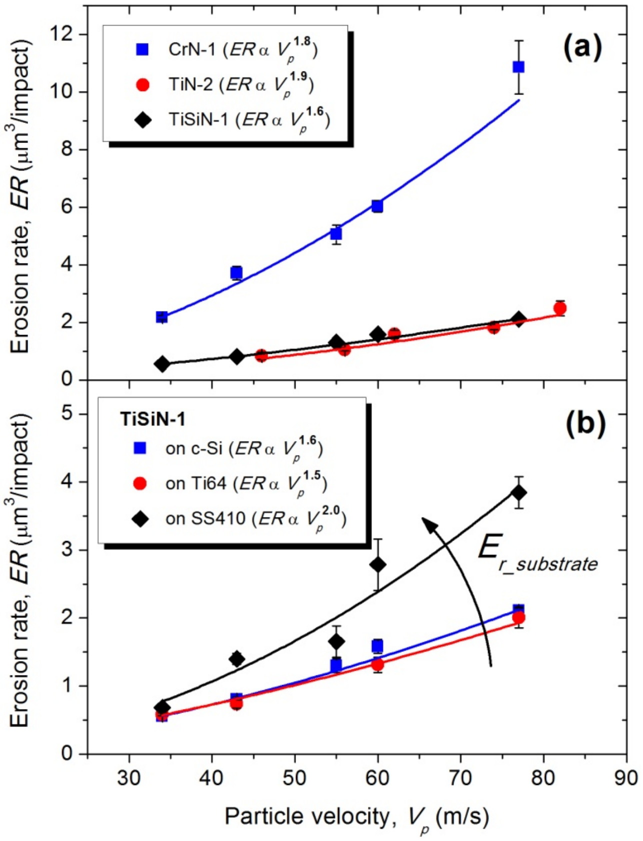

Figure 5.12: *ER* as a function of V_p for (a) the three coatings deposited on c-Si, and (b) TiSiN-1 deposited on various substrates with the substrate E_r trend indicated. The erosion velocity exponents are in parenthesis in each legend.

Although the hardness of TiSiN-1 is nearly 20% higher than that of TiN-2, we do not observe a significant difference in their *ER*s. We believe this to be explained by the lower thickness of the TiSiN-1 coating (6 μm) leading to the substrate influencing the erosion behavior. In fact, Hassani *et al.* [30] have shown by FEM simulation, that coatings with thicknesses below a critical value (8 μm for TiN on a stainless steel substrate) will exhibit enhanced erosion. They also predicted increasing maximum tensile stresses during impact with increasing substrate Young's Modulus [136].

In Figure 5.12 (b), we present SPE test results as a function of V_p of TiSiN-1 deposited on three different substrates. We can clearly see the effect of the substrate on the *ER*s where the coating deposited on SS410 exhibits the highest values. As predicted, the substrate modulus affects the increase of *ER* since Ti64 has the lowest E_r (140 GPa), followed by c-Si (160 GPa) and then SS410 with the highest (220GPa). If *ER* was influenced by the substrate H_t, the coating on Ti64 should show higher rates because the H_t of Ti64 (7 GPa) is significantly lower than that of c-Si (11GPa).

In Figure 5.12, the exponents of the power law function fitting the ER as a function of V_p are presented in parentheses within the legends and are all below 2. These are quite low when compared to theoretical values for brittle mechanisms (2.4 to 3.2) and also when compared to reported experimental values, for hard ceramic materials, which can be much higher (up to 4) due to damage accumulation effects. Although it has been proposed that this exponent can be reduced by a change in particle geometry during impact [77], it does not seem to be the case here. In fact, in Figure 5.13 we show samples of the alumina powder before and after testing on the TiSiN-1 coating at V_p = 60 m/s: One can see that the angular nature of the particles is preserved after impact.

It should be noted that a reduction in mean particle size can be observed for the powder after testing, indicating particle breakup on impact. This breakup could be, in part, a function of impact velocity explaining the low velocity exponents since a greater proportion of the particle KE would be dissipated at higher velocity thus lowering the exponent. However, we do not believe this to be main reason for these low exponents. In fact, the models of erosion by ductile cutting of the surface predict a low exponent of 2 when no contribution from particle rotation is present [53]. In the case of normal particle impact, such as in the SPE tests conducted in this study, particle rotation is not expected to contribute significantly to surface cutting.

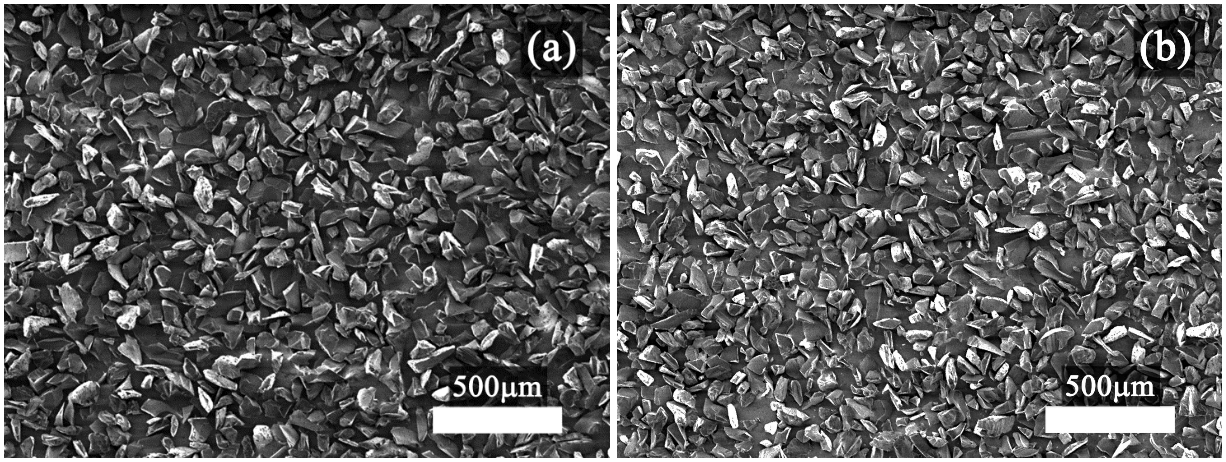

Figure 5.13: Micrographs of the alumina powder before (a) and after (b) SPE testing at V_p = 60 m/s on TiSiN-1 deposited on c-Si.

5.3.4.3 SPE surface morphology

In Figure 5.14, we present SEM micrographs of the surface morphology of the three samples deposited on c-Si in the middle of the wear scar following SPE testing at V_p = 60 m/s. In all three cases, the cumulative damage of many particle impacts can be seen but no signs of brittle material removal or even cracking are present. In fact, only signs of material flow through plastic deformation can be observed. In Figure 5.15 (a) and (b), we present micrographs of single particle impacts on the CrN-1 and TiSiN-1 samples at V_p = 60 m/s. It can be seen quite clearly that elasto-plastic indentation of the surface occurs and that material is displaced forming a lip at the edge of the impact zones. These could then be removed by subsequent impacts. As proposed by Finnie *et al.* [53], as surface roughness develops, the cutting process will reach a steady state and continuous material removal will occur.

Only when V_p was increased could signs of cracking and spalling be observed. In the case of the tougher CrN-1 coating, cracking was observed at 120 m/s (Figure 5.15 (c)) but no chipping could be found. On the other hand, the TiSiN-1 coating with much lower toughness, showed signs of material loss by lateral cracking (Figure 5.15 (d)) at a lower velocity of 100 m/s. This demonstrates that the transition between elasto-plastic and fracture modes of material removal is fairly abrupt. The exact velocity where this transition occurs will depend on material parameters but most notably on the index of brittleness (H_t/K_{IC}) [31] which is highest in the case of the TiSiN-1 coating. Finally, in the case of the tests conducted in this study (V_p < 84 m/s), it seems that the only mechanism of material removal present is plastic cutting, explaining the very low erosion rates, the low velocity exponents and the strong dependence of ER on H_t.

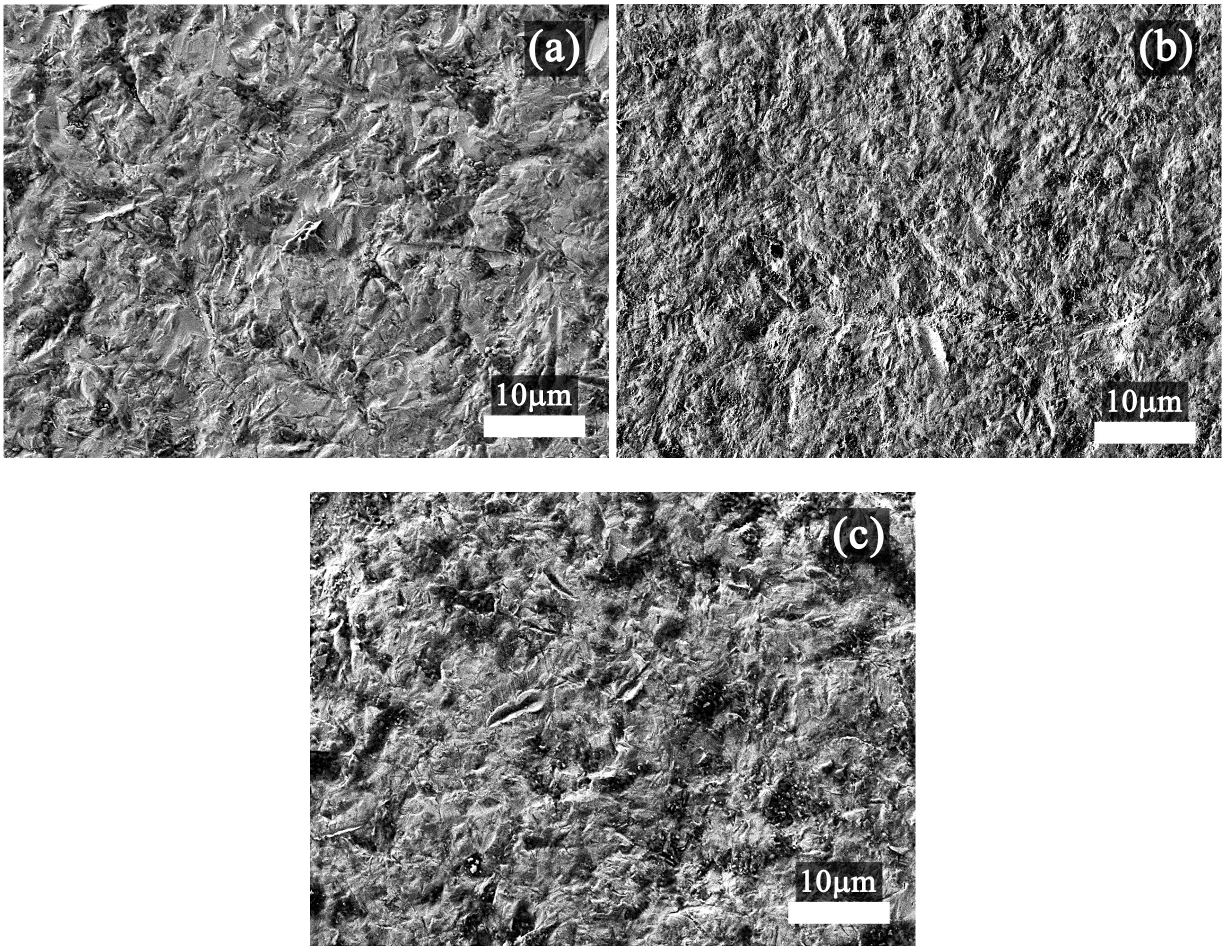

Figure 5.14: Surface morphology in the middle of the wear scar after SPE testing at V_p = 60m/s on (a) CrN, (b) TiN and (c) TiSiN.

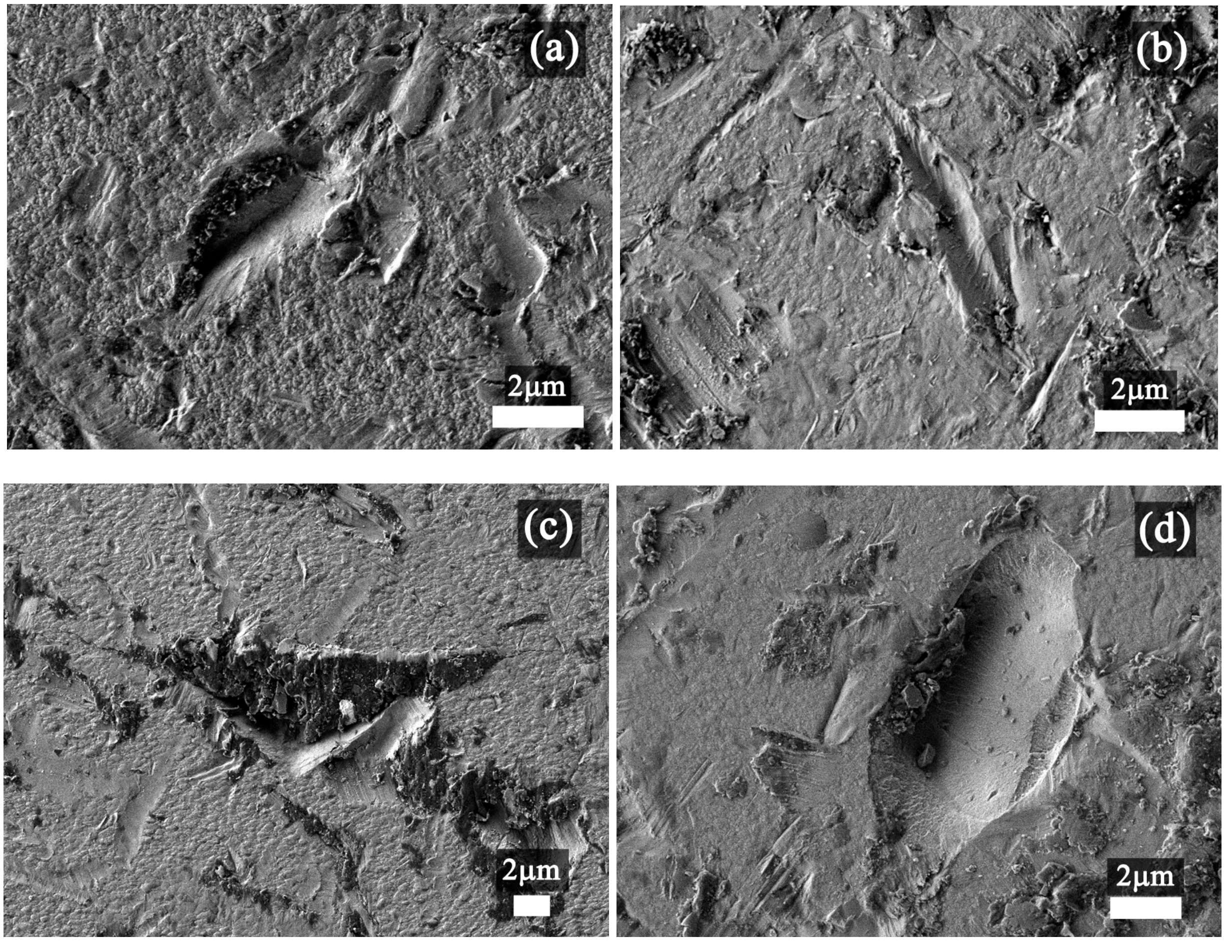

Figure 5.15: Single impact morphology of (a) CrN at V_p = 60 m/s on, (b) TiSiN at V_p = 60 m/s, (c) CrN at V_p = 120 m/s and (d) TiSiN at V_p = 100 m/s.

5.3.5 Particle size distributions

The particle size distribution measurements performed before and after SPE testing at V_p = 60 m/s are presented in Figure 5.16 for three coatings: CrN-1, TiSiN-1 and TiSiN-2. The coatings were chosen because of their wide spread of hardness. It can be observed that the volumetric and surface area distributions shift towards smaller particle sizes after SPE testing, indicating that particle breakup occurs. However, the shift is relatively small with the median particle size of the volumetric distribution shifting from 81 μm to an average of 75 μm for the three coatings. On the other hand, the median particle size decreases as coating hardness increases: 7.0 % decrease for CrN-1 (H_t = 23.3 GPa), 7.3 % for TiSiN-1 (H_t = 29.1 GPa) and 7.8 % for TiSiN-2 (H_t = 35.7 GPa).

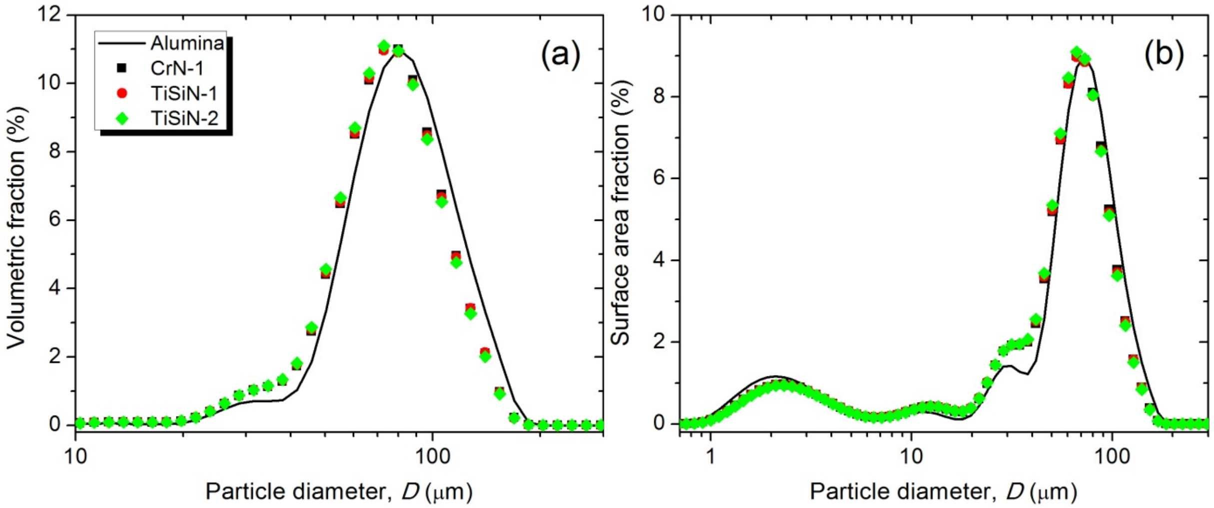

Figure 5.16: Effect of SPE at V_p = 60 m/s on the alumina powder volumetric (a) and surface area (b) distributions.

5.4 General discussion

Several surface parameters have been suggested to affect the SPE performance of coated systems. *H/E* is known to be proportional to the index of plasticity through a linear relationship [25, 205] and has been proposed to control SPE in terms of the transferred energy to the coated surface through the indentation process [73]. In the case of the coatings studied here, the linear relationship between H_t/E_r and R_p is verified (Figure 5.17).

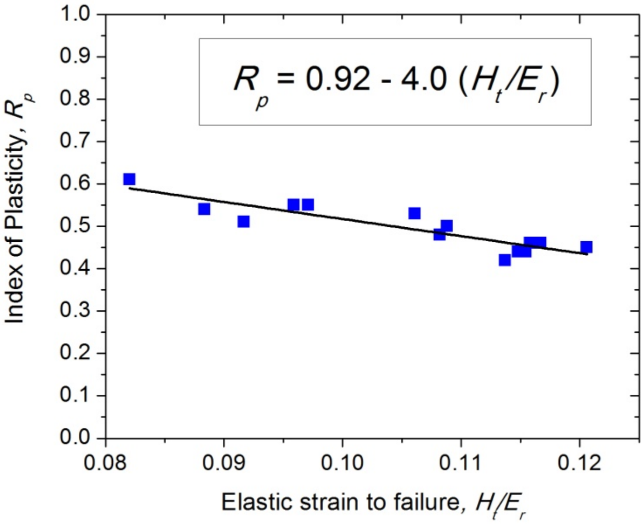

Figure 5.17: R_p as a function of H_t/E_r for all the tested coatings.

Another parameter that has been suggested to influence SPE is H^3/E^2 which is a measure of the material's resistance to the onset of plastic deformation. This parameter has been shown to correlate with various tribological solicitations [19, 28, 29]; particularly, it has been shown by Hassani *et al* [30], through single impact finite element simulations, that the *ER* should increase with a decreasing H^3/E^2.

In order to verify the degree of correlation between the measured erosion rates and the different material parameters (H, H/E and H^3/E^2), we plot the experimental data (using H_t and E_r) and fit a power law function to obtain the coefficient of determination (R^2). As can be seen in Figure 5.18, the only parameter that correlates well with the experimental *ERs* is the surface hardness of the coatings while H_t^3/E_r^2 correlates moderately and H_t/E_r not at all. This result indicates that the erosion behavior of the coatings is strongly influenced by the amount of deformation (related to H_t) caused by particle impact rather than the resistance to plastic deformation or the efficiency of the indentation process ($R_p \propto H_t/E_r$).

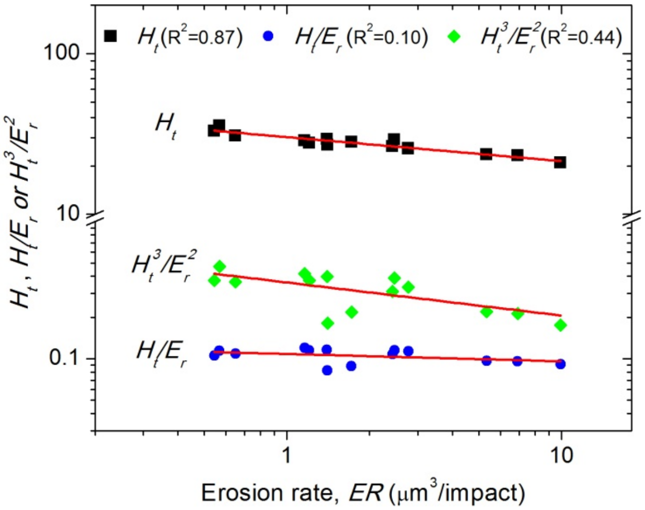

Figure 5.18: Correlation between *ER* and material parameters H, H/E and H^3/E^2.

In Figure 5.19, we present *ER* as a function of H_t for the tests conducted on all the coatings at V_p =60 m/s. The strong effect of H_t on the SPE behavior is represented by the power law function $ER \propto H^{-6.8\pm0.5}$. In the same figure, the H_p/H_t ratio scale is indicated on the top X axis. It can be seen that all the tested coatings have a surface hardness greater than that of the impacting particles (except for CrN-2 which has essentially the same hardness). Several authors have reported a correlation between H_p/H_t and particle breakup or deformation [74, 77, 203]. From the particles size distribution measurements, we did observe that the reduction in median size after SPE was proportional to the increase of surface hardness but, because the change in particle sizes was not very large (between 7.0 and 7.8%), this particle breakup does not seem to be the cause of the large decrease in *ER* with increasing H_t.

It has also been reported that for ceramic materials where $H_p/H_t < 1$ and/or for low velocities, a micro-chipping mechanism was responsible for material loss [12, 31, 81]. However, these studies were conducted on bulk ceramic materials with many protruding crystals that are slowly chipped away by the impacting particles [31, 81]. In the case of our coatings, the surfaces have a mirror like finish prior to erosion meaning that this chipping mechanism cannot occur. In fact, in the case of most coated systems, the micro-chipping mechanism is very unlikely and, to the best of our knowledge, no work has been published on the low velocity erosion mechanisms of these materials. In all our SEM observations of the eroded surfaces, no signs of brittle fracture could be found below V_p = 100 m/s. Actually, the only material loss mechanism that could be observed was by very slow material removal through repeated ductile indentation and cutting of the surface. From a basic analysis of the indentation process, it can be shown that the volume displaced during indentation is proportional to the surface hardness [51]. Therefore, it seems likely that as the hardness of the surface increases and the amount of material displaced decreases, the number of subsequent impacts needed for material removal must then increase significantly. This behavior is the likely reason that the *ER*s decrease to such an extent as H_t increases.

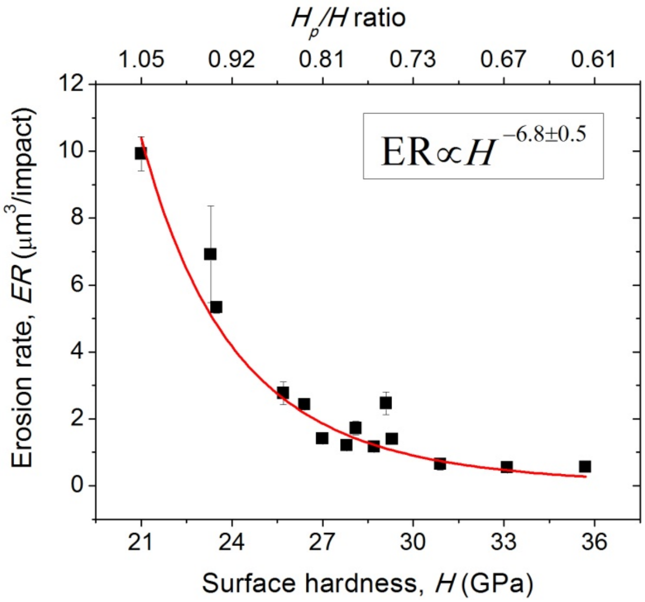

Figure 5.19: *ER* as a function of surface H_t and H_p/H_t.

5.5 Conclusion

In this work, we studied the material loss mechanisms of monolithic coatings subjected to solid particle erosion (SPE) using angular alumina particles with relatively low velocities (below 100m/s). We first validated a new optical profilometry methodology for the accurate measurement of volume loss by scanning the wear scar following SPE testing. We then optimized the testing conditions (V_p, f_r and *WD*) to obtain measured *ERs* free from experimental artefacts. We correlated the measured *ER*s to the mechanical properties, measured by depth sensing indentation, and found that the *ER* was strongly dependent on the hardness of the target materials ($ER \propto H^{-6.8\pm0.5}$). In fact, we found that two nanocomposite coatings, presenting the highest hardness (TiSiN and TiSiCN), offered the best protection against SPE.

From the results of fracture toughness testing, morphological observations of the eroded surfaces and particle size distribution measurements of the powders before and after erosion testing, we found that material removal occurred through repeated ductile indentation and cutting of the surface by impacting particles. Although, particle breakup was proportional to the target hardness, it was not sufficiently large to explain the large drop in *ER*s with increasing H_t. We conclude that as the hardness of the surface increases and the amount of material displaced decreases, a significantly larger number of subsequent impacts is needed for material removal leading to the very strong dependence of erosion rates on target hardness.

5.6 Acknowledgments

The authors gratefully acknowledge the support of the Natural Sciences and Engineering Research Council (NSERC) of Canada, the Consortium for Research and Innovation in Aerospace in Québec (CRIAQ) and the Fonds de recherche du Québec - Nature et Technologies (FQRNT). The authors also wish to thank Francis Turcot for his invaluable technical expertise.

CHAPTER 6 IN SITU REAL-TIME SOLID PARTICLE EROSION TESTING METHODOLOGY FOR HARD PROTECTIVE COATINGS

Article 3: *In Situ* Real-Time Solid Particle Erosion Testing Methodology for Hard Protective Coatings

E. Bousser, L Martinu, J.E. Klemberg-Sapieha*

Department of Engineering Physics, École Polytechnique de Montréal, P.O. Box 6079, Station Centre-ville, Montréal, Québec, Canada H3C 3A7

Abstract

Solid Particle Erosion (SPE) degradation of components in aircraft operating in harsh environments is a well known issue causing severe maintenance and reliability problems. In order to enhance the lifetime of engine components, many different hard protective coatings have been developed and present varying material removal mechanisms depending on their phase constitution and microstructure, and on erodent characteristics. Studying these mechanisms in detail is quite challenging given that SPE testing is notoriously inaccurate due to its aggressive nature and its many methodological uncertainties. In the present work, a novel *in situ* real-time erosion testing methodology has been developed using a quartz crystal microbalance in order to study the SPE of hard protective coating systems. Using conventional mass loss SPE testing, we validate and discuss the advantages and challenges related to such a method. Finally, this time-resolved technique enables us to discuss some transient events present during SPE testing of hard coating systems leading to new insights into the erosion process.

Keywords: Solid Particle Erosion, Coatings, Methodology, *In Situ*, Quartz-Crystal Microbalance (QCM).

* Corresponding author: tel.: +514-340-5747, fax: +514-340-3218

Email: jsapieha@polymtl.ca

6.1 Introduction

Solid particle erosion (SPE) is an abrasive mode of material removal that occurs when hard particles, entrained by a fluid, impact surfaces of components in applications such as aircraft engines, wind turbines or power generation gas turbines. This type of wear can be very severe and a greater understanding of its related mechanisms is needed in order to protect surfaces with the appropriate hard coating systems. However, a lack of precision in experimental methods of evaluating erosion rates (*ER*s) severely limits the understanding of these material loss mechanisms.

SPE is generally defined as the volume loss divided by the mass of particles that have impacted the surface [164]. In most cases, it is the mass loss that is reported since it is much easier to measure the sample's mass before and after testing rather than to measure the actual volume loss. If the density of the target is known, the volume loss can also be reported. However, several difficulties arise in the case of SPE testing of coatings: (i) the density of the coatings is generally not accurately known and, (ii) the coating must be eroded to a significant depth of its total thickness for the material removal to be measurable by a mass loss evaluation. This results in the acquisition of an average *ER* with no information on transient events and, because the coating must not be pierced during testing in order to evaluate its intrinsic erosion resistance, very low mass losses will be encountered. For this last reason, a large variability, leading to a significant uncertainty, is encountered in the evaluation of the SPE of coatings.

Previously, in order to gain insight into the transient behavior of materials under SPE, work has been done at the Cavendish Laboratory to develop an electro-mechanical oscillator type mass loss measurement tool for *in situ* SPE testing [210, 211]. However, the thermal stability of the apparatus and the effect of particle adherence during testing significantly reduced the mass loss measurement precision making this technique unusable for highly resistant materials [211].

Quartz crystal microbalances (QCMs) have been used for the last 50 years in coating systems for very precise mass deposition rate monitoring [212]. More recently, QCMs have been applied in a wide range of fields such as dust and water vapor detectors in a Martian atmosphere [213], the study of fine particle microcontacts [214], etch rate monitoring of polymer films [215], erosion and redeposition in a JET divertor [216], and many more. While the analytical balances typically used for SPE laboratory testing have readabilities as small as 10^{-6} g, a QCM can readily detect mass changes of 10^{-9} g and as little as 10^{-13} g [212]. It is because of this very high sensitivity to mass changes that we develop in the present work a methodology for the use of coated QCM resonators in the study of SPE mechanisms of hard monolithic and multilayer coatings. Comparing the results obtained with this new method to those obtained by conventional mass loss measurements, we will show the validity of the technique in the evaluation of coating SPE rates. The high resolution *in situ* measurements will also enable us to study transient events in the erosion of hard multilayer coatings.

6.2 Experimental methodology

6.2.1 Coating deposition

The coatings in this study were deposited on single crystal silicon (c-Si) as well as on QCM substrates by reactive pulsed DC magnetron sputtering (PDCMS) from a chromium target. The base pressure of the reactor, described in detail in [11] was below 1 x 10^{-6} Torr. Prior to deposition, the single crystal silicon substrates were cleaned in acetone and isopropanol in an ultrasonic bath while the QCMs were inserted directly into the deposition chamber. In order to remove the surface oxide layer of the c-Si and the exposed gold electrode from the QCM, the substrate surface was sputter cleaned in a capacitively coupled radio-frequency (RF) Ar plasma for 5 min at a pressure of 5 mTorr and a negative bias (V_b) of -600V. During deposition, no heating source was used. The samples were only heated by the sputtering process and by the ion bombardment from the RF biased electrode (V_b = -50V).

A chromium adhesion layer was first deposited, followed by monolithic CrN or multilayer Cr/CrN coatings. During the CrN deposition, the N_2 and Ar flows were 10 and 15 sccm respectively, and the total pressure during the deposition was kept constant at 5 mTorr. When depositing Cr, the N_2 flow was interrupted, and the total pressure was maintained at 5 mTorr. During deposition of the multilayer coating, Cr and CrN layers were alternately deposited for the same period of time, starting with Cr and finishing with CrN after five iterations. The top CrN layer was deposited for twice the time compared to all the other layers.

6.2.2 Microstructural and mechanical characterization

The coating thickness (*t*) were determined by scanning electron microscopy (SEM, Jeol JSM7600F) from cleaved QCM and c-Si samples. In order to precisely evaluate the microstructure of the multilayer CrN/Cr sample, cross-sections were cut by focused ion beam (FIB) milling into the coating before and after SPE testing. The trench produced by FIB enabled us to observe the microstructure by SEM at an angle of 30 degrees, which means that the real dimensions are double of those on the micrographs.

The elasto-plastic properties (Hardness (*H*) and reduced Young's modulus (E_r)) were determined by a depth-sensing indentation instrument (Hysitron Inc. Triboindenter) equipped with a Berkovich pyramidal tip. In order to evaluate the elasto-plastic properties as a function of depth and extract the surface properties following the methodology proposed in the ISO standard 14577-4 [195], indentation loads from 1 to 1000 mN were used. Load-displacement plots were analyzed according to the Oliver-Pharr methodology [193]. Before testing, the tip geometry and system compliance were calibrated using a fused quartz standard sample, and, before each indentation, the thermal drift was measured (typically less than 0.1 nm/s) and compensated for.

The shear modulus of each coating was calculated using

$$\mu = \frac{E}{2(1+\upsilon)}, \tag{6.1}$$

where v is the coating Poisson's coefficient (for simplicity, 0.2 was used for all coatings), and E was calculated using:

$$\frac{1}{E_r} = \frac{1-\nu^2}{E} + \frac{1-\nu_i^2}{E_i}, \tag{6.2}$$

where E_r is the reduced modulus evaluated by depth-sensing indentation, E_i is the Young's modulus of diamond (1140 GPa), and v_i is the Poisson's coefficient of diamond (0.07). The properties of the coatings are presented in Table 6.1.

Table 6.1: Mechanical and microstructural properties of the tested coatings.

	Hardness H (GPa)	Young's Modulus E (GPa)	Shear Modulus μ (GPa)	Thickness t (µm)	Density ρ (g/cm^3/)
Monolithic CrN	19.7	290	121	6.1	5.5
Multilayer CrN/Cr	20.6	251	105	10.1	5.9

6.2.3 SPE testing methodology

The SPE testing, based on the ASTM G76 standard [164], was conducted in an in-house gas-blast erosion system using alumina powder with a median size of 70 µm. The particle velocity (V_p) was varied by adjusting the back pressure of an abrasive blasting unit (S.S. White Airbrasive unit) and was calibrated using a double disk time-of-flight technique [166]. The whole unit was mounted on a 30 kg capacity balance precise to 0.1 g (Sartorius LE29000) in order to closely monitor the particle feed during each test.

Two types of SPE tests were conducted. The first one was the conventional test method where the mass of sample was measured before and after testing using an analytical balance (Sartorius LE225D) precise to 0.01 mg. During each test, the sample was exposed to the particle flow for a precise mass of particles (Δm_p) and the mass loss (Δm) of the sample was recorded. For each testing condition, this was repeated a minimum of three times in order to evaluate the experimental error of the measurement.

The second type of method utilized 5.98 MHz QCM samples (PBG Milano) where the mass loss per surface area was recorded *in situ* using the frequency output from a thin film deposition rate monitor (Sycon STM-100). The data acquisition was performed through a PC using LabView software and collected the QCM natural frequency (f) and the incremental projected mass of particles (m_{pi}) leaving the feed unit. We then calculated the incremental mass loss per unit of surface area (m_L), the mass loss rate per unit of surface area ($\dot{m}_L$) using the frequency output, and the particle mass feed rate ($\dot{m}_p$) using the particle mass output as a function of time. In all cases, except during the mask calibration tests, the samples were masked in the QCM holder (Figure 6.1).

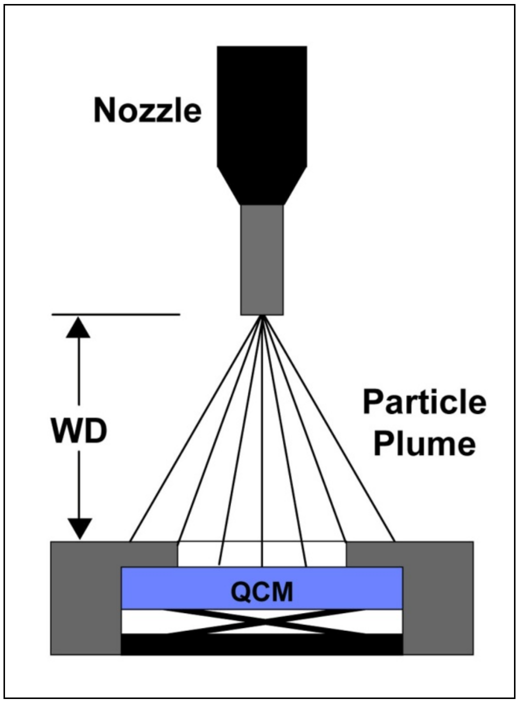

Figure 6.1: SPE velocity exponent as a function of yield pressure.

The particle feed rate was controlled by adjusting the unit's shaker amplitude and the back pressure. In order to stabilize the feed rate to 0.7±0.2 g/min prior to each test, the sand-blast unit was turned on for several minutes, while the sample was shielded by a retractable shutter. The data acquired through the *in situ* measurement permitted accurate evaluation of the feed rate prior to testing. All tests were performed with the particle flow impacting the surface at normal incidence.

Because the QCM tests yield the frequency shift caused by the average mass loss over the entire active surface area of the crystal, it is important to obtain a uniform wear scar. In order to achieve this, we use a short tungsten carbide nozzle (inner diameter of 1.14 mm and length of 9 mm) resulting in a divergent particle flow and a working distance (*WD*) of 100 mm. In Figure 6.2, we present the wear scars of uncoated c-Si samples after exposure to 15 g of particles with V_p = 43 m/s and *WD* from 80 to 110 mm.

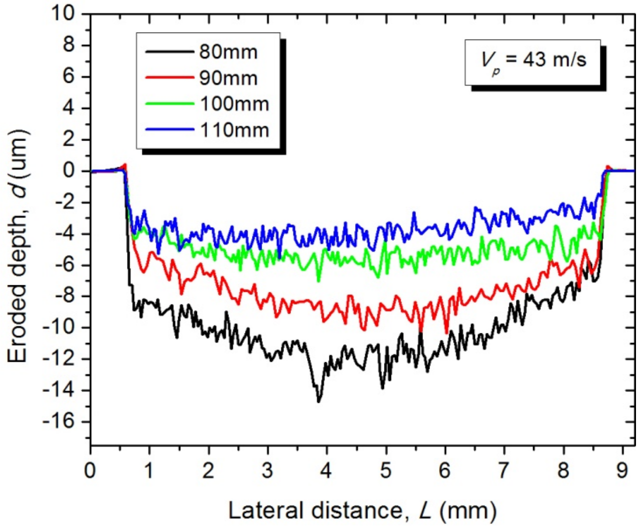

Figure 6.2: Effect of *WD* on wear scar uniformity.

Because the samples are partially masked in the QCM holder, only part of the powder flow will impact the sample and cause material loss. Thus, an evaluation of the fraction of the particle flow penetrating the mask was accomplished by conventional mass loss measurements using c-Si. *ER*s of unmasked samples were measured on 50 mm x 50 mm specimens at five different particle velocities (35 to 85 m/s). Then, 9 mm x 9 mm specimens were tested at the same velocities while placed in the QCM holder leaving only a circular area exposed to the flow of particles (*AE*) of 8 mm in diameter. If the mass loss per particle impact of c-Si is considered to be constant regardless of sample masking, the only difference between the two tests is the amount of particles penetrating the mask orifice and contributing to mass loss. Figure 6.3 plots both masked and unmasked *ER*s as well as the particle penetration ratio (*PR*) between the two (Figure 6.3 inset). We find that on average approximately 30 % of the total particle mass penetrates the QCM holder opening and contributes to sample erosion.

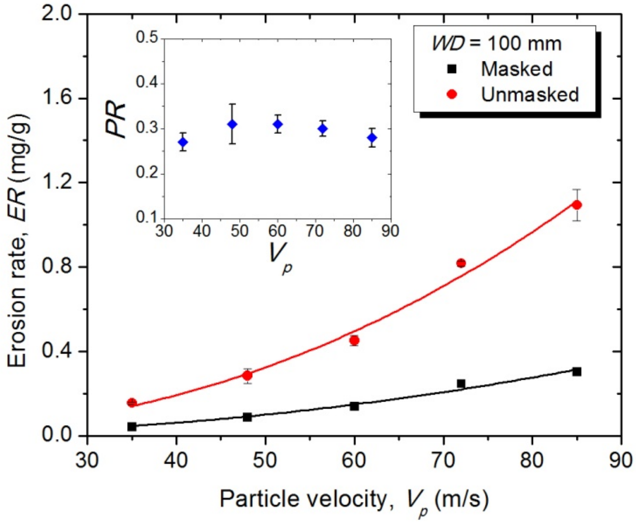

Figure 6.3: Effect of sample masking by the QCM holder on *ER* of c-Si as a function of V_p. The inset presents the percentage of particles penetrating the mask as a function of V_p.

Consequently, *ER* for the conventional testing technique can be calculated from,

$$ER_{conv} = \frac{\Delta m}{\Delta m_p} \frac{1}{PR \cdot AE} \quad \left[\frac{\mu g}{g \cdot cm^2} \right]. \tag{6.3}$$

In the case of the QCM testing technique, the *ER* could be evaluated by differentiating the m_L as a function of m_{pi}. However, we found it more accurate to evaluate $\dot{m}_L$ and to use an average $\dot{m}_p$ to evaluate the *ER* because of the relatively high readability (0.1 g) of the balance used for particle mass measurements. Therefore, *ER* for the *in situ* technique can be calculated from

$$ER_{QCM} = \frac{\dot{m}_L}{\dot{m}_p} \frac{1}{PR} \quad \left[\frac{\mu g}{g \cdot cm^2} \right]. \tag{6.4}$$

6.3 Results and discussion

In this section, we present the results and analysis of the *in situ* real-time SPE measurements while focusing on three groups of experiments. First, we show the effects of the pressurized air flow on the QCM resonator frequency response. In the second part, the validation of the *in situ* technique will be presented through SPE tests conducted on uncoated and CrN coated QCM samples and compared to conventional mass loss SPE results. Finally, the high precision capabilities of the novel technique will be illustrated through a detailed SPE and microstructural study of a 10 layer Cr/CrN multilayer coating.

6.3.1 Air pressure effect

In order to verify the effect of the pressurized air flow used to accelerate the particles in gas-blast SPE testing, we projected air with varying pressures (34.5 to 172.4 kPa) onto the QCM surface while monitoring the crystal's natural frequency. In Figure 6.4, we present the frequency shift (FS) as a function of time. It can be clearly seen that the effect on the QCM is constant regardless of air pressure. For all five pressures, the drop in natural frequency was always around 10 Hz when the shutter was opened and it then recovered by about 30%. Because FS is independent of air pressure, this drop cannot be a result of crystal loading but, rather, could be caused by a slight change in QCM temperature when exposed to the air flow. In fact, at the end of the test (27 min), we interrupted the spot light that was pointed onto the QCM surface and a much greater FS (approximately 40 Hz) was observed. This seems to confirm our hypothesis that the crystal's natural frequency is dependent on temperature.

Although, sudden jumps in frequency can easily be accounted for during analysis, the thermal drift of QCM natural frequency has been observed by several authors [217, 218] and needs to be compensated for. Because we conducted all our testing at room temperature, the thermal drift of the system will be negligible when compared to the FS caused by mass loss during SPE tests. In fact, the FS rate during testing was found to be between 2.5 and 10 Hz/s and the minimum total shift for a test at the lowest particle velocity was more than 300 Hz. However, all pressure changes were adjusted when the shutter was closed so as to not affect the mass loss measurements, and we maintained all possible thermal inputs constant during testing.

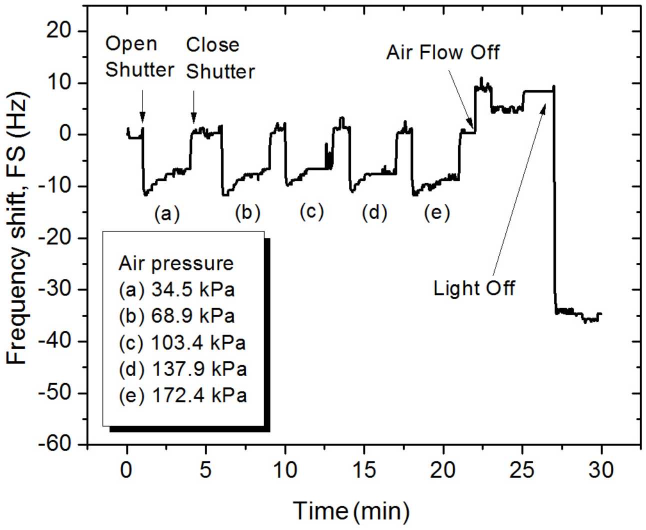

Figure 6.4: QCM natural frequency variation as a function of air pressure and illumination.

6.3.2 In situ SPE testing of uncoated QCM samples

In order to validate the methodology, we conducted SPE tests directly on uncoated QCM crystals using both the conventional and the *in situ* techniques. In order to evaluate the SPE behavior as a function of V_p, we tested the samples by the conventional method using four particle velocities (V_p between 24 and 49 m/s) and by the *in situ* method using seven particle velocities (V_p between 21 and 50 m/s).

Before testing using the *in situ* technique, the QCM gold electrode, left uncovered by the mask, was removed by exposing the samples to a 35 m/s particle flow for one minute. After surface conditioning, the shutter between the nozzle and the sample was closed, and the back pressure was then adjusted to obtain the desired V_p. After letting the flow and feed rates stabilize for two minutes, the shutter was re-opened and the sample was exposed to the flow for a fixed amount of time. This exposure time depended on V_p but was typically between one and two minutes. During the period between the subsequent velocity increase steps, the shutter was closed and the particle feed rate was readjusted and left to stabilize for one to two minutes. In order to obtain the *ER* at the seven different velocities, two QCMs were used and the conventional testing was done on these same samples after the *in situ* testing had been completed.

The mass loss was calculated from the frequency output using the Sauerbrey equation [182], which relates m_L in [g/cm^2] to the observed change in oscillation frequency of the crystal (Δf in [Hz]).

$$m_L = -\frac{\Delta f \cdot N_q \cdot \rho_q}{f_o^{\,2}} \tag{6.5}$$

where,

N_q is the frequency constant for the AT-cut quartz crystal (1.668X10^5 Hz*cm),

ρ_q is the density of quartz (2.648 g/cm^3), and

f_o is the fundamental resonant frequency of the crystal in Hz (we used the frequency of the crystal prior to testing).

In Figure 6.5, we show a typical curve of m_L as a function of particle mass impacting the exposed surface of the QCM ($m_p^* = PR \times m_{pi}$). From this figure, we can see that the slope increases as V_p is increased (segments a to e). During the last segment, the mass loss increases at a catastrophic rate, rapidly leading to crystal failure. Using equations 6.1 and 6.2, we calculated the *ER*s using both techniques. The results are presented in Figure 6.6. We can see close agreement between both techniques although the *in situ ER*s are slightly higher, that could be explained by an incomplete removal of the QCM gold electrode during surface conditioning. The exponents of the power law dependence fitting the *ER* as a function of V_p are presented in parentheses within the legend of each graph. These exponents (2.6 and 2.9 in this test) are also in good agreement and correspond well to the theoretical values (2.4 to 3.2) found when a brittle material removal mechanism is present [65, 66].

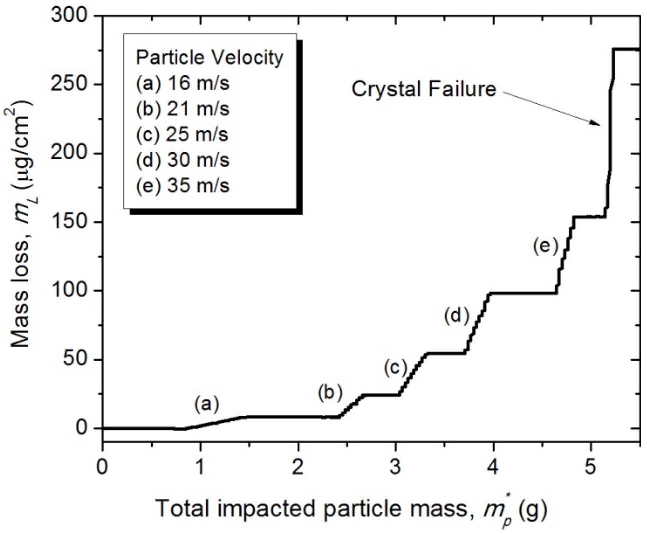

Figure 6.5: Typical uncoated QCM sample mass loss as a function of total particle mass impacting the surface.

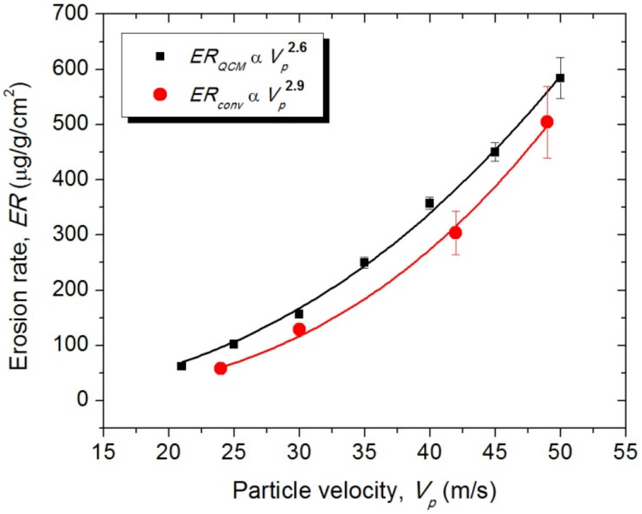

Figure 6.6: Uncoated QCM SPE rates measured by the *in situ* and conventional techniques.

6.3.3 In situ SPE evaluation of single and multilayer coatings

The Sauerbrey equation can only be used for very thin films since it does not take into account the change in elastic properties caused by the deposited film. For thick films such as those studied here, the effect of the coating elasticity on the system's acoustic impedance must be taken into account. Therefore, the mass change of the coated samples was calculated from the Z-Match method proposed by Lu and Lewis [183] which relates m_L to the observed change in oscillation frequency through:

$$m_L = \left[\frac{N_q \rho_q}{\pi Z_f f_L}\right] \tan^{-1}\left[Z_f \tan\left(\frac{\pi(f_u - f_L)}{f_u}\right)\right] ; \qquad (6.6)$$

where

f_u is the unloaded natural frequency in Hz, f_L is the loaded natural frequency in Hz, and

$Z_f = \left[\frac{\rho_q \mu_q}{\rho_f \mu_f}\right]^{1/2}$ is the Z-Factor of the film; μ and ρ are the shear modulus and density of the quartz (index *q*) and of the film (index *f*).

In order to apply equation 6.6, we first need to evaluate the density of the coating. If we consider that the coating is uniformly deposited on the entire surface of the QCM crystal, then ρ_f can be found from equation 6.6 because,

$$\rho_f = \frac{m_o}{t} ; \qquad (6.7)$$

where *t* is the coating thickness and m_o is the total coating mass per unit surface area before SPE testing. Using SEM micrographs, such as the one presented in Figure 6.7, we find for the monolithic CrN coating of $t = 6.1$ μm a density of 5.5 g/cm^3. This value is below the theoretical value of 5.9 g/cm^3 but that is to be expected given the possible porosity of the coating. As a result, using this density and equation 6.6, we can calculate m_L for each data acquisition increment by subtracting the calculated coating mass per surface area from the one calculated in the previous increment (starting with m_o). In Figure 6.8, we present the m_L as a function of m_p^* for the CrN monolithic coating eroded at eight different velocities. As in the uncoated QCM tests, the shutter was closed between each V_p increase step.

In Figure 6.8 (b), we highlight the beginning of the test during which a mass increase can be observed. This phenomenon is systematically observed at the outset of every *in situ* test and is believed to be caused by the electro-static sticking of smaller particles to the QCM surface. During this running-in period, coating m_L and particle sticking vary until a steady state regime is reached after which the *in situ ER* can be evaluated. As the velocity is increased (from 35 to 40 m/s) a rapid mass loss can be observed before quickly reaching a steady state once again. This seems to occur because the higher air pressure removes a certain quantity of the adhering particles from the QCM surface. In addition, the mass gain could be in part caused by particle embedding, but the sudden m_L and the rapid transition to a steady state regime under increased air pressure indicate that particle adhesion is the dominating cause. In should be noted that, from tests we conducted on ductile coatings, the embedding can become a dominating factor making SPE testing very difficult.

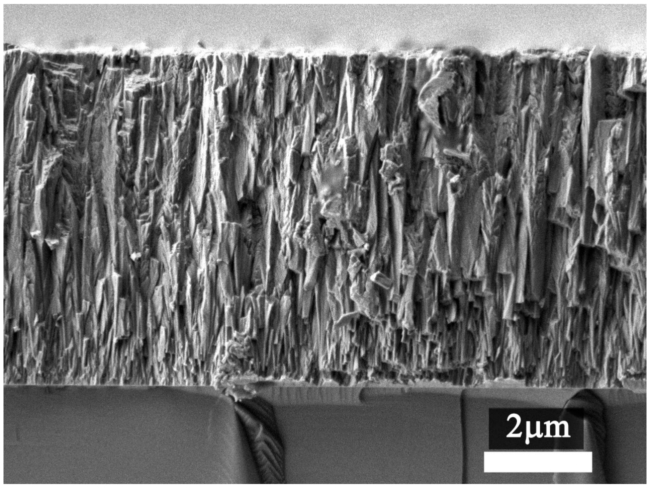

Figure 6.7: Cross-sectional SEM micrograph of the CrN monolithic coating.

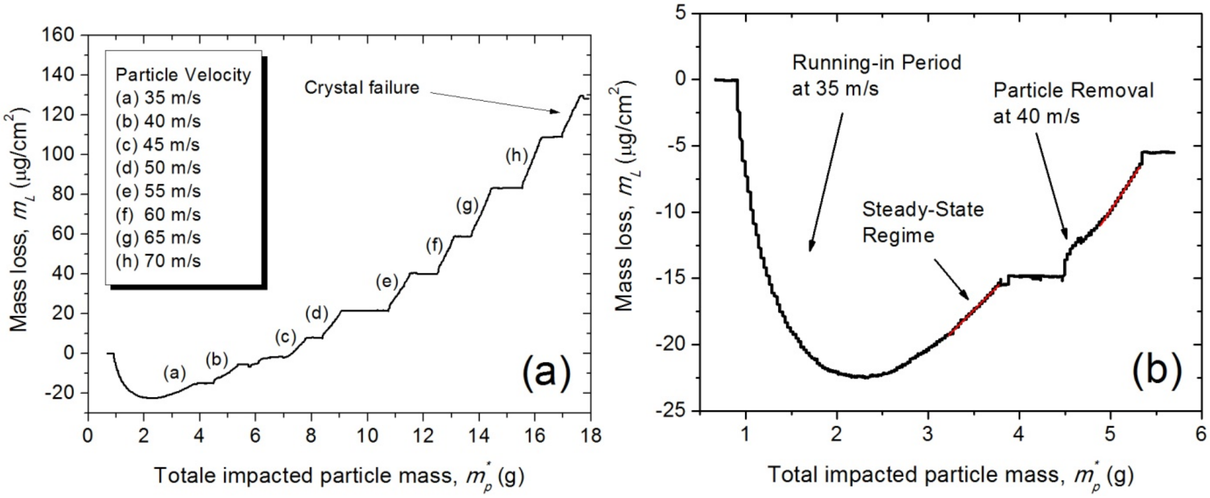

Figure 6.8: Mass loss as a function of total particle mass impacting the surface for the CrN monolithic coating: (a) complete curve and (b) detail of the beginning of the test.

In Figure 6.9, we present the *ER*s of the monolithic CrN coating tested at eight velocities using the *in situ* technique, and at three velocities using the conventional mass loss technique. Similarly to the uncoated QCM tests, we obtain good agreement between the CrN *ER*s produced by both techniques. In this case, there is an even better agreement between the *ER* magnitudes but a larger difference between the velocity exponents. This discrepancy probably resides in the large error associated with high velocity conventional SPE testing where the very small m_L value is close to the readability of the analytical balance. These small m_L values occur because of the very short duration of the tests, necessary to avoid the coating from being pierced.

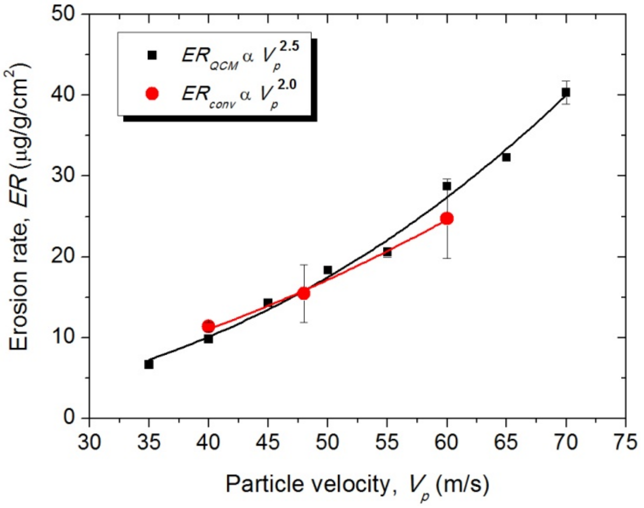

Figure 6.9: Monolithic CrN SPE rates measured by the *in situ* and conventional techniques.

6.3.4 Transient effects in SPE of multilayer coatings

In order to study the effect of a multilayer coating structure on SPE behavior, we tested a Cr/CrN multilayer coating with the *in situ* technique at a constant velocity of 60 m/s. The same methodology described in the previous section was used to measure the time-resolved m_L applied to a film with a total thickness of t = 10.1 μm. The FIB milled cross-section of the 10 layer coating before erosion is shown in Figure 6.10 (a). Specifically, the average thickness of the Cr layers was 0.93 μm, thickness of the CrN layers was 0.90 μm, and the top CrN layer was 1.5 μm thick. Using t and equation 6.6, the resulting average coating density was 5.9 g/cm^3.

In Figure 6.11 (a), the evaluated m_L is presented as a function of m_p^*. Because of the coating architecture with alternating layers, the *ER* was calculated by differentiating the m_L vs. m_p^* plot rather than using steady state rates as previously discussed. The *ER* as a function of m_p^* is presented in Figure 6.11 (b).

From Figure 6.11 (b), we can clearly see the oscillatory nature of the *ER* as the different layers of the coating are worn away. To the best of our knowledge, this type of behavior has not yet been reported, and it demonstrates the high degree of precision and capability of the *in situ* technique. In fact, from the two complete oscillations that can be seen, we deduced that four layers had been eroded by the end of the test. This is confirmed in Figure 6.10 (b) where the FIB milled cross-section reveals that there are six complete layers remaining after testing. Interestingly, using equation 6.7 and the average coating density, we find from the *in situ* data that the remaining coating thickness should be 6.9 μm and not 6.3 μm as measured from Figure 6.10 (b). This difference is attributed to the amount of debris remaining on the surface in the form of displaced material as can be clearly seen at the top of Figure 6.10 (b) and in Figure 6.10 (c) where the top view of the eroded surface is shown. The roughened surface of the eroded sample can clearly be seen to be the result of material mixing through multiple particle impacts. Finally, the average *ER* of the coating was confirmed by conventional testing and it agrees very well with the *in situ* data presented in Figure 6.11 (b).

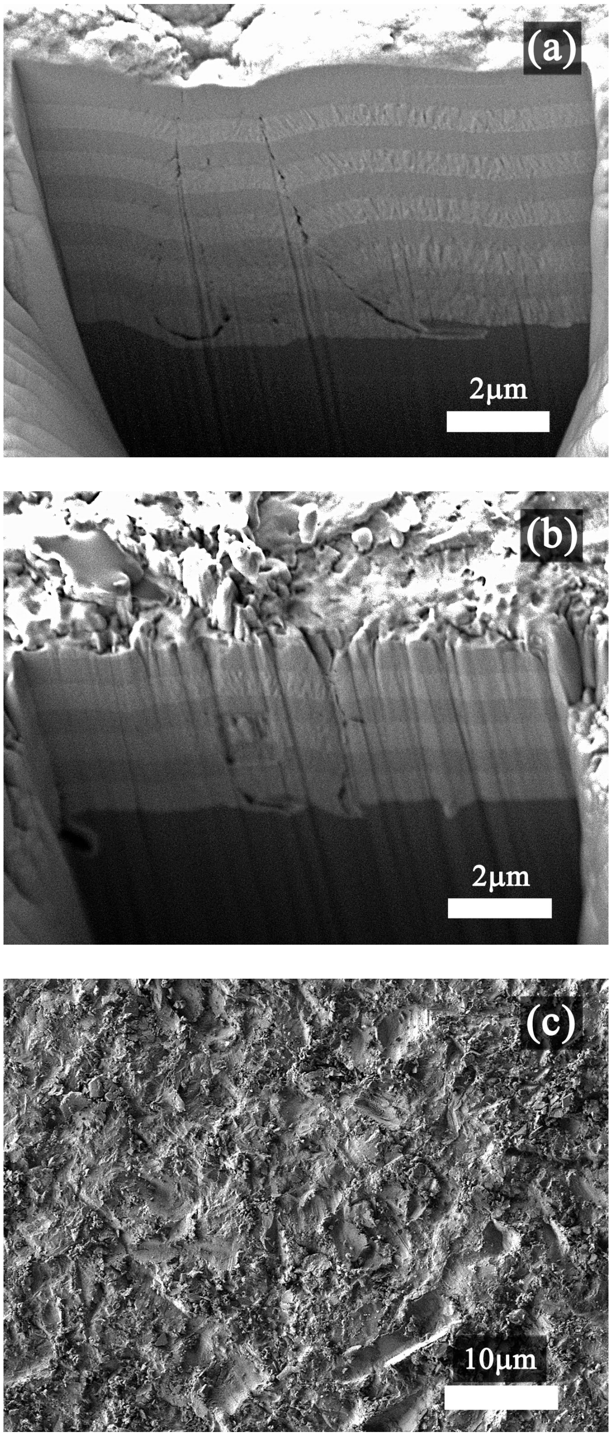

Figure 6.10: SEM micrographs of the Cr/CrN multilayer coating: (a) cross-section prepared by FIB of coating before *in situ* testing, (a) cross-section prepared by FIB of coating after *in situ* testing, and (c) surface of coating after *in situ* testing.

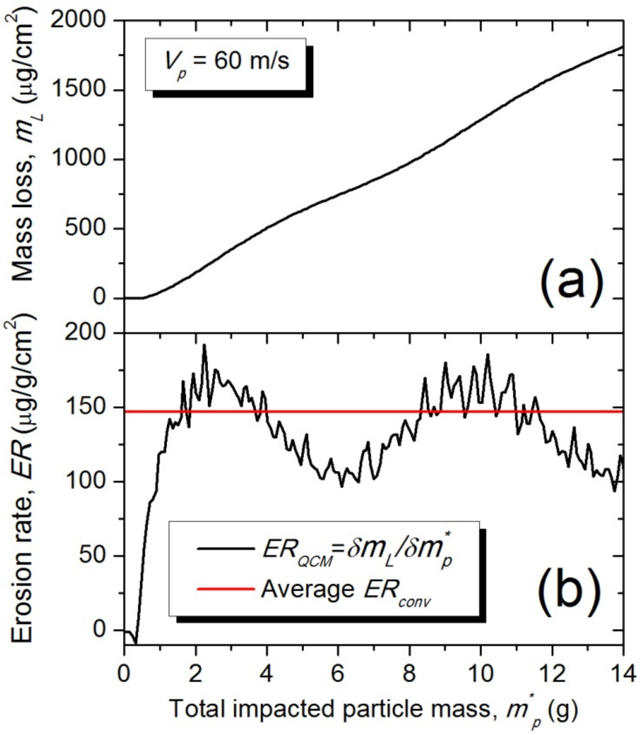

Figure 6.11: SPE of a CrN/Cr multilayer coating: (a) m_L vs. m_p^*, and (b) ER vs. m_p^*.

6.4 Conclusion

Studying the SPE behavior and mechanisms of coatings can be quite challenging, given that conventional testing is notoriously inaccurate due to its aggressive nature and its many methodological uncertainties. In this work, we presented the development of a novel *in situ* real-time testing methodology for the evaluation of coating SPE. This new approach uses coated QCM resonators in order to acquire, in a time-resolved manner, the mass loss of hard protective coating systems during SPE testing. Using conventional mass loss SPE, we validated the *in situ* SPE methodology for uncoated QCM samples and monolithic hard coatings, and found close agreement between both techniques. We then used the *in situ* approach to investigate the SPE behavior of a Cr/CrN multilayer coating revealing a never before reported oscillatory behavior of the *ER* during erosion. From these results, we have demonstrated that this high precision time-resolved method can be used to gain new insights into the erosion process of complex coating systems.

6.5 Acknowledgments

The authors gratefully acknowledge the support of the Fonds de recherche du Québec - Nature et Technologies (FQRNT) through its grant awarded to the Regroupement Québecois sur les Matériaux de Pointe (RQMP), the Consortium for Research and Innovation in Aerospace in Québec (CRIAQ) and the Natural Sciences and Engineering Research Council (NSERC) of Canada. The authors also wish to thank Francis Turcot for his invaluable technical expertise and Dr. Thomas Schmitt for numerous insightful discussions.

CONCLUSIONS, GENERAL DISCUSSION AND OUTLOOK

The design of the appropriate material system for a given tribological solicitation must be guided by an accurate understanding of the degradation mechanisms and the surface response to loading and deformation. In the case of this thesis, the focus was put on surface wear by solid particle erosion (SPE) that can occur when aircraft operate in harsh environments where hard particulate matter is entrained by the air flow into the operating engine. In fact, this type of damage is most prominent in the first stage of the aircraft engine, where the compressor blades can be eroded to such an extent that aerodynamic performance and even structural integrity are compromised.

Much work has been conducted to develop protective approaches to increase component lifetimes. One such technology is the use of hard protective coatings to impede the erosion of the predominantly metallic engine components. However, in order to select the appropriate coating system, the material loss mechanisms must be properly understood.

In the first place, the metallic surfaces to be protected erode in a predominantly plastic mode of material removal through micro-cutting or ploughing mechanisms. On the contrary, the hard ceramic protective coatings are brittle in nature and will present much more complex erosion behaviors. In fact, brittle materials exhibit surface removal mechanisms very similar to those encountered during indentation such as elastic Hertzian cracks under large rounded particle impact and elasto-plastic deformation and fracture for sharp particle impacts. Transitions between these mechanisms occur depending on the coatings' corresponding elastic, plastic and fracture properties and on the fragmentation of the erodent particles upon impact.

Many different coating systems have been proposed for protection against SPE. Multilayer systems have been used because their multilayer design offers the possibility of depositing thicker coatings by relaxing residual stresses and enhancing erosion resistance through the crack tip blunting effect of the ductile layers and the deflection of cracks at interfaces. On the other hand, monolithic coatings are more durable under SPE by small, hard and angular particles because the damage is generally confined to a small volume in the top layer and therefore, the ductile interlayers of the multilayer coating would not be beneficial to erosion resistance.

The SPE resistance of monolithic coatings can be enhanced by using materials with high toughness to prevent crack growth, and high hardness to inhibit crack initiation by dissipating the particle kinetic energy through fragmentation and minimizing the penetration of the particle on impact. However, while it has been observed that hard monolithic coatings exhibit the different brittle fracture modes when impacted by large and/or highly energetic particles, a review of the literature has revealed that no description has been proposed for the mechanism of material loss when erosion by small angular particles with relatively low velocities (< 100m/s) occurs.

It was in this context that this doctoral project was undertaken and in a first step a preliminary study was accomplished on the effect of the addition of silicon (Si) on the microstructure, mechanical properties and, more specifically, on the SPE resistance of thick CrN-based coatings. It was found that the addition of Si significantly improved the erosion resistance and that the SPE results showed a very strong dependence on the surface hardness. These findings led to three interrogations which form the backbone of this thesis: i) what is the material loss mechanism of hard protective coatings during erosion; ii) what is the role of toughness on the erosion mechanism; and iii) what is the role of particle properties on the strong dependence of ER on the hardness of the target material?

Based on these preliminary results, the main objective of this PhD project was to investigate the material loss mechanisms during SPE of hard protective coatings using angular particles at relatively low velocities (below 100 m/s). In order to accomplish this main goal, we aimed to (i) develop a robust methodology for the SPE characterization of coated systems; (ii) investigate the effects of particle properties on the solid particle erosion mechanisms of brittle materials; (iii) establish a systematic relationship between the mechanical properties of coated surfaces and their SPE behavior; and (iv) develop an in situ testing methodology to investigate SPE mechanisms of hard protective coating systems.

Main Results

This doctoral project has been presented in the form of three articles corresponding to chapters four, five and six of the thesis. In the first part of the project (chapter four), we studied the effects of the particle properties on the SPE behavior of six brittle bulk materials by using glass and alumina powders to erode the materials at varying velocities. First, we focused on elasto-plastic and fracture characterization techniques in order to apply a robust methodology to accurately measure and then correlate the materials' mechanical properties to the measured ER. With the help of a morphological study and an analysis of the quasi-static elasto-plastic erosion models, we showed that the tests using both types of powders led to a material loss mechanism related to lateral fracture. However, higher than predicted velocity exponents were observed pointing towards a velocity-dependent damage accumulation mechanism which we correlated to target yield pressure. This damage accumulation effect is more pronounced for the softer glass powder because of larger kinetic energy dissipation through different means. To the best of our knowledge, this dependence of velocity exponent on the surface mechanical properties has never been reported and merits further investigation. However, since it was not the main focus of the study it was not pursued any further at this time.

In order to understand the effects of impact on the particles themselves and to study the energy dissipation related to fragmentation, we analyzed, in this first study, the particle size distributions of the powders before and after erosion testing. We showed that particle breakup and deformation were correlated to the ratio of particle hardness over target hardness but did not find sufficient evidence to support the hypothesis that the disparity between erosion rates when using different powders was due to kinetic energy being dissipated trough particle fracture. In fact, the large difference in brittleness between the alumina and glass powders may be obscuring the real effect of target hardness on particle fragmentation. In order to gain more insight into the energy dissipation mechanisms related to particle impact, testing using a single powder with a much smaller particle size distribution and wider variety of target materials would be needed.

In the second part of the thesis (chapter five), we studied the erosion mechanisms of hard protective coatings deposited by pulsed DC magnetron sputtering. We first validated a new methodology for the accurate measurement of volume loss, and we clearly showed the importance of optimizing the testing parameters in order to obtain results free from experimental artefacts. In fact, it was shown that the particle feed rate and working distance could affect the measured erosion rate by as much as 50%. This new technique for the evaluation of volume loss was shown to be accurate, highly repeatable and quick but could only be applied to erosion tests conducted for a particle flow with normal incidence to the surface because of the necessity of an axisymmetric wear profile. However, normal incidence tests are the standard for materials showing brittle mechanisms of erosion thus making this testing methodology valuable for future research.

We then tested all the coatings using the optimized conditions and correlated the measured erosion rates to the material properties measured by depth-sensing indentation. It was found that the measured erosion rates were much more dependent on the target hardness than what had been predicted by the brittle erosion models proposed in the literature. Therefore, in order to fully understand the material loss mechanisms, we studied in greater detail three of the coating systems deposited on c-Si with the help of fracture characterization and a morphological study of the eroded surfaces. Surprisingly, we found that the coating erosion did do not correlate with coating toughness but only with the coating surface hardness thus excluding the material loss mechanism by brittle fracture. This finding was confirmed by the morphological study which showed the material removal mechanism to occur through repeated ductile indentation and cutting of the surface by the impacting particles. Finally, the particle size distributions measurements of the powders before and after erosion testing showed that particle breakup was not sufficiently large to explain the strong dependence on target hardness. From these results, we concluded that it was likely that the amount of material displaced by each particle impact decreased as the hardness of the surface increased. Consequently, the number of subsequent impacts needed for material removal would increase significantly, explaining the observed dependence on surface hardness.

Studying SPE mechanisms of hard protective coating systems in detail has proven to be quite challenging in the past, given that conventional SPE testing is notoriously inaccurate due to its aggressive nature and its many methodological uncertainties. In the last part of the thesis (chapter six), we presented the development of a novel in situ real-time erosion testing methodology which uses a quartz crystal microbalance for very sensitive monitoring of the coating mass loss during erosion testing. We detailed the methodological considerations in order to obtain applicable data and demonstrated the validity of the technique by comparing the SPE results to those obtained through conventional testing of uncoated QCM samples and of monolithic hard coatings. We found close agreement between both techniques. We then used the *in situ* approach to investigate the SPE behaviour of a Cr/CrN multilayer coating revealing a never before reported oscillatory behaviour of the ER during erosion. From these results, we demonstrated that this high precision time-resolved method can be used to gain new insights into the erosion process of complex coating systems.

General Discussion

In accordance with the main objective stated above, this PhD thesis has contributed significantly to the understanding of the material loss mechanisms present during low velocity SPE of hard coating systems. This has been achieved by a thorough study of the experimental methodology necessary to obtain relevant mechanical properties as well as the erosion rates of the studied materials, an increased understanding of erosion mechanisms of hard and brittle materials and by a more precise comprehension of the effect of particle properties of the erosion process.

Methodological findings

From the various studies in this PhD project, we have demonstrated that the proper understanding and application of the characterisation techniques is essential for the assessment of multi-parameter correlations. This includes calibration, validation and proper application of the techniques, as well as applying rigorous analysis methods and the validation of the obtained data. In fact, through the study of SPE behaviour of highly brittle materials with similar erosion rates, it was clearly illustrated that by applying a robust testing methodology for the precise characterisation of surface mechanical properties, differences in SPE behaviour could be observed. However, the measurement of mechanical properties of coated systems still remains quite open for much advancement. Most notably, there is as yet no largely accepted method for the evaluation of coating toughness and much work needs to be accomplished in validating existing techniques.

In the case of the *in situ* technique, we used an existing QCM system that is traditionally used for deposition rate monitoring which uses very delicate QCM resonators. The deposition of thick hard coatings on these thin crystals is a very difficult task and only a limited amount of coating systems can be deposited for erosion testing because the residual stress of the coating has to be relatively low for the QCM to be viable. Therefore, the first step to expand the *in situ* methodology would be to design a new, more robust, system that enables the testing of complete samples, *i.e.* coatings deposited on technologically relevant substrates such as stainless steel and titanium alloys. This would not only enable the study of a greater variety of coating systems, but also permit the extension of testing to higher velocities and using smaller incidence angles to study ductility effects.

Erosion mechanisms

As could be expected, the brittle bulk materials tested in the study (glasses, c-Si and c-Ge) all presented lateral fracture material loss regardless of particles properties; even though the erosion rates of tests using alumina powder were nearly one order of magnitude larger than when testing with glass powder. In the case of hard protective coatings, the erosion behaviour was found to be much more dependent on target hardness than expected ($ER \propto H^{-6.8\pm0.5}$) and, surprisingly, no dependence on fracture toughness was observed. It should be stated here that this was an unexpected finding. Our initial hypothesis was that the erosion mechanisms of hard ceramic coatings would be brittle in nature as has been proposed in the literature where a micro-chipping mechanism is often hypothesised. Thus, our findings which led to the proposed material removal mechanism resulting from ductile indentation and cutting, are a significant contribution to the field and have advanced the understanding of erosion mechanisms of hard materials.

Effect of particle properties

Following the preliminary study on CrN-based coatings, it was believed that one of the major explanations for the high dependence of erosion rates on target hardness was the breakup of particles upon impact. The study of SPE of brittle materials using alumina and glass powders showed that the softer glass particles deformed and broke up, reducing the efficiency of each impact and resulting in the need of more damage accumulation before material removal. The amount of particle breakup was found to be correlated to target hardness, but the amount of energy dissipated through particle fragmentation was not sufficiently high to cause a change in the erosion mechanism. In the case of the erosion of hard coatings by alumina particles, it was found that although particle breakup increased with increasing target hardness, this increase was not sufficiently large to significantly affect the erosion rate. Both these findings indicate that the effect of target hardness on particle breakup is not as important as previously thought and did not affect SPE behaviour as much as was expected.

Outlook

This thesis is the first study in the area of solid particle erosion testing at the FCSEL and can be placed in the general context of a developing expertise on the tribo-mechanical characterization of hard protective coatings. Consequently, a very large part of the work was dedicated to developing methodologies for complete characterisation of coating mechanical properties and tribological processes. These precise methodologies and the high level of understanding of surface response to tribological solicitations open the door to many new opportunities. However, in order to significantly impact future technological developments, there is a need for a deeper understanding of the influence of coating microstructure on defect driven mechanical properties, such as fracture toughness and hardness, thus completing the design cycle that could lead to the design of ideal SPE protective systems, as illustrated below.

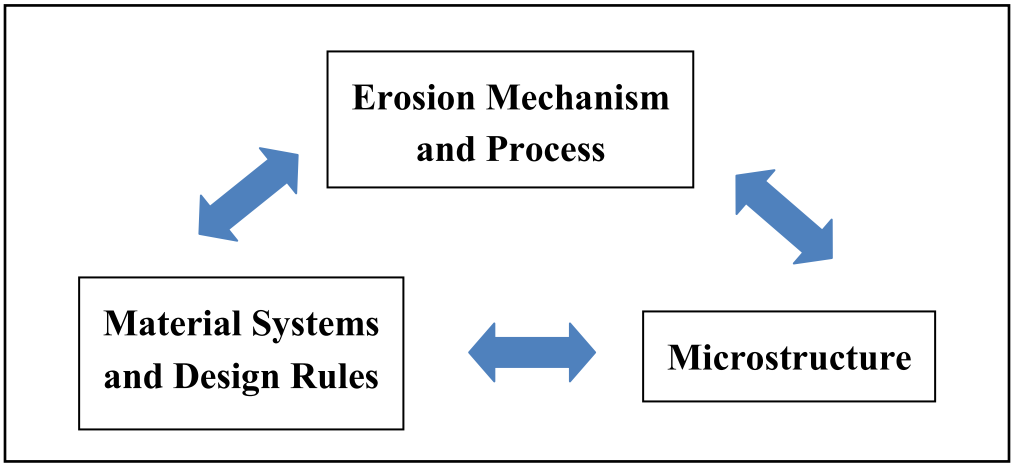

Figure C.12: SPE protective system design cycle.

More specifically, in the continuity of the research presented in this thesis, there are still many areas where a deeper study is necessary. In that respect, the new *in situ* real-time technique could yield very interesting results on fundamental erosion processes such as the effect of surface properties on velocity exponents or the role of coating microstructure and architecture on erosion resistance. One particular material study that would benefit from the high precision of the *in situ* technique is the investigation of the SPE performance of the TiN-based nanocomposite coatings developed at the FCSEL over the years. It would be interesting to investigate, for example, the effect of silicon or carbon addition on the SPE resistance and thus enable us to tune the mechanical properties of the coating to operational conditions where high hardness may be desirable at low velocities for resistance to plastic deformation, while higher toughness would be prescribed for higher velocities, where fracture related processes occur.

In terms of coating design, many new concepts also need to be investigated such as the effect of kinetic energy restitution through the coatings' elastic recovery, most notably in the case of super-elastic materials or the use of graded coating architectures instead of the traditional multilayer. In fact, as described in the literature review, many erosion resistant systems use multilayer architectures for increased resistance to fracture related SPE mechanisms and for increased energy dissipation during impact. However, there is still a significant lack of understanding on the SPE of the multilayer systems. Indeed, much of the design work on multilayer coatings is actually done by a trial and error process which can be both time consuming and unsuccessful. Therefore, there is a significant need to develop more rigorous design criteria for enhanced protection under different operational conditions. In order to achieve this, much more work is needed in modeling of the SPE process and the corresponding detailed experimental work needed to validate new design tools.

REFERENCES

[1] J. Gagnon. (2010, March 13th 2013). *Profil de l'industrie au Québec*. Available: http://affaires.lapresse.ca/portfolio/archive/industrie-aeronautique/201011/30/01-4347807-profil-de-lindustrie-au-quebec.php

[2] R. C. Sirs, "The Operation of Gas Turbine Engines in Hot & Sandy Conditions – Royal Air Force Experiences in the Gulf War," *AGARD-CP-558,* p. Paper no2, 1994.

[3] M. Selinger. (July 16th 2007). *Pratt & Whitney Modifying Lead Engine For JSF*. Available: http://www.aviationweek.com

[4] A. Hamed and e. al., "Experimental and numerical simulation of the effects of ingested particles in gas turbine engines," in *83rd Symposium of Propulsion and Energetics Panel on Turbines*, Rotterdam, 1994, pp. 11-1.

[5] A. A. Hamed*, et al.*, "Turbine blade surface deterioration by erosion," *Journal of Turbomachinery,* vol. 127, pp. 445-452, 2005.

[6] M. Klein and G. Simpson, "The development of innovative methods for erosion testing a russian coating on GE T64 gas turbine engine compressor blades," Vienna, Austria, 2004, pp. 347-352.

[7] W. Tabakoff. (March 10th 2013). *Erosion Presentation*. Available: http://www.ase.uc.edu/tmel/public_html/TabakoffErosionPresentation.pdf

[8] R. F. Cook and G. M. Pharr, "Direct observation and analysis of indentation cracking in glasses and ceramics," *Journal of the American Ceramic Society,* vol. 73, pp. 787-817, 1990.

[9] P. Jedrzejowski*, et al.*, "Real-time in situ growth study of TiN- and TiCxNy-based superhard nanocomposite coatings using spectroscopic ellipsometry," *Applied Physics Letters,* vol. 88, 2006.

[10] E. Bousser*, et al.*, "Effect of microstructure on the erosion resistance of Cr-Si-N coatings," *Surface and Coatings Technology,* vol. 203, pp. 776-780, 2008.

[11] M. Benkahoul*, et al.*, "Microstructure and mechanical properties of Cr-Si-N coatings prepared by pulsed reactive dual magnetron sputtering," *Surface and Coatings Technology,* vol. 202, pp. 3975-80, 2008.

[12] P. H. Shipway and I. M. Hutchings, "Role of particle properties in the erosion of brittle materials," *Wear,* vol. 193, pp. 105-113, 1996.

[13] K. Holmberg and A. Matthews, *Coatings Tribology: Properties, Mechanisms, Techniques and Applications in Surface Engineering*, 2nd Edition ed. Amsterdam: Elsevier, 2009.

[14] P. Jedrzejowski, "Mechanical and optical properties of plasma deposited superhard nanocomposite coatings," PhD, Engineering physics, École Polytechnique de Montréal, Montreal, 2003.

[15] D. Tabor, "Hardness and strength of metals," *Institute of Metals -- Journal,* vol. 79, pp. 1-18, 1951.

[16] R. Hill, "General features of plastic-elastic problems as exemplified by some particular solutions," in *American Society of Mechanical Engineers -- Meeting A-13, Nov 28-Dec 3 1948*, New York, NY, United States, 1948, p. 6.

[17] M. Ohring, *Material science of thin films*: Academic Press, 1992.

[18] (March 13th 2013). *Crack tip separation modes*. Available: http://jeb.biologists.org/content/210/13/2213/F3.expansion.html

[19] A. Leyland and A. Matthews, "On the significance of the H/E ratio in wear control: a nanocomposite coating approach to optimised tribological behaviour," *Wear,* vol. 246, pp. 1-11, 2000.

[20] B. R. Lawn*, et al.*, "Elastic/plastic indentation damage in ceramics: The median/radial crack system," *Journal of the American Ceramic Society,* vol. 63, pp. 574-81, 1980.

[21] D. B. Marshall*, et al.*, "Elastic/plastic indentation damage in ceramics: the lateral crack system," *Journal of the American Ceramic Society,* vol. 65, pp. 561-566, 1982.

[22] G. R. Anstis*, et al.*, "A critical evaluation of indentation techniques for measuring fracture toughness. I. Direct crack measurements," *Journal of the American Ceramic Society,* vol. 64, pp. 533-8, 1981.

[23] T. L. Oberle, "Properties influencing wear of metals," *American Institute of Mining and Metallurgical Engineers -- Journal of Metals,* vol. 3, pp. 438-439, 1951.

[24] C. Rebholz*, et al.*, "Structure, hardness and mechanical properties of magnetron-sputtered titanium-aluminium boride films," in *26th International Conference on Metallurgical Coatings and Thin Films, 12-15 April 1999*, Switzerland, 1999, pp. 412-17.

[25] Y.-T. Cheng and C.-M. Cheng, "Relationships between hardness, elastic modulus, and the work of indentation," *Applied Physics Letters,* vol. 73, pp. 614-614, 1998.

[26] R. Yang*, et al.*, "Theoretical analysis of the relationships between hardness, elastic modulus, and the work of indentation for work-hardening materials," *Journal of Materials Research,* vol. 25, pp. 2072-2077, 2010.

[27] K. L. Johnson, *Contact Mechanics*. Cambridge: Cambridge University Press, 1987.

[28] T. Y. Tsui*, et al.*, "Nanoindentation and nanoscratching of hard coating materials for magnetic disks," in *Thin Films: Stresses and Mechanical Properties V. Symposium, 28 Nov.-2 Dec. 1994*, Pittsburgh, PA, USA, 1995, pp. 767-72.

[29] J. Musil and M. Jirout, "Toughness of hard nanostructured ceramic thin films," *Surface and Coatings Technology,* vol. 201, pp. 5148-5152, 2007.

[30] S. Hassani*, et al.*, "Predictive tools for the design of erosion resistant coatings," *Surface and Coatings Technology,* vol. 203, pp. 204-10, 2008.

[31] I. M. Hutchings, "Transitions, threshold effects and erosion maps," *Key Engineering Materials,* vol. 71, pp. 75-92, 1992.

[32] B. A. Movchan and A. V. Demchishin, "Study of the structure and properties of thick vacuum condensates of nickel, titanium, tungsten, aluminum oxide and zirconium dioxide," vol. 28, pp. 653-60, 1969.

[33] J. A. Thornton, "Influence of apparatus geometry and deposition conditions on the structure and topography of thick sputtered coatings," *Journal of Vacuum Science and Technology,* vol. 11, pp. 666-670, 1974.

[34] R. Messier*, et al.*, "Revised structure zone model for thin film physical structure," in *Proceedings of the 30th National Symposium of the American Vacuum Society, 31 Oct.-4 Nov. 1983*, USA, 1984, pp. 500-3.

[35] P. J. Kelly and R. D. Arnell, "Development of a novel structure zone model relating to the closed-field unbalanced magnetron sputtering system," *Journal of Vacuum Science & Technology A: Vacuum, Surfaces, and Films,* vol. 16, pp. 2858-2858, 1998.

[36] A. Anders, "A structure zone diagram including plasma-based deposition and ion etching," *Thin Solid Films,* vol. 518, pp. 4087-4090, 2010.

[37] R. F. Bunshah, *Handbook of hard coatings: Deposition Technologies, Properties and Applications*. Park Ridge, NJ, USA: Noyes Publications, 2001.

[38] E. O. Hall, "The deformation and ageing of mild steel: III Discussion of results," *Proc. Roy. Soc. London,* vol. B64, p. 474, 1951.

[39] N. J. Petch, " The cleavage of polycrystals," *Jour. Iron Steel Inst.,* vol. 174, p. 25, 1953.

[40] M. Shinn*, et al.*, "Growth, structure, and microhardness of epitaxial TiN/NbN superlattices," *Journal of Materials Research,* vol. 7, pp. 901-11, 1992.

[41] U. Helmersson*, et al.*, "Growth of single-crystal TiN/VN strained-layer superlattices with extremely high mechanical hardness," *Journal of Applied Physics,* vol. 62, pp. 481-4, 1987.

[42] R. Hauert and J. Patscheider, "From alloying to nanocomposites - Improved performance of hard coatings," *Advanced Engineering Materials,* vol. 2, pp. 247-259, 2000.

[43] A. Duck*, et al.*, "Ti/TiN multilayer coatings: Deposition technique, characterization and mechanical properties," *Surface and Coatings Technology,* vol. 142-144, pp. 559-584, 2001.

[44] D. C. Cameron*, et al.*, "Structural variations in CrN/NbN superlattices," *Surface and Coatings Technology,* vol. 142-144, pp. 567-572, 2001.

[45] M. Nordin*, et al.*, "Mechanical and tribological properties of multilayered PVD TiN/CrN, TiN/MoN, TiN/NbN and TiN/TaN coatings on cemented carbide," *Surface and Coatings Technology,* vol. 106, pp. 234-241, 1998.

[46] S. Zhang*, et al.*, "Recent advances of superhard nanocomposite coatings: A review," Singapore, 2003, pp. 113-19.

[47] P. Jedrzejowski*, et al.*, "Quaternary hard nanocomposite TiCxNy/SiCN coatings prepared by plasma enhanced chemical vapor deposition," *Thin Solid Films,* vol. 466, pp. 189-96, 2004.

[48] P. Jedrzejowski*, et al.*, "Relationship between the mechanical properties and the microstructure of nanocomposite TiN/SiN_{1.3} coatings prepared by low temperature plasma enhanced chemical vapor deposition," *Thin Solid Films,* vol. 426, pp. 150-9, 2003.

[49] S. Veprek and A. S. Argon, "Towards the understanding of mechanical properties of super- and ultrahard nanocomposites," *Journal of Vacuum Science and Technology B: Microelectronics and Nanometer Structures,* vol. 20, pp. 650-664, 2002.

[50] J. Patscheider*, et al.*, "Structure-perfonnance relations in nanocomposite coatings," San Diego, CA, USA, 2001, pp. 201-8.

[51] I. M. Hutchings, *Tribology: friction and wear of engineering materials*. London: CRC Press, 1992.

[52] I. Finnie, "The Mechanism of Erosion of Ductile Metals," *Proceedings of the 3rd US National Congress of Applied Mechanics,* pp. 527-532, 1958.

[53] I. Finnie, "Some reflections on the past and future of erosion," *Wear,* vol. 186-187, pp. 1-10, 1995.

[54] I. Finnie*, et al.*, "The influence of impingement angle on the erosion of ductile metals by angular abrasive particles," *Wear,* vol. 152, pp. 91-8, 1992.

[55] G. P. Tilly, "A two stage mechanism of ductile erosion," *Wear,* vol. 23, pp. 87-96, 1973.

[56] R. Bellman, Jr. and A. Levy, "Erosion mechanism in ductile metals," *Wear,* vol. 70, pp. 1-27, 1981.

[57] A. V. Levy, "The solid particle erosion behavior of steel as a function of microstructure," *Wear,* vol. 68, pp. 269-87, 1981.

[58] R. A. Mayville, "Mechanisms of material removal in the solid particle erosion of ductile metals," Mechanical Engineering, University of California, Berkeley, CA, USA, 1978.

[59] I. Finnie and D. H. McFadden, "On the velocity dependence of the erosion of ductile metals by solid particles at low angles of incidence," *Wear,* vol. 48, pp. 181-90, 1978.

[60] G. L. Sheldon and A. Kanhere, "An investigation of impingement erosion using single particles," *Wear,* vol. 21, pp. 195-209, 1972.

[61] I. Finnie*, et al.*, "Erosion of metals by solid particles," *ASTM Journal of Materials,* vol. 2, pp. 682-700, 1967.

[62] G. L. Sheldon and I. Finnie, "Mechanism of material removal in erosive cutting of brittle materials," *American Society of Mechanical Engineers -- Transactions -- Journal of Engineering for Industry,* vol. 88, pp. 393-400, 1966.

[63] H. L. Oh*, et al.*, "Mechanism of ultrasonic machining of brittle solids," *IEE Conference Publication,* pp. 109-113, 1974.

[64] B. R. Lawn and E. R. Fuller, "Equilibrium penny-like cracks in indentation fracture," *Journal of Materials Science,* vol. 10, pp. 2016-2024, 1975.

[65] S. M. Wiederhorn and B. J. Hockey, "Effect of material parameters on the erosion resistance of brittle materials," *Journal of Materials Science,* vol. 18, pp. 766-80, 1983.

[66] A. G. Evans*, et al.*, "Impact damage in brittle materials in the elastic-plastic response regime," *Proceedings of the Royal Society of London, Series A (Mathematical and Physical Sciences),* vol. 361, pp. 343-65, 1978.

[67] S. M. Wiederhorn and B. R. Lawn, "Strength degradation of glass impacted with sharp particles. I. Annealed surfaces," *Journal of the American Ceramic Society,* vol. 62, pp. 66-70, 1979.

[68] M. Buijs, "Erosion of glass as modeled by indentation theory," *Journal of the American Ceramic Society,* vol. 77, pp. 1676-8, 1994.

[69] P. J. Slikkerveer*, et al.*, "Erosion and damage by sharp particles," *Wear,* vol. 217, pp. 237-50, 1998.

[70] G. L. Sheldon and I. Finnie, "On ductile behavior of nominally brittle materials during erosive cutting," *American Society of Mechanical Engineers -- Transactions -- Journal of Engineering for Industry,* vol. 88, pp. 387-392, 1966.

[71] M. A. Verspui*, et al.*, "Validation of the erosion map for spherical particle impacts on glass," *Wear,* vol. 215, pp. 77-82, 1998.

[72] S. M. Wiederhorn and B. R. Lawn, "Strength degradation of glass resulting from impact with spheres," *Journal of the American Ceramic Society,* vol. 60, pp. 451-458, 1977.

[73] S. J. Bull, "Using work of indentation to predict erosion behavior in bulk materials and coatings," *Journal of Physics D (Applied Physics),* vol. 39, pp. 1626-34, 2006.

[74] P. H. Shipway and I. M. Hutchings, "The influence of particle properties on the erosive wear of sintered boron carbide," *Wear,* vol. 149, pp. 85-98, 1991.

[75] P. J. Slikkerveer*, et al.*, "Alumina particle degradation during solid particle impact on glass," *Journal of the American Ceramic Society,* vol. 83, pp. 2263-2266, 2000.

[76] D. W. Celotta*, et al.*, "Sand erosion testing of novel compositions of hard ceramics," *Wear,* vol. 263, pp. 278-83, 2007.

[77] L. Murugesh and R. O. Scattergood, "Effect of erodent properties on the erosion of alumina," *Journal of Materials Science,* vol. 26, pp. 5456-66, 1991.

[78] S. Wada, "Effects of hardness and fracture toughness of target materials and impact particles on erosion of ceramic materials," *Key Engineering Materials,* vol. 71, pp. 57-74, 1992.

[79] J. L. Routbort and R. O. Scattergood, "Solid particle erosion of ceramics and ceramic composites," *Key Engineering Materials,* vol. 71, pp. 23-50, 1992.

[80] J. E. Ritter, "Strength degradation of ceramics due to solid-particle erosion," *Key Engineering Materials,* vol. 71, pp. 93-106, 1992.

[81] S. Amirhaghi*, et al.*, "Diamond coatings on tungsten carbide and their erosive wear properties," *Surface and Coatings Technology,* vol. 135, pp. 126-138, 2001.

[82] J. Barber*, et al.*, "The development of sub-surface damage during high energy solid particle erosion of a thermally sprayed WC-Co-Cr coating," 2005, pp. 125-134.

[83] S. J. Matthews*, et al.*, "Microstructural influence on erosion behaviour of thermal spray coatings," *Materials Characterization,* vol. 58, pp. 59-64, 2007.

[84] L. A. Dobrzanski and M. Adamiak, "Structure and properties of the TiN and Ti(C,N) coatings deposited in the PVD process on high-speed steels," *Journal of Materials Processing Technology,* vol. 133, pp. 50-62, 2003.

[85] L. A. Dobrzanski and K. Lukaszkowicz, "Erosion resistance and tribological properties of coatings deposited by reactive magnetron sputtering method onto the brass substrate," *Journal of Materials Processing Technology,* vol. 157-158, pp. 317-323, 2004.

[86] W. Kwasny*, et al.*, "Ti + TiN, Ti + Ti(CxN1-x), Ti + TiC PVD coatings on the ASP 30 sintered high-speed steel," *Journal of Materials Processing Technology,* vol. 157-158, pp. 370-379, 2004.

[87] J.-P. Immarigeon*, et al.*, "Erosion testing of coatings for aero engine compressor components," *Advanced Performance Materials,* vol. 4, pp. 371-388, 1997.

[88] V. R. Parameswaran*, et al.*, "Titanium nitride coating for aero engine compressor gas path components," *Surface and Coatings Technology,* vol. 52, pp. 251-260, 1992.

[89] M. Bromark*, et al.*, "Influence of substrate material on the erosion resistance of TiN coated tool steels," *Wear,* vol. 186-187, pp. 189-194, 1995.

[90] A. Leyland and A. Matthews, "Thick Ti/TiN multilayered coatings for abrasive and erosive wear resistance," *Surface and Coatings Technology,* vol. 70, pp. 19-25, 1994.

[91] F. Cai*, et al.*, "Tribological behaviors of titanium nitride-and chromium-nitride-based physical vapor deposition coating systems," *Journal of Engineering for Gas Turbines and Power,* vol. 134, 2012.

[92] J. Deng*, et al.*, "Erosion wear of CrN, TiN, CrAlN, and TiAlN PVD nitride coatings," *International Journal of Refractory Metals and Hard Materials,* vol. 35, pp. 10-16, 2012.

[93] A. Feuerstein and A. Kleyman, "Ti-N multilayer systems for compressor airfoil sand erosion protection," *Surface and Coatings Technology,* vol. 204, pp. 1092-1096, 2009.

[94] C. Maurer and U. Schulz, "Erosion resistant titanium based PVD coatings on CFRP," 2013.

[95] M. Antonov*, et al.*, "Assessment of gradient and nanogradient PVD coatings behaviour under erosive, abrasive and impact wear conditions," *Wear,* vol. 267, pp. 898-906, 2009.

[96] M. W. Reedy*, et al.*, "Erosion performance and characterization of nanolayer (Ti,Cr)N hard coatings for gas turbine engine compressor blade applications," *Surface and Coatings Technology,* vol. 206, pp. 464-472, 2011.

[97] Q. Yang*, et al.*, "Erosion resistance performance of magnetron sputtering deposited TiAlN coatings," *Surface and Coatings Technology,* vol. 188-189, pp. 168-173, 2004.

[98] L. Swadzba*, et al.*, "Influence of coatings obtained by PVD on the properties of aircraft compressor blades," *Surface and Coatings Technology,* vol. 78, pp. 137-143, 1996.

[99] L. A. Dobrzanski*, et al.*, "Relationship between erosion resistance and the phase and chemical composition of PVD coatings deposited onto high-speed steel," *Journal of Materials Processing Technology,* vol. 92-93, pp. 184-189, 1999.

[100] X. T. Zeng, *et al.*, "Erosive wear properties of Ti-Si-N nanocomposite coatings studied by micro-sandblasting," *Journal of Vacuum Science & Technology A (Vacuum, Surfaces, and Films),* vol. 23, pp. 288-92, 2005.

[101] B. A. Eizner, *et al.*, "Deposition stages and applications of CAE multicomponent coatings," *Surface and Coatings Technology,* vol. 79, pp. 178-191, 1996.

[102] V. P. S. Swaminathan, *et al.*, "Nanotechnology coatings for erosion protection of turbine components," *Journal of Engineering for Gas Turbines and Power,* vol. 132, 2010.

[103] R. Wei, *et al.*, "Solid particle erosion protection of turbine blades with thick nitride and carbonitride coatings from magnetron sputter deposition," Seattle, WA, United States, 2006, pp. 78-84.

[104] W. Ronghua, *et al.*, "Microstructure and tribological performance of nanocomposite Ti-Si-C-N coatings deposited using hexamethyldisilazane precursor," *Journal of Vacuum Science & Technology A (Vacuum, Surfaces, and Films),* vol. 28, pp. 1126-32, 2010.

[105] M. Nordin and M. Larsson, "Deposition and characterization of multilayered PVD TiN/CrN coatings on cemented carbide," *Surface and Coatings Technology,* vol. 116-119, pp. 108-115, 1999.

[106] B. Borawski, *et al.*, "Multi-layer coating design architecture for optimum particulate erosion resistance," *Wear,* vol. 271, pp. 2782-2792, 2011.

[107] B. Borawski, *et al.*, "The influence of ductile interlayer material on the particle erosion resistance of multilayered TiN based coatings," *Wear,* vol. 271, pp. 2890-2898, 2011.

[108] T. Groegler, *et al.*, "Erosion resistance of CVD diamond-coated titanium alloy for aerospace applications," *Surface and Coatings Technology,* vol. 112, pp. 129-132, 1999.

[109] S. Amirhaghi, *et al.*, "Growth and erosive wear performance of diamond coatings on WC substrates," *Diamond and Related Materials,* vol. 8, pp. 845-849, 1999.

[110] D. W. Wheeler, "Solid particle erosion of CVD diamond," Ph.D., University of Southampton (United Kingdom), England, 2001.

[111] D. W. Wheeler and R. J. K. Wood, "Solid particle erosion behaviour of CVD boron phosphide coatings," *Surface and Coatings Technology,* vol. 200, pp. 4456-4461, 2006.

[112] D. W. Wheeler and R. J. K. Wood, "The erosion of CVD diamond by diamond particles," *Philosophical Magazine Letters,* vol. 85, pp. 367-75, 2005.

[113] D. W. Wheeler and R. J. K. Wood, "CVD diamond: Erosion resistant hard material," *Surface Engineering,* vol. 19, pp. 466-470, 2003.

[114] D. W. Wheeler and R. J. K. Wood, "High velocity sand impact damage on CVD diamond," *Diamond and Related Materials,* vol. 10, pp. 459-462, 2001.

[115] D. W. Wheeler and R. J. K. Wood, "Solid particle erosion of diamond coatings under non-normal impact angles," *Wear,* vol. 250-251, pp. 795-801, 2001.

[116] D. W. Wheeler and R. J. K. Wood, "Erosive wear behaviour of thick chemical vapour deposited diamond coatings," *Wear,* vol. 225-229, pp. 523-536, 1999.

[117] D. W. Wheeler and R. J. K. Wood, "Erosion damage in diamond coatings by high velocity sand impacts," *Philosophical Magazine,* vol. 87, pp. 5719-40, 2007.

[118] D. W. Wheeler and R. J. K. Wood, "Fracture of diamond coatings by high velocity sand erosion," *Philosophical Magazine,* vol. 89, pp. 285-310, 2009.

[119] D. W. Wheeler and R. J. K. Wood, "Erosive wear behaviour of thick chemical vapour deposited diamond coatings," in *Proceedings of the 1999 12th International Conference on Wear of Materials, WOM-99, April 25, 1999 - April 29, 1999*, Atlanta, GA, USA, 1999, pp. 523-536.

[120] D. W. Wheeler and R. J. K. Wood, "Solid particle erosion of CVD diamond coatings," in *Proceedings of the 1998 International Conference on Erosive and Abrasive Wear (ICEAW) - 9th International Conference on Erosion by Liquid and Solid Impact (ELSI IX), September 13, 1998 - September 17, 1998*, Cambridge, UK, 1999, pp. 306-318.

[121] V. Shanov*, et al.*, "CVD diamond coating for erosion protection at elevated temperatures," *Journal of Materials Engineering and Performance,* vol. 11, pp. 220-225, 2002.

[122] F. A. Almeida*, et al.*, "Erosive wear resistance of NCD coatings produced by pulsed microwave discharges," *Diamond and Related Materials,* vol. 19, pp. 484-488, 2010.

[123] I. S. Trakhtenberg*, et al.*, "Effect of adhesion strength of DLC to steel on the coating erosion mechanics," *Diamond and Related Materials,* vol. 10, pp. 1824-1828, 2001.

[124] P. Pekko, "Tetrahedral amorphous carbon deposited with the pulsed plasma arc-discharge method as a protective coating against solid impingement erosion," *Diamond and Related Materials,* vol. 9, pp. 1524-1528, 2000.

[125] Y. I. Oka*, et al.*, "Evaluation of erosion and fatigue resistance of ion plated chromium nitride applied to turbine blades," *Wear,* vol. 263, pp. 379-385, 2007.

[126] Y. Gachon*, et al.*, "Erosion by solid particles of W/W-N multilayer coatings obtained by PVD process," *Surface and Coatings Technology,* vol. 113, pp. 140-148, 1999.

[127] S. Hassani*, et al.*, "Mechanical, tribological and erosion behaviour of super-elastic hard Ti-Si-C coatings prepared by PECVD," *Surface and Coatings Technology,* vol. 205, pp. 1426-30, 2010.

[128] W. Tabakoff, "Erosion resistance of superalloys and different coatings exposed to particulate flows at high temperature," *Surface and Coatings Technology,* vol. 120-121, pp. 542-547, 1999.

[129] K. Bose and R. J. K. Wood, "Response of CVD boron carbide to repetitive indentation cycles to simulate solid particle impact erosion mechanisms," Washington, D.C., United States, 2005, pp. 481-482.

[130] K. Bose and R. J. K. Wood, "High velocity solid particle erosion behaviour of CVD boron carbide on tungsten carbide," *Wear,* vol. 258, pp. 366-376, 2005.

[131] K. Bose*, et al.*, "High energy solid particle erosion mechanisms of superhard CVD coatings," *Wear,* vol. 259, pp. 135-144, 2005.

[132] P. C. Jindal*, et al.*, "Performance of PVD TiN, TiCN, and TiAlN coated cemented carbide tools in turning," *International Journal of Refractory Metals and Hard Materials,* vol. 17, pp. 163-170, 1999.

[133] R. Rachbauer*, et al.*, "Increased thermal stability of Ti-Al-N thin films by Ta alloying," *Surface and Coatings Technology,* vol. 211, pp. 98-103, 2012.

[134] C. Li*, et al.*, "A comparative research on magnetron sputtering and arc evaporation deposition of Ti-Al-N coatings," *Thin Solid Films,* vol. 519, pp. 3762-7, 2011.

[135] S. Hassani*, et al.*, "Impact stress absorption and load spreading in multi-layered erosion-resistant coatings," *Wear,* vol. 268, pp. 770-6, 2010.

[136] S. Hassani*, et al.*, "Design of hard coating architecture for the optimization of erosion resistance," *Wear,* vol. 265, pp. 879-87, 2008.

[137] B. Borawski, "Multilayer erosion resistant coatings for the protection of aerospace components," PhD, Engineering sciences and mechanics, Pennsylvania State University, 2011.

[138] V. Shanov and W. Tabakoff, "Erosion resistance of coatings for metal protection at elevated temperatures," *Surface and Coatings Technology,* vol. 86-87, pp. 88-93, 1996.

[139] V. Shanov*, et al.*, "Erosion behavior of uncoated Waspaloy and Waspaloy coated with titanium carbide," *Surface and Coatings Technology,* vol. 94-95, pp. 64-69, 1997.

[140] V. Shanov*, et al.*, "Study of CVD coated and uncoated INCO 718 exposed to particulate flow," Atlanta, GA, USA, 1996, pp. 227-234.

[141] V. Shanov*, et al.*, "Erosion behavior of thermally treated pyrophyllite coated with titanium carbide," *Surface and Coatings Technology,* vol. 68-69, pp. 92-98, 1994.

[142] V. Shanov*, et al.*, "Erosive wear of CVD ceramic coatings exposed to particulate flow," San Diego, CA, USA, 1992, pp. 25-31.

[143] W. Tabakoff, "Engine deterioration when exposed to particulate flows," Barcelona, Spain, 2006, pp. 1041-1050.

[144] W. Tabakoff, "Deterioration and retention on coated and uncoated compressor and turbine blades," Reno, NV, United States, 2004, pp. 8006-8015.

[145] W. Tabakoff, "Erosion rate testing at high temperature of alloys and coatings for use in turbomachinery," Stockholm, Sweden, 1998, p. 8.

[146] W. Tabakoff, "High-temperature erosion resistance of coatings for use in turbomachinery," *Wear,* vol. 186-187, pp. 224-229, 1995.

[147] W. Tabakoff, "High temperature erosion resistance of coatings for use in gas turbine engines," *Surface and Coatings Technology,* vol. 52, pp. 65-79, 1992.

[148] W. Tabakoff*, et al.*, "High-temperature erosion resistance of coatings for gas turbine," *Journal of Engineering for Gas Turbines and Power, Transactions of the ASME,* vol. 114, pp. 242-249, 1992.

[149] W. Tabakoff and M. Metwally, "Coating effect on particle trajectories and turbine blade erosion," *Journal of Engineering for Gas Turbines and Power, Transactions of the ASME,* vol. 114, pp. 250-257, 1992.

[150] W. Tabakoff*, et al.*, "High-temperature coatings for protection against turbine deterioration," *Journal of Engineering for Gas Turbines and Power, Transactions of the ASME,* vol. 117, pp. 146-151, 1995.

[151] W. Tabakoff and V. Shanov, "Erosion rate testing at high temperature for turbomachinery use," *Surface and Coatings Technology,* vol. 76-77, pp. 75-80, 1995.

[152] J. R. Nicholls*, et al.*, "Comparison between the erosion behaviour of thermal spray and electron beam physical vapour deposition thermal barrier coatings," *Wear,* vol. 233-235, pp. 352-361, 1999.

[153] J. R. Nicholls and D. J. Stephenson, "Monte Carlo modelling of erosion processes," *Wear,* vol. 186-187, pp. 64-77, 1995.

[154] J. R. Nicholls*, et al.*, "Erosion of thermal barrier coatings," Woburn, UK, 2003, pp. 207-18.

[155] R. G. Wellman*, et al.*, "The effect of TBC morphology and aging on the erosion rate of EB-PVD TBCs," *Tribology International,* vol. 38, pp. 798-804, 2005.

[156] R. G. Wellman*, et al.*, "The effect of TBC morphology on the erosion rate of EB PVD TBCs," *Wear,* vol. 258, pp. 349-356, 2005.

[157] R. G. Wellman and J. R. Nicholls, "A review of the erosion of thermal barrier coatings," *Journal of Physics D: Applied Physics,* vol. 40, pp. 293-305, 2007.

[158] R. G. Wellman and J. R. Nicholls, "On the effect of ageing on the erosion of EB-PVD TBCs," Seoul, South Korea, 2004, pp. 80-8.

[159] R. G. Wellman and J. R. Nicholls, "A Monte Carlo model for predicting the erosion rate of EB PVD TBCs," *Wear,* vol. 256, pp. 889-899, 2004.

[160] R. G. Wellman and J. R. Nicholls, "A mechanism for the erosion of EB PVD TBCs," Le Embiez, France, 2001, pp. 531-8.

[161] R. G. Wellman and J. R. Nicholls, "Some observations on erosion mechanisms of EB PVD TBCS," *Wear,* vol. 242, pp. 89-96, 2000.

[162] R. J. L. Steenbakker*, et al.*, "Erosion of gadolinia doped EB-PVD TBCs," *Surface and Coatings Technology,* vol. 201, pp. 2140-2146, 2006.

[163] D. J. Stephenson and J. R. Nicholls, "Modelling the influence of surface oxidation on high temperature erosion," *Wear,* vol. 186-187, pp. 284-290, 1995.

[164] ASTM-G76, "Standard Test Method for Conducting Erosion Tests by Solid Particle Impingement Using Gas Jets." West Conshohocken, PA: ASTM International, 2007, p. 6.

[165] T. Deng*, et al.*, "A comparison of the gas-blast and centrifugal-accelerator erosion testers: The influence of particle dynamics," *Wear,* vol. 265, pp. 945-955, 2008.

[166] A. W. Ruff and L. K. Ives, "Measurement of solid particle velocity in erosive wear," *Wear,* vol. 35, pp. 195-9, 1975.

[167] D. Ciampini*, et al.*, "Simulation of interference effects in particle streams following impact with a flat surface. Part II. Parametric study and implications for erosion testing and blast cleaning," *Wear,* vol. 254, pp. 250-264, 2003.

[168] A. N. J. Stevenson and I. M. Hutchings, "Influence of nozzle length on the divergence of the erodent particle stream in a gas-blast erosion rig," *Wear,* vol. 189, pp. 66-69, 1995.

[169] P. H. Shipway and I. M. Hutchings, "Method for optimizing the particle flux in erosion testing with a gas-blast apparatus," *Wear,* vol. 174, pp. 169-175, 1994.

[170] A. Ghobeity*, et al.*, "Computer simulation of particle interference in abrasive jet micromachining," *Wear,* vol. 263, pp. 265-269, 2007.

[171] P. J. Slikkerveer, "Mechanical etching of glass by powder blasting," Dr., Technische Universiteit Eindhoven (The Netherlands), Netherlands, 1999.

[172] P. J. Slikkerveer and F. H. in't Veld, "Model for patterned erosion," *Wear,* vol. 233-235, pp. 377-386, 1999.

[173] M. A. Verspui*, et al.*, "Simulation model for the erosion of brittle materials," Cambridge, UK, 1999, pp. 436-43.

[174] T. Burzynski and M. Papini, "Analytical model of particle interference effects in divergent erosive jets," *Tribology International,* vol. 43, pp. 554-567, 2010.

[175] D. Ciampini and M. Papini, "A cellular automata and particle-tracking simulation of abrasive jet micromachining that accounts for particle spatial hindering and second strikes," *Journal of Micromechanics and Microengineering,* vol. 20, 2010.

[176] D. Ciampini*, et al.*, "Simulation of interference effects in particle streams following impact with a flat surface Part I. Theory and analysis," *Wear,* vol. 254, pp. 237-249, 2003.

[177] A. Ghobeity*, et al.*, "Surface evolution models in abrasive jet micromachining," *Wear,* vol. 264, pp. 185-198, 2008.

[178] C. Gomes-Ferreira*, et al.*, "The effect of inter-particle collisions in erosive streams on the distribution of energy flux incident to a flat surface," *Tribology International,* vol. 37, pp. 791-807, 2004.

[179] M. Papini, "Organic coating removal by single particle impact," Ph.D., University of Toronto (Canada), Canada, 1999.

[180] M. Papini*, et al.*, "Computer modelling of interference effects in erosion testing: Effect of plume shape," *Wear,* vol. 255, pp. 85-97, 2003.

[181] M. Papini and J. K. Spelt, "Plowing erosion of organic coatings by spherical particles," *Wear,* vol. 222, pp. 38-48, 1998.

[182] G. Sauerbrey, "Use of quartz vibrator for weighing thin layers and as a micro-balance," *Zeitschrift fur Physik,* vol. 155, pp. 206-222, 1959.

[183] C.-S. Lu and O. Lewis, "Investigation of film-thickness determination by oscillating quartz resonators with large mass load," *Journal of Applied Physics,* vol. 43, pp. 4385-4390, 1972.

[184] ASTM-C1327, "Standard Test Method for Vickers Indentation Hardness of Advanced Ceramics." West Conshohocken, PA: ASTM International, 2008, p. 9.

[185] A. C. Fischer-Cripps, *Nanoindentation*. New York, NY, USA: Springer, 2004.

[186] B. Jonsson and S. Hogmark, "Hardness measurements of thin films," *Thin Solid Films,* vol. 114, pp. 257-269, 1984.

[187] P. J. Burnett and D. S. Rickerby, "The mechanical properties of wear-resistant coatings. II. Experimental studies and interpretation of hardness," *Thin Solid Films,* vol. 148, pp. 51-65, 1987.

[188] P. J. Burnett and D. S. Rickerby, "The mechanical properties of wear-resistant coatings. I. Modelling of hardness behaviour," *Thin Solid Films,* vol. 148, pp. 41-50, 1987.

[189] D. Chicot and J. Lesage, "Absolute hardness of films and coatings," *Thin Solid Films,* vol. 254, pp. 123-130, 1995.

[190] A. M. Korsunsky*, et al.*, "On the hardness of coated systems," *Surface and Coatings Technology,* vol. 99, pp. 171-183, 1998.

[191] H. Ichimura*, et al.*, "The composite and film hardness of TiN coatings prepared by cathodic arc evaporation," *Surface and Coatings Technology,* vol. 127, pp. 138-43, 2000.

[192] G. M. Pharr*, et al.*, "The indentation size effect: A critical examination of experimental observations and mechanistic interpretations," *Annual Review of Materials Research,* vol. 40, pp. 271-292, 2010.

[193] W. C. Oliver and G. M. Pharr, "An improved technique for determining hardness and elastic modulus using load and displacement sensing indentation experiments," *Journal of Materials Research,* vol. 7, pp. 1564-83, 1992.

[194] J. Chen and S. J. Bull, "A critical examination of the relationship between plastic deformation zone size and Young's modulus to hardness ratio in indentation testing," *Journal of Materials Research,* vol. 21, pp. 2617-27, 2006.

[195] ISO14577-4, "ISO 14577-4:2007 Metallic materials -- Instrumented indentation test for hardness and materials parameters -- Part 4: Test method for metallic and non-metallic coatings." Geneva, Switzerland: International Organization for Standardization, 2007, p. 24.

[196] I. M. Hutchings, "A model for the erosion of metals by spherical particles at normal incidence," *Wear,* vol. 70, pp. 269-81, 1981.

[197] B. R. Lawn*, et al.*, "Strength degradation of brittle surfaces: sharp indenters," *Journal of the American Ceramic Society,* vol. 59, pp. 193-7, 1976.

[198] B. J. Hockey*, et al.*, "Erosion of brittle materials by solid particle impact," *Clays and Clay Minerals,* vol. 3, pp. 379-402, 1978.

[199] B. J. Hockey and S. M. Wiederhorn, "Erosion of ceramic materials: the role of plastic flow," *Proceedings of the Annual Industrial Pollution Conference,* pp. 26-1, 1979.

[200] J. G. A. Bitter, "Study of erosion phenomena -- 1," *Wear-Usure-Verschleiss,* vol. 6, pp. 5-21, 1963.

[201] B. R. Lawn and A. G. Evans, "A model for crack initiation in elastic/plastic indentation fields," *Journal of Materials Science,* vol. 12, pp. 2195-9, 1977.

[202] S. M. Wiederhorn*, et al.*, "Erosion of brittle materials by solid particle impact," *Dimensions NBS,* vol. 64, pp. 20-1, 1980.

[203] S. Srinivasan and R. O. Scattergood, "Effect of erodent hardness on erosion of brittle materials," *Wear,* vol. 128, pp. 139-152, 1988.

[204] L. Murugesh and R. O. Scattergood, "Effect of indentation load on fragmentation of erosion particle tips," *Wear,* vol. 141, pp. 115-24, 1990.

[205] R. Yang*, et al.*, "Experimental verification and theoretical analysis of the relationships between hardness, elastic modulus, and the work of indentation," *Applied Physics Letters,* vol. 92, 2008.

[206] J.-i. Jang and G. M. Pharr, "Influence of indenter angle on cracking in Si and Ge during nanoindentation," *Acta Materialia,* vol. 56, pp. 4458-4469, 2008.

[207] G. B. J. de Boer*, et al.*, "Laser diffraction spectrometry: Fraunhofer diffraction versus Mie scattering," *Particle Characterization,* vol. 4, pp. 14-19, 1987.

[208] E. D. Palik, *Handbook of Optical Constants of Solids*: Academic Press Inc., 1985.

[209] D. Chicot*, et al.*, "New developments for fracture toughness determination by Vickers indentation," *Materials Science and Technology,* vol. 20, pp. 877-84, 2004.

[210] D. R. Andrews, "A gravity-insensitive technique for measuring mass changes in hostile environments including erosion," *Journal of Physics E (Scientific Instruments),* vol. 16, pp. 803-6, 1983.

[211] F. P. M. Heukensfeldt Jansen, "An electronically maintained mechanical oscillator for measuring small mass loss of specimens in solid particle erosion studies," *Journal of Physics E (Scientific Instruments),* vol. 22, pp. 343-9, 1989.

[212] V. M. Mecea, "From Quartz Crystal Microbalance to Fundamental Principles of Mass Measurements," *Analytical Letters,* vol. 38, pp. 753-767, 2005/03/01 2005.

[213] R. Battaglia*, et al.*, "Development of a micro-balance system for dust and water vapour detection in the Mars atmosphere," *Advances in Space Research,* vol. 33, pp. 2258-2262, 2004.

[214] E. Vittorias*, et al.*, "Studying mechanical microcontacts of fine particles with the quartz crystal microbalance," *Powder Technology,* vol. 203, pp. 489-502, 2010.

[215] T. Dumont*, et al.*, "Changes in the etch rate of photosensitive polymers as a function of the pulse number," in *7th International Conference on Laser Ablation (COLA'03), 5-10 Oct. 2003*, Germany, 2004, pp. 1271-4.

[216] A. Widdowson*, et al.*, "An overview of erosion-deposition studies for the JET Mk II high delta divertor," in *12th International Workshop on Plasma-Facing Materials and Components for Fusion Applications, PFMC-12, May 11, 2009 - May 14, 2009*, Julich, Germany, 2009.

[217] A. Rahtu and M. Ritala, "Compensation of temperature effects in quartz crystal microbalance measurements," *Applied Physics Letters,* vol. 80, pp. 521-521, 2002.

[218] M. N. Rocklein and S. M. George, "Temperature-induced apparent mass changes observed during quartz crystal microbalance measurements of atomic layer deposition," *Analytical Chemistry,* vol. 75, pp. 4975-4982, 2003.

[219] R. J. K. Wood, "The sand erosion performance of coatings," *Materials and Design,* vol. 20, pp. 179-91, 1999.

[220] M. A. M. Ibrahim*, et al.*, "Corrosion of stainless steel coated with TiN, (TiAl)N and CrN in aqueous environments," *Corrosion Science,* vol. 44, pp. 815-28, 2002.

[221] J. Musil, "Hard and superhard nanocomposite coatings," Strasbourg, France, 2000, pp. 322-30.

[222] E. Martinez*, et al.*, "Electrical, optical and mechanical properties of sputtered CrNy and Cr1-xSixN1.02 thin films," in *Proceedings of the 30th International Conference on Metallurgie, April 28, 2002 - May 2, 2002*, San Diego, CA, United states, 2004, pp. 332-336.

[223] D. Mercs*, et al.*, "Mechanical and tribological properties of Cr-N and Cr-Si-N coatings reactively sputter deposited," *Surface and Coatings Technology,* vol. 200, pp. 403-7, 2005.

[224] L. Castaldi*, et al.*, "High temperature phase changes and oxidation behavior of Cr-Si-N coatings," *Surface and Coatings Technology,* vol. 202, pp. 781-5, 2007.

[225] L. Jyh-Wei and C. Yue-Chyuan, "A study on the microstructures and mechanical properties of pulsed DC reactive magnetron sputtered Cr-Si-N nanocomposite coatings," *Surface and Coatings Technology,* vol. 202, pp. 831-6, 2007.

[226] A. Guiner, *Théorie et Technique de Radiocristallographie*. Paris: Dunod, 1964.

[227] C. Gautier*, et al.*, "Comparative study of mechanical and structural properties of CrN films deposited by D.C. magnetron sputtering and vacuum arc evaporation," in *23rd International Conference on Metallurgical Coatings and Thin Films, 22-26 April 1996*, Switzerland, 1996, pp. 254-62.

[228] S. Zhang*, et al.*, "Toughness measurement of thin films: a critical review," *Surface and Coatings Technology,* vol. 198, pp. 74-84, 2005.

[229] S. Kodambaka*, et al.*, "TiN(001) and TiN(111) island coarsening kinetics: In-situ scanning tunneling microscopy studies," in *3rd International Conference on Coatings on Glass (ICCG), 29 Oct.-2 Nov. 2000*, Switzerland, 2001, pp. 164-8.

[230] A. G. Evans, "Impact damage in ceramics," *Clays and Clay Minerals,* vol. 3-4, pp. 303-331, 1978.

APPENDIX

APPENDIX A – Effect of Microstructure on the Erosion Resistance of Cr-Si-N Coatings

E. Bousser, M. Benkahoul, L. Martinu, J.E. Klemberg-Sapieha*

Engineering Physics Department, École Polytechnique de Montréal, P.O. Box 6079, Station Centre-ville, Montréal, Québec, Canada H3C 3A7

Abstract

Erosion by solid particle impact can cause severe damage to critical components of airplanes, helicopters and other systems, thus affecting their overall performance, cost and most notably safety. In our search for novel high performance erosion resistant coatings, we studied Cr-Si-N coatings (8 to 13 μm thick) deposited on AISI 410 stainless steel substrates by DC reactive dual magnetron sputtering using Cr and Si targets. Microstructure, composition and the mechanical properties were studied as a function of the silicon content (C_{Si}) using XRD, ERD-TOF, and the depth sensing and Vickers indentation techniques. A maximum hardness of 26.6 GPa was found for Cr-Si-N with C_{Si} = 6.7 at.%, while that of pure CrN was 19.4 GPa. Solid particle erosion (SPE) tests were performed according to the ASTM G76 standard on a test rig developed by our laboratory: Al2O3 particles with an average diameter of 50 μm were projected onto the coating surface, with a mean velocity of 70 m/s and a normal (90^o) incidence angle. The 90^o erosion rate of Cr-Si-N with C_{Si} = 11.6 at.% was found to be 5.2 x 10-3 mg/g, one order of magnitude lower than that of pure CrN and 20 times lower than that of the substrate. We specifically discuss the SPE behavior of the Cr-Si-N coatings with respect to their mechanical (hardness, reduced Young's modulus and toughness) and microstructural (texture and morphology) characteristics.

Keywords: CrN, Cr-Si-N, Nanocomposite, Erosion, Microstructure, Toughness.

* Corresponding author: tel.: +514-340-5747, fax: +514-340-3218

Email: jsapieha@polymtl.ca

A.1 Introduction

Solid particle erosion (SPE) is an important problem for aircraft flying in desert and other dusty environments. In particular, the leading edge of helicopter blades and compressor components of jet engines can be severely damaged by the impacting particles. Such material degradation leads to reduced performance and reliability, increased maintenance costs, ultimately compromising the safety of passengers and the flight crew. Therefore, in order to minimize the effects of SPE, component erosion resistance can be improved by depositing highly erosion resistant coatings to protect the affected surfaces.

For several years now many different erosion resistant coatings have been developed [219]. Titanium nitride (TiN)-based multilayer coatings is a system often used in actual applications, but other promising transition metal nitride (MeN) coatings have also been tested. One such system is chromium nitride (CrN), which typically presents a lower erosion resistance than TiN [85], but offers excellent corrosion resistance [220].

It has been found that the addition of other elements such as silicon (Si) in MeN systems can have profound effects on their mechanical, chemical and tribological properties [11, 14, 221-225]. These changes have been explained by two main mechanisms: the formation of a nanocomposite microstructure formed by the segregation of MeN grains separated by a mono-layer thick SiN_x matrix [14, 221, 223] and solid solution hardening [11, 222] due to the substitution of Me atoms by Si in the MeN lattice.

Several studies have been performed in order to evaluate the effect of Si addition on the properties of CrN thin films. While Mercs *et al.* [223] proposed a nanocomposite hardening mechanism, Martinez *et al.* [222], and more recently Benkahoul *et al.* [11], proposed that hardening is better explained by a solid solution mechanism. In fact, the different studies find that maximum hardness is obtained for silicon concentrations (C_{Si}) varying from 2 to 10 at.%. Depending on the proposed hardening mechanism, it has been reported that these concentrations either correspond to the limit of solubility of Si in the CrN lattice, or to the percolation threshold of the nanocomposite system.

In the present work, we investigate the effect of silicon addition to monolithic CrN coatings on their erosion resistance. Specifically, we correlate the SPE characteristics of Cr-Si-N coatings with their mechanical (hardness, Young's modulus and toughness) and microstructural (texture and morphology) characteristics.

A.2 Experimental

A.2.1 Deposition

The coatings were deposited by pulsed DC dual-magnetron reactive sputtering from two targets inclined with respect to the normal of a heated, biased and rotating substrate holder [11]. Prior to deposition, the AISI 410 stainless steel substrates (SS410) were polished to a mirror-like finish and cleaned before being inserted into the deposition chamber. AISI 410 is a martensitic stainless steel with the following chemical composition (wt%): 0.1-0.15 C, 1.00 Mn, 0.04 P, 0.03 S, 1.00 Si, 11.5-13.5 Cr and the balance being Fe. In order to increase the hardness and the toughness, the substrates were annealed at 982°C during 30 min, quenched in air, and then tempered at 575°C for 2 hours. Following adhesion optimization, the Cr-Si-N coatings were deposited with the C_{Si} values in the films being adjusted by changing the current on the Si target. During deposition, the substrates were heated to a temperature of 240°C, while applying a negative bias of V_b = -200 V. The base pressure of the reactor was below 1 x 10^{-6} Torr, N_2 and Ar flows were 15 and 14 sccm, respectively, and the total pressure during the deposition was 9 mTorr. The thickness of the deposited films was between 8 and 13 μm, as determined by observations using a JEOL JSM840 scanning electron microscope (SEM).

A.2.2 Microstructural characterization

Compositional depth profiles in the coatings were determined by elastic recoil detection in the time-of-flight regime (ERD-TOF). The crystalline structure, grain size (d_g) and preferential crystallographic orientation (texture) of the films were determined by X-ray diffraction (XRD; monochromatized Cu K_α radiation) in a Bragg-Brentano (θ-2θ) configuration using a Philips X'Pert diffractometer. D was calculated using the Scherrer formula [226]. Finally, following immersion in liquid nitrogen the coatings were cleaved and then observed by cross-sectional SEM in order to observe the morphology of the coatings and erosion scars.

A.2.3 Tribo-mechanical characterization

Hardness (*H*), reduced Young's modulus (E_r) and plasticity (R_p), defined as the ratio of plastic deformation over total deformation during an indentation test, were determined by depth-sensing indentation (DSI) using a Hysitron Triboindenter instrument equipped with a Berkovich pyramidal tip. Load-displacement plots were analyzed according to the Oliver-Pharr method [193].

The coating micro-hardness (H_v) and fracture toughness (K_{IC}) were evaluated using a CSEM Micro Scratch Tester with loads varying from 1 to 10 N. The hardness was evaluated by measuring the diagonal trace (*d*) of the imprint made by the Vickers indenter and expressed by:

$$H_v = 0.002\cos 22^o \frac{P}{d^2}, \tag{A.1}$$

where *P* is the applied load. K_{IC} was qualitatively evaluated by determining the load at which circular cracking first occurs under Vickers indentation. These circular cracks typically appear around the indentation trace and are observed optically when indenting in hard coatings deposited on softer substrates.

The SPE tests were performed according to the ASTM G76 standard on a test rig fabricated in our laboratory. Al_2O_3 angular particles (with an average diameter of 50 μm and hardness H_p = 13.4 GPa) were projected onto the coating surface, with a normal incidence angle (θ) and a mean velocity of 70 m/s, measured with a double disk apparatus [166]. In order to monitor the sample mass loss as a function of the mass of impacting particles, the samples were weighed before and after testing with a Sartorius LE225D analytical balance (precise to 0.01 mg) in a vibration, humidity and temperature controlled environment. Three samples of each coating composition were tested. The presented values are average erosion rates for each composition. The standard deviation for each sample varied from 1 to 16% of the ER_{90} value.

A.3 Results

A.3.1 Microstructure

In the first part of this work, we studied the relationship between the composition and the crystalline structure of the Cr-Si-N coatings. The C_{Si} values obtained by ERD-TOF together with the values of d_g are summarized in Table A.1. For $1.4 \leq C_{Si} \leq 6.7$ at.%, d_g is found to be constant ($d_g \sim 8$ nm), but decreases sharply for $C_{Si} = 11.6$ at.% ($d_g \sim 4$ nm). The columnar structure of the deposited coatings is illustrated in Figures A.1 (a) and (b) by SEM micrographs of CrN and Cr-Si-N films, the latter is characterized by $C_{Si} = 11.6$ at.%.

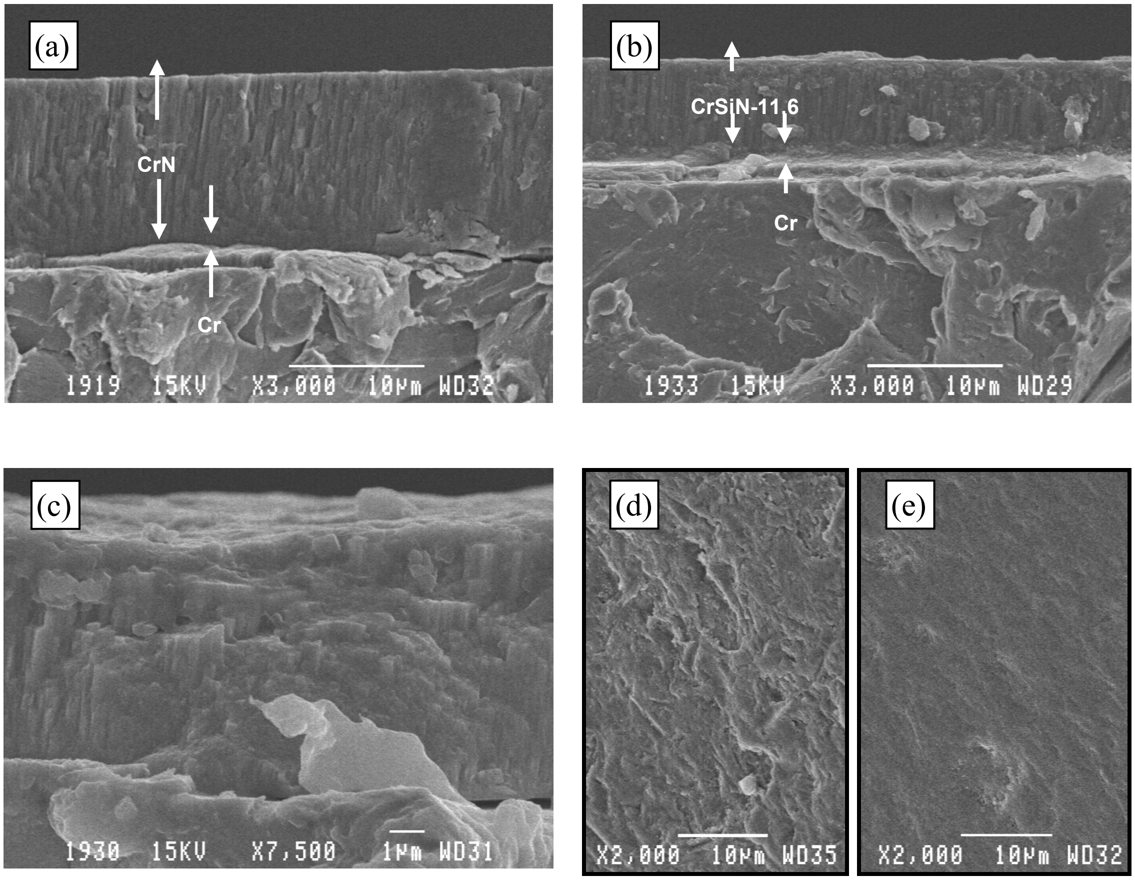

Figure A.1: SEM micrographs of, (a) as deposited CrN, (b) as deposited Cr-Si-N with $C_{Si} = 11.6$ at.%, (c) eroded CrN film showing brittle SPE behavior (d) eroded surface of a CrN coating, and (e) eroded surface of a Cr-Si-N coating with $C_{Si} = 11.6$ at.%.

Table A.1: Substrate and coating properties.

Sample	Si concentration (C_{Si})	DSI Hardness (H)	Vickers Hardness (H_v)	Reduced Young's Modulus (E_r)	Thickness (t)	Grain size (d_g)	90° erosion rate (ER_{90})	$(h/t)_c$	H_s/H_v	R_p
	at.%	GPa	GPa	GPa	µm	nm	mg/g			
SS410	N/A	4.8	4.8	216	N/A	N/A	0.108	N/A	N/A	N/A
CrN	0	19.4	18.2	250	13.0	6.5	0.056	0.58	0.26	0.52
CrSiN-1.4	1.36	25.3	24.4	260	10.4	8.3	0.014	0.35	0.20	0.45
CrSiN-2.3	2.33	23.8	22.5	243	11.3	8.9	0.014	0.40	0.21	0.46
CrSiN-6.7	6.69	26.6	20.9	270	7.8	7.4	0.015	0.44	0.23	0.45
CrSiN-11.6	11.64	24.8	28.0	260	8.9	4.5	0.005	0.47	0.17	0.45

XRD patterns, presented in Figure A.2, show that all coatings are heavily textured. We find that with the addition of Si, the preferred crystallographic orientation of the planes parallel to the surface changes from [110] to [111]. This latter orientation prevails up to C_{Si} = 6.7 at.%; for C_{Si} = 11.6 at.% the coating becomes highly textured with a preferred [100] orientation.

Preferred (220) planes are generally found for CrN coatings when resputtering occurs because of substrate biasing [227]. In the work by Benkahoul *et al.*, preferred [100] orientation has been reported for all C_{Si} upon Si addition for thin Cr-Si-N films.

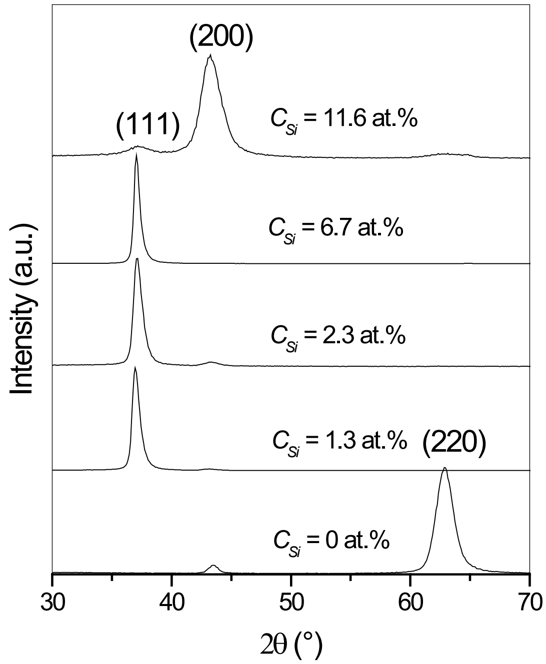

Figure A.2: Bragg-Brentano XRD patterns for Cr-Si-N coatings with various C_{Si}.

A.3.2 DSI-derived elasto-plastic properties

The elasto-plastic properties of the substrate and coatings are presented in Table A.1 (H, E_r and R_p). These properties obtained by DSI are slightly different from those previously published by Martinez *et al.* [222] and Benkahoul *et al.* [11] for similar coatings deposited on c-Si substrates. In fact, we can clearly observe a significant increase in H upon Si addition. As C_{Si} increases, hardness values seem to remain fairly constant, considering typical standard deviations of 1 GPa for coatings deposited on SS410 substrates.

A.3.3 Vickers micro-hardness

Although DSI remains the reference when assessing thin film mechanical properties, the values thus obtained do not necessarily reflect the application-specific coating performance. During erosion, small sharp particles impact and indent the surface of the coating. Using the elasto-plastic model developed by Wiederhorn *et al.* [67] for the SPE of brittle materials, the depth of penetration of a 50 μm alumina particle travelling at 70 m/s is found to be one to two microns. Similar depths of penetration were also found by finite element modeling for a TiN coating on SS410 by Hassani *et al.* [136]. For this reason, we have used Vickers indentation to measure the coating hardness (H_v) at an indentation depth (h) of one micron. However, in order to obtain relevant data, the actual coating hardness (H_f) has to be deconvoluted from the composite hardness (H_c), while considering the substrate hardness (H_s). Jedrzejowski *et al.* [48] have studied different geometrical models used to evaluate the coefficient a in the mixture law, namely

$$H_c = H_s + a(H_f - H_s)\,. \qquad (A.2)$$

When appropriately applied, these models provide accurate values for H_v for systems including hard and superhard coatings. In this study we have used the model proposed by Ichimura *et al.* [191], where

$$a = 3\left(\frac{H_f}{E_f}\right)^{1/2} \frac{t}{d} \tan^{1/3} 68^o\,, \qquad (A.3)$$

and E_f is the Young's modulus of the coating.

This technique was applied to indentation with loads ranging from 1 to 10 N. Taking into account the effect of elastic recovery on the residual indentation trace, $H_v = H_f$ was obtained by extrapolation for an indentation depth of 1 μm. The results are presented in Table A.1 where an important increase in H_v upon adding Si can be seen. H_v is seen to present a maximum value of 28.0 GPa for C_{Si} = 11.6 at.%.

A.3.4 Toughness

Circular cracking generally occurs around the periphery of an indentation mark when indenting hard coatings on soft substrates. In fact, Musil and Jirout [29] have described this behavior in detail for different coating systems (Zr-Cu-O, Zr-Cu-C and Me-Si-N) on steel 15330 substrates. They reported on the importance of the ratio of the indentation depth (h) over the coating thickness (t) at the cracking onset and showed that the resistance to film cracking increases with an increasing H^3/E^2 ratio, which represents the resistance of the material to plastic deformation [221]. Also, Zhang *et al.* [228] have indicated that coating plasticity (R_p) should be a "rough" indication of K_{IC}.

Therefore, in order to qualitatively assess K_{IC}, we identified the h/t ratio at which circular cracking first appeared ($(h/t)_c$) when indenting with a Vickers indenter at increasing loads. As indicated in Table A.1, the CrN coating exhibits the highest value of $(h/t)_c$. It can be observed that the $(h/t)_c$ values are proportional to R_p as measured by DSI, but they also correlate well with the inverse of H_v^3/E_r^2. The results bring to light an apparent contradiction between the theories predicting a proportionality relationship between K_{IC}, R_p and H_v^3/E_r^2.

We believe that these conflicting results are obtained because the formation of circular cracking is not governed by toughness but rather by the inability of the coating to accommodate the important plastic deformation of the substrate. We found that the onset of cracking is also proportional to the ratio of the hardness of the substrate over that of the coating (H_s/H_f). These results indicate that the less the substrate plastically deforms relative to the coating (high value of H_s/H_f) and the better the coating can accommodate a plastic deformation (high value of R_p), the more such a coating will resist to circular cracking. In fact, the coating with the lowest H_v^3/E_r^2 ratio resists best to circular cracking because of higher R_p and H_s/H_f values.

Although the above observations suggest that this test is not representative of coating toughness, we believe that the interesting relationship between circular cracking, R_p and H_s/H_f is important to take into account when evaluating the materials resistance to mechanical intrusion.

A.3.5 Erosion

The erosion rates for $\theta = 90^\circ$ (ER_{90}) are presented in Table A.1. We can observe an important drop in ER_{90} values from the SS410 substrate to CrN and Cr-Si-N coatings. ER_{90} remains constant until reaching its minimum of 5.2 x 10^{-3} mg/g for C_{Si} = 11.6 at.%. The brittle nature of the erosion behavior can be most notably observed in Figure A.1 (c) where brittle fracture of the columnar structure of the CrN coating is observed, and in Figure A.1 (d) where severe chipping of the surface is seen. Moreover, this surface damage cannot be observed in Figure A.1 (e) for the Cr-Si-N coating with C_{Si} = 11.6 at.% indicating a high resistance to SPE.

A.4 Discussion

In order to establish an appropriate relationship between the ER and the films elasto-plastic properties we plot, in Figure A.3, the values of ER_{90}, H_v and of the H_v^3/E_r^2 ratio measured at an indentation depth of 1 μm with respect to C_{Si}. It can be clearly seen that the ER_{90} value is inversely proportional to H_v and H_v^3/E_r^2 for our Cr-Si-N coating system.

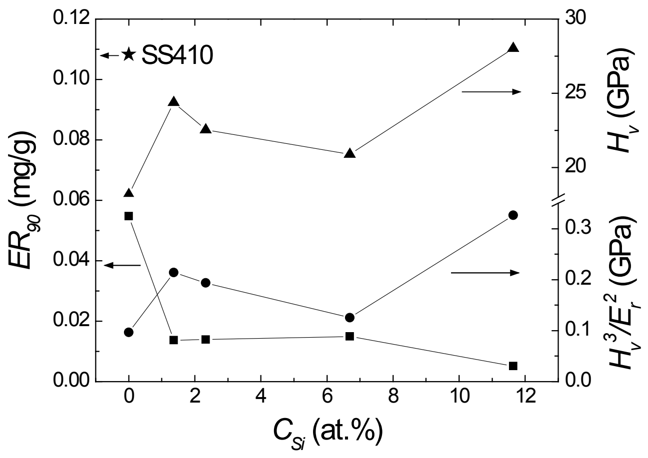

Figure A.3: Erosion rate (■), H_v (▲) and H_v^3/E_r^2 (●) as a function of C_{Si}.

Because of the relatively large contact area during particle impact, many grains and columns are deformed. We believe that it is for this reason that H_v (Vickers) is more representative of ER_{90} than H (DSI). While DSI is representative of intrinsic material properties, the small scale of such a method confines the indentations to single columns and does not measure the micrometric material properties which are representative of the SPE mechanisms. Upon adding Si to CrN, an increase in H and H_v is observed as well along with a change in the texture from [110] to [111] orientations. The latter effect suggests that Me substitution by Si atoms causes increased strain in the CrN lattice since preferred orientation changes from [110] to [111] typically occur because of the better ability of the latter one to accommodate lattice strain [227]. The Cr-Si-N coating with C_{Si} = 11.6 at.% presents a texture change from (111) to (200), indicative of coating densification because (111) textured coatings typically possess a more opened structure, with more voids between the columns [229]. The important decrease of d_g combined with the change in texture seems to indicate that for this latter coating, the limit of solubility has been exceeded and that segregation of SiN_x around CrN grains has occurred, changing the growth mechanism [4-8]. This nanostructural change resulting in microstructural densification seems to lead to an increased H_v with a related decrease in ER_{90}.

The volume removed by SPE (V_e) for brittle materials has been modeled by the following general expression [202, 230]:

$$V_e \propto V_p^a D^b \rho_p^c K_{ICt}^d H_t^e, \tag{A.4}$$

where V_p, D and ρ_p are the velocity, radius and density of the impacting particles. K_{ICt} and H_t are the toughness and hardness of the target material. These models were developed for bulk brittle materials where material removal is governed by the generation of lateral crack systems under very hard impacting solid particles. Because of their high thickness and adherence, the coatings evaluated in this study should exhibit bulk behavior. However, because alumina has a lower hardness then the studied coatings (H_p/H_t = 0.48 to 0.74), these models may not apply. In fact, Shipway and Hutchings [12] showed that for $H_p/H_t > 1$ lateral cracking occurred and W presented a weak dependence on H_t. On the other hand, when $H_p/H_t < 1$ small scale chipping occurred and V_e presented a strong dependence on H_t. It seems likely that our tested coatings exhibit this second material removal mechanism since we observe a very strong dependence of V_e on H_t ($ER_{90} \propto H_v^{-6.1}$) and that evidence of chipping can be observed in Figures A.1 (c) and (d). Furthermore, the occurrence of this chipping mechanism is additionally supported by the observed high values of H_v^3/E_r^2 for which materials resist more readily to the onset of plastic deformation. In fact, according to the above mentioned erosion models, V_e is proportional to the plastically deformed volume under the impact site. Because materials with high values of H_v^3/E_r^2 are highly resistant to plastic deformation, SPE should therefore be significantly reduced because plastic deformation is significantly diminished or simply does not occur.

A.5 Conclusions

In this study, we have studied the effect of silicon addition to CrN-based coatings on their microstructure, mechanical properties and more specifically on their resistance to SPE. We have found that:

1) Circular cracking during Vickers indentation of hard coatings on ductile substrates is not representative of coating toughness.
2) Addition of Si to CrN-based coatings significantly increases their resistance to SPE.
3) SPE is more closely correlated to micro-hardness than to nano-hardness because of the large volume of interaction during single impact events during SPE.
4) Because $H_p < H_t$ the material removal mechanism is not by lateral fracture but by a chipping mechanism.
5) H_v^3/E_r^2 possibly influences the erosion mechanism by reducing or eliminating the plastically deformed volume under individual impact sites.

Acknowledgements

The authors wish to thank Dr. Philippe Robin for helpful discussions. This work has been supported by NSERC CRDPJ 328038-05 and CRIAQ.